AN EXPERIMENTAL AND ANALYTICAL STUDY OF THE EFFECT OF GRAIN REFINEMENT ON STRENGTH AND FORMABILITY OF METALS

by

Xiang Li

A dissertation submitted in partial fulfillment
of the requirements for the degree of
Doctor of Philosophy
(Materials Science and Engineering)
In The University of Michigan
2008

Doctoral Committee:

Professor Amit K. Ghosh, Chair
Professor Michael Atzmon
Professor Elijah Kannatey-Asibu Jr
Professor Richard E. Robertson

To my parents Siyi Li and Suyue Huang,
my parents-in-law Xicong Yang and Xiangwei Jiang,
my wife Yu Yang, my sister Yun Li and brother-in-law Jianxing Guo,
with gratitude, admiration, and love.

and

To the death in 5.12 earthquake in China
with condolence, sympathy

ACKNOWLEDGEMENTS

I extend my sincere gratitude and appreciation to my research advisor, Professor Amit Ghosh for supporting and leading me through this research work. His enthusiasm and strong interest on research have made a deep impression on me. His insightful and extensive comments made me sharpen my understanding of mechanical metallurgy which is embodied both in and outside this thesis. I feel privileged to have worked with him. I am highly indebted to Professor William Hosford whose valuable suggestions have helped my research and writing of this thesis, though he is not in my committee eventually. It is my great honor to obtain advice from a renowned metallurgist such as him. I am also grateful to the other committee members, Professor Richard E. Robertson, Professor Michael Atzmon and Professor Elijah Kannatey-Asibu Jr, for their joining in my committee and valuable input in this thesis, and Dr. Ray Decker and Professor Suman Das for their help in some work.

I would like to express my thanks to Dr. Yi Liu and Dr. Qi Yang for helpful discussions and assistance in this work. I would also like to thank Ms. Qi Ying for giving me instructions on using experimental equipments. Thanks to Dr. Kai Sun and Dr. Haiping Sun for their help on the use of electon microscope at EMAL. Thanks are also due to Ms. Nancy Polashak, Ms. Renee Hilgendorf, Mr. Keith Mcltyre, Mr. Justin Scanlon and Mr.

Kevin Worth for providing much assistance during my graduate study. The help from my friends Rick Lee, Bilal Mansoor, Sibasish Mukherjee, Jia Tao, Dajun Yuan, Yanbin Cheng and any other people who are not mentioned here are acknowledged as well.

I gratefully acknowledge the financial and materials support from the U.S. National Science Foundation through award DMR 0314218, Air Force, US Steel and Thixomat Inc.

Especially, I would like to give my special thanks to my wife Yu Yang whose patience, love and encouragement have enbled me to complete this work. The unselfish support from my parents Siyi Li and Suyue Huang, my parents-in-law Xicong Yang and Xiangwei Jiang, my sister Yun Li and my brother-in-law Jianxing Guo is highly appreciated.

TABLE OF CONTENTS

DEDICATION …….…….. ii
ACKNOWLEDGEMENTS ……...… iii
LIST OF TABLES ……...…….. ix
LIST OF FIGURES ……...…....… x
CHAPTER
1. GENERAL INTRODUCTION ……....… 1
1.1 Background ……..... 2
1.1.1 Observations of strengthening and its explanation ……... 2
1.1.2 Observations of enhanced formability ……...4
1.1.3 Observations on weakening effect ……..... 7
1.1.4 The role of grain boundary …….……... 8
1.2 Analytical Study ……..... 10
1.3 Experimental Studies on Fine Grain Metal Alloys ……...… 10
1.4 References ……..…….... 12

2. ESTIMATING STRESS-STRAIN RESPONSE FOR SINGLE CRYSTAL AND POLYCRYSTAL BY ANISOTROPIC CONTINUUM PLASTICITY APPROACH
Purpose and Organization ….....……...… 16
Abstract of Part A: Effect of Single Crystal Orientation and Crystal Size …..17
2A.1 Introduction …….…... 18
2A.1.1 Crystal orientation …….…… 18
2A.1.2 Crystal size ……...…. 20
2A.2 Approach ……..…….....… 22
2A.3 Results and Discussions ...…….. 24
2A.3.1 Effect of loading direction, crystal anisotropy and strain hardening rate …….…….. 24
2A.3.2 Effect of crystal size …….……. 27
2A.3.3 Effect of *p* and *A* in Equation (2A-5) …….…... 28
2A.3.4 Effect of varying crystal size …….…… 29

2A.4 Conclusions ……..……...… 31
2A.5 References ..……..……..… 44

Abstract of Part B: Effect of Grain Size and Mantle Zone Response ……..... 45
2B.1 Introduction …… 46
2B.2 Approach …… 51
2B.3 Results and Discussions …...…….. 53
2B.3.1 General stress-strain responses ……..... 53
2B.3.2 Effect of material constants on the stress-strain behavior ……... 55
2B.3.3 Grain size dependence of strength …...……..... 59
2B.3.4 Evaluation of calculated flow stability ……..……... 60
2B.3.5 Detailed examination on grain size dependence of strength …..... 62
2B.4 Summary and Conclusions …….……..... 64
2B.5 References ...……..……… 85
Appendix 1 Finite Element Modeling Procedure …….....… 88
A1.1 Modeling Steps ……..... 88
A1.2 Definition and Data Input ……...……... 116
Part A. Single crystal ….……... 116
Part B. Polycrystal ……...…. 119
Appendix 2 Literature Review on the Grain Size Strengthening and Weakening effect ……..... 131
Appendix 3 Justification for Choice of Grain Boundary Mantle Zone Thickness in Simulation……..... 137

3. EFFECT OF SEVERE PLASTIC DEFORMATION ON THIXOMOLDED® AZ91D MG ALLOY

Abstract …….…...…. 145
3.1 Introduction …….…...…. 146
3.2 Experimental Methods …...…….……..... 148
3.2.1 Material …….……. 148
3.2.2 Processing …….……. 149
3.2.3 Microstructure ……..…...… 150
3.2.4 Mechanical tests …….…...… 151
3.2.5 Texture measurement ……...…. 152
3.3 Results ……...……. 153
3.3.1 Pure compression …….….... 153

3.3.2 ABRC processing ……. 155
3.3.3 Texture evolution ……..…… 158
3.4 Discussions ……...……...…… 159
3.3.1 Pure compression ……..... 159
3.3.2 ABRC processing ……. 161
3.3.3 Texture evolution ……..…… 162
3.5 Conclusions ……...…. 163
3.6 References …….……. 185

4. LOW-TEMPERATURE SUPERPLASTICITY OF SUBMICROCRYSTALLINE TI-6AL-4V PROCESSED BY NON-ISOTHERMAL SEVERE PLASTIC DEFORMATION

Abstract ……...…..… 187
4.1 Introduction …… 188
4.2 Materials and Procedures ……...… 190
4.2.1 Materials …… 190
4.2.2 Setup of equipment and processing ……..……...…. 191
4.2.3 Experimental procedures ……...… 191
4.3 Results ……...……. 195
4.3.1 Microstructural evolution …….…. 195
4.3.2 Superplastic properties ……...… 197
4.4 Discussions …...……..…… 206
4.4.1 Microstructure evolution ……... 206
4.4.2 Enhanced superplasticity ……... 208
4.4.3 Strain-rate sensitivity ……..… 209
4.4.4 Activation energy for deformation ...……. 210
4.5 Conclusions ……..... 212
4.6 References …….. 230

5. ROLE OF DEFORMATION TEMPERATURE ON TRANSFORMATION INDUCED PLASTICITY IN ADVANCED TRIP STEEL SHEET

Abstract ……..… 233
5.1 Introduction ……..… 234
5.2 Materials and Experiments ……..... 235
5.2.1 Materials …… 235
5.2.2 Microstructure analysis ……..... 235

5.2.3 Mechanical tests ……..…... 235
5.3 Results ……..... 237
5.3.1 Microstructure ……..…. 237
5.3.2 Stress-strain behaviors ……..... 238
5.3.3 Mechanical properties ……...… 239
5.3.4 Effects of strain hardening and strain rate hardening ……... 241
5.3.5 Post-deformed properties ……..…. 241
5.4 Discussions ……...……. 242
5.5 Conclusions ……...… 246
5.6 References ……..… 266

6. SUMMARY AND RECOMMENDATIONS FOR FUTURE WORK
6.1 Summary ……..… 267
6.2 Recommendations for Future Work ……..……..…. 269

LIST OF TABLES

Table

2A.1 Nomenclature for single crystal model ……..……... …... 33

2A.2 Constitutive equations describing stress-strain behavior of single crystal …….……34

2A.3 The values of stress ratios for input of FEM analysis (r_x = 1.5 and r_x = 2.0 were assumed for the present study) ..... …... 35

2B.1 Nomenclature for polycrystals model …….....…... 66

2B.2 Parameters in constitutive equation describing the stress-strain properties of grain and grain boundary (“Mantle Zone”) …..... …... 67

A1.1 Physical sample size represented by simulation cell …..... …. 121

A1.2 Area fraction of grain boundary region (“Mantle Zone”) for cases with different grain diameter ……..… …. 122

A1.3 Relation between *SCU** and physical dimension ……..…. …. 123

3.1 Mechanical Property of Test Materials …….…… …. 165

3.2 Microhardness of thixomolded AZ91D at different processing step …….…… …. 166

3.3 Elongation to failure of thixomolded AZ91D with different processing conditions …….……..... 167

4.1 Elongation to failure for UFG Ti-6Al-4V alloys with various temperature and strain rate …….…….. 214

4.2 Determination of diffusion coefficient for UFG Ti-6Al-4V alloy ……. 215

5.1 Chemical composition of commercial TRIP steel used in this study, % ……...……...…. 248

5.2 Mechanical properties of TRIP steel for tests at various temperatures ……...…..249

LIST OF FIGURES

Figure

2A.1 Micropillar compression test showing crystal size dependent of strength of single crystal from literature [13] ……..……... …..... 36

2A.2 Orientation of single crystal with respect to the loading direction (2). The axis of crystal anisotropy is Z direction, (transverse anisotropy; X-Y plane is isotropic) ……..……..……...…37

2A.3 Stress-strain curves are shown for different crystal orientation of single crystal. Crystal orientation, θ is defined as the angle between sample plane normal and axis of anisotropy, Z. Effect of different strain hardening rate is shown (a) n = 0.05 and (b) n = 0.15 ……..…..……... …….. 38

2A.4 Stress-strain curves are shown in (a) for different crystal orientation of single crystal. Crystal orientation, θ is defined as the angle between sample plane normal and axis of anisotropy, Z. Flow stress for ε = 0.15 are shown in (b) as a function of θ …….…….. 39

2A.5 Stress-strain curves are shown (a) for different crystal orientation of single crystal (l = 0.422 μm). Crystal orientation, θ is defined as the angle between sample plane normal and axis of anisotropy, Z; (b) for various crystal sizes, where crystal orientation (θ = 0). The uniform strain and peak flow stress are plotted as functions of crystal size in (c) ……....……..……..… 40

2A.6 Stress-strain curves for various crystal sizes are shown in (a). The uniform strain and peak flow stress in tension direction are, shown as functions of crystal size in (b) …….……..…….. 41

2A.7 Stress-strain curves are shown for various crystal sizes in (a), (b) and (b) are for different values of crystal size-related constants, A and p ……...…….. 42

2A.8 The difference between the flow strength at 2% true strain (σ) for a crystal size, l and the flow strength for large crystal size (σ_0), as determined by simulation results, is plotted as a function of crystal size, l ……..……..... 43

2B.1 Schematic representation of hexagonal grain in polycrystalline metals subjected to tensile deformation. The dotted cell shown within this polycrystalline aggregate is taken as a representative unit cell for FEM simulation. The details of this unit cell (SCU) show grain boundary region with different orientations of crystals across them ……... ……..... 68

2B.2 Calculated stress-strain curves are shown for different grain size and strain rate (A = 5 $MPa.\mu m$, p = 1, B = 3 GPa and q = 0.1) (assumed r = 1.5) ……... …….. 69

2B.3 Calculated stress-strain curves are shown for different grain size and strain rate (A = 5 $MPa.\mu m$, p = 1, B = 15 GPa and q = 0.1) (assumed r = 1.5) ……... ……..... 70

2B.4 Calculated stress-strain curves are shown for different grain size and strain rate (A = 15 $MPa.\mu m$, p = 1, B = 3 GPa and q = 0.1) (assumed r = 1.5) ……... …...…... 71

2B.5 Calculated stress-strain curves are shown for different grain size and strain rate (A = 15 $MPa.\mu m$, p = 1, B = 15 GPa and q = 0.1) (assumed r = 1.5) ……... ……..... 72

2B.6 Calculated stress-strain curves are shown for different grain size and strain rate (A = 15 $MPa.\mu m^{0.9}$, p = 0.9, B = 3 GPa and q = 0.1) (assumed r = 1.5) ……... 73

2B.7 Calculated stress-strain curves are shown for different grain size and strain rate (A = 15 $MPa.\mu m^{0.9}$, p = 0.9, B = 3 GPa and q = 0.3) (assumed r = 1.5) ……..……...…….. 74

2B.8 Calculated stress-strain curves are shown for different grain size and strain rate (A = 15 $MPa.\mu m^{0.6}$, p = 0.6, B = 3 GPa and q = 0.1) (assumed r = 1.5) ……..……...…….. 75

2B.9 Equivalent plastic strain maps for polycrystals with grain size of 4.92 nm showing the strain distribution within grain interior and mantle zone at two different strain rates and 3% total strain (A = 5 $MPa.\mu m$, p = 1, B = 3 GPa and q = 0.1) ……..…..... 76

2B.10 Stress-strain curves for polycrystals with various grain sizes showing the effect of grain interior and mantle zone properties on the stress-strain behaviors for a grain boundary misorientation represented 0 – 75^{o} twist orientation, r = 1.5, p = 1 and q = 0.1 ……..…..... 77

2B.11 Stress-strain curves for polycrystals with various grain sizes showing the effects of grain size exponent, p and strain rate on the stress-strain behaviors for a grain boundary misorientation represented 0 – 75° twist orientation, r = 1.5, A = 15 $MPa \bullet \mu m^{0.9}$, B = 3 GPa, and q = 0.1 …….. ……..... 78

2B.12 Equivalent plastic strain maps for polycrystals with grain size of 4.92 nm showing the strain distribution within the grain interior and mantle zone for two different p values and 2% total strain (A = 5 $MPa.\mu m$, B = 3 GPa, q = 0.1 and strain rate: $3.5 \times 10^{-2} s^{-1}$) …….. 79

2B.13 Stress-strain curves for polycrystals with various grain sizes showing the effect of viscosity parameter, q on the stress-strain behaviors for a grain boundary misorientation represented 0 – 75° twist orientation, r = 1.5, A = 15 $MPa \bullet \mu m^{0.9}$, p = 0.9 and B = 3 GPa ……...……...…. …..…… 80

2B.14 Equivalent plastic strain map for polycrystal with grain size of 4.92 nm showing the strain distribution within the grain interior and mantle zone (A = 15 $MPa.\mu m^{p}$, p = 0.9, B = 3 GPa, q = 0.3, and strain rate: $3.5 \times 10^{-2} s^{-1}$) …….…….. ……. 81

2B.15 Calculated strength value is plotted as a function of $d^{-1/2}$ for various constants in equations for grain interior and mantle zone ……...…….. 82

2B.16 Calculated flow stability for polycrystals for various grain sizes and constants in equations for grain interior and mantle zone ……..……...…….. 83

2B.17 The difference between the flow strength at true strain of 0.01 for a given grain size and the flow strength for large grain size, as determined by simulation results, are plotted as a function of grain size …… …….. 84

A1.1 Simulation cell used for modeling stress-strain response of single crystal, (a) test sample geometry, (b) boundary condition and (c) FEM representation mesh …….. …...…. 124

A1.2 Orientation of single crystal with respect to the loading direction (2). The axis of crystal anisotropy is Z direction, (transverse anisotropy; X-Y plane is isotropic) …….……...…… 125

A1.3 Selection of simulation cell unit as described in text ……..…… 126
A1.4 Grain structure for various physical grain diameters, (a) 4.92 *nm*, (b) 58.8 *nm* and (c) 5.98 μm ……..…. ……..... 127
A1.5 Equivalent grain diameter based on area for hexagonal grains used in simulation cell geometry, and ratios of physical size of grain to simulation cell size ……..…. …… 128
A1.6 Schematic illustration of boundary conditions for polycrystal model at various locations in test specimen ……..……. 129
A1.7 Meshing for specific cases of geometry used for representing various physical grain sizes, 4.92 *nm*, (b) 58.8 *nm* and (c) 5.98 μm …….. …… 130
A2.1 The Hall-Petch relation for different polycrystalline metals, (a) electrodeposited nickel, (b) mild steel, (c) aluminum, copper and silver, (d) α-titanium, (e) 70:30 brass and (f) iron ……..…… 134
A2.2 The relationships between strength properties and grain diameter of polycrystalline metals showing deviation from Hall-Petch relation ((a) palladium, (b) TiO_2, (c) nickel, (d) copper), or even inverse Hall-Petch relation ((e) copper and palladium, and (f) Ni-P alloy) ……..……..... 135
A2.3 The relationships between strength properties and grain diameter of polycrystalline metals showing strengthening and weakening effect vs. decreasing grain size in the same materials, (a) copper and (b) nickel ……. ……..... 136
A3.1 Dislocation arrays in boundaries of different misorientation …… …… 139
A3.2. Influence of grain boundary structure on packing density and traction of grain boundary. (a) Various atomic models of grain boundary structure and (b) corresponding packing density. Atomic structures of Σ5, Σ41 and Σ61 [100] twist boundaries in fcc as generated by the GCSN model [A3-4], and (c) First-princiles calculated traction curves for decohesion between (100) planes, (111) planes and a Σ9, symmetric tilt boundary in fcc aluminum [A3-5] ……..…… 140
A3.3 Mantle region shown on High Resolution TEM image of a grain boundary in nanograin Al 1420 [A3-6] ……..…… 141

A3.4 Grain boundary in a Cast Ni-base Superalloy showing large size grain boundary undulations [A3-7] …… 142
A3.5 Strain map showing strain concentration on the grain boundary perturbations [A3-8] ……...…… 143
3.1 Thixomolded microstructure of AZ91D alloy (a) showing primary solid phase (b) and eutectic phase (c) ……...…… 168
3.2 Particle size distribution of α particles of thixomolded AZ91D Mg alloy, (a) middle section, (b) near-surface section ……...…… 169
3.3 Illustrations of processing methods for thixomolded AZ91D alloy at elevated temperature: a) Pure compression, b) Alternate Biaxial Reverse Corrugation (ABRC) ……... …… 170
3.4 Microstructure of thixomolded AZ91D after pure compression at 120 ^{o}C with different strain level (Primary solid particle) (a) ε = 0.24, (b) ε = 2.37, and (c) shows the method for measuring the angle between twinning plane and compression axis …… …… 171
3.5 Distributions of angles between the twinning plane and compression axis in thixomolded AZ91D after pure compression at 120 ^{o}C with various strain level, (a) ε = 0.24, (b) ε = 1.64, (c) ε = 1.96, (d) ε = 2.37 ……..…… 172
3.6 Twinning characteristics, (a) the average values of angle between the twinning plane and compression axis and twin density in primary solid α particles vs. strain of thixomolded AZ91D after pure compression at 120 ^{o}C, (b) the number density of particles with twin (number/μm^2) vs. strain of thixomolded AZ91D after pure compression at 120^{o}C …… …… 173
3.7 Size distributions of primary solid particles that are twinned in the thixomolded AZ91D after pure compression at 120^{o}C vary with strains ……..…… 174
3.8 Variation of microhardness of the AZ91D alloy at different processing step ……...…… 175
3.9 Microstructure of thixomolded AZ91D after pure compression at 120^{o}C with strain of 2.37 and annealing at (a) 150^{o}C and (b) 250^{o}C …….. …… 176

3.10 Microstructure of thixomolded AZ91D alloy after ABRC processing with true strain 4.13 and grain size distribution (a) low magnification showing original primary solid phase and eutectic phase, (b) fine grain region, (c) grain size distribution … ……..... 177

3.11 Room-temperature mechanical properties of thxiomolded and ABRC-processed AZ91D alloys, (a) the relationship of Vickers hardness vs. grain size, (b) room-temperature tensile stress versus strain curve, and (c) tensile strength vs elongation …….……..... 178

3.12 SEM image of fracture surface of ABRC-processed thixomolded AZ91D after room-temperature tensile test ……... …… 179

3.13 Stress-strain curves of thixomolded AZ91D with different processing condition …….. …… 180

3.14 Dome height of ABRC-processed thixomolded AZ91D alloy and as-thixomolded material after gas pressure forming, showing that as-received alloy fractures prematurely under biaxial tension while as-processed material of fine grain structure shows improved biaxial formability ……. …… 181

3.15 Observation of fracture surfaces of biaxially deformed samples shows that ABRC-processed material has more homogeneous structure (a) as-thixomolded, (b) ABRC-processed ……...…… 182

3.16 Pole figures for (0002) crystallographic plane of (a) as-thixomolded AZ91D, (b) after pure compression and (c) after ABRC processing ……...…… 183

3.17 Sketch of subdivison of initial coarse primary solid grain. (a) Twinning at low strain level, (b) Slip within inter-twin region at medium strain level and (c) Shearing off with high strain level …… 184

4.1 Microstructure of as-received Ti-6Al-4V alloy showing equiaxial alpha (gray in color) + beta matrix (white in color); average grain size of alpha phase is 8 μm ……..……..……. …… 216

4.2 Illustration of setup for severe compression under superimposed hydrostatic pressure, (a) setup of equipment and (b) setup of specimen and pressure medium (steel block with hole in center) . …… 217

4.3 Schedule of step heating and loading shows simultaneously rising temperature during deformation …….. …… 218

4.4 Microstructures of Ti-6Al-4V alloy after beta heat treated at 1020 ^{o}C and 30 minutes show needle-shaped martensite alpha phase, (a) Optical Image and (b) Secondary Electronic Image. Many group of parallel martensite intersect with each other to subdivide the coarse into small segments …….. …… 219

4.5 Microstructures of Ti-6Al-4V alloy after beta heat treated 1020^{o}C for 30 minutes and static annealing (a) Annealed from room temperature to 350 ^{o}C for 60 minutes, (b) Annealed from room temperature to 350 ^{o}C for 60 minutes plus secondary annealing from 350 ^{o}C to 475 ^{o}C for 60 minutes, Microstructure shows stable martensite structure under static thermal condition ..……..... 220

4.6 SEM (a) and TEM (b) micrograph of Ti-6Al-4V alloy after non-isothermal severe plastic deformation shows submicrocrystalline and equiaxed grain structure …….. …… 221

4.7 Stress-strain curves for both UFG and commercial Ti-6Al-4V alloys tested at various temperature and strain rate ……... …… 222

4.8 Pictures of samples before and after tensile testing ……... …… 223

4.9 Extension measurements on different regions of a tensile tested specimen …… …… 224

4.10 Calculation of activation energy for superplastic tensile testing of UFG Ti-6Al-4V within temperature range of interest ……... …… 225

4.11 Evaluation of strain-rate sensitivity of ultra-fine grain Ti-6Al-4V alloy by decremental step-strain rate test at 600 ^{o}C ……... …… 226

4.12 Evaluation of strain rate sensitivity of ultra-fine grain Ti-6Al-4V alloy by jump test at 650 ^{o}C ……... …… 227

4.13 Evolution of grain size with true strain for ultra-fine grain Ti-6Al-4V alloy at 650 ^{o}C and 5×10^{-4} s^{-1} ……. …… 228

4.14 Grain growth behaviors of ultra-fine grain Ti-6Al-4V alloy during superplastic tensile testing at 700 ^{o}C …….. …… 229

5.1 Schematics of test methods to determine *m*-value (a) CHS jump test, and (b) stress-relaxation test ……... …… 250

5.2 Microstructure of as-received TRIP steel (a) Light optical image, (b) SEM image ……... …… 251

5.3 X-ray diffraction pattern of as-received TRIP steel ……... …… 252

5.4 Stree-strain curves of as-received TRIP steel, (a) engineering stress- strain, (b) true stress-strain, (c) log stress-log strain ……..…… 253
5.5 Stree-strain curves of cold-rolled TRIP steel (ε = 0.28), (a) engineering stress- strain, (b) true stress- strain, (c) log stress-log strain ……..…… 254
5.6 Mechanical properties of investigated TRIP steels …… 255
5.7(a) Fracture surfaces of tensile tested specimen at various temperatures for as-received TRIP steel …… ……..... 256
5.7(b) Fracture surfaces of tensile tested specimen at various temperatures for cold-rolled TRIP steel ……..…… 257
5.7(c) Changes of fracture strain with temperature show that increasing temperature increases the strain in thickness ……..…… 258
5.8 Changes of *n-value* and *m-value* of investigated TRIP steel with temperature …… …… 259
5.9 Microhardness of investigated TRIP steel for various temperatures (a) As-received, (b) Cold-rolled ……... …… 260
5.10 Effects of temperature on the strength and strain of high-Mn and low-Mn TRIP steel (in presnt study). The data of black curves is from reference [2], the data of red curves is for the present study. Note: $R_{p0.2}$ --- Yield stress, R_m --- Tensile strength, e_{un} --- Uniform elongation, and e_f --- Total elongation …… …… 261
5.11 Microstructures of specimen tested at 250^oC for as-received TRIP steel, (a) grip region, (b) gauge region ……..…… 262
5.12 Temperature and strain effects on the change of volume fraction of non-ferrite phase ……..…… 263
5.13 Deformed microstructure of as-received TRIP steel tested at room temperature ……...…… 264
5.14 Deformed microstructure of as-received TRIP steel tested at 400^oC, (a) grip region, (b) gauge region ……..…… 265

CHAPTER 1

GENERAL INTRODUCTION

This research is about the effect of grain refinement on the strength and formability of polycrystalline metals. The size of grain or microstructure is important for mechanical properties of polycrystalline materials, as it affects the strength, ductility, elevated temperature flow and formability of materials. These effects of size occur from coarse grain size down to the grain size of micrometer as well as to the grain size in the nanometer range. In studying the effects of grain refinement on the mechanical behaviors of polycrystalline materials, two different paths are taken:

1) Analytically determining the mechanical response of polycrystalline material based on the response of its constituents, which are grain interior with crystal slips and mantle zone with viscous behavior;

2) Studying grain refinements of materials by different processing methods, such as sinewave deformation, compression under constraint and rolling, and determining their effects on mechanical properties at room temperature and elevated temperature at different strain rates. Such effects were done with hcp magnesium alloy, hcp titanium alloy and bcc-fcc structure steel (TRIP steel).

1.1 Background

1.1.1 Observations of strengthening and its explanation

Originated from Hall [1] and Petch [2], an empirical relation between the strength properties and grain size of polycrystalline metal materials was established on the basis of experimental observations, which was called Hall-Petch relation and can be described as $\sigma = \sigma_0 + kd^{-1/2}$, where σ is flow stress of materials, σ_0 is the friction stress, k is the stress intensity, and d is grain size. In light of the principle of this well-known relation, the strength properties can be greatly improved by refining the grain structure of materials.

It is well-known that the grain refinement brings substantial advantages to the low-temperature mechanical properties of polycrystalline materials. Investigated by Petch [3] and Armstrong [4], the increase of lower yield stress, flow stress at various strain values, and true ductile fracture stress of mild steel were shown to depend on the grain refinement. Similar influences of grain refinement on the flow stress were reported to Ag [5], Al [6] Cu [7, 8], Mg and Mg alloys [9], Ti [10], and Ni and Ni-based alloys [11-13]. The effect of grain refinement on strengthening of polycrystalline materials was explained via dislocation pile-up theory by Eshelby, Frank and Nabarro [14], and Cottrell [15]. It was suggested the yield strength increases as grain size decreases because pile-ups in the fine-grained materials contain fewer dislocations, the stress at the tip of

the pile-up decrease and, thus, a larger applied stress is required for dislocations to "burst" through the grain boundaries [14], or to activate dislocations in the adjacent grain [15] by Frank-Read source. Experiments on accurate measurements of the slip band step heights via interferometric observation provided the information about the early stages of plastic deformation in polycrystals [16, 17], which presented the direct evidence for verifying the dislocation pile-up model [18]. Instead of using Pile-up model, Li [19] proposed a composite model to explain the Hall-Petch relation, and suggested that grain boundary was a source of dislocations, and the onset of yielding in polycrystals was associated with the activation of the grain-boundary dislocation. According to Li, it is the grain-boundary ledges that generated dislocations, and "pumping" them into the grain. These dislocations act as *Taylor* forests in regions close to the boundary. Flow stress is the stress required to move dislocations through these forests. By assuming the same ledge density per unit area for various grain sizes, the density of dislocation forests is proportional to the grain boundary surface, which is inversely proportional to the grain size. This theory of grain boundary dislocation source is increasingly accepted because of the regular dislocation arrays. However, in contrast to the Pile-up model and Composite model, the Work-hardening model proposed by Conrad [20] emphasized the motion of dislocations through the grain rather than the behavior in the immediate vicinity of the grain boundary, and assumed that the specimens of small grain size have a higher dislocation density than the one of large grain size at a given value of plastic strain. Conrad's theory unfortunately fails to recognize that the onset of plastic flow is a highly

localized process where only the grain boundaries and the regions closely adjoining them participate. Other explanation based on the work-hardening model [21] and composite model [22] also attempted to rationalize the Hall-Petch relation. Furthermore, besides yield stress, flow stress and fracture stress, the twinning stress [23] also showed the dependence on the grain diameter similar to that in Hall-Petch relation. All in all, the experiments and theories mentioned above demonstrate the well-established of Hall-Petch relation for polycrystalline materials. More detailed about strengthening effect of grain refinement in polycrystals is discussed in Appendix 2 of Chapter 2.

In addition to the strengthening effect of grain refinement in polycrystals, single crystal also shows strong dependence of strength on crystal size. Recent development of micro-pillar compression on the single crystals revealed that strength of single crystal increases with decreasing crystal size [24-27]. The dependence of strength on crystal size varies in different crystal size regimes. Different slopes of *log* (strength) versus *log* (crystal size) curves have been reported by different investigators. About strengthening effect of small crystal is discussed in more detailed in Part A of Chapter 2.

1.1.2 Observations of enhanced formability

Besides the strengthening effect, grain refinement can sometimes enhance the room-temperature ductility of polycrystalline materials due to the more homogeneous

strain distribution due to the smaller dislocation slip length, and reduced stress concentration. Tests on superplastic Pb-Sn alloy at room temperature show high elongation to failure (>500%) with a fine-grain structure (3.3 μm) compared to a coarse grain structure [28]. AZ31B Mg alloys processed by severe plastic deformation exhibit highly improved room-temperature ductility with 29% elongation to failure compared to the coarse grain sample (13.5% elongation to failure) [29]. Investigation on MA8 alloy [30] showed the greatly increased yield strength as well as elongation to failure. Similar result was also found on the study of pure magnesium and Mg-0.9Al alloy [31]. In austenitic stainless steel, Mannan and et al. [32] reported a sharp increase in ductility with grain size until optimal value was reached around 100 μm at room temperature. For hard-to-work materials, grain refinement to submicron size (<1 μm) not only decreases the temperatures of the brittle-ductile transition, but also increases the room-temperature plasticity of Ti_3Al [33]. However, it was also found on Mg alloys that the grain refinement reduced the strain hardening rate of materials [29, 30], which is attributed to the absorption of dislocations in the grain boundary. Although the low strain hardening rate results in lower uniform strain, the higher strain rate sensitivity due to grain boundary sliding can compensate for this with the refined grain structure [29], to produce a higher tensile elongation. Nevertheless, with further reduction in grain diameter, an inverse effect of grain size on the ductility can result. Nanocrystalline materials often exhibit low tensile ductility at room temperature. The elongation to failure is typically less than a few percent; the regime of uniform deformation is even smaller [34-40]. Koch

[41] indentified three major sources of limited ductility in nanocrystalline materials, namely: artifacts from processing, tensile instability and crack nucleation or shear instability. Three factors can contribute to the ductility of a metal: the work hardening, the strain rate sensitivity and thermal softening. Wang and et al. reported [42] the high tensile ductility in a nanostructured pure Cu. In this case, a bimodal grain structure was developed, within which micro-meter grains embedded inside a matrix of nanocrystalline and ultrafine grains. The matrix grains impart high strength as expected from an extrapolation from the Hall-Petch relationship. Meanwhile, the inhomogeneous microstructure induces high strain hardening that stabilize the tensile deformation, leading to a high tensile ductility – 65% elongation to failure, and 30% uniform elongation.

For the deformation at elevated temperature, earlier investigations have demonstrated that grain refinement can lower the deformation temperature for forming and increase the strain rate for superplasticity of materials, even some poor formable materials [43-47]. It is suggested that decreasing grain size enhances the participation of grain boundary activity such as grain boundary sliding and diffusion during straining due to the increasing volume fraction of grain boundary. Moreover, decreasing the grain size can decrease the flow stress at all strain rates, and increase the maximum value of strain rate exponent (*m-value*), and moves the strain rate for peak m to higher strain rate.

1.1.3 Observations on weakening effect

Hall-Petch relation is found to describe the strength of the materials with the grain size of 1-100 μm. For nickel and iron with nano-scale grain size of about 12 *nm*, it has been reported that this relation may still be valid [48, 49]. In recent decades, the nanocrystalline materials (generally, grain diameter < 100 *nm*) have attracted increasing attention in materials science community because of their promising mechanical behavior. The grain size scale of interest has been refined to the nanometer scale. If Hall-Petch relation was extrapolated down to nanometer scale, the strength of the materials would approach the theoretical strength. However, many studies have reported that the Hall-Petch slope gradually decreases with finer grain size [50-53] or even becomes negative [54-56], which was sometimes called inverse Hall-Petch relation. After reviewing the methods used to prepare nanocrystalline materials, Koch and Narayan, and Fougere et al. [50, 57] questioned the validity of the inverse Hall-Petch effect for the artifacts introduced during processing and for accurate determination of grain size and grain size distribution at nanometer scale. But inverse Hall-Petch effect was also reported in some cases for which samples were free from obvious artifacts [52, 58, and 59], and therefore it is necessary to understand this anomaly. The transition from strengthening to weakening within the same material was also exhibited. Therefore, it was suggested that the inverse Hall-Petch effect can be a real effect but processing defects can change the magnitude of this behavior; and the classical dislocation deformation mechanisms may

not applicable to the finest nanocrystalline grain size metals due to the large volume of grain boundary in these structures. More detailed about weakening effect of grain refinement in polycrystals is discussed in Appendix 2 of Chapter 2.

1.1.4 The role of grain boundary

In contrast to the grain interior where lattice is generally periodic in nature, grain boundary region is characterized with atomic disorder due to high density of defects in these regions, such as dislocations network [60], steps, ledges, vacancies and interstitials. For a given bulk volume, volume fraction of grain boundary in polycrystalline material increases with decreasing grain size. Grain boundaries lead to rate sensitive response in the polycrystalline materials, as proposed by Zener [61]; and Ke demonstrated the viscous behavior from grain boundary lead to an internal friction peak during stress-cycle damping experiments and for stress-relaxation experiments [61]. It is considered that basic process associated with the observed internal friction peak is viscous sliding of the grain boundary, which drags the dislocation substructure in the vicinity of the boundary [62]. The rate-sensitive property of grain boundary is closely related to the viscous nature of thermally activated flow between atoms in this region. The joining of two neighboring grains through this region is considered to be in the form that several atom layers on either side of the boundary is to be involved in the deformation process as a cohesive layer sometimes referred to as a “Mantle Zone” [63, 64]. The viscous behavior of

"Mantle Zone" is associated with dislocation glide-climb process during deformation process, which is non-Newtonian viscous. It was observed that superplasticity always occurs in fine-grained structure materials for which high strain-rate sensitivity is found at a certain strain rate and temperature [65]. The high strain-rate sensitivity is generally associated with the grain boundary sliding or shearing near grain boundary region with grain boundary diffusion playing an important role. Since amorphous alloys seem to possess very high strength due to lack of slip deformation, and exhibit viscous response, a parallel is expected in the behavior of grain boundaries that represent a non-equilibrium structure. More detailed about grain boundary mantle region is discussed in Appendix 3 of Chapter 2.

When ultrafine grain structures approach nanometer dimensions, increasing fraction of atoms in the solid are located within the grain boundary mantle zone. Therefore, in such cases, the viscous effects are likely to influence the observed strength. Enhanced ductility in these materials is also expected at elevated temperature. In the analysis of strengthening and weakening in polycrystalline materials, in general, the plastic response of grain interior (strain hardening) and grain boundaries (non-periodic and viscous) must therefore be incorporated in a manner as a composite material.

1.2 Analytical Study

In the literature, there is no clear understanding of the combined effects of strengthening in crystals via slip process and simultaneous viscous relaxation along grain boundaries. In this work, effort is made to combine the known responses from these regions by considering unit cell composed of grain interior and mantle zone. The role of mantle zone in the polycrystalline aggregate was considered. Finite element simulation provides a convenient way to analyze the plastic strain developing in different region of the polycrystalline materials.

In Chapter 2, a continuum mechanical model was used to combine the responses outlined above for polycrystalline materials, after calibrating the continuum approach with anisotropic response of single crystals and size effect of single grain on strength as determined in recent studies. With this model, stress-strain response of polycrystalline, strengthening and weakening effect of fine grain were predicted.

1.3 Experimental Studies on Fine Grain Metal Alloys

Experimental work was not directly connected with verifying the analytical work performed here, but with the aim of studying formability and strengthening in fine-grained magnesium alloy, titanium alloy and new iron-based alloy. These alloys are currently of interests in regard to application related to weight reduction in transportation

vehicles. Work involved grain refinement studies as well as mechanical property characterization at room temperature and elevated temperature.

Chapter 3 examined the applicability of a severe plastic deformation process, e.g. the Alternate Biaxial Reverse Corrugation (ABRC) process [66] on thixomolded® AZ91D Mg alloy, and studied the deformability of AZ91D Mg alloys and observed the forming behavior of this material after microstructure evolution during severe plastic deformation. In Chapter 4, a new method of severe plastic deformation for producing the ultra-fine grained Ti-6Al-4V alloy was introduced. As-processed microstructure and enhanced superplasticity were examined. The kinetics of static and dynamic grain growth accompanying superplastic deformation, and potential rate controlling mechanisms were discussed. In Chapter 5, the mechanism of strengthening and improved ductility of low-Mn TRIP (transformation-induced plasticity) [67] steel was studied at room temperature and elevated temperature. The mechanical properties of low-alloyed TRIP steel (0.15wt%C - 2.22wt%Mn - 0.08wt%Si - 1.35wt%Al) were investigated at the temperature range of 25 ~ 400^{o}C. Thermal-assisted effects on the transformation process have been examined by monitoring the hardening rate and fracture during tensile test. The results help to understand the strengthening mechanism at elevated temperature, and provide the way to understand temperature dependence of ductility in these materials.

1.4 References

[1] Hall EO. Proceedings of the Physical Society (Section B) 1951; 64:747.

[2] Petch NJ. J Iron Steel Inst 1953; 174:25.

[3] Heslop J, Petch NJ. Phil Mag 1956; 1:866.

[4] Armstrong R, Codd I, Douthwaite RM, Petch NJ. Phil Mag 1962; 7:45.

[5] Carreker RP. J Metals 1957; 9:112.

[6] Carreker RP, Hibbard WR. J Metals 1957; 9:1157.

[7] Carreker RP, Hibbard WR. Acta Metall 1953; 1:654.

[8] Phillips WL, Armstrong RW. Metall Trans 1972; 3:2571.

[9] Sambasiva Rao G, Prasad YVRK. Mater Letters 1983; 1:171.

[10] Hu Hsun, Cline RS. Trans Metall Soc AIME 1968; 242:1013.

[11] Sonon DE, Smith GV. Metall Soc AIMM Trans 1968; 242:1527.

[12] Thompson AW. Acta Metall 1977; 25:83.

[13] Taub AI, Huang SC, Chang KM. Metall Trans A 1984; 15A:399.

[14] Eshelby JD, Frank FC, Nabarro FRN. Phil Mag 1951; 42:351.

[15] Cottrell AH. Metall Soc AIMM Trans 1958; 212:192.

[16] Margolin H, Hazaveh F, Yaguchi H. Scripta Metall 1978; 12:1141.

[17] Margolin H, Longo RB. Scripta Metall 1979; 13:561.

[18] Jagannadham K, Armstrong RW. Scripta Metall 1987; 21:1459.

[19] Li JCM. Trans Metall Soc 1963; 227:239.

[20] Conrad H. Acta Metall 1963; 11:75.

[21] Ashby MF. Phil Mag 1970; 21:399.

[22] Kocks UF. Metall Trans 1970; 1:1121.

[23] Armstrong RW, Worthington PJ. Metallurgical Effects at High Strain Rates, ed. Rohde RW, Butcher BM, Holland JR, Karnes CH. Plenum Press, New York 1973; 401

[24] Dimiduk DM, Uchic MD, Parthasarathy TA. Acta Mater 2005; 53:4065.

[25] Greer JR, Oliver WC, Nix WD. Acta Mater 2005; 53:1821.

[26] Uchic MD, Dimiduk DM, Florando JN, Nix WD. Science 2004; 305:986.

[27] Kiener D, Motz C, Schöberl T, Jenko M, Dehm G. Adv Engin Mater 2006 ; 8 :1119

[28] Ahmed MMI, Langdon TG. J Mater Sci Letters 1983; 2:337.

[29] Yang Q, Ghosh AK. Acta Mater 2006; 54:5159.

[30] Valiev RZ, Krasilnikov NA, Tsenev NK. Mater Sci Eng A 1991; 137:35.

[31] Yamashita A, Horita Z, Langdon TG. Mater Sci Eng A 2001; 300:142.

[32] Mannan SL, Samuel KG, Rodriguez P. Mater Sci Eng 1985; 68:143.

[33] Gabdullin NK, Imaev RM, Salishchev GA. Phys Metals Metall 1998; 85:106.

[34] Koch CC, Morris DG, Lu K, Inoue A. Res Soc Bull1999; 24:54.

[35] Weertman JR, Farkas D, Hemker K, Kung H, Mayo M, Mitra R, van Swygenhoven H. Res Soc Bull 1999; 24:44.

[36] Sanders PG, Youngdahl CJ, Weertman JR. Mater Sci Eng A 1997; 234–236:77.

[37] Sanders PG, Eastman JA, Weertman JR. Acta Mater 1997; 45:4019.

[38] Lergos M, Elliott BR, Rittner MN, Weertman JR, Hemker KJ. Phil Mag A 2000;

80:1017.

[39] Valiev RZ, Alexandrov IV, Zhu YT, Lowe TC. J Mater Res 2002; 17:5.

[40] Gertsman VY, Valiev RZ, Akhmadeev NA, Mishin OV. Mater Sci Forum 1996; 225–227:739.

[41] Koch CC. Nanocryst Mater 2003; 18:9.

[42] Wang Y, Chen M, Zhou F, Ma E. Nature 2002; 419:912.

[43] Watanabe H, Mukai T, Mabuchi M, Higashi K. Scripta Mater 1999; 41:209.

[44] Chan KC, Wang CL, Zhang KF. Mater Trans 2004; 45:2558.

[45] Lin HK, Huang JC. Mater Trans 2002; 43:2424.

[46] Mishra RS, Valiev RZ, McFadden SX, Islamgaliev RK, Mukherjee AK. Phil Mag A 2001; 81:37.

[47] Hulbert DM, Jiang D, Kuntz JD, Kodera Y, Mukherjee AK. Scripta Mater 2007; 56:1103.

[48] Hughes GD, Smith SD, Pande CS, Johnson HR, Armstrong RW. Scripta Metall 1986; 20:93.

[49] Jang JSC, Koch CC. Scripta Metall Mater 1990; 24:1599.

[50] Nieman GW, Weertman JR, Siegel RW. *Scripta Metall* 1989; 23:2013.

[51] Höfler HJ, Averback RS. Scripta Metall Mater 1990; 24:2401.

[52] El-Sherik AM, Erb U, Palumbo G, Aust KT. Scripta Metall Mater 1992; 27:1185.

[53] Gertsman VY, Hoffmann M, Gleiter H, Birringer R. Acta Metall Mater 1994; 42:3539.

[54] Chokshi AH, Rosen A, Karch J, Gleiter H. Scripta Metall 1989; 23:1679.

[55] Lu K, Wei WD, Wang JT. Scripta Metall Mater 1990; 24:2319.

[56] Fougere GE, Weertman JR, Siegel RW, Kim S. Scripta Metall Mater 1992; 26: 1879.

[57] Koch CC, Narayan J. Mater Res Soc Symp 2001; 634:B5.1.1.

[58] Erb U. NanoStruct Mater 1995; 6:533.

[59] Narayan J. J Nanopart Res 2000; 2:91.

[60] Hirth JP, Lothe J. Theory of Dislocations, John Wiley & Sons 1982, 697

[61] Ke TS. Metall Mater Trans A 1999; 26:2267.

[62] Guan XS, Ke TS. J Alloys Comp 1994; 211/212:480.

[63] Ghosh AK. Mater Sci Forum 1994; 170-172:39.

[64] Ghosh AK. Constitutive Equations, Metalworking: Bulk Forming, ASM Handbook 2005, Vol. 14A, 582.

[65] Edington JW, Melton KN, Cutler CP. Prog Mater Sci 1976; 21:61.

[66] Yang Q, Ghosh AK. Acta Mater 2006; 54:5147.

[67] Zackay VF, Parker ER, Fahr D, Busch R. Trans ASM 1967; 60:252.

CHAPTER 2

ESTIMATING STRESS-STRAIN RESPONSE FOR SINGLE CRYSTAL AND POLYCRYSTAL BY ANISOTROPIC CONTINUUM PLASTICITY APPROACH

Purpose and Organization

The purpose of this chapter is two fold: (1) to isolate the effect of size and orientation of single crystal on strengthening, and (2) incorporate single crystal size effect with viscous response from mantle zone to derive the response of polycrystals. These two objectives are described in the following pages as:

Part A: Effect of Single Crystal Orientation and Crystal Size

and

Part B: Effect of Grain Size and Grain Boundary Response

Part A

Abstract: Effect of Single Crystal Orientation and Crystal Size

Experimental observations on single crystals have revealed a strong effect of crystal size on strength of crystals, especially when crystal size is small (This is similar to grain size effect in polycrystals). By calibrating dependence of strength on crystal size, and using power law strain hardening equations and strain rate sensitivity, the expected mechanical response of single crystal was calculated for conventional metals such as steel or aluminum. Anisotropic plasticity of single crystal was described by Hill's 1948 yield criterion. While Hill's theory represents oversimplification of crystals with ideal orientation, it is convenient for input into Part B of research related to polycrystals. This avoids complicating the modeling effort by "crystalline plasticity" based models. The continuum approach thus provides an efficient way to incorporate anisotropic effects while studying size effect, hardening rate, rate sensitivity etc. Finite element analysis was performed to evaluate these effects and calculate the changes in stress-strain response of single crystal as a function of loading direction. For the stress-strain response of single crystal, the material anisotropy, parameters that described strain hardening, strain rate sensitivity and crystal size effect, were chosen and varied in the simulation as needed.

2A.1 Introduction

2A.1.1 Crystal orientation

It is well-known that the stress-strain response of metallic single crystal is dependent on the crystallographic orientation due to the nature of asymmetric crystal structure [1-6]. For single crystal, it is known that critical resolved shear stress (*CRSS*) varies for different slip systems. The crystallographic orientation of a single crystal related to the loading direction determines the resolved shear stress on various slip systems; then the active dislocation slip system. This dependence results in the strengthening or weakening effect of crystals under loading. The theory of crystalline plasticity has been widely accepted to describe the anisotropic response of single crystals [7]. For polycrystalline material, a strongly textured polycrystalline material can be expected to exhibit stress-strain response quite similar to that of single crystal of the same composition. It is well-known that Hill's 1948 yield criterion has the ability to describe the anisotropy of polycrystalline metals to a reasonable degree of accuracy [8]. In present simulation, crystal plasticity model is not used because the primary goal of this work is grain size or sample size effect. In experiments, anisotropy of materials is described by Lankford's anisotropy (*r* value), which is measured by the ratio of width strain to thickness strain of tensile tested sample ($r = \varepsilon_w / \varepsilon_t$, ε_w is true strain in width direction and ε_t is true strain in thickness direction). For application of this anisotropic parameter in finite element software, the strain ratio was converted into 3-dimension matrix as shown in

Appendix 1 (Page 117).

The strain hardening behavior in metals arises from the crystallographic slip, and dislocation multiplication and interaction on the multiple slip planes within the crystals [9]. Strain hardening is often expressed by a power law equation as follows:

$$\sigma = k\varepsilon^n \tag{2A-1}$$

where σ refers to flow stress of materials, k refers to strength constant, ε refers to imposed true strain, and n refers to strain hardening rate. Metals also show strain-rate sensitivity because of the fact that dislocation movement is subject to rate dependent drag forces. The constitutive equation incorporated with strain hardening and strain rate hardening is generally expressed in the following form [10]:

$$\sigma = k\varepsilon^n \cdot \dot{\varepsilon}^m \tag{2A-2}$$

where $\dot{\varepsilon}$ refers to imposed strain rate and m refers to strain rate sensitivity. The product form of Equation (2A-2) indicates a thermally activated process to be under all conditions, except when m = 0. However, if a critical shear stress on the slip plane needs to be overcome before activation of slip, a threshold stress term can be added into constitutive equation as in Equation (2A-3), taken from reference [11].

$$\sigma = k(\varepsilon + \varepsilon_0)^n \cdot \dot{\varepsilon}^m \qquad \text{(2A-3)}$$

where ε_0 refers to prestrain. In this equation, both imposed strain and prestrain contribute to strain hardening effect; and have a product relation with strain-rate component. Furthermore, Equation (2A-3) has the feature of incorporating the prestrain term that may be appropriate in fine grain alloys produced by severe plastic deformation.

2A.1.2 Crystal size

Recent development of micro-pillar compression on the single crystals revealed the strong effect of sample size on the yield strength of materials [12-15]. As shown in Figure 2A.1 [13], the dependence of strength on the crystal size varies in different size ranges indicated by slopes of *log*(stress) versus *log*(crystal diameter) curves, such as slope is - 6.28 in small size range, - 0.93 in intermediate size range and - 0.34 in large size range. The slope was also reported to be - 0.64 [12] and - 0.4 [15]. One of possible interpretations of this strengthening is the concept of dislocation starvation, which attributes the strengthening of small crystals to the reducing probability of dislocation multiplication processes. However, it is demonstrated that dislocation starvation need not occur after many dislocations move through the crystal with large plastic strain [16]. In this case, it is thought that the resistance to eject slip steps cutting through specimen

surface is the reason related to the observed strengthening in small dimension specimens [16]. Therefore, to estimate the stress-strain response of single crystal, it is necessary to consider the strain hardening effect, rate sensitivity and crystal size, especially for the crystals with small size.

Based on the observation from Figure 2A.1, the crystal size effect is incorporated into power-law equation for strain hardening with strain rate sensitivity. However, whether the resistance of surface to eject slip steps has strain hardening effect or only contributes to the strength of crystal is not clear. Thus, the crystal size effect is formulated in two different ways. In one equation, the strain hardening effect is considered to be contributed by both imposed strain and surface resistance, which is expressed as follows:

$$\sigma = k(\varepsilon + \frac{B}{l})^n \cdot \dot{\varepsilon}^m \tag{2A-4}$$

where B refers to a size-related constant in unit of μm and l refers to crystal size in unit of μm. Definition of B here is to incorporate crystal size effect on strength into equation with an additive term to the imposed strain. Another possibility is that surface resistance contributes to strength of crystal but does not affect strain hardening. For this assumption, the strain hardening component is additive to the size effect as follows:

$$\sigma = (k\varepsilon^n + \frac{A}{l^p}) \cdot \dot{\varepsilon}^m \qquad \text{(2A-5)}$$

where A refers to a size-related stress component in $MPa \cdot \mu m^p$, l is crystal size in μm, and p is the crystal size exponent. In this equation, $k\varepsilon^n$ contributes to strain hardening effect, but the overall form of σ is rate sensitive.

In this study, both of equations with size effect and without size effect are summarized in Table 2A.1 and 2A.2. Values of constants in equation are varied to estimate the stress-strain response of single crystal. As a constituent of polycrystals, the stress-strain response of single crystal with orientation and crystal size dependence included must be the basis for incorporating into polycrystalline model.

2A.2 Approach

In present study, the commercial software ABAQUS®/ Standard analysis module are used to accomplish the modeling work. The finite element modeling procedure of ABAQUS is elaborated in Appendix 1 (Page 88).

Prior to the modeling of single crystal, some statements about the mechanical properties of materials were presumed:

(1) Elasticity of single crystal is assumed to be isotropic.

Since the present analysis is more interested in plastic response of material, the elasticity of material is assumed to be isotropic for simplicity. The small difference of strain resulted from anisotropic elasticity is neglected. For the elastic properties of the single crystal, 200 *GPa* was assumed for the Young's modulus, and 0.3 for the Poisson's ratio (Table 2A.2 (b)).

(2) Plasticity of single crystal has strain hardening effect and is strain rate sensitive

Equations summarized in Table 2A.2 (a) are used to estimate stress-strain response of single crystal. Those equations consider power-law strain hardening and strain rate hardening, with and without crystal size effect.

It should be mentioned that the material properties used in present analysis refer to general materials. However, it could be ranged in the property of bcc steels or fcc high-strength aluminum alloys.

(3) The anisotropy of the single crystal is described by Hill's 1948 yield criterion.

A strongly textured polycrystalline material can be expected to exhibit stress-strain response quite similar to that of single crystal of the same composition. Therefore, the anisotropic property of single crystal can be reasonably simulated by the yield criterion for textured polycrystalline materials and without being complicated by crystalline plasticity model. Several anisotropic yield criteria were suggested to

describe the anisotropic behavior of polycrystalline metals, such as Hill's 1948 yield criterion [8], Hill's 1979 yield criterion [17], Hosford's 1979 yield criterion [18] and Hosford's 1985 yield criterion [19]. Due to the setup of Hill's 1948 yield criterion in ABAQUS, it is impossible to use other criteria. In Table 2A.3, two *r*-values (Lankford's anisotropy) are assumed, and converted to the requested stress ratios by the equations listed in Appendix 1(Page 117).

(4) For the definition of materials orientation, Figure 2A.2 exhibits the coordinate relation between the loading direction and crystal axes. The sample axes were denoted with 1, 2 and 3, while the crystal axes was denoted with x, y and z. In present analysis, transverse anisotropy was assumed to the analyzed part. That is, the material has isotropic mechanical properties in x-y plane, while anisotropic mechanical properties in z direction. The loading direction is parallel to the 2-axis, which is the longitudinal direction of the part geometry. To evaluate the stress-strain response of material with different orientation with respect to the loading direction, the crystal axes of sample are rotated around the 1-axis of part, which is parallel to the x-axis of crystal.

2A.3 Results and Discussions

2A.3.1 Effect of loading direction, crystal anisotropy and strain hardening rate

In this section, crystal size was not varied. Equation (2A-2), $\sigma = k\varepsilon^n \cdot \dot{\varepsilon}^m$, with power-law

strain hardening and strain rate hardening is evaluated first. For most metals at room temperature, the magnitude of strain rate sensitivity (m) is quite small (between 0 and 0.03), m = 0.02 was thereby assumed for present evaluation. With regard to the strain hardening behavior, based on the compression and tension results from single crystals [3, 13, 14], modest strain hardening rate were selected for n = 0.05 and 0.15 because only single slip or simple multi-slip occurs in deformation of single crystals. Figure 2A.3 shows the estimated true stress-true strain curves (n = 0.05) of single crystal at the strain rate of 3.5×10^{-2}/s, which exhibits the dependence on the orientation of crystal relative to the loading direction. Due to the assumption of transverse anisotropy (r = 2.0), only the out-plane orientations of crystal were considered. The range of orientation was chosen between 0^o and 90^o. Namely, when the orientation is 0^o, the isotropic plane is parallel to the loading direction; when the orientation is 90^o, the anisotropic axis is parallel to the loading direction. It can be seen that 90^o orientation has the highest flow stress as the assumed r value is larger than 1, while the lowest flow stress occurs at the 45^o. Flow stress is found to decrease with crystal orientation increasing from 0^o to 45^o; but flow stress increases with increasing orientation from 45^o to 90^o. Moreover, in Figure 2A.3 (a), the solid circle on each curve indicates calculated uniform strain (ε_u) which is determined by Considere construction when $\frac{d\sigma}{d\varepsilon}=\sigma$. It can be seen that the crystal orientation has little influence on uniform strain of single crystal. Compared with the estimation results with strain-hardening rate of 0.15 (Figure 2A.3 (a)), the smaller strain-hardening rate generates much larger yielding points, and the stress variation

resulted from the crystal orientation are also slightly larger.

Figure 2A.4 (a) shows the simulation results based on Equation (2A-3), $\sigma = k(\varepsilon + \varepsilon_0)^n \cdot \dot{\varepsilon}^m$. It can be seen from that the estimated stress-strain curves by this equation exhibit a similar dependence on crystal orientation to the results estimated by Equation (2A-2), $\sigma = k\varepsilon^n \cdot \dot{\varepsilon}^m$. A larger strength at the same strain level should be expected by adding pre-strain in equation. However, compared with the results shown in Figure 2A.3, it inversely shows smaller stress level due to the assumed larger strain hardening rate (n = 0.3). In Figure 2A.4 (b), the stresses collected at true strain of 0.15 are plotted with the crystal orientation, which explicitly show the dependence of stress on crystal orientation similar to the results estimated from Equation (2A-2), $\sigma = k\varepsilon^n \cdot \dot{\varepsilon}^m$. Although the equations without size-dependent term are incapable of predicting the crystal size effect on stress-strain response of single crystal observed in experiments, the results about the effect of crystal orientation on the stress-strain response has predicted the anisotropic response of single crystal, which is applicable to other equations incorporated with size-dependent term; and suggests that if polycrystals are considered with adjoining grains having different orientations, a composite-like behavior is expected with hard or soft grains next to each other in the polycrystals.

2A.3.2 Effect of crystal size

In Equation (2A-4), $\sigma = k(\varepsilon + \frac{B}{l})^n \cdot \dot{\varepsilon}^m$, constant B (μm) is assumed to be 0.001 μm to fit reasonable values of stress observed in real materials. In Figure 2A.5 (a), the dependence of stress-strain curves on crystal orientation estimated by this equation is similar to that by Equation (2A-2), $\sigma = k\varepsilon^n \cdot \dot{\varepsilon}^m$. The dots representing uniform strain for each orientation are added to evaluate the flow instability of single crystal regarding to the crystal orientation, where crystal size is assigned with $0.422\mu m$. It shows that crystal orientation has little effect on uniform strain. By assuming different crystal size in the equation, it can be seen from the Figure 2A.5 (b) that, the flow stresses for different crystal size are quite close for small values of B. For large values of B, they are further apart. Moreover, when the crystal size increases from 3.48 *nm* to 41.6 *nm*, the flow stress decreases, and the stress-strain curves show smooth transition from elasticity to plasticity and continuous work hardening. Furthermore, the crystal size effect on uniform strain and corresponding stress is also estimated in Figure 2A.5 (c). It shows that uniform strain decreases as crystal size decreases.

Another form of equation incorporating crystal size effect is Equation (2A-5), $\sigma = (k\varepsilon^n + \frac{A}{l^p}) \cdot \dot{\varepsilon}^m$. This equation can be interpreted as the surface contributing to strength of crystal with additive strain hardening term. In Figure 2A.6 (a), the crystal size effect on the stress-strain response of single crystal was estimated. In this calculation, A

was assumed with $400\,MPa\cdot\mu m^{0.05}$, and p is set at 0.05, which is equal to the strain hardening rate. It can be seen from the stress-strain curves that the flow stress increases as the crystal size decreases. In Figure 2A.6 (b), uniform strain increases with increasing crystal size, while the flow stress at uniform strain decreases with increasing crystal size. Obviously, the evaluated crystal size range is quite wide from 3.48 *nm* to 4.23 μm; however, the estimated size effect does not match the observed compression results in [12-15]. Although the tension results from the similar small-scale single crystals are unavailable so far, they should have similar dependence on the crystal size to that of compression result if the interpretation of [16] is reasonable. Therefore, an alternative way is to increase the value of crystal size exponent (*p*).

2A.3.3 Effect of *p* and *A* in Equation (2A-5)

In Figure 2A.7 (a), the calculation was also based on Equation (2A-5), $\sigma = (k\varepsilon^n + \frac{A}{l^p})\cdot\dot{\varepsilon}^m$, where $n = 0.15$, $A = 5\,MPa\cdot\mu m$, $p = 1$ and $r = 1.5$. Compared the calculation with small crystal size exponent ($p = 0.05$), the case with $p = 1$ shows large effect of crystal size on the flow stress. The flow stress increases rapidly with decreasing crystal size from 422 *nm* to 3.48 *nm*, while this effect weakens for larger crystal size. By adding $d\sigma_{22}/d\varepsilon_{22}$ *vs.* ε_{22} curves (dash line and the point of uniform strain denoted by open circle) to the stress-strain plot, it can be found that uniform strain increases with increasing crystal size. Comparing the results in Figure 2A.7 (a) and Figure 2A.7 (b), it

can be seen that the increasing the A value from 5 to 15 $MPa \cdot \mu m$ enlarges the crystal size effect on the flow strength of single crystals. Furthermore, compared the results in Figure 2A.7 (b) with Figure 2A.7 (c), it can be found that increasing the crystal size exponent has the same effect as increasing the A value.

Compared with the experimental observations [12-15], the flow strength dependence on the crystal size estimated by Equation (2A-5), $\sigma = (k\varepsilon^n + \frac{A}{l^p}) \cdot \dot{\varepsilon}^m$, with large crystal size exponent is more reasonable, though the crystal sizes used in compression test are larger than 400 *nm*; and extending the application of this equation to describe the stress-strain response for smaller crystal size, is acceptable.

2A.3.4 Effect of varying crystal size

For above calculated results, to examine how crystal size influences strength, plots are made of $\log(\sigma - \sigma_0)$ *versus* $\log(l)$ in Figure 2A.8, where σ is the strength of single crystal at the true strain of 0.02, σ_0 refers to the strength of large single crystal estimated at the same strain, and l is crystal size. The results are estimated by Equation (2A-5), $\sigma = (k\varepsilon^n + \frac{A}{l^p}) \cdot \dot{\varepsilon}^m$, and $k = 480MPa$, $n = 0.15$ and $m = 0.02$. For crystal size exponent p in this equation, it is assumed to be 1 in present calculation; and the crystal size dependence of strength is denoted by the slope of curve. The purpose of this is to compare such results with experimental observations. As mentioned above, the slope for

relation between strength and crystal size in experiments was reported that it can be - 0.64 in [12], - 6.28, - 0.93 and - 0.34 in [13] and - 0.4 in [15], which differ from different investigators. Some people also try to use constant slope to describe this relation [12, 15]. For present calculation, it can be seen that, when $A = 15\,MPa \cdot \mu m$, the flow stress has the relation with crystal size with slope = - 1 in small crystal size range, in the intermediate crystal size range, slope is decreased to - 0.80; and in the large crystal size range, the slope is - 0.51; when $A = 5\,MPa \cdot \mu m$, the flow stress also varies in different crystal size range. In the small crystal size range, the slope is - 1; in the intermediate crystal size range, slope is decreased to - 0.77; and in the large crystal size range, the slope is - 0.29. The above results have two suggestions. One is that the value of A possibly be responsible for the relation between strength and crystal size observed in single crystals. Another suggestion is, experimentally observed various slopes in different regimes of crystal size can be predicted by simulation in this study with $p = 1$. It is possible that p is higher than or lower than p in reality due to the fact that experimentally observed slope varies for different investigators. If large value of p was chosen for simulation, the calculated slope will be higher.

Based on the calculation results on the stress-strain behaviors of single crystal, therefore, Equation (2A-5), $\sigma = (k\varepsilon^n + \frac{A}{l^p}) \cdot \dot{\varepsilon}^m$, is suggested to be capable of describing the stress-strain responses of single crystal for size effect; to be used in estimating the stress-strain responses of polycrystals.

2A.4 Conclusions

Finite element analysis was performed to estimate the combined effect of crystal size and orientation on the stress-strain response of single crystals of metals with specific input values of strain hardening, plastic anisotropy, strain rate sensitivity parameters and constants for size effect. Specific conclusions are stated as follows:

(1) Crystal strength increases as the axis of anisotropy approaches the tensile axis, for r = 1.5 and 2.0. The highest flow stress is seen when loading axis coincides with anisotropy axis ($\theta = 90^{o}$ in Figure 2A.2); the lowest flow stress occurs when axis of anisotropy is at 45 degrees orientation to the loading direction.

(2) This suggests that if polycrystals are considered with adjoining grains having different orientations, a composite-like behavior is expected in polycrystals with hard and soft grains next to each other.

(3) The crystal orientation has little influence on uniform strain before the onset of necking.

(4) A strong crystal size effect on the strength of crystal is simulated by considering strain hardening behavior of crystal with an additive size-dependent term, $\frac{A}{l^{p}}$.

(5) For crystal size effect, with exponent $p = 1$, various possible slopes have been demonstrated for log (σ-σ_0) *vs.* log (l) curve, in different regimes of crystal size as observed experimentally. Comparison with experimental results suggests that the

value of p for real materials would differ from unity.

(6) The additive term for size dependence evaluated in this work suggests that the resistance to surface fracture during slip process could possibly be responsible for the added strength, and crystal size effect through the constant A is observed in the additive relation.

Table 2A.1 Nomenclature for single crystal model

σ	Flow stress, *MPa*
k	Strength constant, *MPa*
ε	Tensile strain
$\dot{\varepsilon}$	Strain rate
ε_0	Pre-strain
n	Strain hardening rate
B	Size-related constant, μm
A	Size-related stress component, $MPa \times \mu m^p$
p	Crystal size exponent
m	Strain-rate sensitivity
E	Young's modulus
v	Poisson's ratio
r	Lankford's anisotropy
R_{ij}	Stress ratio
ℓ	Crystal size, μm

Table 2A.2 Constitutive equations describing stress-strain behavior of single crystal

(a) Plastic properties

Equations		Parameters						
		K, MPa	ε_0	n	$B, \mu m$	$A, MPa \cdot \mu m^p$	p	m
Without crystal size effect	$\sigma = k\varepsilon^n \cdot \dot{\varepsilon}^m$	480	---	0.05	---	---	---	0.02
		480	---	0.15	---	---	---	0.02
	$\sigma = k(\varepsilon + \varepsilon_0)^n \cdot \dot{\varepsilon}^m$	480	0.002	0.3	---	---	---	0.02
With crystal size effect	$\sigma = k(\varepsilon + \frac{B}{l})^n \cdot \dot{\varepsilon}^m$	480	---	0.05	0.001	---	---	0.02
	$\sigma = (k\varepsilon^n + \frac{A}{l^p}) \cdot \dot{\varepsilon}^m$	480	---	0.05	---	400	0.05	0.02
		480	---	0.15	---	5	1	0.02
		480	---	0.15	---	15	1	0.02
		480	---	0.15	---	15	0.9	0.02

(b) Elastic properties

Parameters	
E, GPa	**v**
200	0.3

Table 2A.3 The values of stress ratios for input of FEM analysis ($r_x = 1.5$ and $r_x = 2.0$ were assumed for the present study)

Component		R_{xx}	R_{yy}	R_{zz}	R_{xy}	R_{xz}	R_{yz}
Value	$r_x = 1.5$	1	1	1.118	0.968	0.926	0.926
	$r_x = 2.0$	1	1	1.225	0.949	0.866	0.866

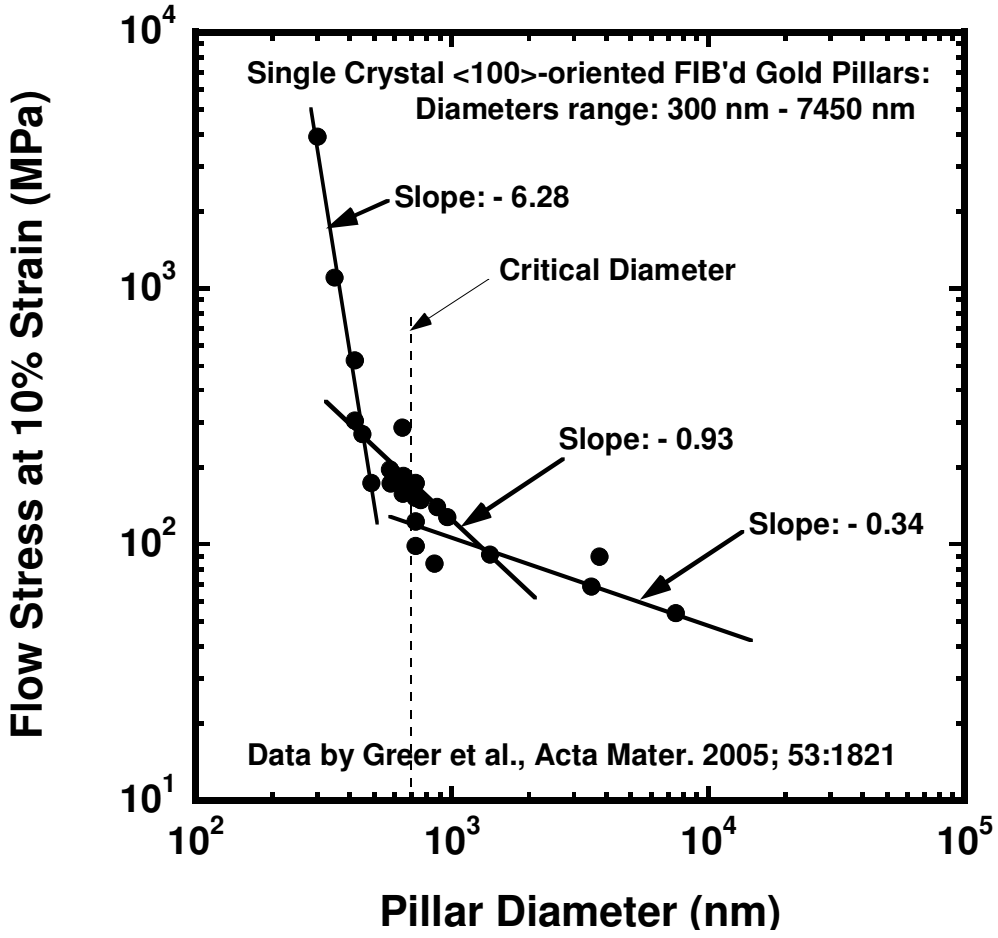

Figure 2A.1 Micropillar compression test showing crystal size dependent of strength of single crystal from literature [13].

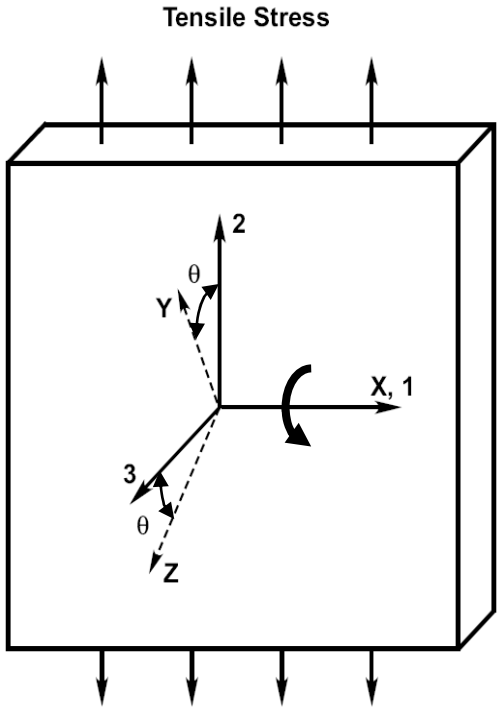

Sample Axes --- 1, 2, 3; Crystal Axes --- X, Y, Z

Axis of Anisotropy --- Z (Assume: Transverse anisotropy)

Figure 2A.2 Orientation of single crystal with respect to the loading direction (2). The axis of crystal anisotropy is Z direction, (transverse anisotropy; X-Y plane is isotropic). Crystal orientation, θ is defined as the angle between sample plane normal and axis of anisotropy, Z, where tension direction is in the plane of sheet.

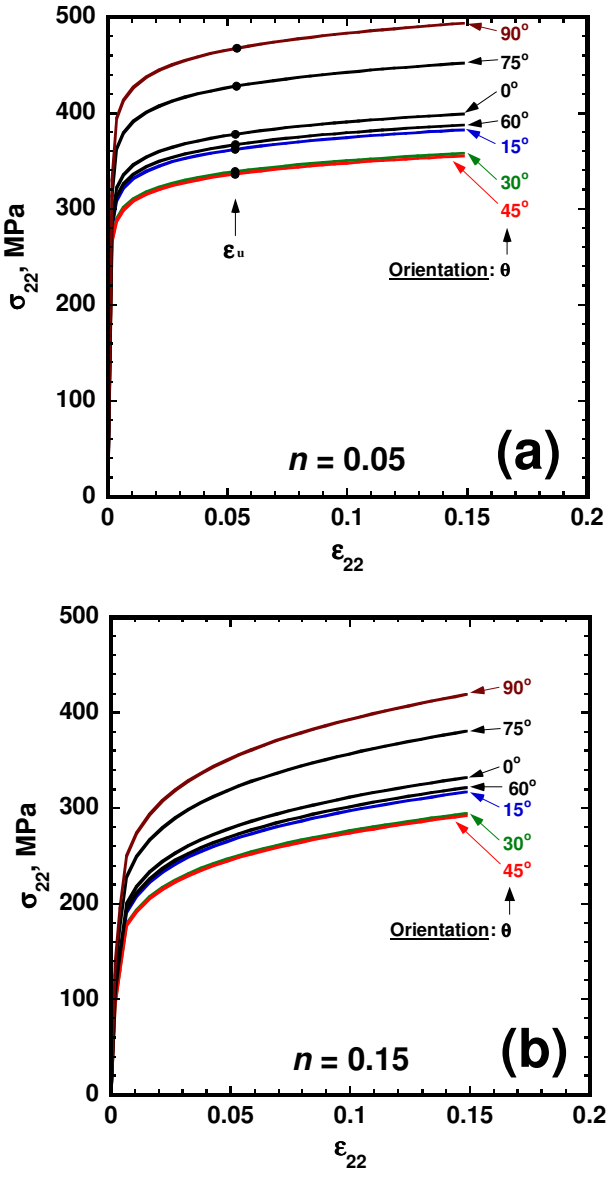

Figure 2A.3 Stress-strain curves are shown for different crystal orientation of single crystal. Crystal orientation, θ is defined as the angle between sample plane normal and axis of anisotropy, Z. Effect of different strain hardening rate is shown (a) *n* = 0.05 and (b) *n* = 0.15. Calculations are based on an equation $\sigma = k\varepsilon^n \dot{\varepsilon}^m$, where $k = 480MPa$ **and** $m = 0.02$ **(strain rate: 3.5×10^{-2} s^{-1} and assumed *r* = 2.0).**

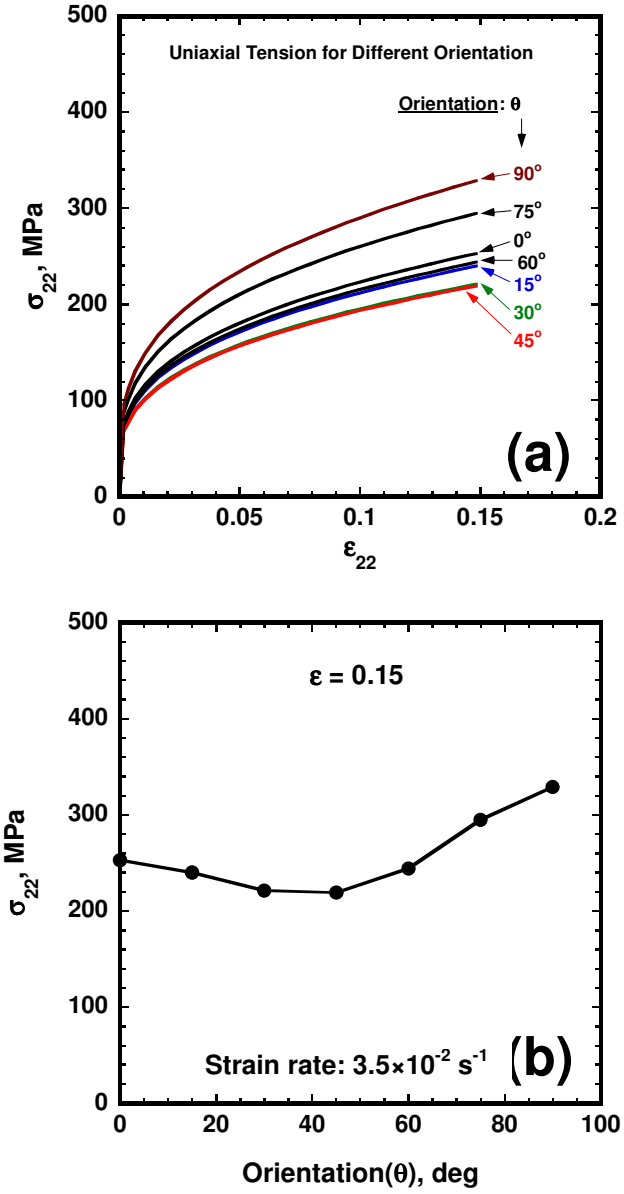

Figure 2A.4 Stress-strain curves are shown in (a) for different crystal orientation of single crystal. Crystal orientation, θ is defined as the angle between sample plane normal and axis of anisotropy, Z. Flow stress for ε = 0.15 are shown in (b) as a function of θ. Calculations are based on an equation $\sigma = k(\varepsilon + \varepsilon_o)^n \dot{\varepsilon}^m$, **where** $k = 480MPa$, $\varepsilon_o = 0.002$, $n = 0.3$ **and** $m = 0.02$. **(strain rate: 3.5×10^{-2} s^{-1} and assumed *r* = 2.0)**

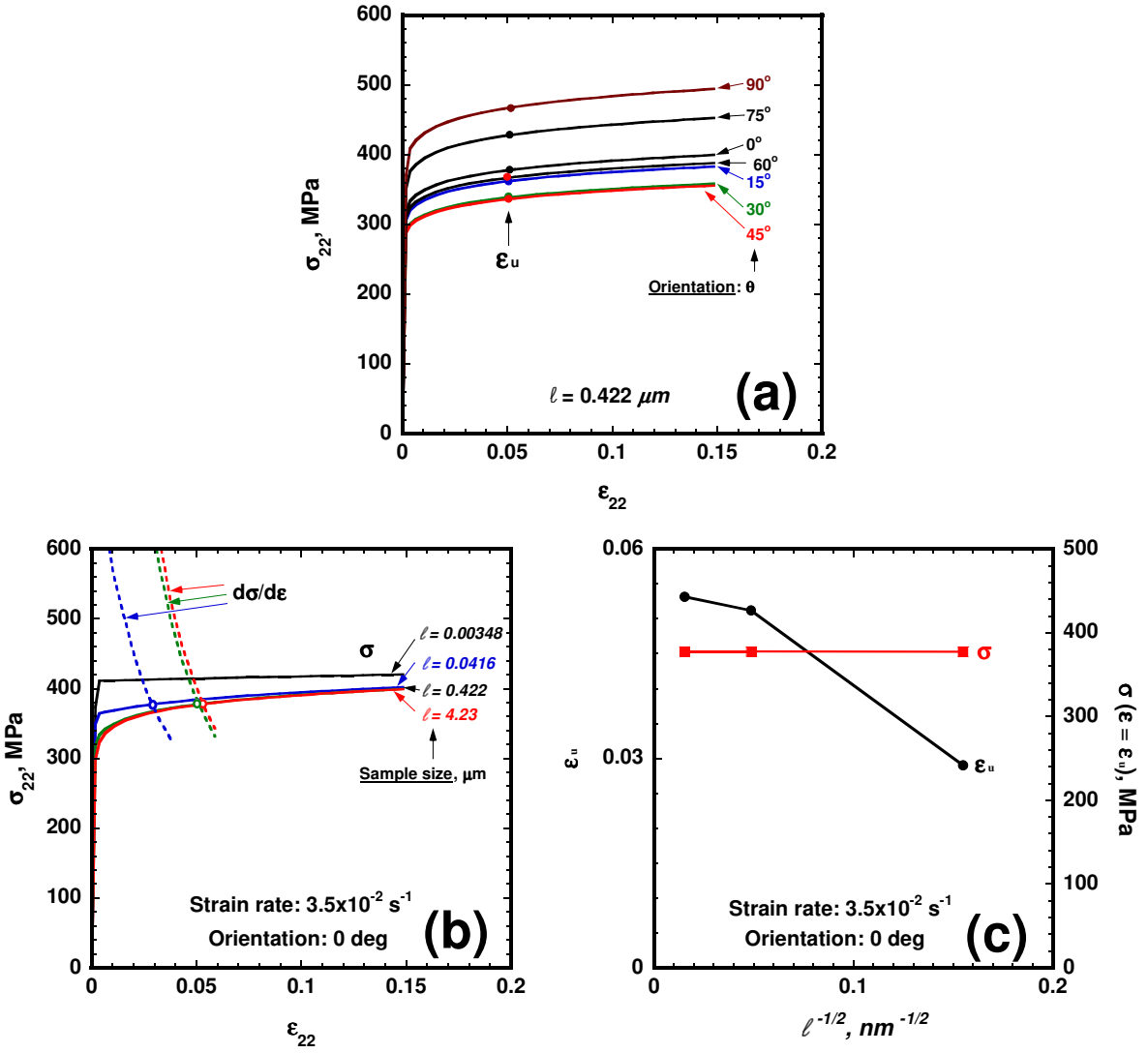

Figure 2A.5 Stress-strain curves are shown (a) for different crystal orientation of single crystal (l = 0.422 μm). Crystal orientation, θ is defined as the angle between sample plane normal and axis of anisotropy, Z; (b) for various crystal sizes, where crystal orientation (θ = 0). The uniform strain and peak flow stress are plotted as functions of crystal size in (c). Calculations are based on an equation $\sigma = k(\varepsilon + \frac{B}{l})^n \cdot \dot{\varepsilon}^m$, where $k = 480MPa$, $B = 0.001\mu m$, $n = 0.05$ and $m = 0.02$ (strain rate: $3.5\times10^{-2}\ s^{-1}$ and assumed r = 2.0)

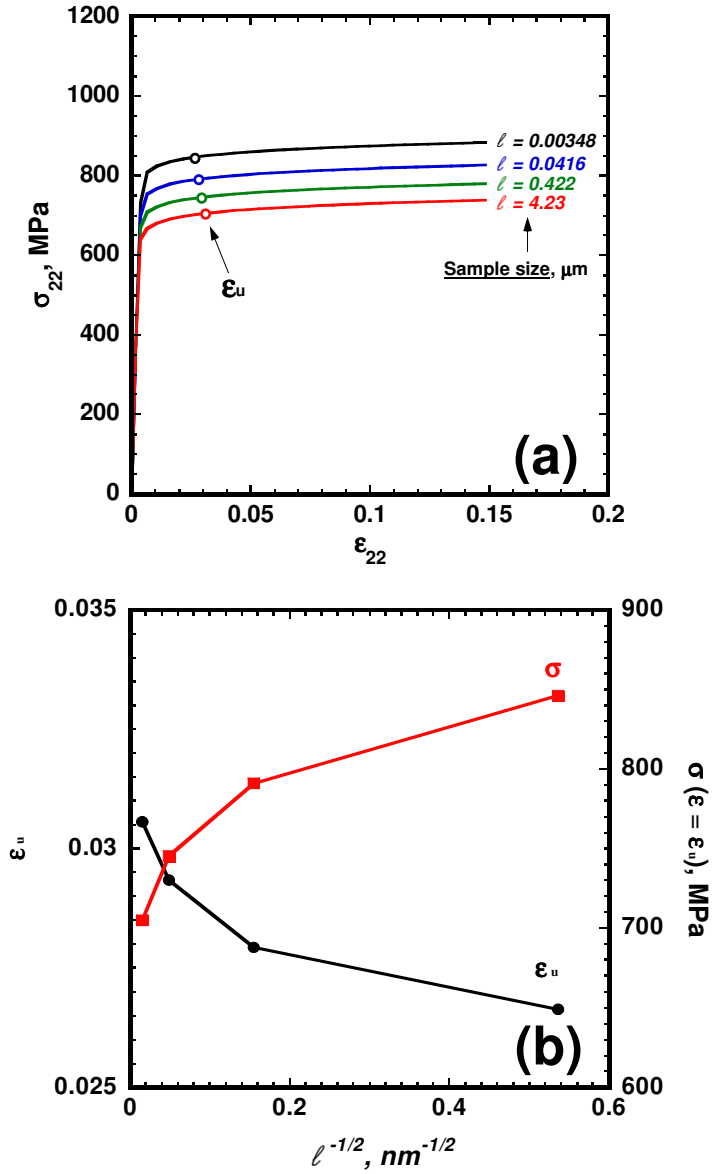

Figure 2A.6 Stress-strain curves for various crystal sizes are shown in (a). The uniform strain and peak flow stress in tension direction are shown as functions of crystal size in (b). Calculations are based on Equation $\sigma = (k\varepsilon^n + \frac{A}{l^p}) \cdot \dot{\varepsilon}^m$, where $k = 480MPa$, $n = 0.05$, $m = 0.02$, $A = 400MPa \cdot \mu m^p$ **and** $p = 0.05$ **(strain rate: 3.5× 10^{-2} s^{-1}, orientation: 0 deg, and assumed *r* = 2.**0)

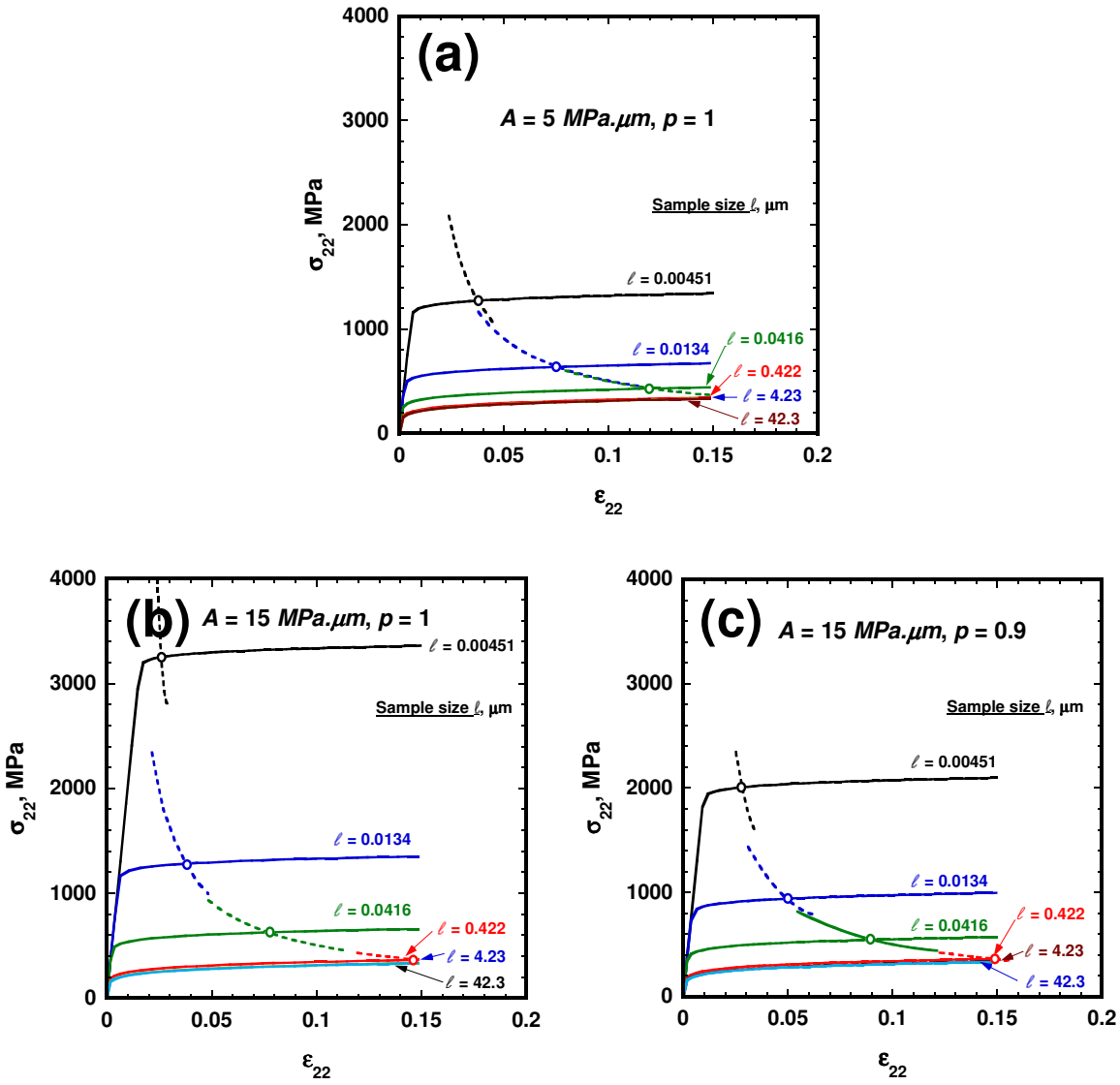

Figure 2A.7 Stress-strain curves are shown for various crystal sizes in (a), (b) and (c) are for different values of crystal size-related constants, A and p. Calculation are based on Equation $\sigma = (k\varepsilon^n + \frac{A}{l^p}) \cdot \dot{\varepsilon}^m$, where $k = 480MPa$, $n = 0.15$ and $m = 0.02$. (strain rate: $3.5\times10^{-2}\ s^{-1}$, orientation: 0 deg, and assumed r = 1.5)

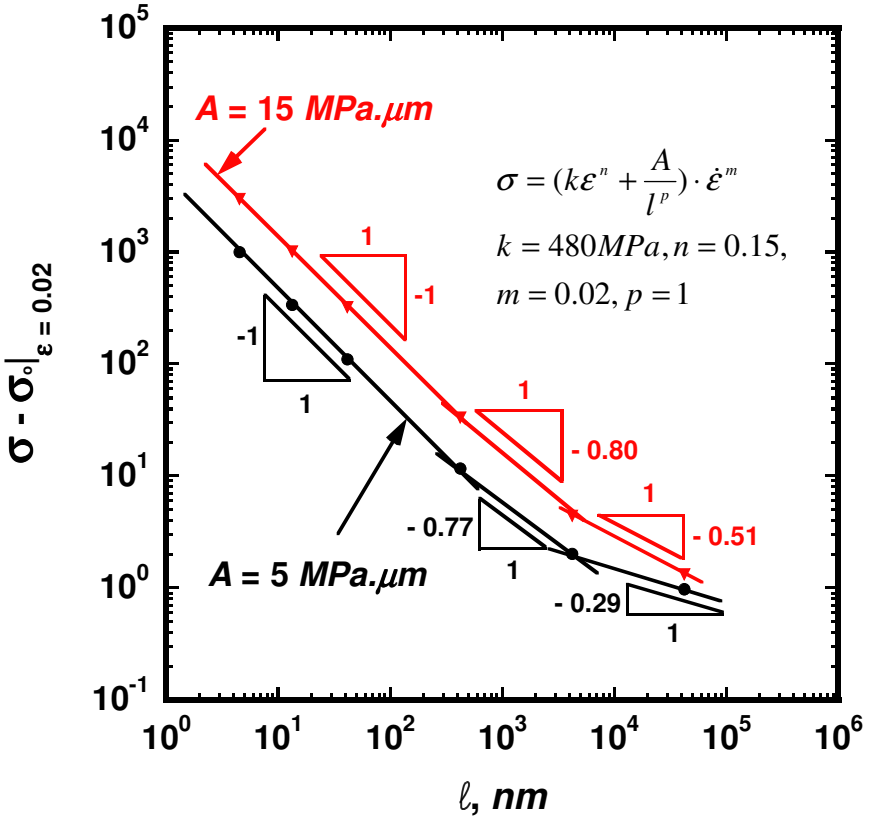

Figure 2A.8 The difference between the flow strength at 2% true strain (σ) for a crystal size, ℓ and the flow strength for large crystal size (σ_0), as determined by simulation results, is plotted as a function of crystal size, l. (strain rate: 3.5×10^{-2} s^{-1}, orientation: 0 deg, and assumed r = 1.5).

2A.5 References

[1] Kehand AS, Nakada Y. Canadian Journal of Physics 1967; 215:1101.

[2] Kelley EW. Ph.D. Thesis, University of Michigan, 1967.

[3] Hosford WF, Fleischer RL, Backofen WA. Acta Metall 1960; 8:187.

[4] Wonsiewicz BC, Backofen WA. Trans Metall Soci AIME 1967; 239:1422.

[5] Bowen DK, Christian JW, Taylor G. Canadian Journal of Physics 1967; 45:903.

[6] Levine ED. Transactions of the Metallurgical Society of AIME 1966; 236:1558.

[7] Asaro RJ. J Applied Mech 1983; 50:921.

[8] Hill R. Proc R Soc Lond Ser A 1948; 193:281.

[9] Clarebrough LM, Hargreaves ME. Progress in Metal Physics 1959; 8:1.

[10] Ghosh AK. Acta Metall 1977; 25:1413.

[11] Swift H. Engineering 1946; 162:381.

[12] Dimiduk DM, Uchic MD, Parthasarathy TA. Acta Mater 2005; 53:4065.

[13] Greer JR, Oliver WC, Nix WD. Acta Mater 2005; 53:1821.

[14] Uchic MD, Dimiduk DM, Florando JN, Nix WD. Science 2004; 305:986.

[15] Kiener D, Motz C, Schöberl T, Jenko M, Dehm G. Adv Engin Mater 2006 ; 8 :1119

[16] Ghosh AK. Acta Mater 2008; 56:2353.

[17] Hill R. Math Proc Camb Soc 1979; 75:179.

[18] Logan RW, Hosford WF. Int J Mech Sci 1980; 22:419.

[19] Hosford WF. Int J Mech Sci 1985; 27:423.

Part B

Abstract: Effect of Grain Size and Mantle Zone Response

Size of crystals in a polycrystalline aggregate affects its strength and formability. Based on stress-strain response of single crystal estimated in Part A, a continuum mechanical model was used to evaluate stress-strain response of polycrystal, which consists of a crystalline matrix and intercrystalline region. Crystalline matrix is characterized by strain hardening, strain rate hardening, as well as the anisotropy of single grain with size dependence of crystal on strength assumed in Part A of study. For simplicity, grain boundary region ("Mantle Zone") is given a fixed thickness of 1 *nm* with homogeneous and uniform viscous response, considering several atom layers on either side of the boundary to be involved in deformation process as a cohesive layer with the grain. For selected misorientation across the boundary of a grain, i.e. different grain orientation on either side of grain boundary, and by varying the constants in the equations for the viscous part as well as the size dependence for grain interior, the strengthening and weakening effects of grain size for polycrystal are estimated. Many behavioral trends are simulated that appear to match reported experimental trends for metals.

2B.1 Introduction

Strengthening effect resulting from the grain refinement for polycrystalline metals is well-established as Hall-Petch relation ($\sigma = \sigma_0 + kd^{-1/2}$, where σ is flow stress of materials, σ_0 is the friction stress, k is the stress intensity, and d is grain size). A literature review in regard to this is given in Appendix 2 (Page 131). Toward the nanometer scale of grain size, the deviation of strengthening effect from the classical $d^{-\frac{1}{2}}$ relation is found or even inverse Hall-Petch effect, i.e. weakening, has been reported (see Appendix 2). Even in the large grain regime, deviation from $d^{-\frac{1}{2}}$ relation as stated by Hall and Petch is found. The underlying mechanisms for transition between grain size strengthening and grain size weakening effect near the nanometer scale are somewhat unclear though grain boundary sliding effects have been attributed as the source of the effects found at extremely small size.

Since the volume fraction of mantle zone increases with decreasing grain size, the role of mantle zone on the properties of polycrystalline aggregates is expected to be magnified. Some main interpretations with and without considering the influence of grain boundary region have attempted to analysis the grain size effect on the strength of polycrystalline materials [14, 15, 19 and 20]. However, a systematic and quantitative investigation involving grain size, geometry, and grain misorientation has not been undertaken over a wide range of grain size, coupled with the mantle zone property to address the effects

resulted from grain refinement. Finite element simulation provides a convenient way to analyze plastic strain developing in different part of the materials. An analytical approach is also useful because experimental results can be affected by artifacts introduced by improper material preparation methods.

Deformation of polycrystals is the sum of crystal slip motions within each crystal and the accommodation of grain rotation and lattice distortion through boundary activities. Due to the crystallographic asymmetry of single crystal, mechanical property of single crystal generally show dependence on crystal orientation with respect to loading direction, which is the basis for the anisotropic mechanical response of polycrystalline aggregate. The crystallographic orientation distribution of crystals within polycrystalline aggregate thereby influences the strength of materials. If a strong texture exists in polycrystalline materials, they can be expected to exhibit stress-strain responses quite similar to that of single crystals of the same composition. It is well-known that Hill's 1948 yield criterion has ability to describe the anisotropy of polycrystalline materials [31]. Therefore, the anisotropic property of single crystal can be reasonably simulated without complicating with crystalline plasticity model, and incorporated into polycrystalline model.

To connect the mechanical response of single crystal to polycrystal behavior, the response of grain boundary region must be considered. From the viewpoint of grain boundary geometry which is expressed within the framework of ***Coincidence Site Lattice*** (***CSL***)

model [32], grain boundary can be classified into tilt boundary, twist boundary and general boundary (combination of tilt and twist boundary). Computational examinations on the tilt and twist grain boundary show that grain boundary geometry has strong effect on the properties of materials [33, 34]. From the viewpoint of grain boundary structure, grain boundary region is characterized with atomic disorder due to the high density of defects, such as dislocations, steps or ledges, vacancies and interstitials. The grain boundary mantle region is thought to have viscous response [35]. Several layers of atoms on either side of the grain boundary between two adjoining grains may be thought to be a part of a cohesive zone involved in deformation process sometimes referred to as a "Mantle Zone" [36]. Discussion about this region can be found in Appendix 3 (Page 137).

When evaluating the stress-strain response and texture development of polycrystals, the original and extended Taylor's models [37, 38] ignored the role of grain boundary property on the general properties of polycrystals. In contrast with coarse-grain materials, fine-grained alloys may have more contribution to deformation from the mantle region. It has been suggested that the activation volume for plastic deformation decreases with decreasing grain size, which is associated with the increasing strain-rate sensitivity and enhanced grain boundary dislocation activity [39]. Therefore, the grain boundary region is an important constituent for polycrystals with nanometer scale size. Generally, grain boundaries are regions where lattice atomic structure is disturbed. Deformation accommodation by slip in these regions is unclear because grain boundary consists of

disordered atomic configuration somewhat like amorphous structure, and dislocation motion can not be properly defined. But it is known from internal friction stress and damping studies that response from grain boundary can be significantly rate-sensitive in character. Moreover, at elevated temperature, grain boundary is known to produce non-Newtonian viscous response (e.g. Nabarro-Herring creep and Coble creep) or Newtonian viscous response. Thus, a polycrystalline metal is inherently heterogeneous, having a more composite-like structure and property.

In mantle-core deformation model [36], the overall superplastic creep rate is obtained by assuming that both mantle and core deformation contribute to the overall deformation; that is,

$$\dot{\varepsilon} = \dot{\varepsilon}_m + \dot{\varepsilon}_c \tag{2B-1}$$

where $\dot{\varepsilon}$ refers to overall creep rate, $\dot{\varepsilon}_m$ refers to mantle's contribution to tensile strain rate and $\dot{\varepsilon}_c$ refers to creep rate contributed by grain core. $\dot{\varepsilon}_m$ can be written as:

$$\dot{\varepsilon}_m = \frac{A}{d^2}(\sigma - \sigma_o)^{1+Q} \tag{2B-2}$$

where A is temperature-dependent constant, d is grain size, σ is tensile stress, σ_o is

the tensile equivalent of τ_o (minimum value of local stress τ at grain boundary) and Q is exponent for dislocation source activation. The detailed discussion about Equation (2B-2) can be found in [36]. By rewriting and simplifying Equation (2B-2), flow stress on mantle region can be expressed as a function of strain rate.

$$\sigma = B\dot{\varepsilon}^{q} \tag{2B-3}$$

where σ refers to flow stress, B refers to strength constant, $\dot{\varepsilon}$ refers to strain rate at mantle region and q refers to strain rate sensitivity. Viscous response described by this equation is associated with dislocation glide and climb near grain boundary region, which is non-Newtonian viscous. However, when q approaches unity, this response becomes Newtonian viscous. Furthermore, the grain boundary mantle zone thickness is defined as the thickness of a region. That is several atomic layers on either side of grain boundary as observed in TEM micrograph, based on the concept of "Mantle Zone". The justification of mantle zone thickness in simulation can be found in Appendix 3 (Page 137).

2B.2 Approach

In the present study, the commercial software ABAQUS®/ Standard analysis module was used to accomplish the modeling work. The finite element modeling procedure in ABAQUS was elaborated in Appendix 1 (Page 88). For polycrystals, a continuum mechanical model combining the stress-strain response of single crystal and viscous mantle zone property was used. For the polycrystal modeling, since the role of mantle zone property will be evaluated, some statements about the mechanical properties of mantle zone should be mentioned as follows (the nomenclature for polycrystals model is summarized in Table 2B.1):

(1) Mantle zone is assumed to be elastically isotropic.

For the elastic properties of the mantle zone, because of the disorder arrangement of atoms in this region, and high density of defects, the non-directional and lower elastic modulus would be resulted compared with bulk crystal, therefore 140 *GPa* was assumed for Young's modulus, and 0.3 for the Poisson's ratio (Table 2B.2 (c)).

(2) Mantle zone has perfect plasticity and is strain-rate sensitive.

The constitutive equation for mantle zone property is listed In Table 2B.2 (b). Within the equation, σ is the flow stress (*MPa*), B is a material constant (*GPa*) and q is the strain-rate sensitivity. The effects of B and q values on the stress-strain response

of polycrystal were evaluated in present study. The mantle zone is given a fixed thickness of 1 nm, which is justified in Appendix 3 (Page 137).

(3) Geometry of polycrystals in simulation cell

For polycrystal model, the 3D geometry was created with 40 *units* (length) ×5.625 *units* (width) in-plane rectangle and 0.2 *units* for thickness (as shown in Figure 2B.1). The bulk geometry was partitioned into 17 hexagon regions and strip layers between hexagons, which represents grain interior and mantle zone within the polycrystals respectively (as denoted in Figure 2B.1). For the principle of geometric similitude in *FEM* calculation, the results of calculation are independent of geometric sample size. Therefore, the geometric dimension in *FEM* can be used to represent different physical dimensions. The various physical sample sizes represented by simulation cell are summarized in Appendix 1.

Figure 2B.1 also shows the definition of grain boundary misorientation. As illustrated in Figure 2B.1, two neighboring crystals are assigned different orientations. Crystal 1 has its *x*-*y* plane and *y* direction parallel to the loading direction, while crystal 2 is rotated around 1-axis (in-plane horizontal direction) by 75 degrees, and has its *x* direction parallel to the 1-axis. This orientation relation between two neighboring crystals creates the boundary misorientation, which is defined as 0-75^{o} twist boundary in present study. For the grain orientations, as shown in Figure 2B.1, all the grains on

left side are of 0^o orientation. Whereas, all the grains on right side are of 75^o out-plane orientation. In this preliminary study, only the twist type of grain boundary was considered.

2B.3 Results and Discussions

Based on the evaluation of single crystals on mechanical properties, a continuum mechanical model was used to estimate the stress-strain response of polycrystals. The mechanical responses of grain interior and mantle zone are described by Equation (2A-5), $\sigma = (k\varepsilon^n + \frac{A}{d^p}) \cdot \dot{\varepsilon}^m$, and Equation (2B-3), $\sigma = B\dot{\varepsilon}^q$, respectively.

2B.3.1 General stress-strain responses

The calculated stress-strain curves were plotted in Figure 2B.2 to 2B.8 in terms of true stress *vs.* true strain along the tensile direction. Some $d\sigma_{22}/d\varepsilon_{22}$ vs. ε_{22} curves were added to determine uniform strain. Some cases do not show the $d\sigma_{22}/d\varepsilon_{22}$ *vs.* ε_{22} curves, since the imposed true tensile strain (up to 10%) is less than uniform strain in those cases. Due to the limit space of plots, only three cases with grain size of 4.92 *nm*, 18.9 *nm* and 59.8 μm are shown. From Figure 2B.2 to 2B.8, a general view can be seen that flow stress increases with decreasing grain size and increasing strain rate. Generally, yield stress is known to have similar dependence on grain size to hardness for metals. It

was reported that increasing hardness of nickel and iron with nanometer scale grain size was observed down to 12 *nm* which well follow the Hall-Petch relation [3, 10], while lots of investigation on the materials with the grain size of a few nanometers show weakening effect [20, 21, 28 and 29].

As seen from Figure 2B.2 (A = 5 $MPa.\mu m$, p = 1, B = 3 GPa and q = 0.1), the strain rate effect becomes more pronounced when the grain size decreases. This could be due to the increasing volume fraction of viscous grain boundary mantle region. Then, strain contributed by this region to deformation process increases.

Moreover, it can be seen that higher strain rate results in higher rate of work hardening. This higher work hardening rate generates larger uniform strain. The uniform strain also increases with increasing grain size. From the equivalent plastic strain map in Figure 2B.9 (a), it can be seen that more strain occurs within mantle region when applied strain rate is low. Strain concentration zone near the mantle indicates this region undergoes shearing. At high strain rate, rate hardening occurs in the mantle region, causing high strength in mantle region, forcing deformation in the grain interior (as shown in Figure 2B.9 (b)), and strain in mantle region is reduced. The higher rate of work hardening could increase the stability of deformation. These behavioral trends based on simulation appear to match reported experimental trend for metals, such as the results in Ref. [40].

For those cases where mantle region is stronger than grain interior or for coarser grain materials, the role of mantle region property is reduced. For such cases, it has been found that variation in strain distribution from one grain to its adjoining grain is caused by the different orientations of the crystals relative to the loading direction. This finding will be reported in a publication at later time.

2B.3.2 Effect of material constants on the stress-strain behavior

The effects of various material constants on stress-strain behavior have been calculated and shown in Figures 2B.2 to 2B.8. These parameters are such as the item related to surface fracture resistance, A, grain size exponent, p, strength constant for mantle zone, B, and strain-rate sensitivity for mantle zone, q. In this section, summary plots based on Figures 2B.2 to 2B.8 are presented below to discuss the effect of those parameters.

1) Effect of A in crystal size-dependent part

For the effect of A, it can be seen, by comparing Figure 2B.10 (a) and Figure 2B.10 (b) that, increasing A increases the overall stress level of materials. This effect is more pronounced in smaller grain size. It is known in Part A that strength of single crystal is dependent on crystal size. As grain size becomes smaller, more strain is expected to be contributed by grain boundary mantle region. Therefore, the increasing rate sensitivity of

materials with smaller grain size is believed to be resulted from the increasing contribution of viscous response of mantle zone. Another effect of increasing *A* is decreasing uniform strain. This is also due to the increasing strain in viscous grain boundary mantle which increases the heterogeneous deformation in polycrystalline solid, and weakens the stability of deformation process. Comparing the Figure 2B.10 (c) and (d), similar effect of *A* value can be seen as increasing the strength constant of mantle zone, *B*, though the stress-strain response is somewhat different.

2) Effect of strength constant of mantle zone, *B*

Compared the results in Figure 2B.10 (a) and Figure 2B.10 (c), it can be seen that, by increasing the strength of mantle zone (strong boundary), not only the flow stress but also the work hardening rate are significantly increased, especially for the structure of smaller grain size. Moreover, uniform strain is increased too, while the rate sensitivity is reduced. It can be expected that stronger boundary will reduce the strain contribution from mantle region to the overall deformation of materials, and increase the overall strength of materials. The strain imposed on materials is mainly accommodated by the dislocation slip within grain interior. The enhanced work hardening rate is contributed by grain interior also. However, the effect of *B* value is inconspicuous for larger grain size due to the small volume fraction of mantle zone. Furthermore, the weak grain interior increases the stability of deformation due to larger work hardening. For the effects of increasing *B*

value, similar results can be seen by comparing Figure 2B.10 (b) and Figure 2B.10 (d).

3) Effect of grain size exponent, *p*

To evaluate the effect of grain size exponent (p), two p value are assumed, such as $p = 1$ and $p = 0.6$, with two strain rates ($\dot{\varepsilon}$=3.5×10^{-2} s^{-1} and $\dot{\varepsilon}$=3.5×10^{-5} s^{-1}). For other material constants, it is assumed that $A = 15\ MPa{\cdot}\mu m^p$, $B = 3\ GPa$, and $q = 0.1$. The results are shown in Figure 2B.11. By comparing Figure 2B.11 (a) and (b), it can be seen that, when decreasing the p from 1 to 0.6, the stress-strain curves have much smoother transition from elasticity to plasticity. Moreover, uniform strain is increased, but overall flow stresses for different grain size are decreased. As seen from the comparison between Figure 2B.11 (c) and (d) having different strain rate, the effect of p is more pronounced at high strain rate and for smaller grain size. In present analysis, the constitutive equation for grain interior is $\sigma = (k\varepsilon^n + \frac{A}{d^p}) \cdot \dot{\varepsilon}^m$, where the unit of grain size (d) is micron. When reducing the p, it decreases the value of $\frac{A}{d^p}$, and reduces the strength of grain interior when the grain size is smaller than 1 μm. Accordingly, the overall flow stress is decreased. The strain contribution from grain interior will be increased, and strain rate sensitivity of materials caused by viscous mantle zone will decrease. Considering the effect of strain rate, it can be seen that rate hardening effect developed during high strain rate deformation results in stronger boundary, which enlarge grain size effect on strength. In Figure 2B.12, the equivalent plastic strain maps for $p = 1$ and $p = 0.6$ are shown.

Obviously, when p = 1, more strain distributes within mantle zone, and tends to develop strain concentration along boundary (Figure 2B.12 (a)); when p = 0.6, strain concentrates within grain interior (Figure 2B.12 (b)). In contrast, the grain size effect is weakened by the strain contribution from grain boundary at low strain rate. This obviously is relative strength between grain interior and mantle zone. However, the p effect is not clear for larger grain size structure due to the small volume fraction of mantle zone within the materials.

4) Effect of strain-rate sensitivity, q (mantle region)

The effect of q is shown in Figure 2B.13. The other material constants are assumed that A = 15 $MPa{\cdot}\mu m^{0.9}$, p = 0.9 and B = 3 GPa. For Figure 2B.13 (a), the viscous nature of mantle zone brings in the large rate effect on the stress-strain response. Overall, the flow stress increases with decreasing grain size. When decreasing the strain rate, the grain size effect is reduced, which is believed to be resulted from the contribution of mantle zone to the total strain. When increasing the q from 0.1 to 0.3 for weak boundary, flow stresse for different grain sizes decreases; the grain size effect is significantly reduced, and even changed for low strain rate. It can be seen from Figure 2B.13 (b) with strain rate of 3.5×10^{-5} s^{-1} that, the flow stress for the grain structure with grain size of 4.92 nm is even lower than that of 18.9 nm. In Figure 2B.14, equivalent plastic strain map for this calculation shows that the total strain of polycrystals is contributed completely by strain

in mantle zone. Grain boundary shearing was found. This is similar to the observation on high temperature deformation where thermal-assisted diffusion process and grain boundary sliding dominate the deformation process. Even, room-temperature diffusion creep has been suggested to accommodate the deformation process [20, 21], which was related to the observed weakening effect of grain refinement in experiments.

2B.3.3 Grain size dependence of strength

An empirical form similar to Hall-Petch relation was used in this section to study the grain size dependence of strength in polycrystals. To evaluate the grain size effect on the flow stress, the flow stress at 1% strain versus square root of grain size ($d^{-1/2}$) is plotted in Figure 2B.15. In Figure 2B.15 (a), it can be seen that the increasing A increases the Hall-Petch slope. Moreover, the strain rate has small effect on slope. As seen from Figure 2B.15 (b), grain size exponent (p) also changes the slope of Hall-Petch relation, where the slope decreases with decreasing p value. As discussed previously about the effect of p on the stress-strain responses of polycrystal model, reducing p value will decrease the strengthening effect of grain size. However, q shows complex effect on slope (shown in Figure 2B.15 (c)). For q = 0.1 (strong boundary), increasing strain rate increases the slope. When increasing the q value to 0.3 (weak boundary) with high strain rate, the relation between flow stress and square root of grain size is almost linear, but negative slope was found at low strain rate. This results from weak boundary of high strain rate sensitivity.

To examine the grain size dependence of strength in great detail, in Section 2B.3.5, additional plots of similar results are also presented.

2B.3.4 Evaluation of calculated flow stability

Evaluation of flow instability for polycrystals is in term of $\gamma = (\frac{d\sigma}{d\varepsilon})\frac{1}{\sigma}|_{\varepsilon=0.1}$ versus $\log d$, which is shown in Figure 2B.16. The line of $\gamma = 1$ is denoted in this Figure, which is criterion of evaluating the flow stability of materials during tension. When $\gamma > 1$, the materials has uniform deformation; when $\gamma < 1$, materials tends to develop localized deformation.

In Figure 2B.16 (a), it can be seen that the decreasing p value reduces the dependence of flow instability on grain size. When p = 1 and 0.9, the increasing grain size improves the flow stability. When p = 0.6, γ is large than unit for various except of the smallest grain size (d = 4.92 nm). The strain rate effect on the flow stability is small. It can be expected that, as grain size decreases, the volume fraction of mantle zone increases. More strain within materials is contributed by this region, causing heterogeneous deformation, and then it deteriorates the flow stability of polycrystals. As discussed in **Section 2B.3.2** about the effect of p on the stress-strain responses of polycrystalsl, decreasing p decreases the strength of crystals, and reduces the grain size effect on the strength of polycrystals. Consequently, the dependence of flow stability on grain size is reduced. The flow

stability was affected by the relative strength between grain and mantle zone. As p value decreases to 0.6, the strength of grain interior is relative small compared with mantle zone; and then more strain occurs within the grain interior. The deformation within the grain interior generates higher work hardening, which increases the flow stability of polycrystalline materials.

In Figure 2B.16 (b), the effect of A value on the flow stability of polycrystals is shown, where $p = 1$, $B = 3$ GPa and $q = 0.1$. It can be seen that decreasing A value increases the flow stability due to the enhanced deformation within the grain interior. $\gamma > 1$ occurs for large grain size.

However, when increasing the strength constant of mantle zone (B) from 3 GPa to 15 GPa, which refers to strong boundary, the grain size and strain rate effects on the flow stability become complicated (shown in Figure 2B.16 (c)). Under this condition, $\gamma > 1$ for all grain size was found when $A = 5$ $MPa \cdot \mu m^{0.9}$ at different strain rate and $A = 15$ $MPa \cdot \mu m^{0.9}$ at high strain rate. However, change of γ with grain size is quite different for different strain rates. At high strain rate, the results show that γ decreases with increasing grain size at small grain size regime, and then increased with increasing grain size at large grain size regime; inversely, when strain rate is low, γ increases with increasing grain size at small grain size regime, and decreased with increasing grain size at large grain size regime. Obviously, the changes of γ with grain size are determined

by the relative strength between grain and mantle zone, which affect the fraction of total strain contributed by grain interior and mantle zone. If more strain are contributed by grain interior, γ is larger, which means higher flow stability; while more strain are contributed by mantle zone, γ is smaller, which means more heterogeneous deformation along the boundary occurs, and then deteriorates the flow stability of polycrystals.

2B.3.5 Detailed examination on grain size dependence of strength

As shown in previous **Section 2B.3.3**, the strengthening and weakening effect in polycrystals were examined in a form similar to Hall-Petch relation. In this section, a more detailed examination was carried out in a general form to study the grain size dependence of strength. The flow stresses at the true strain of 0.01 for different grain size were collected and plotted in term of $\log(\sigma - \sigma_0)$ *versus* $\log(d)$ in Figure 2B.17; and the slope of curves indicates the effect of grain size on strength. The slope for polycrystals has been reported that it can be $\frac{1}{2}$, $\frac{1}{3}$ or 1 [15]. As seen from Figure 2B.17 (a), reducing the grain size exponent, p can lower the slope for whole grain size range. When p = 1, slope is - 0.84 in the small grain size range, - 0.98 in intermediate grain size range, and – 1.22 for large grain size range; when p = 0.6, slope is - 0.8 in the small grain size range, - 0.56 in intermediate grain size range, and - 0.7 for large grain size range, which are in agreement with Hall-Petch relation. The effect of p on slope can be related

to its effect on the strength of grain interior. That is, when decreasing p, the strength of grain interior is small, and this accordingly decreases the slope.

Furthermore, in Figure 2B.17 (b), when being strained at low strain rate and weak boundary condition (A = 15 $MPa.\mu m^p$, p = 0.9, B = 3 GPa and q = 0.3), weakening effect of grain refinement was found at the smallest grain size, where slope is 0.74. However, when being strained at same condition but the strength of grain interior is smaller (A = 5 $MPa.\mu m^p$, p = 0.6), no weakening effect is found; and slope is constant (- 0.42) within wide range of grain size, which is close to Hall-Petch relation of the - 0.5 slope. It is believed that relative strength between grain interior and mantle zone results in this effect. When grain interior is weaker than mantle zone, no weakening effect will result in.

2B.4 Summary and Conclusions

Finite element simulations were performed to estimate stress-strain behavior of polycrystals. The property of each crystal in the polycrystal incorporates work hardening term, strain rate sensitive term, anisotropic behavior, and size effect of each crystal used to describe the stress-strain behavior of grain interior. Grain boundary region was described by a cohesive Mantle Zone exhibiting viscous behavior. Anisotropic continuum plasticity approach is used to analyze the stress-strain response of each crystal in the polycrystal. The simulation used a cell (SCU) containing 17 grains and a fixed thickness of Mantle Zone of 1 nm. By varying the material constants in the equations, the calculated results have demonstrated the following results:

(1) The continuum model in present study provides an efficient way to incorporate anisotropic response and size effect of single crystal as well as viscous grain boundary mantle response to predict the strengthening and weakening effect caused by grain refinement in polycrystals.

(2) Many behavioral trends are simulated that appear to match reported experimental trends for metals.

(3) Predicted dependence of flow instability on grain size was found to be affected by the relative strength of mantle region to grain interior. When mantle region is weaker than grain interior, flow instability occurs due to localized strain in this region.

(4) Predicted dependence of strength on grain size was in agreement with Hall-Petch relation, but dependence of strength on grain size showed varieties from (grain size)$^{-0.38}$ to (grain size)$^{-1.22}$ in various regimes of grain sizes.

(5) Weakening effect was predicted in some cases when mantle region was weak at very fine grain size. If grain interior is weaker than mantle region, no weakening effect was found.

(6) Simulation results suggest that weakening effect of grain refinement may be resulted from increasing volume fraction of grain boundary with low viscosity when strain map near grain boundary mantle regions exhibit shearing concentration in the mantle regions.

Table 2B.1 Nomenclature for polycrystals model

σ	Flow stress, *MPa*
k	Strength constant, *MPa*
ε	Tensile strain
n	Strain hardening rate
A	Size-related stress component, $MPa \times \mu m^p$
p	Grain size exponent
m	Strain-rate sensitivity of grain interior
B	Strength constant for mantle zone, *GPa*
$\dot{\varepsilon}$	Strain rate
q	Strain-rate sensitivity of mantle zone
E	Young's modulus
v	Poisson's ratio
r	Lankford's anisotropy
d	Grain diameter, μm

Table 2B.2 Parameters in constitutive equation describing the stress-strain properties of grain and grain boundary ("Mantle Zone")

(a) Plastic properties for grain

Equations	Parameters				
	K, MPa	n	$A, MPa \cdot \mu m^p$	p	m
$\sigma = (k\varepsilon^n + \frac{A}{d^p}) \cdot \dot{\varepsilon}^m$	480	0.15	5	1	0.02
	480	0.15	15	1	0.02
	480	0.15	15	0.9	0.02
	480	0.15	15	0.6	0.02

(b) Plastic properties for mantle zone

Equations	Parameters	
	B, GPa	q
$\sigma = B\dot{\varepsilon}^q$	3	0.1
	3	0.3
	15	0.1

(c) Elastic properties for mantle zone

Parameters	
E, GPa	***ν***
140	0.3

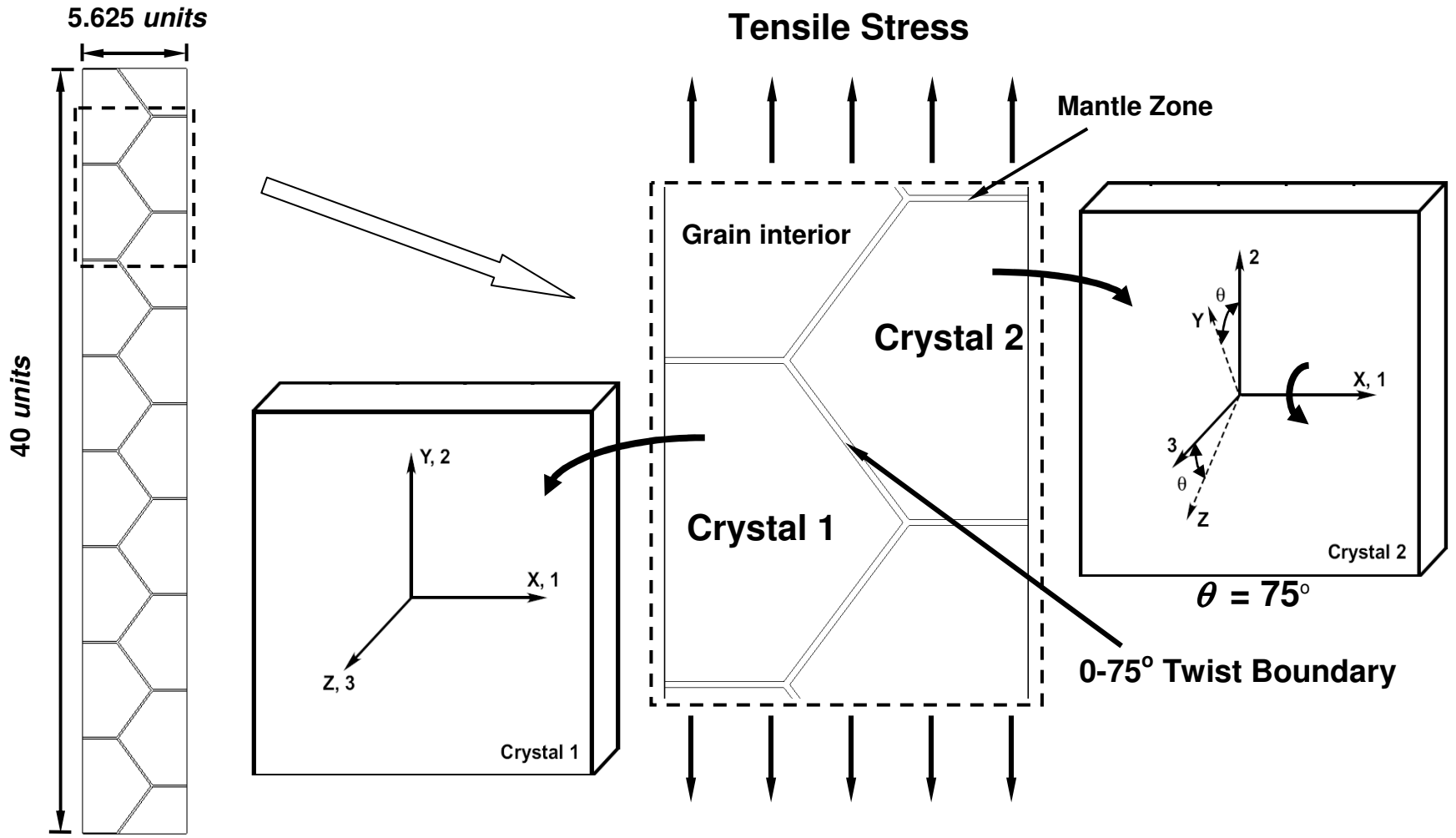

Figure 2B.1 Schematic representation of hexagonal grain in polycrystalline metals subjected to tensile deformation. The dotted cell shown within this polycrystalline aggregate is taken as a representative unit cell for FEM simulation. The details of this unit cell (SCU) show grain boundary region with different orientations of crystals across them.

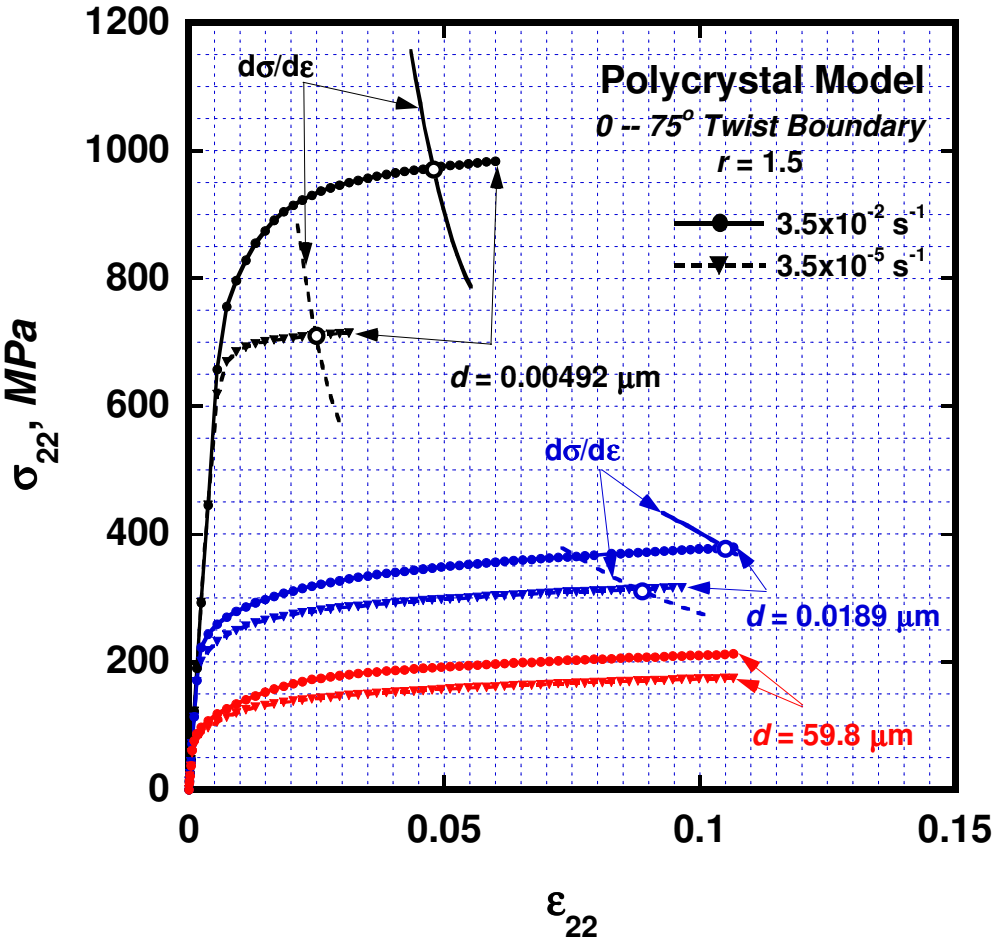

Grain interior

$$\sigma = (k\varepsilon^n + \frac{A}{d^p}) \cdot \dot{\varepsilon}^m$$

$k = 480MPa, n = 0.15$

$A = 5MPa \cdot \mu m, p = 1, m = 0.02$

$E = 200GPa$

Mantle zone

$\sigma = B\dot{\varepsilon}^q$

$B = 3GPa, q = 0.1$

$E = 140GPa$

Figure 2B.2 Calculated stress-strain curves are shown for different grain size and strain rate (A = 5 *MPa.μm*, p = 1, B = 3 *GPa* and q = 0.1) (assumed r = 1.5)

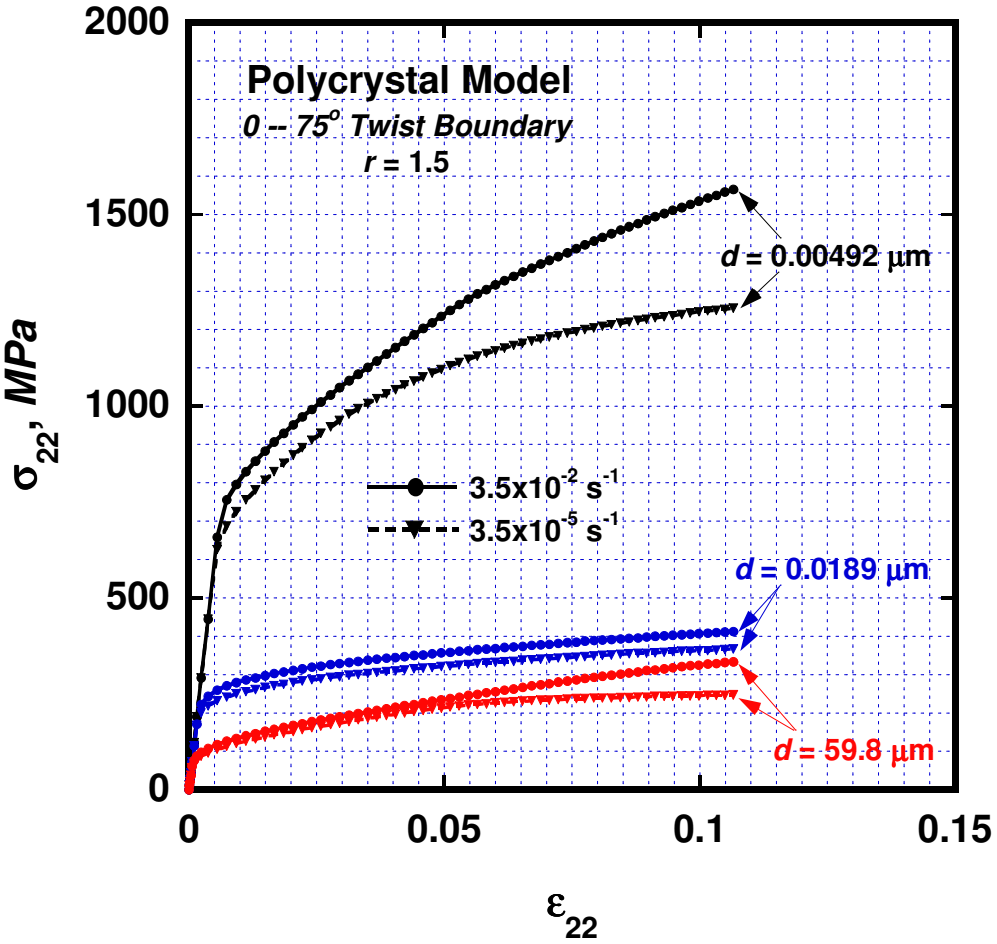

Grain interior

$\sigma = (k\varepsilon^n + \frac{A}{d^p}) \cdot \dot{\varepsilon}^m$

$k = 480MPa, n = 0.15$

$A = 5MPa \cdot \mu m, p = 1, m = 0.02$

$E = 200GPa$

Mantle zone

$\sigma = B\dot{\varepsilon}^q$

$B = 15GPa, q = 0.1$

$E = 140GPa$

Figure 2B.3 Calculated stress-strain curves are shown for different grain size and strain rate

(A = 5 $MPa.\mu m$, p = 1, B = 15 GPa and q = 0.1) (assumed r = 1.5)

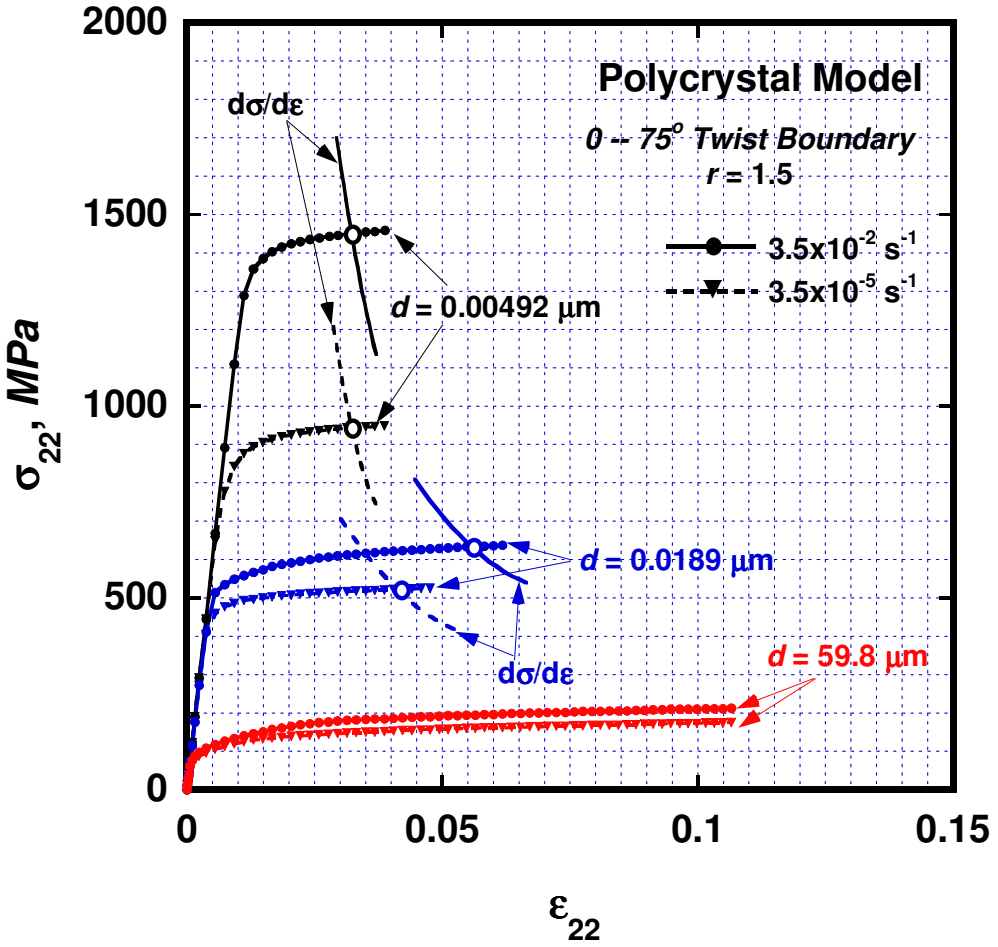

Grain interior

$\sigma = (k\varepsilon^n + \frac{A}{d^p}) \cdot \dot{\varepsilon}^m$

$k = 480MPa, n = 0.15$

$A = 15MPa \cdot \mu m, p = 1, m = 0.02$

$E = 200GPa$

Mantle zone

$\sigma = B\dot{\varepsilon}^q$

$B = 3GPa, q = 0.1$

$E = 140GPa$

Figure 2B.4 Calculated stress-strain curves are shown for different grain size and strain rate

(A = 15 $MPa.\mu m$, p = 1, B = 3 GPa and q = 0.1) (assumed r = 1.5)

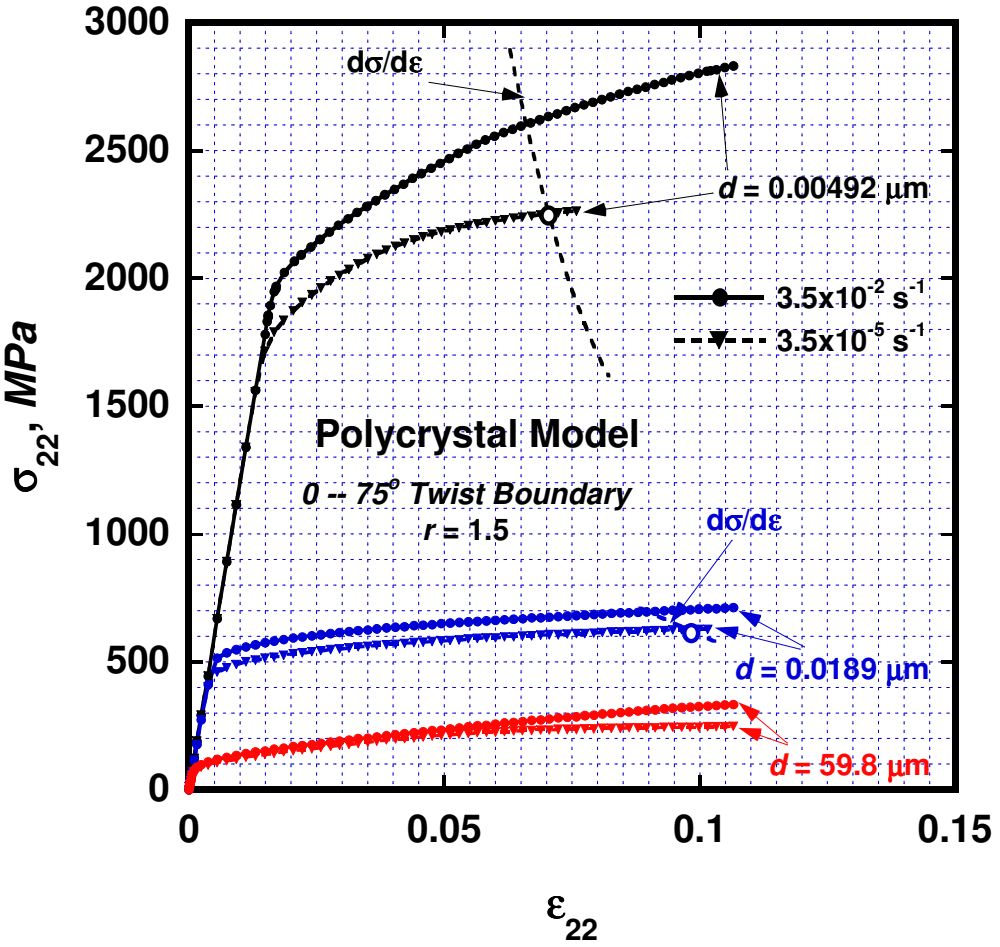

Grain interior

$\sigma = (k\varepsilon^n + \frac{A}{d^p}) \cdot \dot{\varepsilon}^m$

$k = 480MPa, n = 0.15$

$A = 15MPa \cdot \mu m, p = 1, m = 0.02$

$E = 200GPa$

Mantle zone

$\sigma = B\dot{\varepsilon}^q$

$B = 15GPa, q = 0.1$

$E = 140GPa$

Figure 2B.5 Calculated stress-strain curves are shown for different grain size and strain rate (A = 15 $MPa.\mu m$, p = 1, B = 15 GPa and q = 0.1) (assumed r = 1.5)

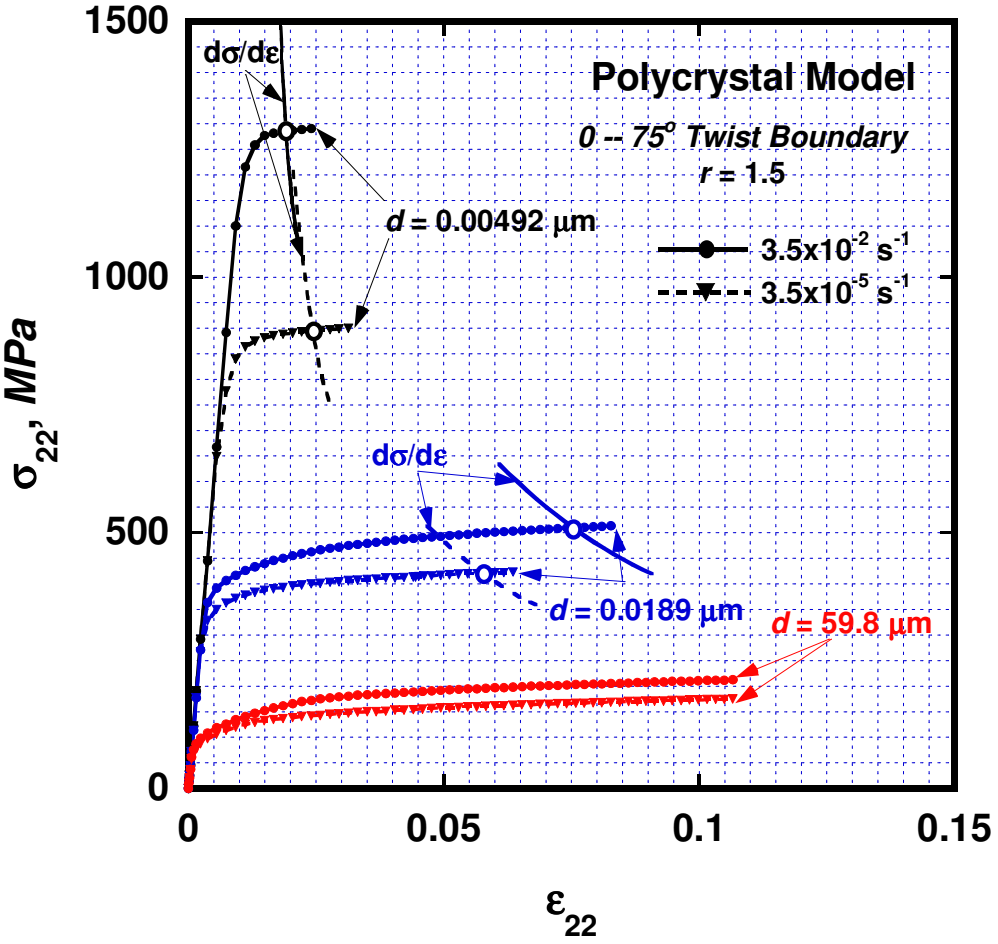

Grain interior

$\sigma = (k\varepsilon^n + \frac{A}{d^p}) \cdot \dot{\varepsilon}^m$

$k = 480MPa, n = 0.15$

$A = 15MPa \cdot \mu m^{0.9}, p = 0.9, m = 0.02$

$E = 200GPa$

Mantle zone

$\sigma = B\dot{\varepsilon}^q$

$B = 3GPa, q = 0.1$

$E = 140GPa$

Figure 2B.6 Calculated stress-strain curves are shown for different grain size and strain rate (A = 15 $MPa.\mu m^{0.9}$, p = 0.9, B = 3 GPa and q = 0.1) (assumed r = 1.5)

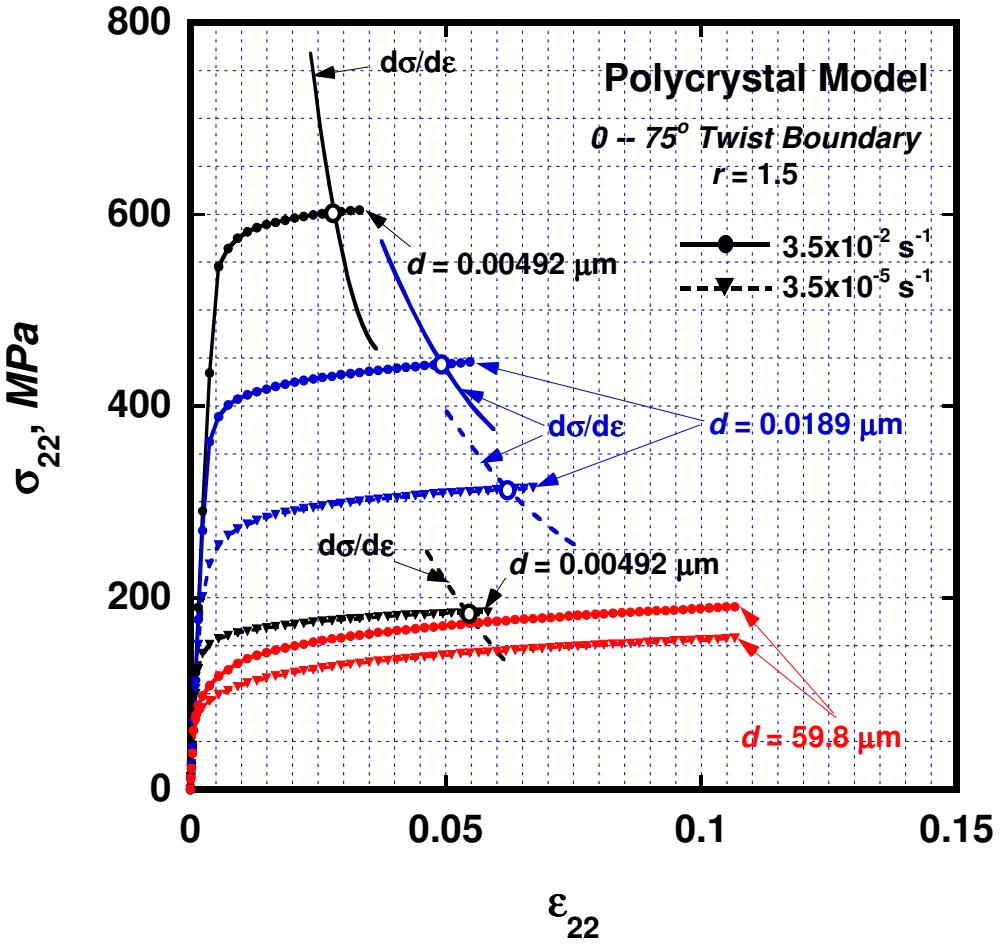

Grain interior

$$\sigma = (k\varepsilon^n + \frac{A}{d^p}) \cdot \dot{\varepsilon}^m$$

$k = 480MPa, n = 0.15$

$A = 15MPa \cdot \mu m^{0.9}, p = 0.9, m = 0.02$

$E = 200GPa$

Mantle zone

$\sigma = B\dot{\varepsilon}^q$

$B = 3GPa, q = 0.3$

$E = 140GPa$

Figure 2B.7 Calculated stress-strain curves are shown for different grain size and strain rate (A = 15 $MPa.\mu m^{0.9}$, p = 0.9, B = 3 GPa and q = 0.3) (assumed r = 1.5)

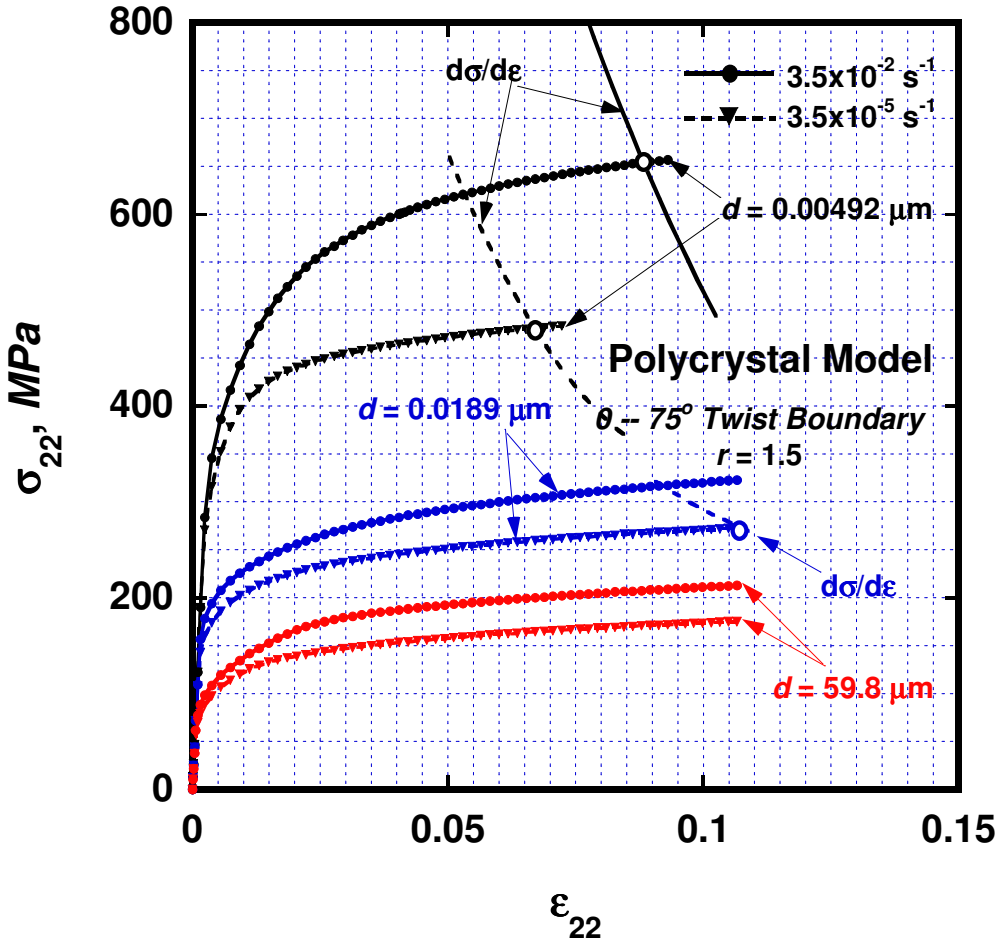

Grain interior

$\sigma = (k\varepsilon^n + \frac{A}{d^p}) \cdot \dot{\varepsilon}^m$

$k = 480 MPa, n = 0.15$

$A = 15 MPa \cdot \mu m^{0.6}, p = 0.6, m = 0.02$

$E = 200 GPa$

Mantle zone

$\sigma = B\dot{\varepsilon}^q$

$B = 3GPa, q = 0.1$

$E = 140 GPa$

Figure 2B.8 Calculated stress-strain curves are shown for different grain size and strain rate (A = 15 $MPa.\mu m^{0.6}$, p = 0.6, B = 3 GPa and q = 0.1) (assumed r = 1.5)

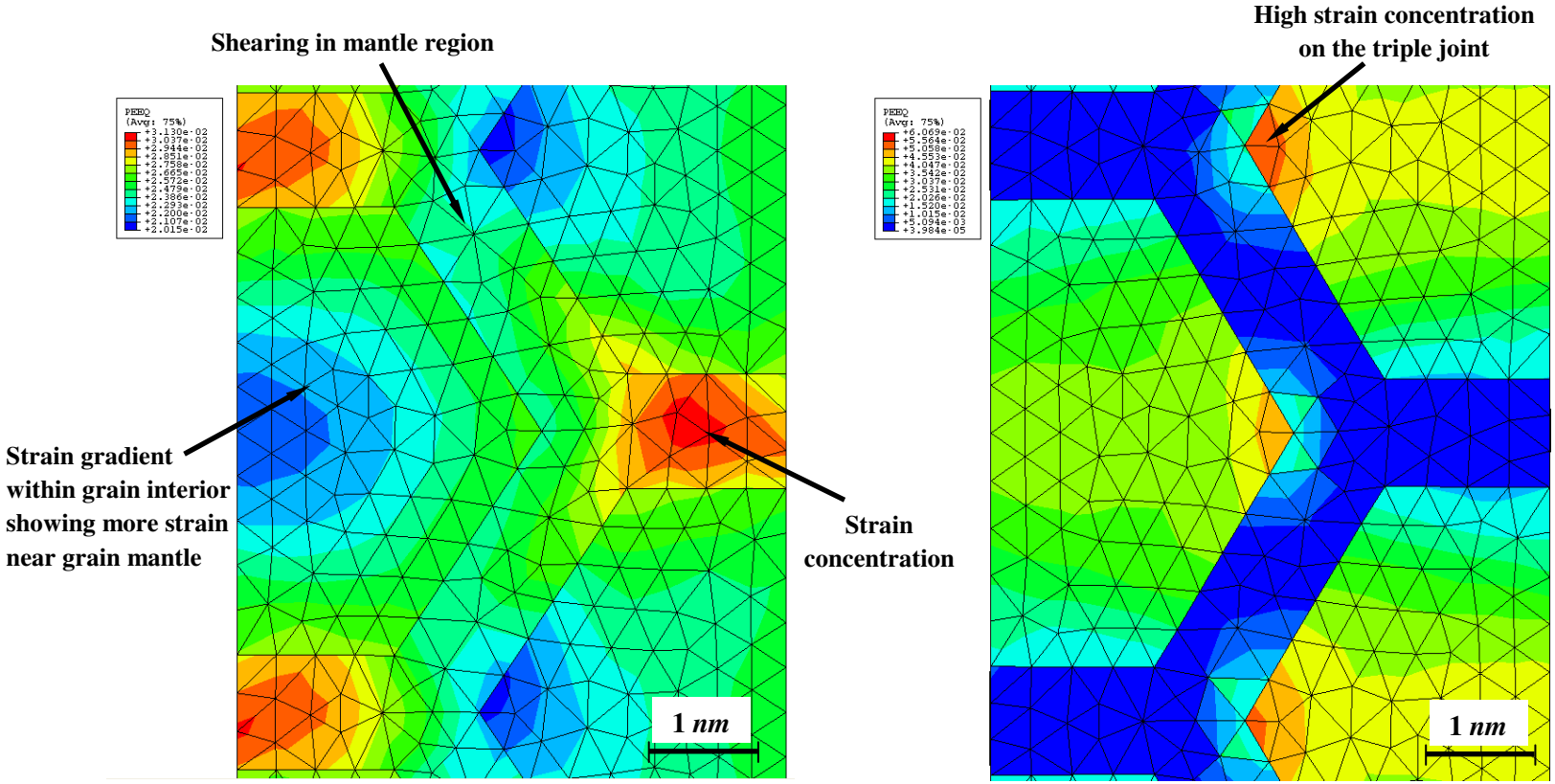

(a) $\dot{\varepsilon} = 3.5 \times 10^{-5}\, s^{-1}$ **(b)** $\dot{\varepsilon} = 3.5 \times 10^{-2}\, s^{-1}$

Figure 2B.9 Equivalent plastic strain maps for polycrystals with grain size of 4.92 *nm* showing the strain distribution within grain interior and mantle zone at two different strain rates and 3% total strain (*A* = 5 *MPa.μm*, *p* = 1, *B* = 3 *GPa* and *q* = 0.1). Strain concentration and shearing in mantle zone are observed in (a), where the constants used for mantle zone make this zone weaker than grain interior at low strain rate; while mantle region shows reduced strain, and strain within grain interior increases when high strain rate is used.

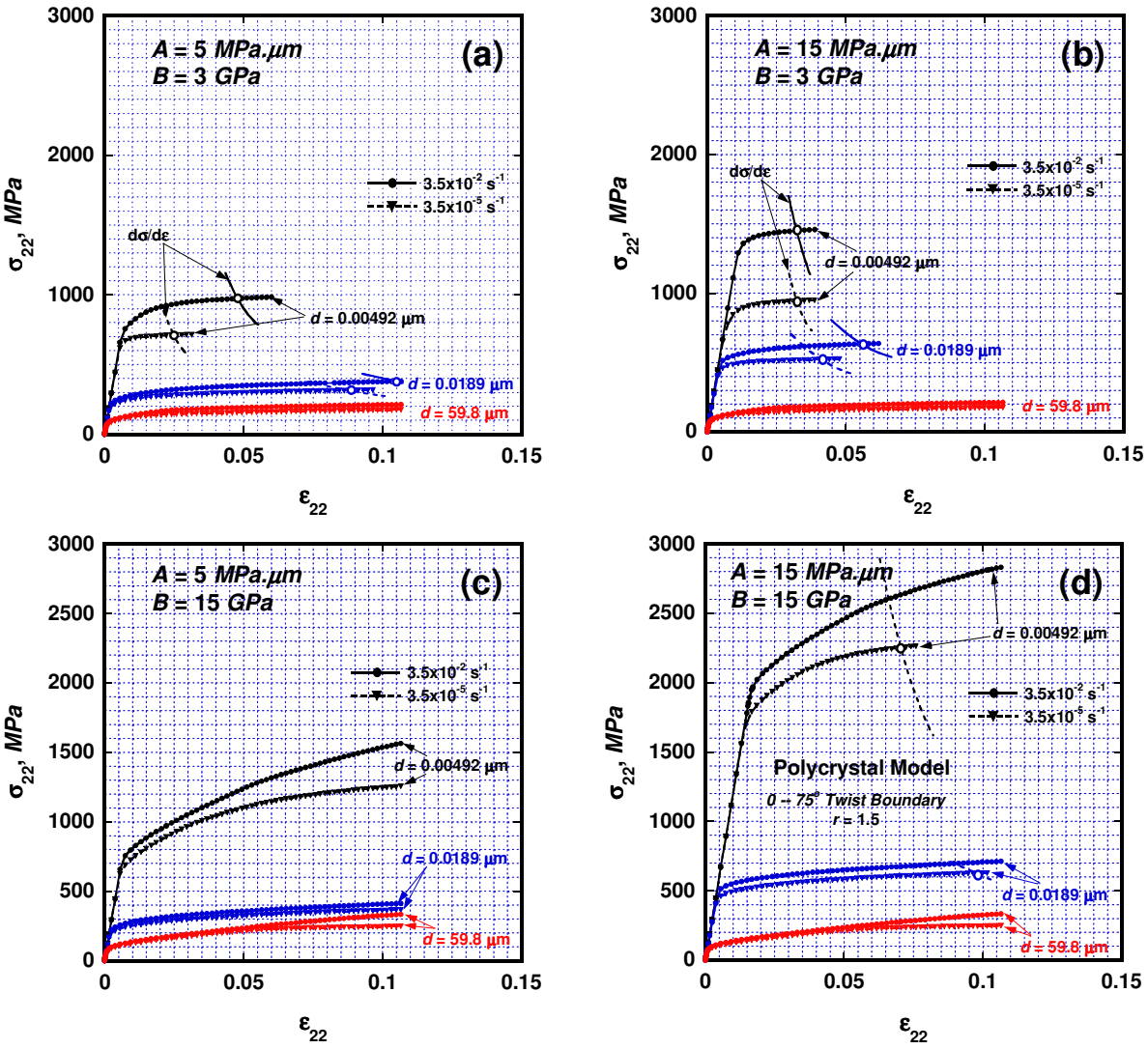

Figure 2B.10 Stress-strain curves for polycrystals with various grain sizes showing the effect of grain interior and mantle zone properties on the stress-strain behaviors for a grain boundary misorientation represented 0 – 75° twist orientation, $r = 1.5$, $p = 1$ and $q = 0.1$.

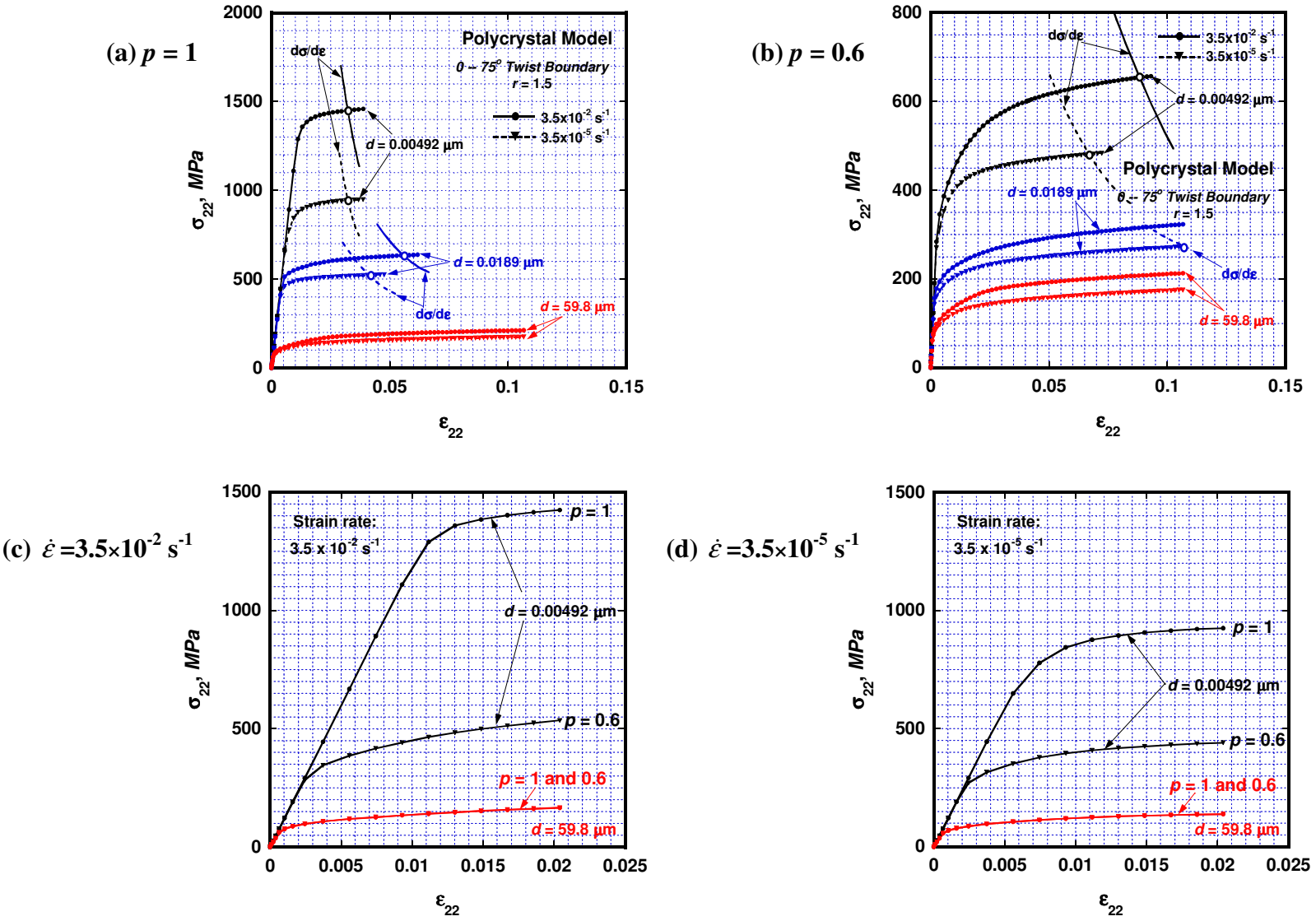

Figure 2B.11 Stress-strain curves for polycrystals with various grain sizes showing the effects of grain size exponent, *p* and strain rate on the stress-strain behaviors for a grain boundary misorientation represented 0 – 75° twist orientation, *r* = 1.5. *A* = 15 *MPa•μm*$^{0.9}$. *B* = 3 *GPa*. and *a* = 0.1.

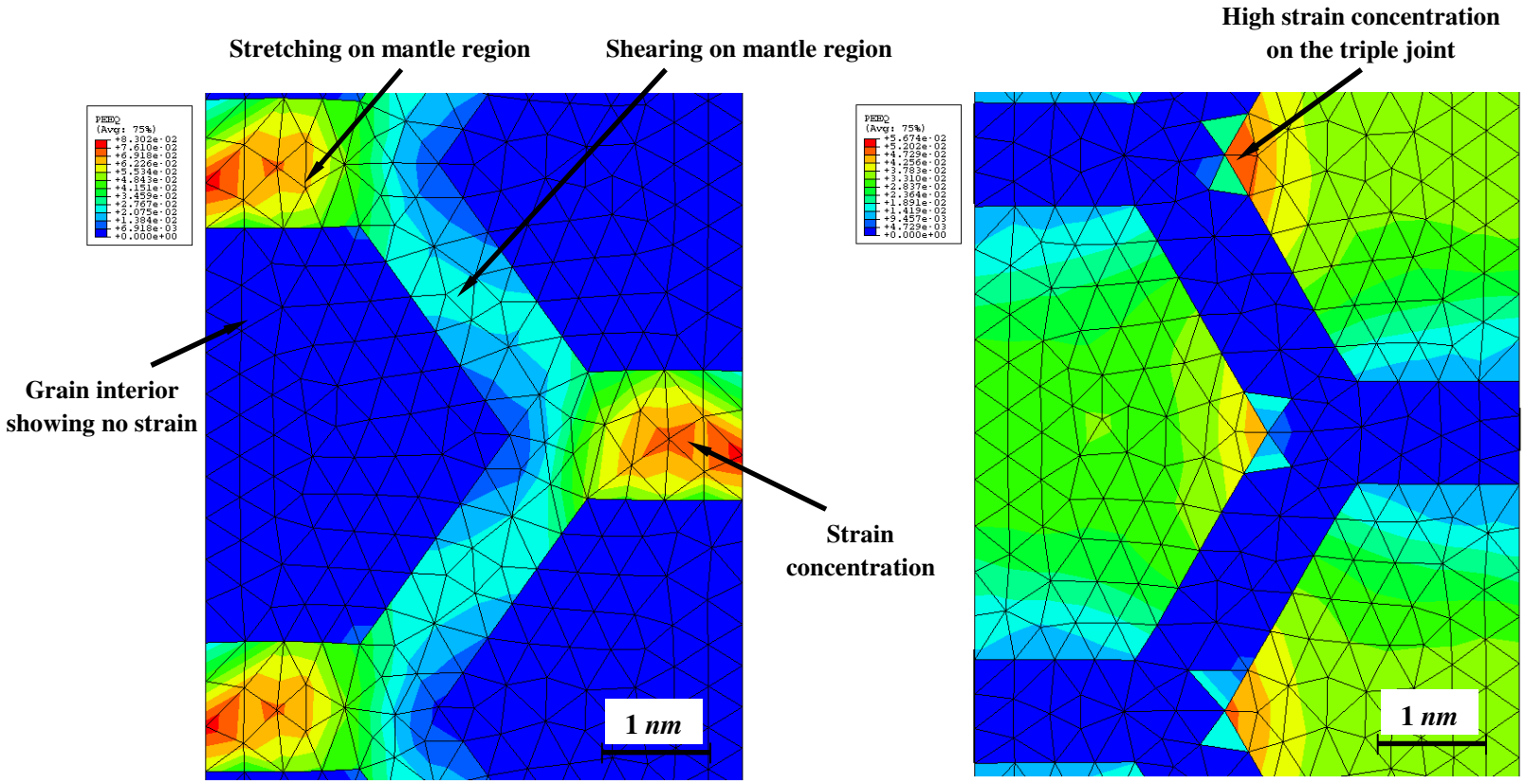

(a) $p = 1$ (b) $p = 0.6$

Figure 2B.12 Equivalent plastic strain maps for polycrystals with grain size of 4.92 *nm* showing the strain distribution within the grain interior and mantle zone for two different p values and 2% total strain ($A = 5$ *MPa.μm*, $B = 3$ *GPa*, $q = 0.1$ and strain rate: $3.5 \times 10^{-2} s^{-1}$). With $p = 1$, strain mainly distributes within mantle region due to relatively higher strength of grain interior to mantle zone, and stretching, shearing and strain concentration are observed in mantle region (a); while, with $p = 0.6$, strain mainly distributes within grain interior due to relatively lower strength of grain interior to mantle zone, and strain concentration is shown in triple joint region (b).

(a) $q = 0.1$

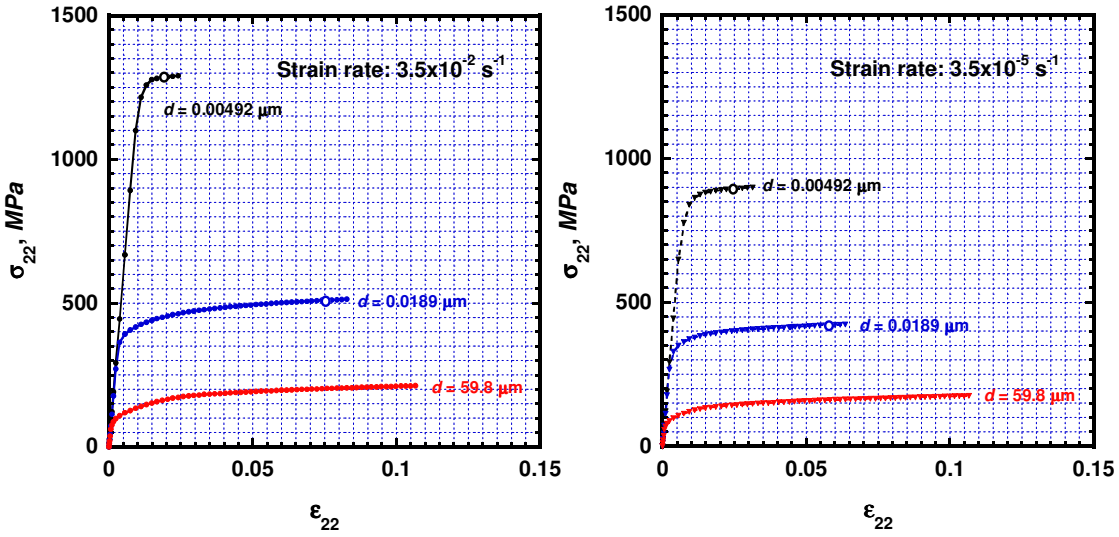

(b) $q = 0.3$

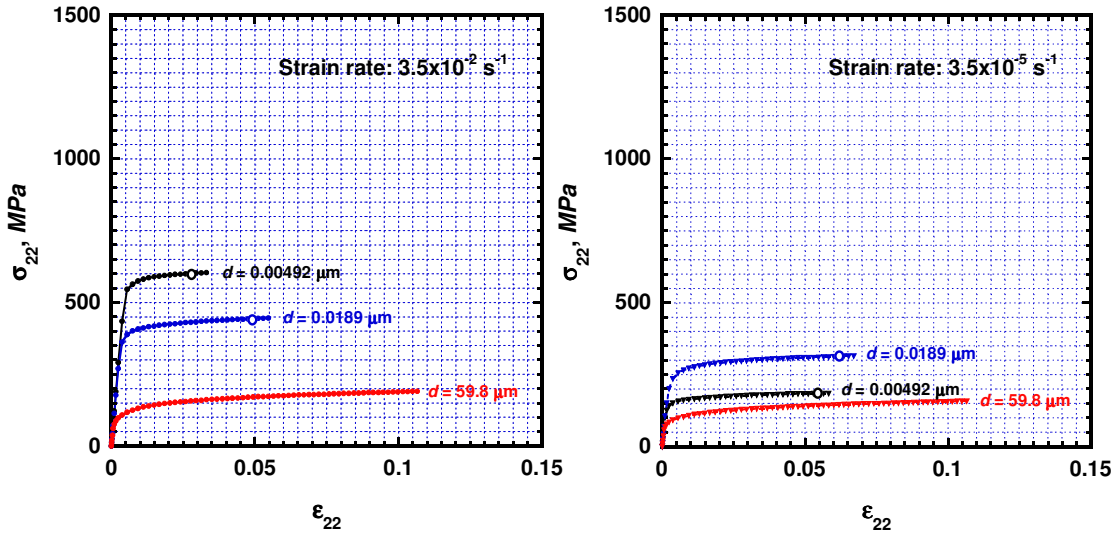

Figure 2B.13 Stress-strain curves for polycrystals with various grain sizes showing the effect of viscosity parameter, q on the stress-strain behaviors for a grain boundary misorientation represented 0 – 75° twist orientation, r = 1.5, A = 15 $MPa{\cdot}\mu m^{0.9}$, p = 0.9 and B = 3 GPa. (a) low strain rate sensitivity, q = 0.1, and (b) high strain rate sensitivity, q = 0.3.

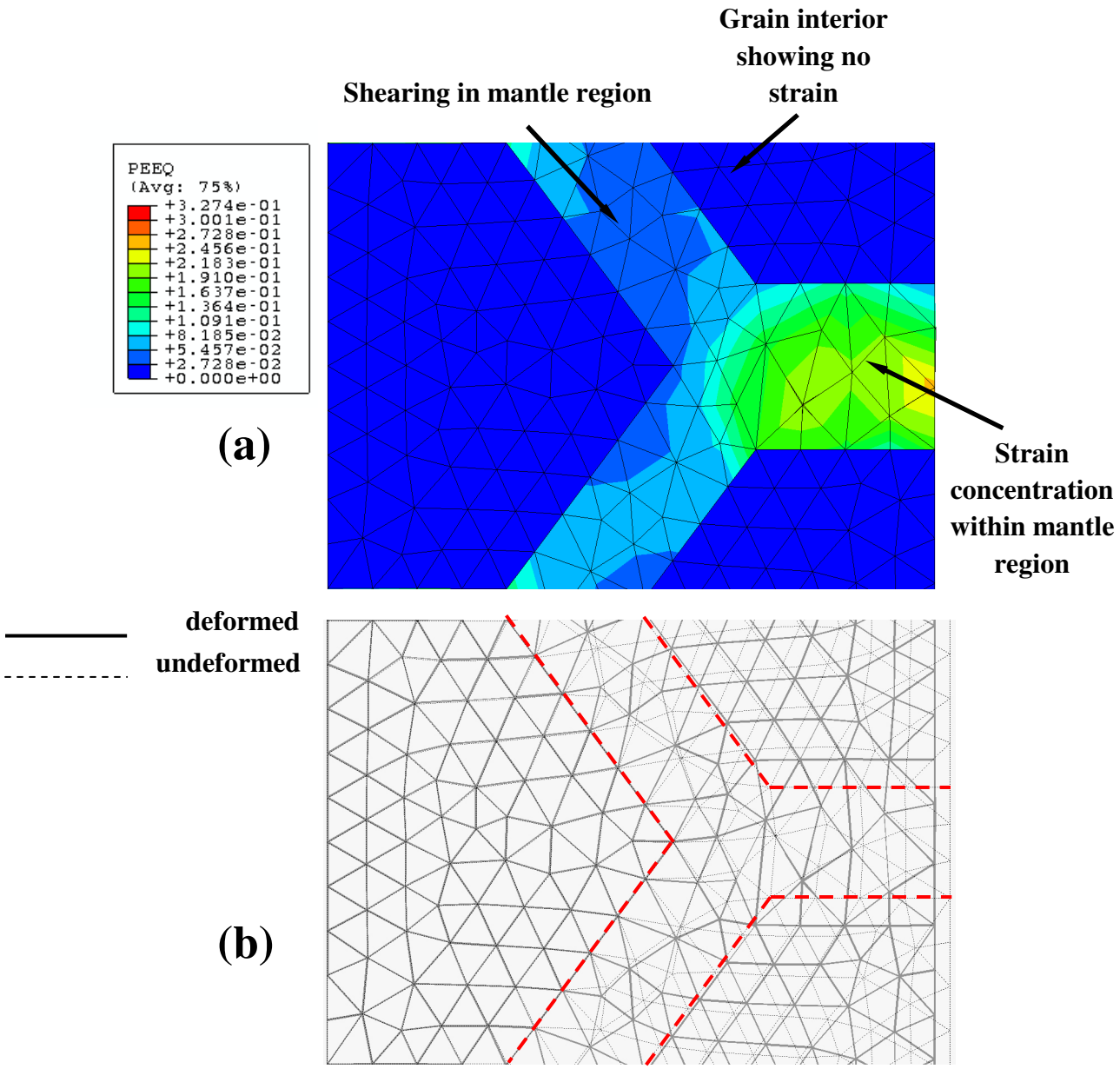

Figure 2B.14 Equivalent plastic strain map for polycrystal with grain size of 4.92 *nm* showing the strain distribution within the grain interior and mantle zone (A = 15 $MPa.\mu m^p$, p = 0.9, B = 3 *GPa*, q = 0.3, and strain rate: $3.5\times10^{-5}s^{-1}$). In this simulation, weak mantle region (B = 3 *GPa*, q = 0.3, and strain rate: $3.5\times10^{-5}s^{-1}$) was assumed, results show strain concentration, and shearing occur within mantle region. (a) shows equivalent plastic strain contour map, and (b) shows the distorted mesh (solid line), which is overlapping on the undistorted mesh (dash line).

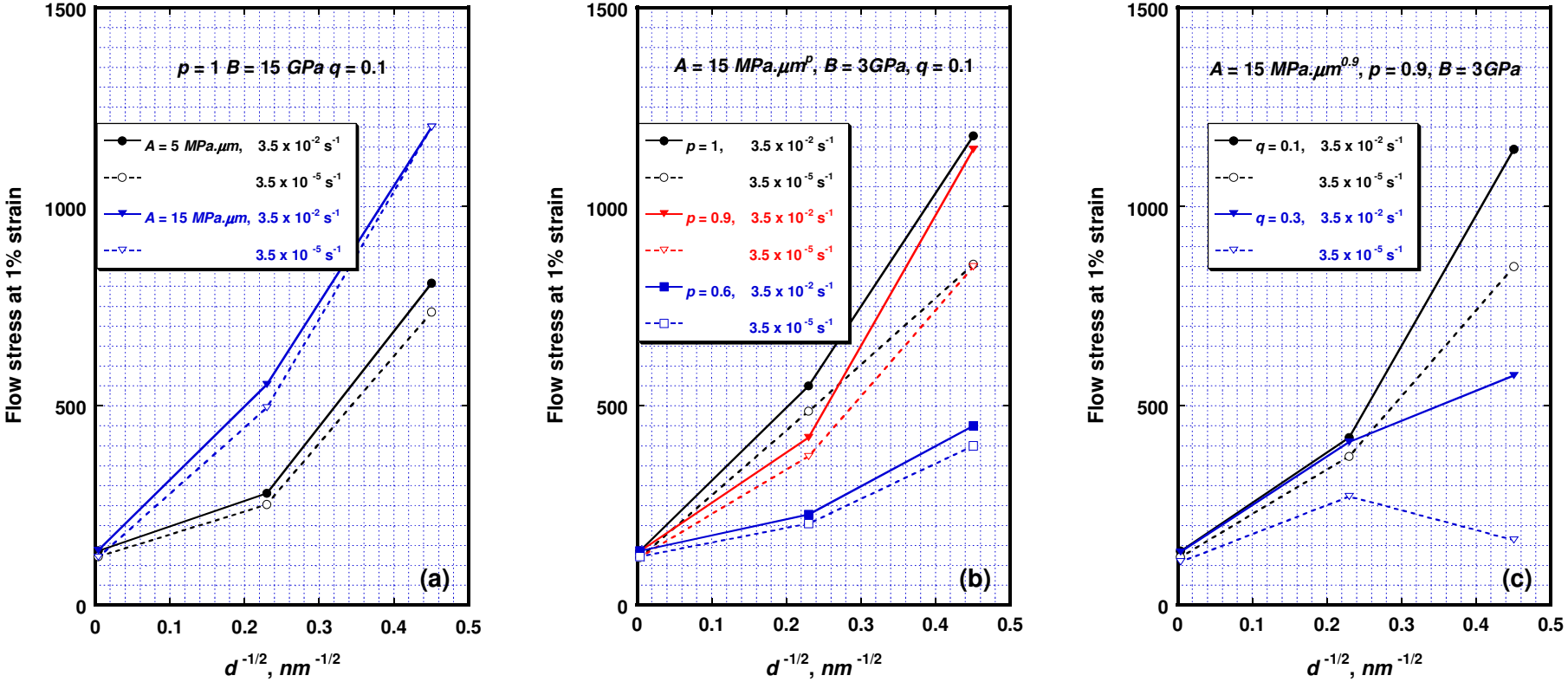

Figure 2B.15 Calculated strength value is plotted as a function of $d^{-1/2}$ for various constants in equations for grain interior and mantle zone.

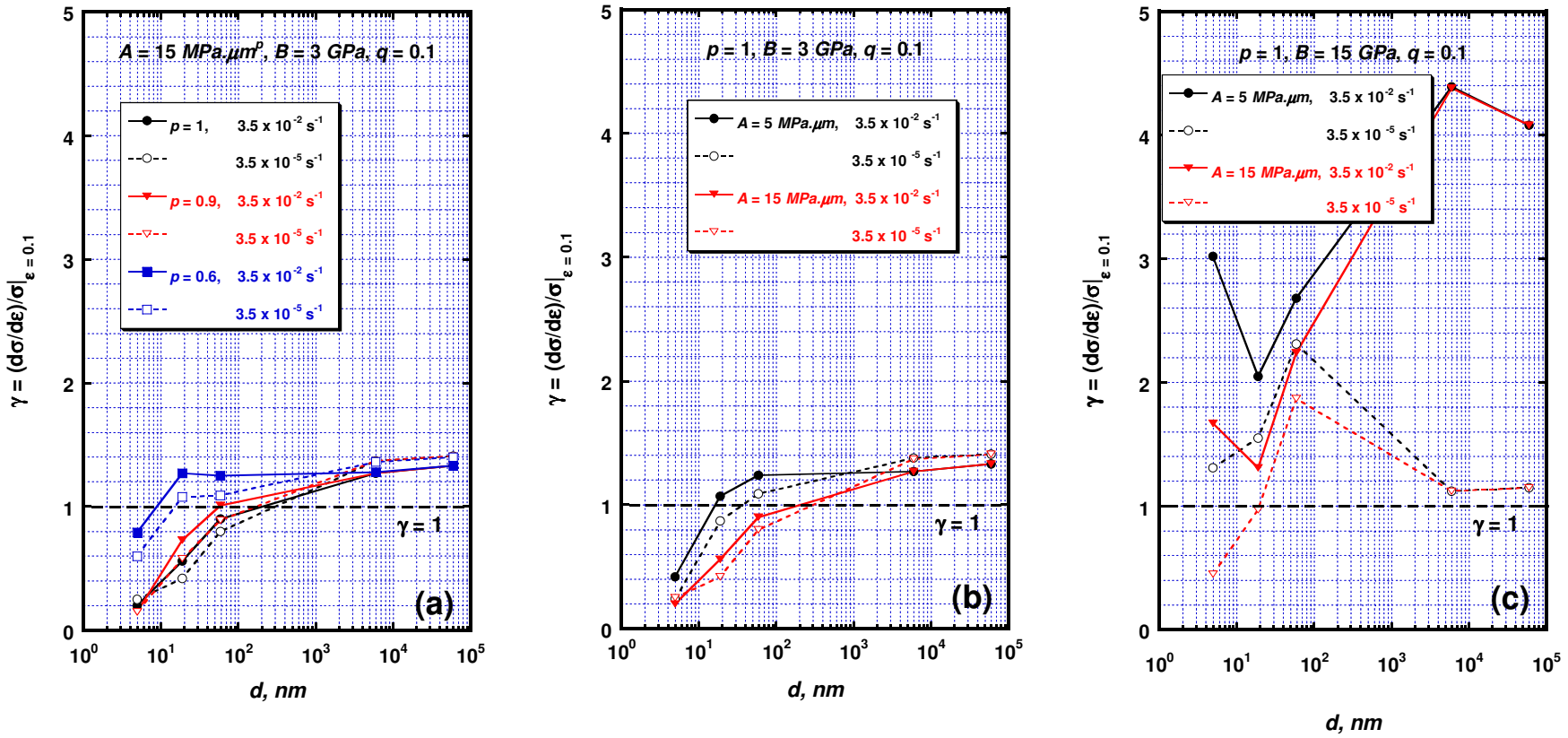

Figure 2B.16 Calculated flow stability ($\gamma = (\frac{d\sigma}{d\varepsilon})\frac{1}{\sigma}|_{\varepsilon=0.1}$) for polycrystals for various grain sizes and constants in equations for grain interior and mantle zone.

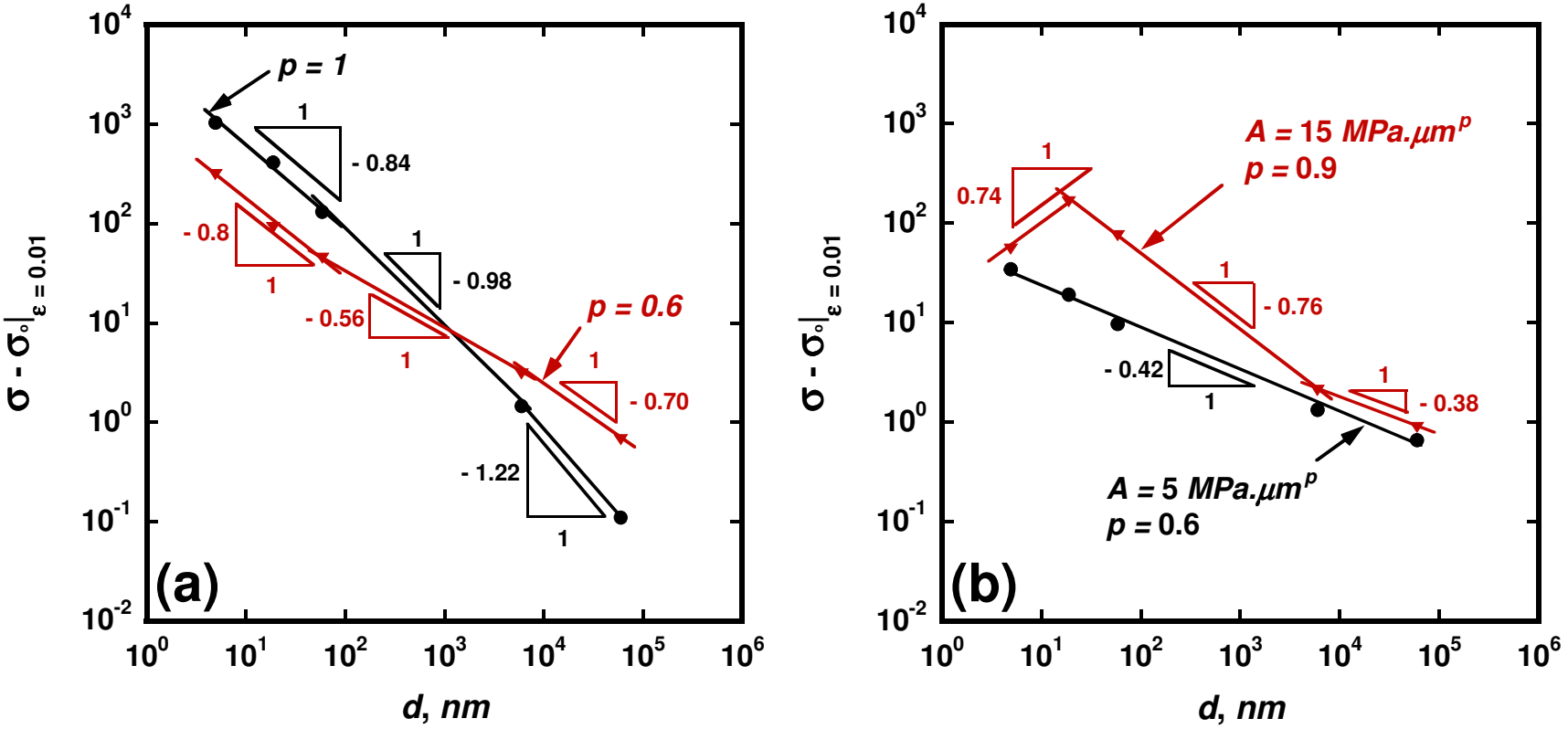

Figure 2B. 17 The difference between the flow strength at true strain of 0.01 for a given grain size and the flow strength for large grain size, as determined by simulation results, are plotted as a function of grain size. (a) A = 15 $MPa.\mu m^p$, B = 3 GPa and q = 0.1 (strain rate: 3.5×10^{-2} s^{-1}), and (b) B = 3 GPa and q = 0.3 (strain rate: 3.5×10^{-5} s^{-1}). In (a), assuming small grain size exponent, p = 0.6, the calculated relation of strength and grain size is in agreement with Hall-Petch relation. In (b), it shows that weakening effect of grain refinement is due to the weak mantle region (B = 3 GPa, q = 0.3 and strain rate = 3.5×10^{-5} s^{-1}) and strong grain interior (A = 15 $MPa.\mu m^p$, p = 0.9).

2B.5 References

[1] Hall EO. Proceedings of the Physical Society (Section B) 1951; 64:747.

[2] Petch NJ. J Iron Steel Inst 1953; 174:25.

[3] Hughes GD, Smith SD, Pande CS, Johnson HR, Armstrong RW. Scripta Metall 1986; 20:93.

[4] Armstrong R, Codd I, Douthwaite RM, Petch NJ. Phil Mag 1962; 7:45.

[5] Carreker RP, Hibbard WR. J Metals 1957; 9:1157.

[6] Hu Hsun, Cline RS. Trans Metall Soc AIME 1968; 242:1013

[7] Phillips WL, Armstrong RW. Metall Trans 1972; 3:2571.

[8] Carreker RP, Hibbard WR. Acta Metall 1953; 1:654.

[9] Carreker RP. J Metals 1957; 9:112.

[10] Jang JSC, Koch CC. Scripta Metall Mater 1990; 24:1599.

[11] Eshelby JD, Frank FC, Nabarro FRN. Phil Mag 1951; 42:351.

[12] Margolin H, Hazaveh F, Yaguchi H. Scripta Metall 1978; 12:1141.

[13] Margolin H, Longo RB. Scripta Metall 1979; 13:561.

[14] Jagannadham K, Armstrong RW. Scripta Metall 1987; 21:1459.

[15] Baldwin WM. Acta Metall 1958; 6:139.

[16] Nieman GW, Weertman JR, Siegel RW. *Scripta Metall* 1989; 23:2013.

[17] Höfler HJ, Averback RS. Scripta Metall Mater 1990; 24:2401.

[18] El-Sherik AM, Erb U, Palumbo G, Aust KT. Scripta Metall Mater 1992; 27:1185.

[19] Gertsman VY, Hoffmann M, Gleiter H, Birringer R. Acta Metall Mater 1994; 42:3539.

[20] Chokshi AH, Rosen A, Karch J, Gleiter H. Scripta Metall 1989; 23:1679.

[21] Lu K, Wei WD, Wang JT. Scripta Metall Mater 1990; 24:2319.

[22] Fougere GE, Weertman JR, Siegel RW, Kim S. Scripta Metall Mater 1992; 26: 1879.

[23] Pande CS, Masumura RA, Armstrong RW. NanoStruct Mater 1993; 2:323.

[24] Palumbo G, Thorpe SJ, Aust KT. Scripta Metall Mater 1990, 24:1347.

[25] Suryanarayana C, Mukhopadhyay D, Patankar SN, Froes FH. J Mater Res 1992; 7:2114.

[26] Koch CC, Narayan J. Mater Res Soc Symp 2001; 634:B5.1.1.

[27] Morris DG. Materials Science Foundations, No. 2 ed., Magini M, Wohlbier FH. (Uetikon – Zurich, Switzerland: Trans. Tech. Pubs., 1998), 43.

[28] Erb U. NanoStruct Mater 1995; 6:533.

[29] Narayan J. J Nanopart Res 2000; 2:91.

[30] Ke M, Hackney SA, Milligan WW, Aifantis EC. NanoStruct Mater 1995; 5:689.

[31] Hill R. The Mathematical Theory of Plasticity, Oxford University Press, 1983 Chapter XII.

[32] Randle V. Acta Mater 1997; 46:1459.

[33] Wolf D. Acta Metall Mater 1990; 38:781.

[34] Wolf D. Acta Metall Mater 1990; 38:791.

[35] Ke TS. Metall Mater Trans A 1999; 30A:2267.

[36] Ghosh AK. Constitutive Equations, Metalworking: Bulk Forming ASM Handbook 2005, Vol. 14A, 582.

[37] Taylor GI. J Inst Metals 1938; 62:307.

[38] Asaro RJ, Needleman A. Acta Metall 1985; 33:923.

[39] Wang YM, Hamza AV, Ma E. Acta Mater 2006; 54:2715.

[40] Daisuke Terada, Seiya Inoue, Nobuhiro Tsuji, J Mater Sci 2007; 42:1673.

Chapter 2 - Appendix 1: Finite Element Modeling Procedure

For finite-element modeling, commercial software ABAQUS®/ Standard analysis module was used to create the single crystal and polycrystal models. The details of modeling procedure are described as follows:

A1.1 Modeling Steps

(1) Start up: Launch "ABAQUS/CAE", and choose the option of "Create Model Database" to create a new model or choose the option of "Open Database" to open an existing model, the window will enter the module of "Part".

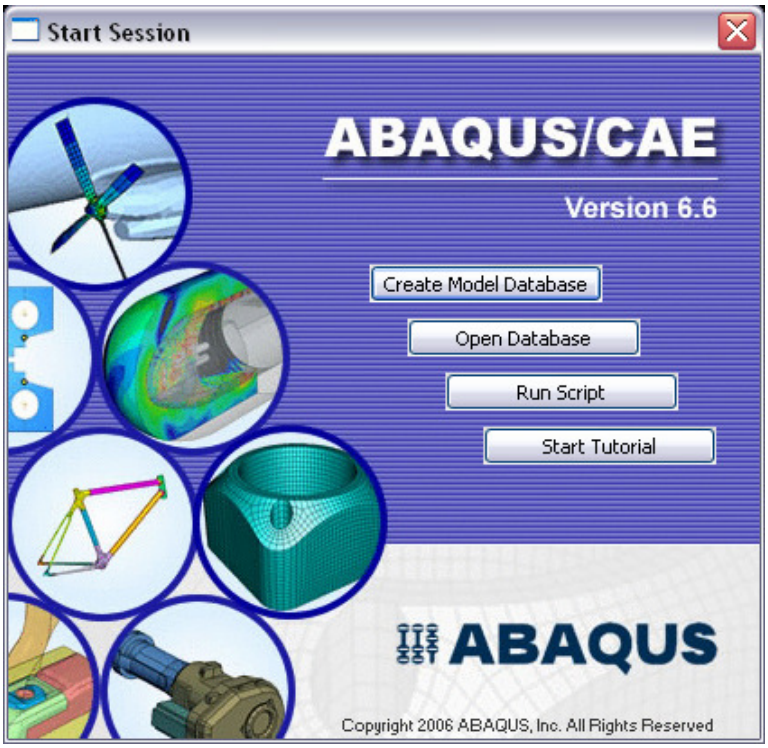

(2) Create part: Click Part Manager, and a dialog box of “Part Manager” will pop up

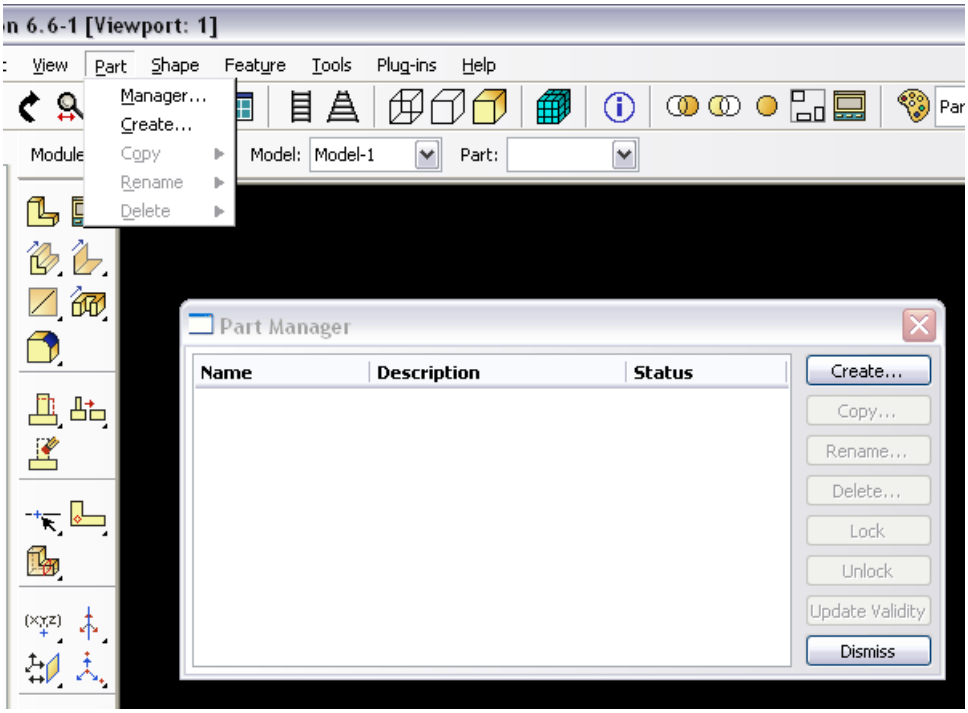

(3) Features of part: Click the “Create” button to pop up the frame of “Create Part”. In this frame, define a name for the part; choose the options for “Modeling Space”, “Type” and “Base Feature” including “Shape” and “Type”. Finally, input the value for “Approximate Size”. Click the “Continue” button to enter the mode of drawing. The dialog box of “Part Manager” can be closed by click the button of “Dismiss”

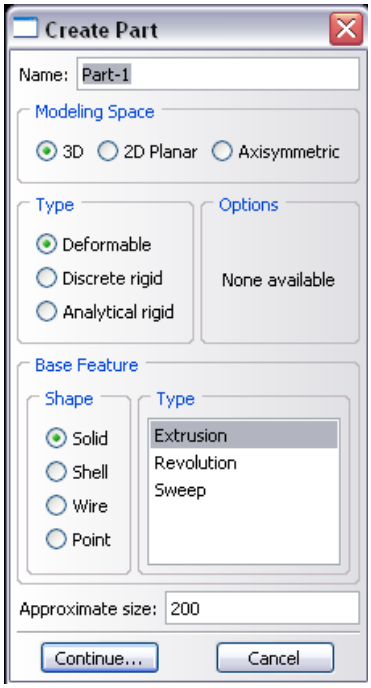

(4) Sketching: Use the drawing tools on the left size of screen to draw the section for the part. Choose the basic geometry for the section of a part. Two methods can be used to sketch the section. One is using the mouse to directly draw the sketch of the part on the screen. Another method is to input the coordinates for the section of a part into the dialog box on the bottom of screen labeling with “Pick a starting corner for the rectangle -- or enter X, Y”

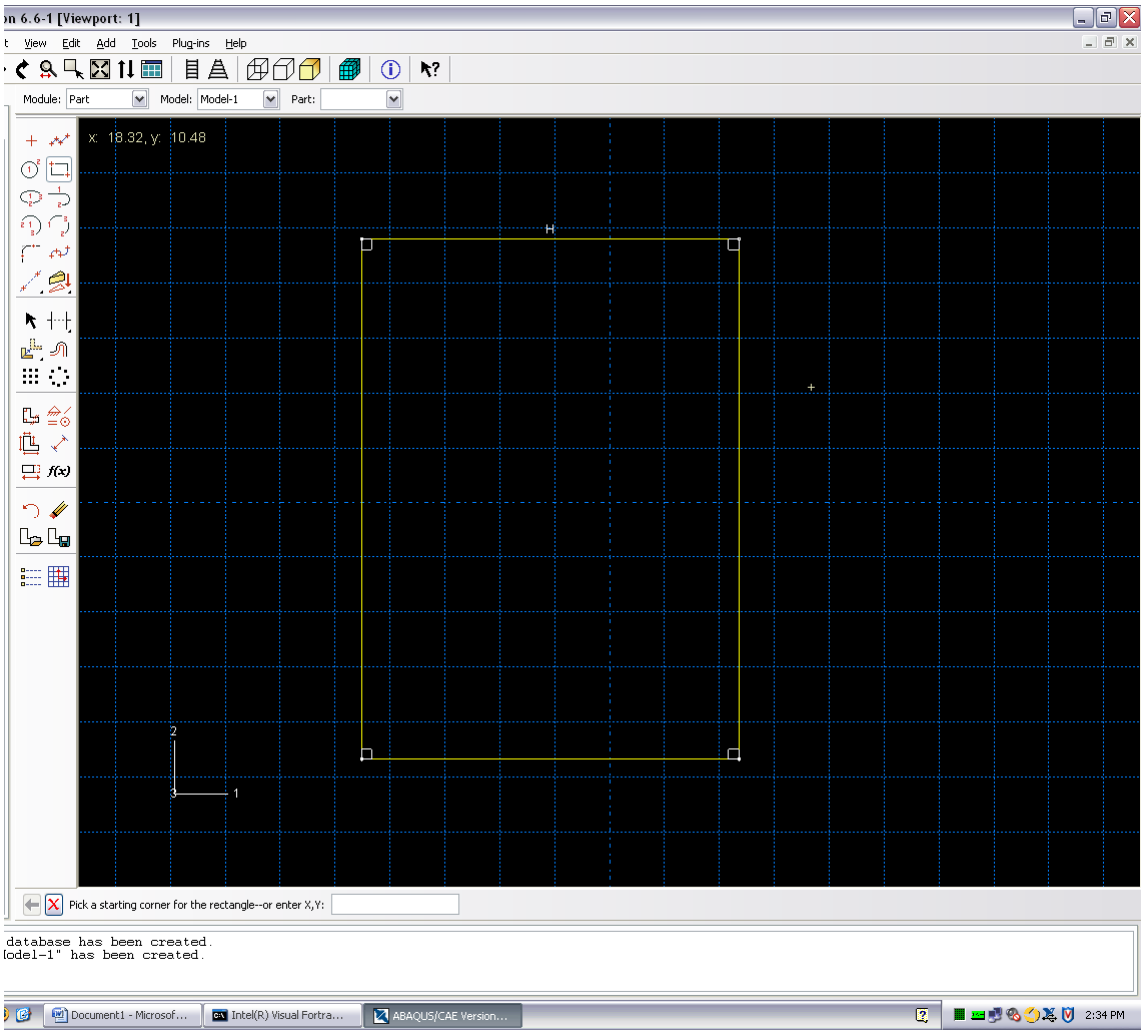

(5) Define the thickness: When the sketch of section is finished, press the “Esc” button on the keyboard to exit the drawing mode. Then, click the “Done” button to fulfill the drawing process. A dialog box of “Edit Base Extrusion” will pop up, provided that the option of “Extrusion” for the type of base feature was chosen. In this dialog box, input the value for depth to define the thickness for the part. For the other inputs just keep the default value as it is. Finally, click the “OK” button to finish the creation of part.

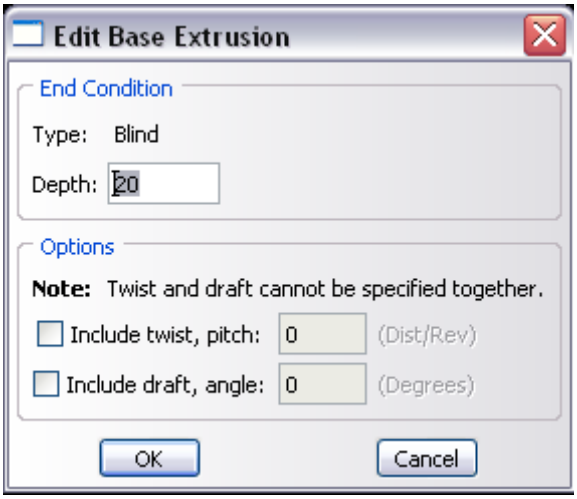
Edit Base Extrusion
End Condition
Type: Blind
Depth: 20
Options
Note: Twist and draft cannot be specified together.
Include twist, pitch: 0 (Dist/Rev)
Include draft, angle: 0 (Degrees)
OK
Cancel

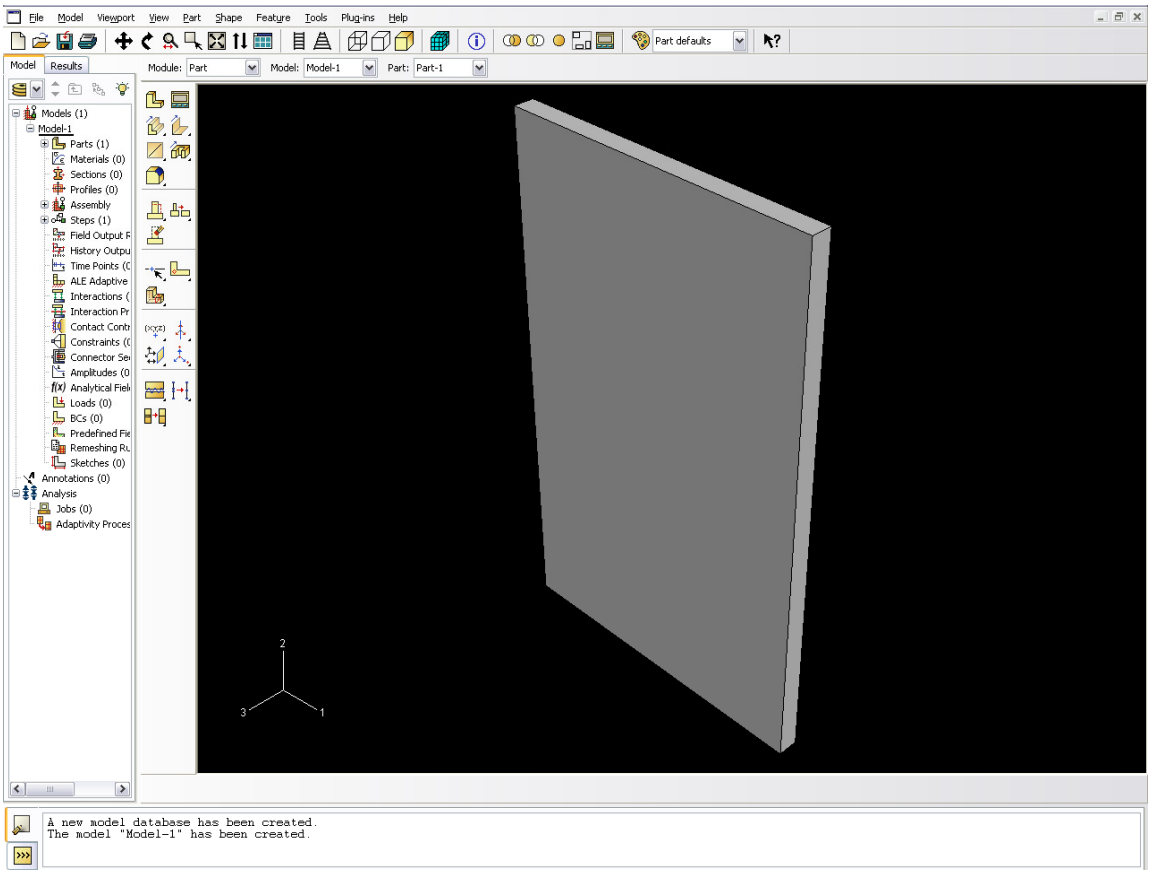
File Model Viewport View Part Shape Feature Tools Plug-ins Help
Model Results
Module: Part Model: Model-1 Part: Part-1
Part defaults
Models (1)
Model-1
Parts (1)
Materials (0)
Sections (0)
Profiles (0)
Assembly
Steps (1)
Loads (0)
BCs (0)
Sketches (0)
Annotations (0)
Analysis
Jobs (0)
A new model database has been created.
The model "Model-1" has been created.

(6) If needed, partition within the existing part can be created. Click the “Views Toolbox” button on the toolbar, and choose the section of the existing part to be shown. For single crystal model, Step (6) ~ (9) can be skipped.

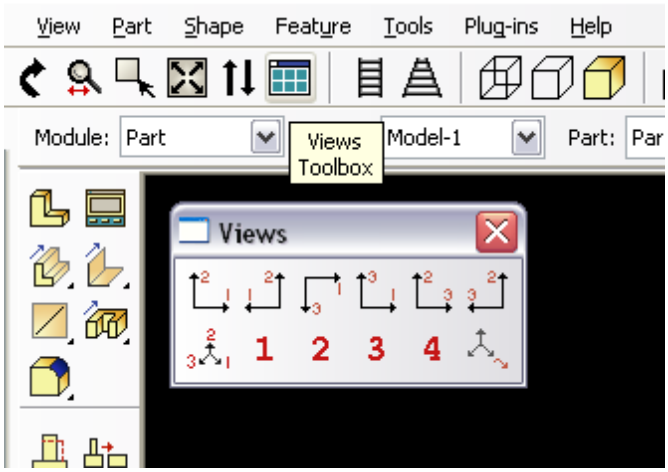

(7) Create datum: Before the partition, the datum points need to be defined first. From the menu of “Tool”, choose the function of “Datum”. A pop-up dialog box will appear which is labeled with “Create Datum”. Choose the “Point” for the datum type and “Enter coordinates” for method. Then, click “Apply” to proceed to input the coordinates for the datum. Repeat the step to define all the datum points needed.

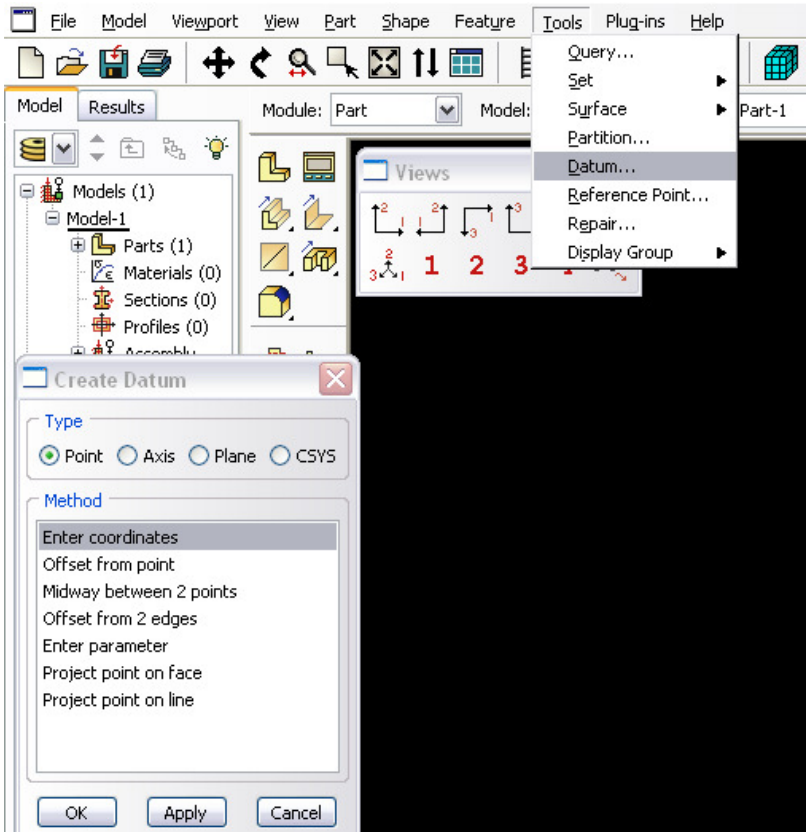

(8) 2D partition: Then, from the menu of “Tool”, choose the function of partition. To create the partition for 3-dimension part, there are two steps need to be completed. The first step is creating the partition for 2-dimension section. In the dialog box of “Create Partition”, choose the “Face” for partition type and “Use the shortest path between 2 points” for method, where the “Points” refers to the datum points created in previous step. For each time, connect every 2 datum points to create 2-dimension partition. Repeat the process to create the desired 2-dimension partition in the section of part. Next, it is to convert the 2-dimension partition into 3-dimension partition.

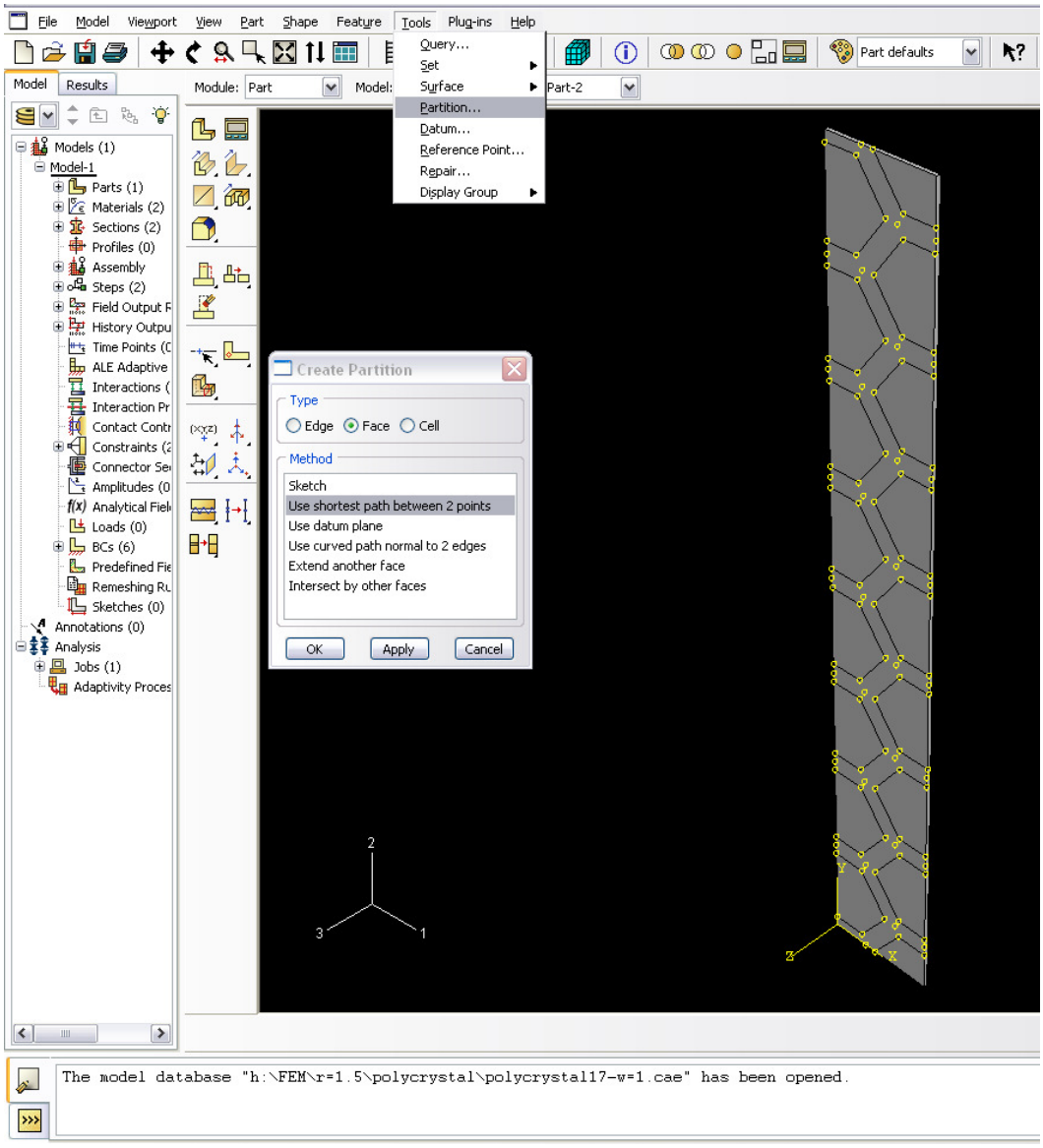

(9) 3D partition: Use the same dialog box as the previous step; choose “Cell” for partition type and “Extrude/Sweep edges” for method. Then, click the button of “Apply”. Next, before selecting the lines, the cell for partition needs to be selected. The following is to select the line within the selected cell as reference edge for “Extrude/Sweep”. To select the multi-lines as reference edges, the “Shift” key on the keyboard should be hold during the selection of lines. Finally, click “Done”. On the bottom of the window, choose the button of “Sweep Along the Edge”, and then, select any line lying along the thickness direction to be the sweep path, then click “Create Partition” to extend the 2-dimension partition to 3-dimension partition. Repeat this process to fulfill the desired 3-dimension partition for the part.

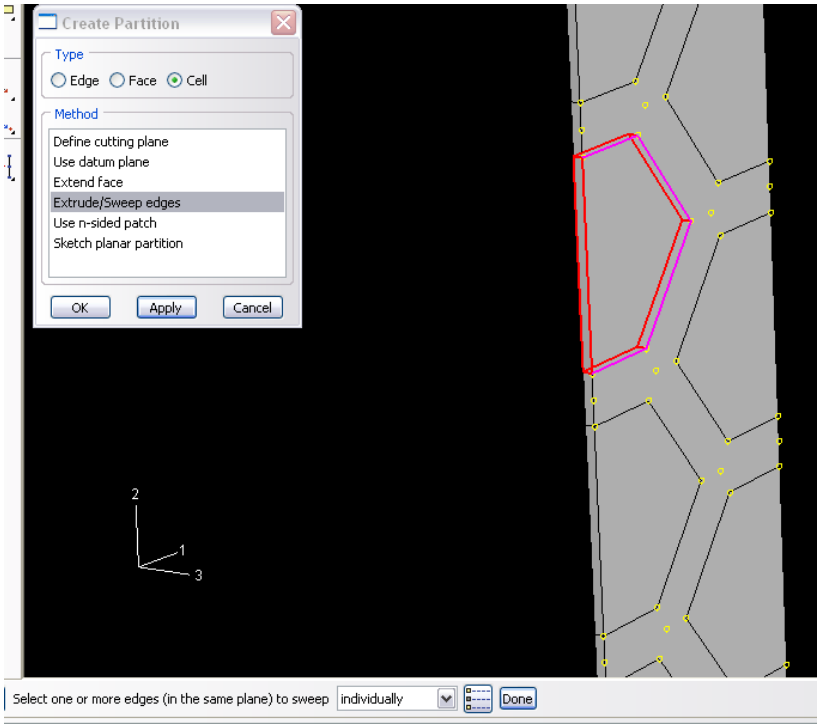

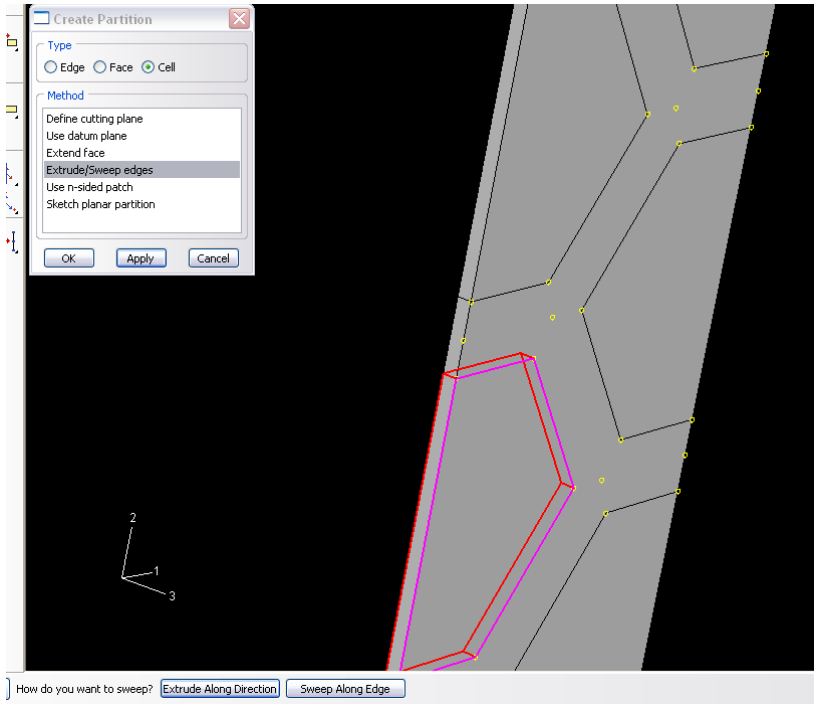

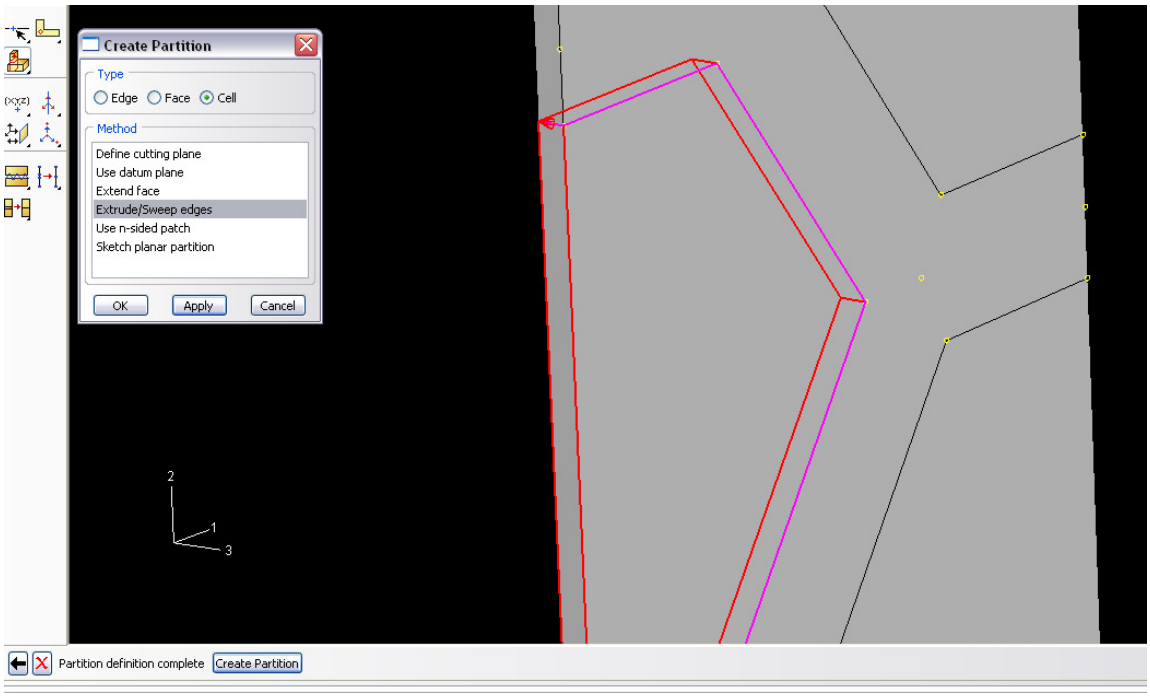

(10) From the menu of “Module”, select the function of “Property” to enter the step for define the materials properties.

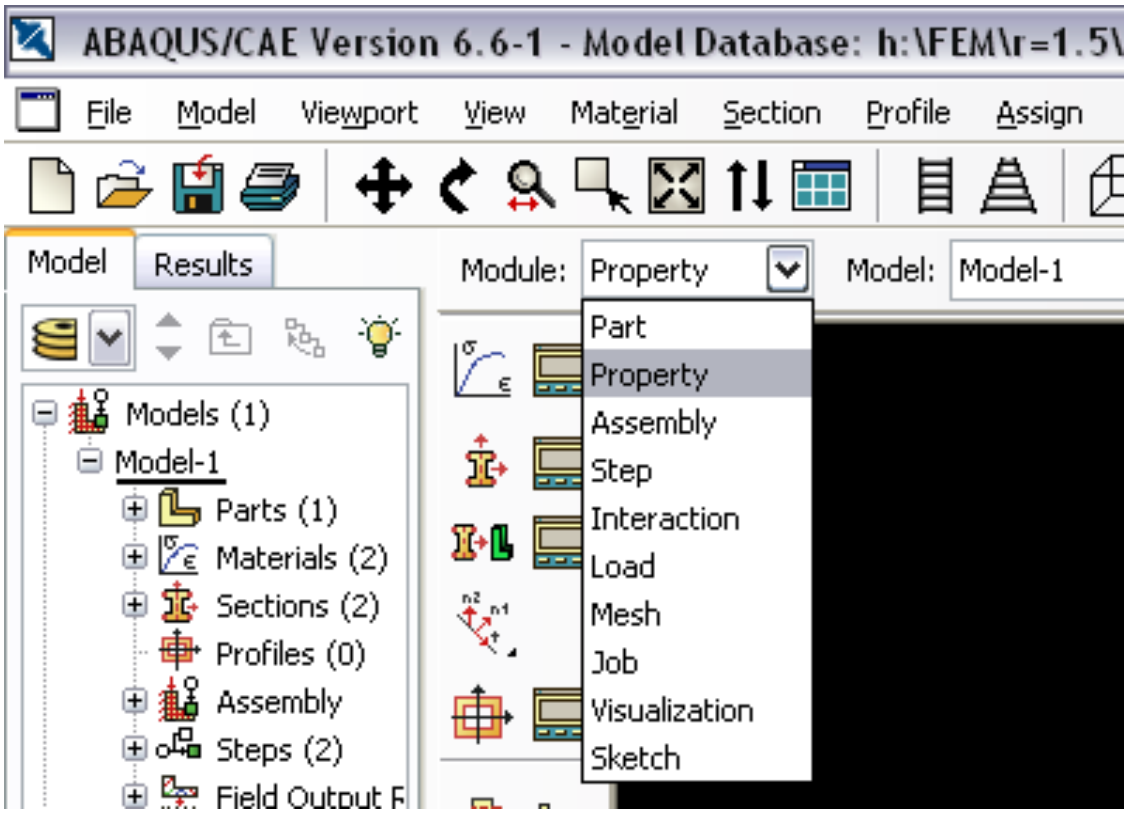

(11) In the “Property” module, click the icon of “Material Manager”, a dialog box of “Material Manager” will appear on the screen, then click the “Create” button in this box to pop up the frame of “Edit Material”. In this box, there are four categories of material properties can be used to define the parts, including “General”, “Mechanical”, “Thermal” and “Other”.

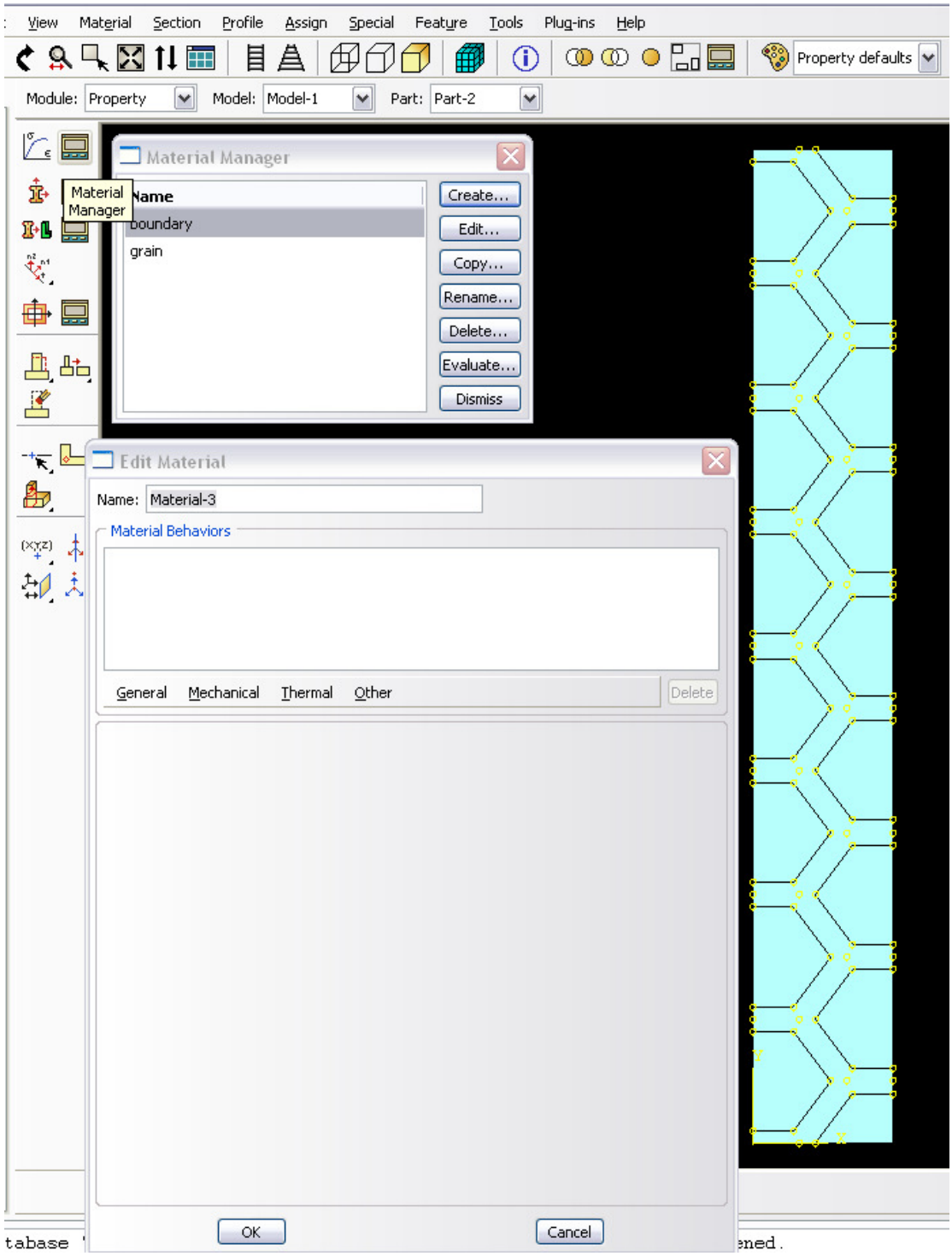

(12) Define the elasticity: Click the category of “Mechanical”, and put the arrow on the option of “Elasticity”. A sublist will show on the right size. Then choose the “Elastic”. The dialog box will switch to the data sheet for elasticity. Input the value for “Young’s Modulus” and “Poisson’s Ratio”.

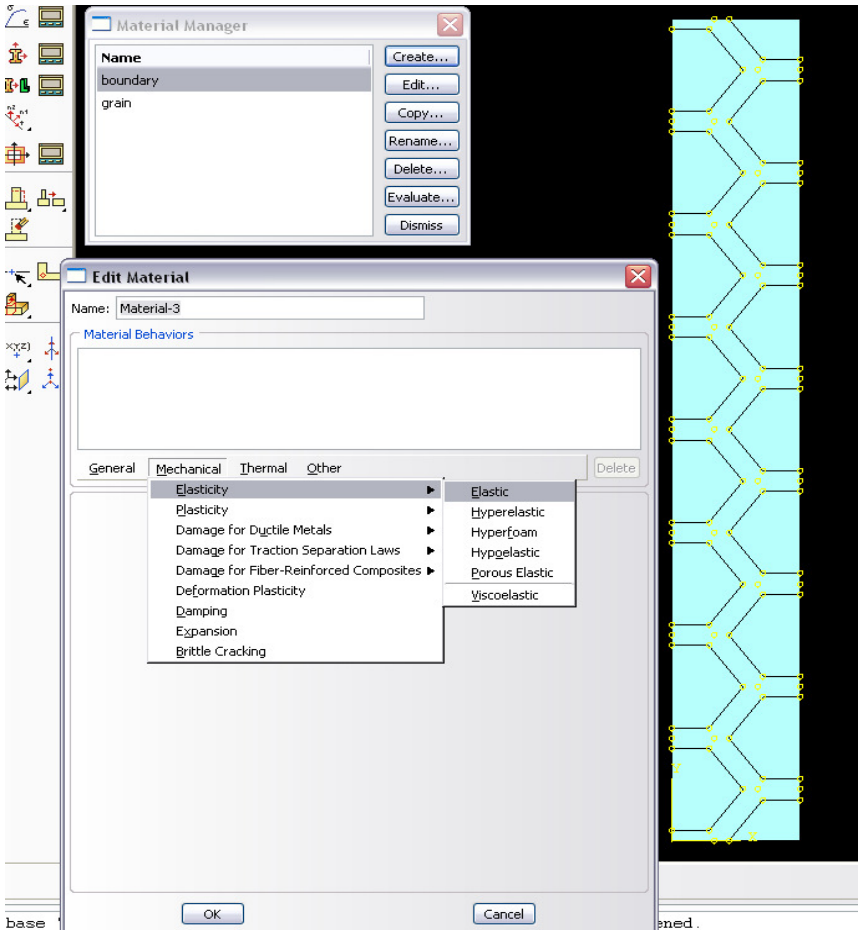

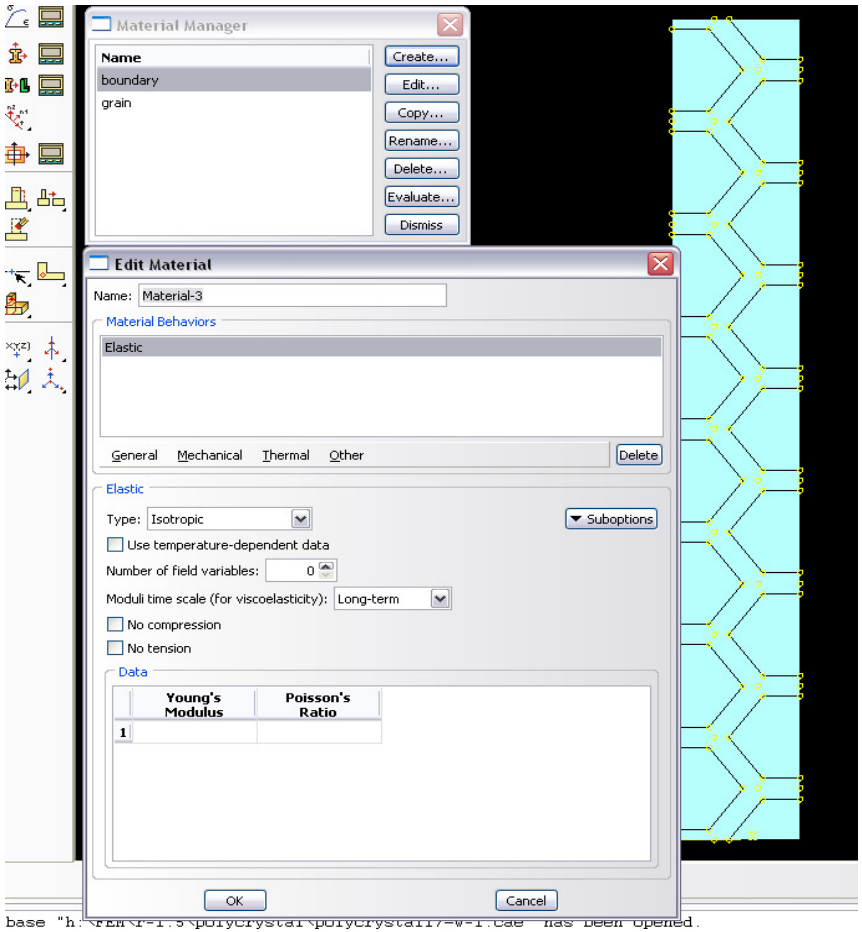

(13) Define the plasticity: Next, click the category of “Mechanical”, and put the arrow on the option of “Plasticity”. A sublist will show on the right size. Then choose the “Plastic”. The dialog box will switch to the data sheet for Plasticity. Check the box of “Use strain-rate-dependent data”. In the three columns about “Yield Stress”, “Plastic Strain” and “Rate”, input the data points.

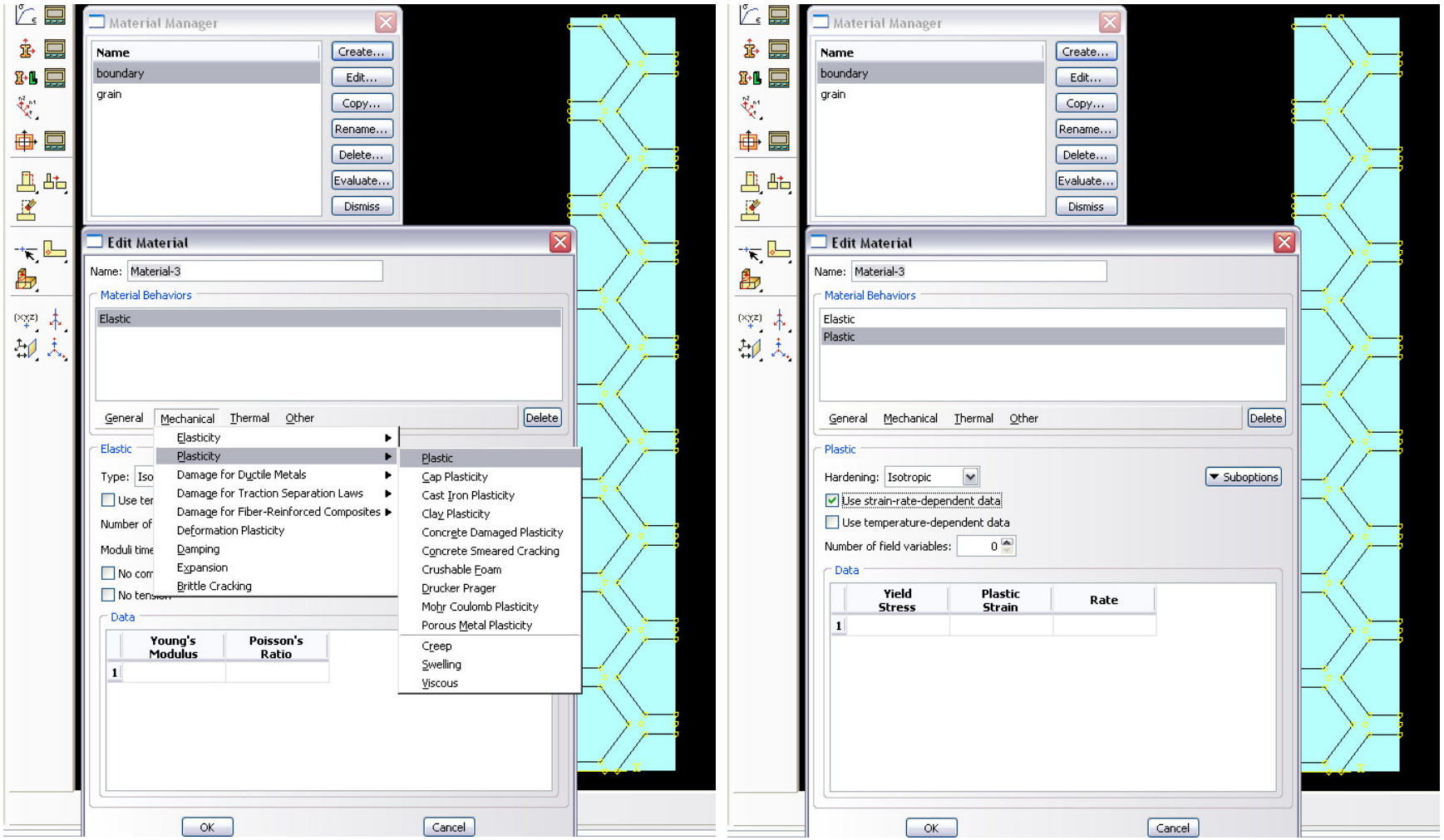

(14) Define the potential: In the same dialog box, click the button of “Suboptions”, a down list will appear, choose the option of “Potential” to define the anisotropy of material. A pop-up box will show the data sheet for stress ratios. In this box, input the stress ratios for 6 components (R11, R22, R33, R12, R23 and R13).

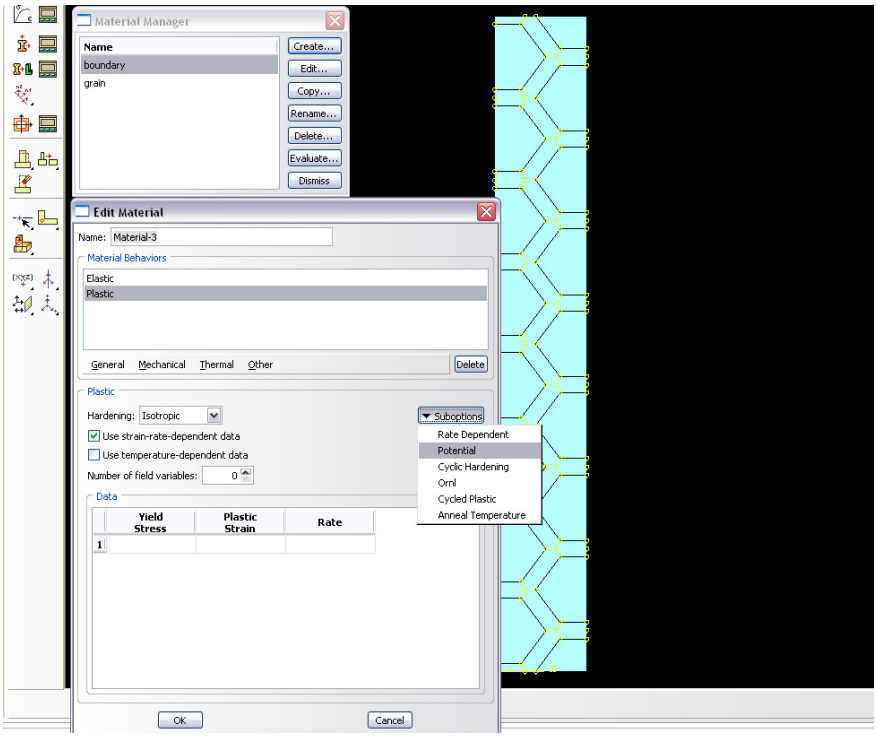

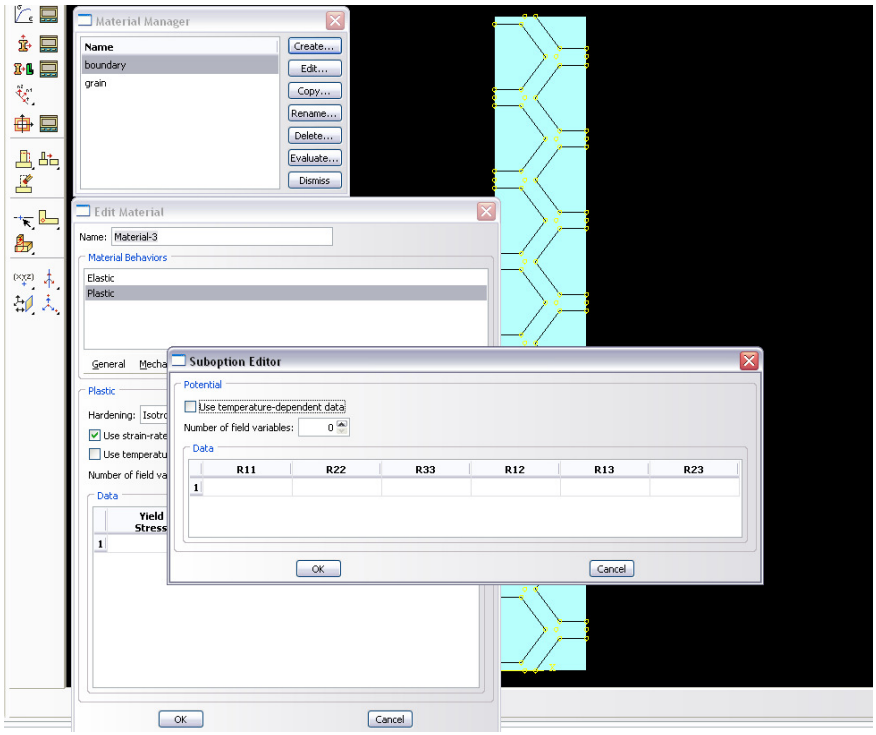

(15) Create section: Click the menu of “Section” on the top of window and the option of “Manager” from the down list. The dialog box of “Section Manager” will pop up; then click “Create” button to show the frame of “Create Section”. In this box, input a name for the section and choose the “Solid” for the section category and “Homogeneous” for section type, then click “Continue”. A new dialog box of “Edit Section” will appear, within which select the previously defined material in the box of “Material” and input the value in the box of “plane Stress/Strain Thickness”. Finally, click “OK” to finish this step.

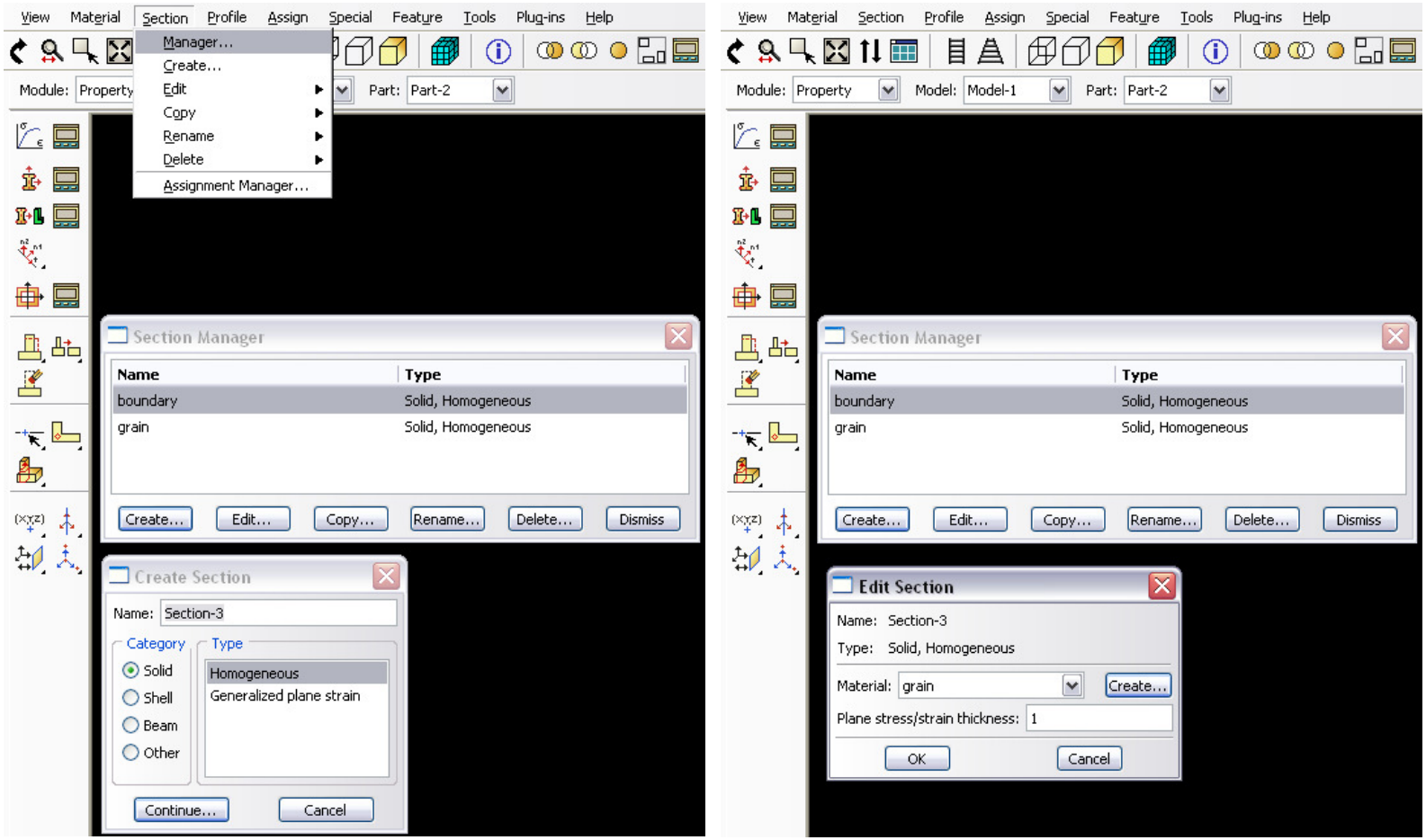

(16) Section assignment: Click the menu of “Assign” and the option of “Section” from the down list to assign the previous defined section to the geometrical part. Choose the any region from the unpartitioned or partitioned part for assigning. After selecting the desired region, click “Done” to switch the dialog box to “Edit Section Assignment”, and then select the section and click “OK”.

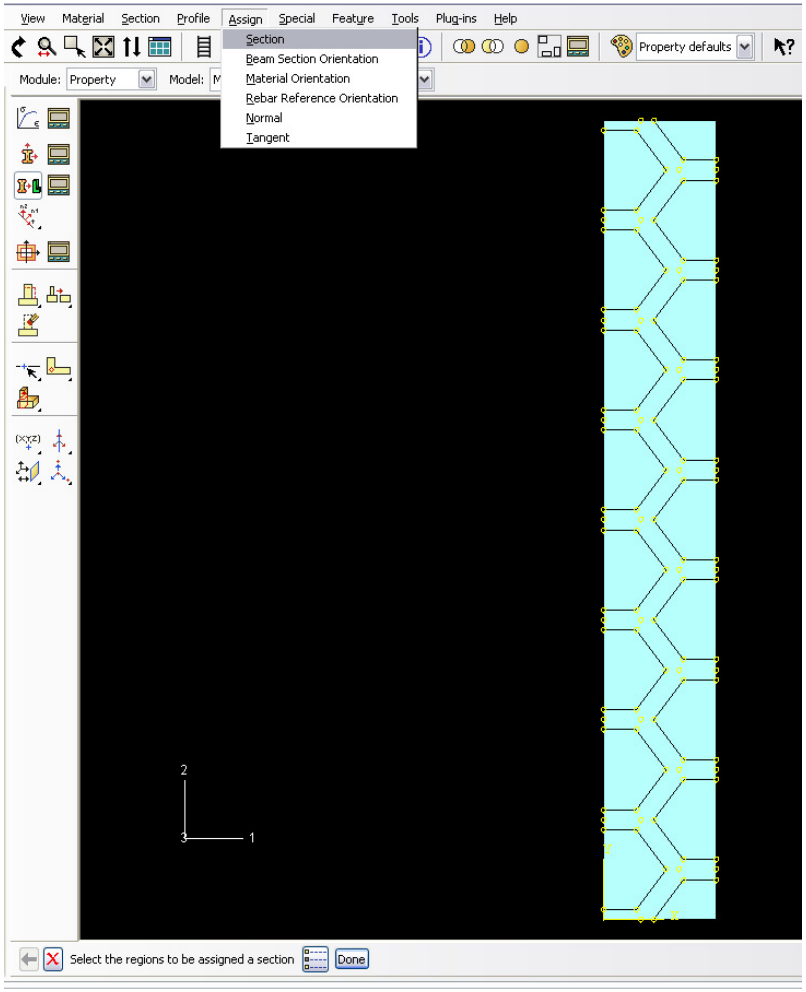

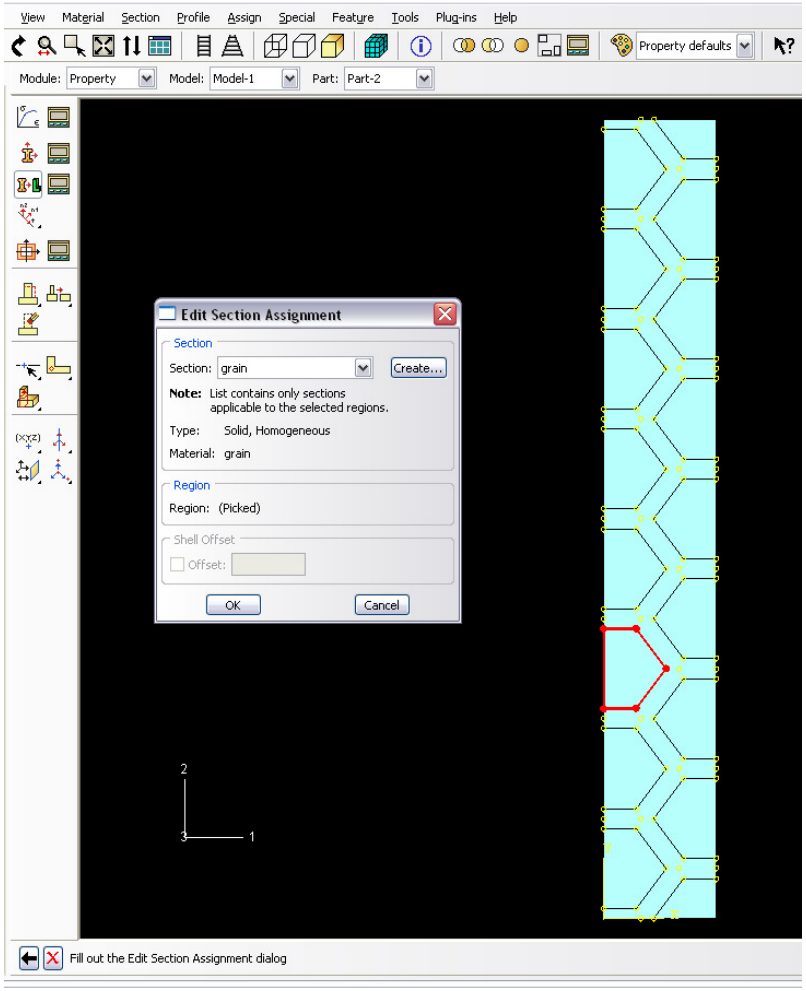

(17) Define the local coordinate system: Before assigning the material orientation to the geometrical part, a local coordinate system needs to be defined. From the menu of “Tool”, choose the option of “Datum”. A pop-up dialog box will appear which is labeled with “Create Datum”. Select the “CSYS” for datum type and “3 points” for method. Then, click “Apply” button. A new dialog box will pop up, within which define the name for the local coordinate system and select the “Rectangular” for the coordinate system type. Then, on the bottom of the screen, set the origin of the local coordinate system, X-Y plane and the positive direction for Z axis.

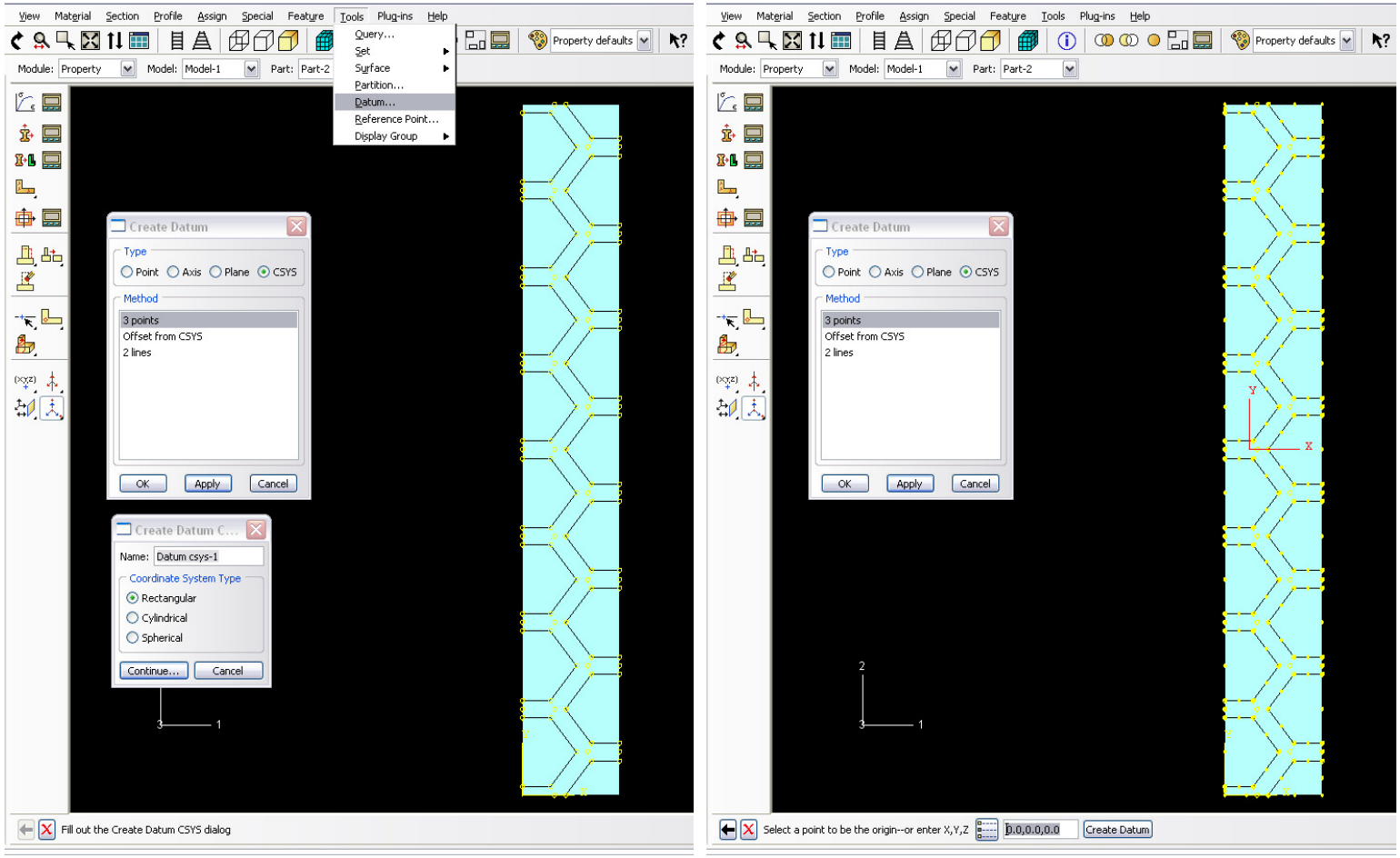

(18) Material Orientation Assignment: Click the menu of “Assign” and the option of “Material Orientation” from the down list to assign the material orientation to the geometrical part. Choose the any region from the unpartitioned or partitioned part for assigning. After selecting the desired region, click “Done”. Then, click the button of “Datum CSYS List” on the right corner of screen to pop up the box listing the previously defined local coordinate system and select the desired coordinate system.

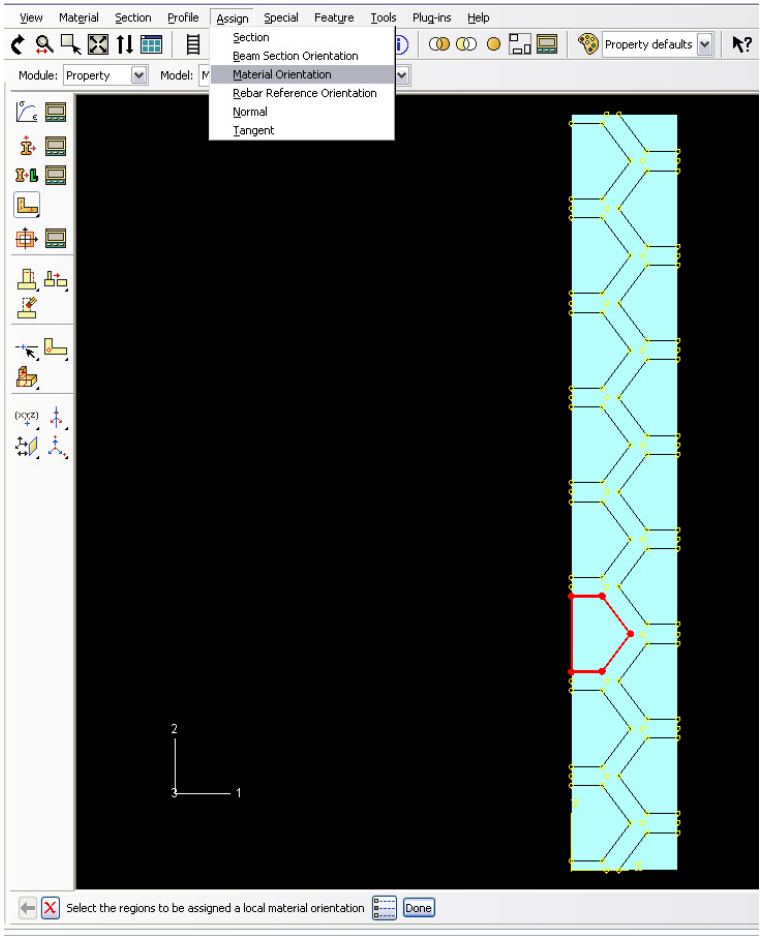

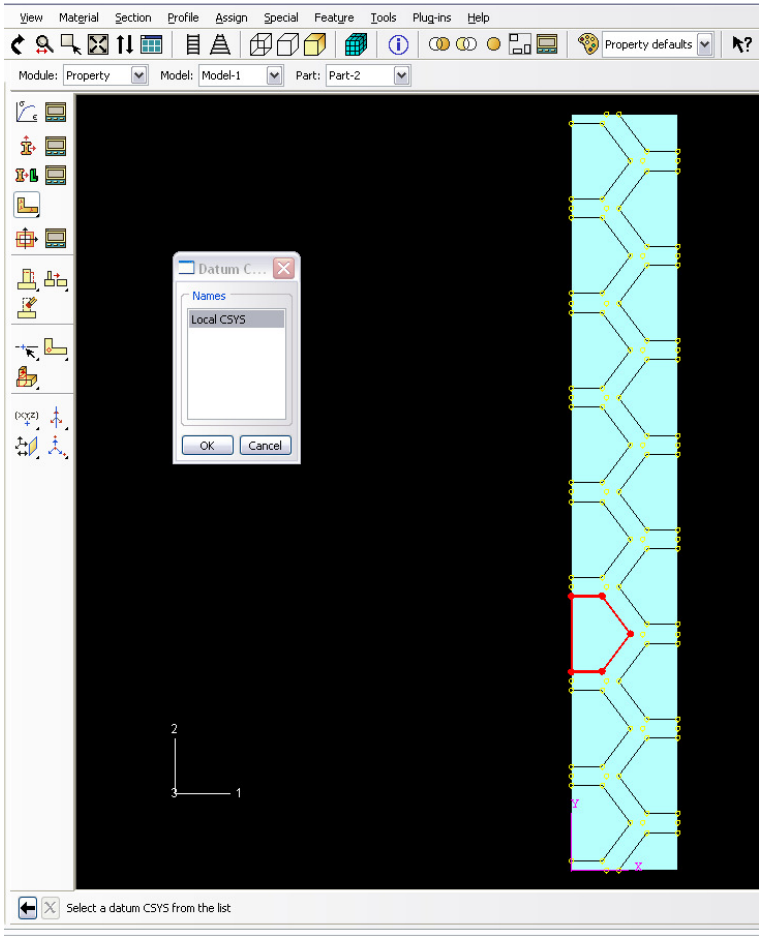

(19) Select direction (Axis-1, Axis-2 and Axis-2) on the local coordinate system for additional axis rotation showing on the bottom of screen and input the value of degree for rotation.

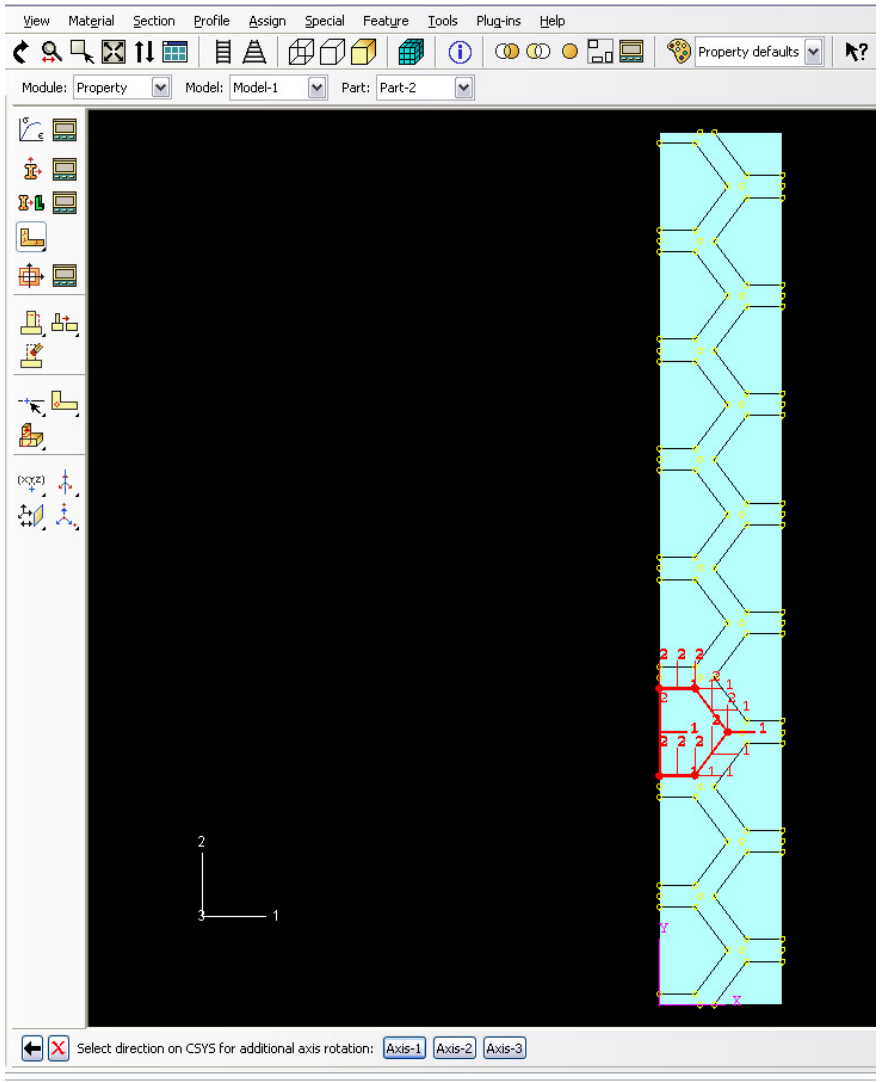

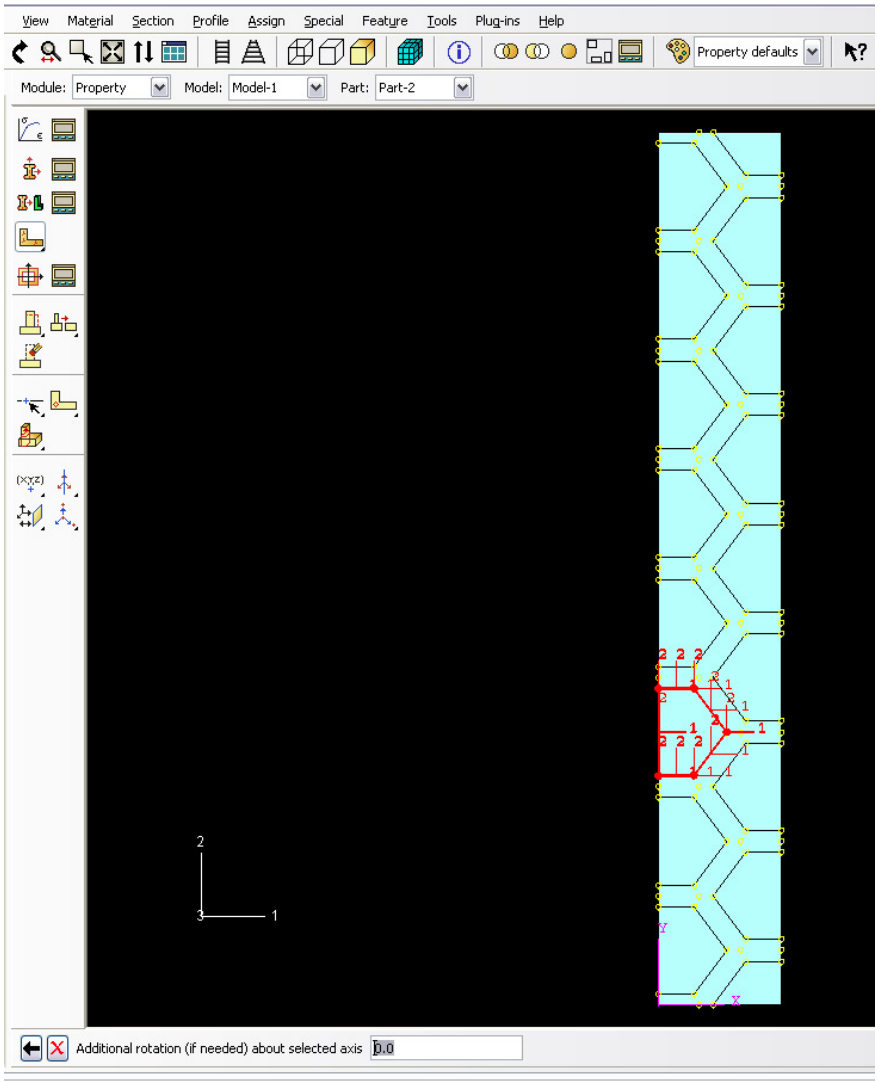

(20) Assembly: Enter the module of “Assembly”. Click the icon of “Instance Part” to show the dialog box of “Create Instance”. Select the desired part to add and click “OK”. This assemble consists of an instance only, no constraint condition need to be added.

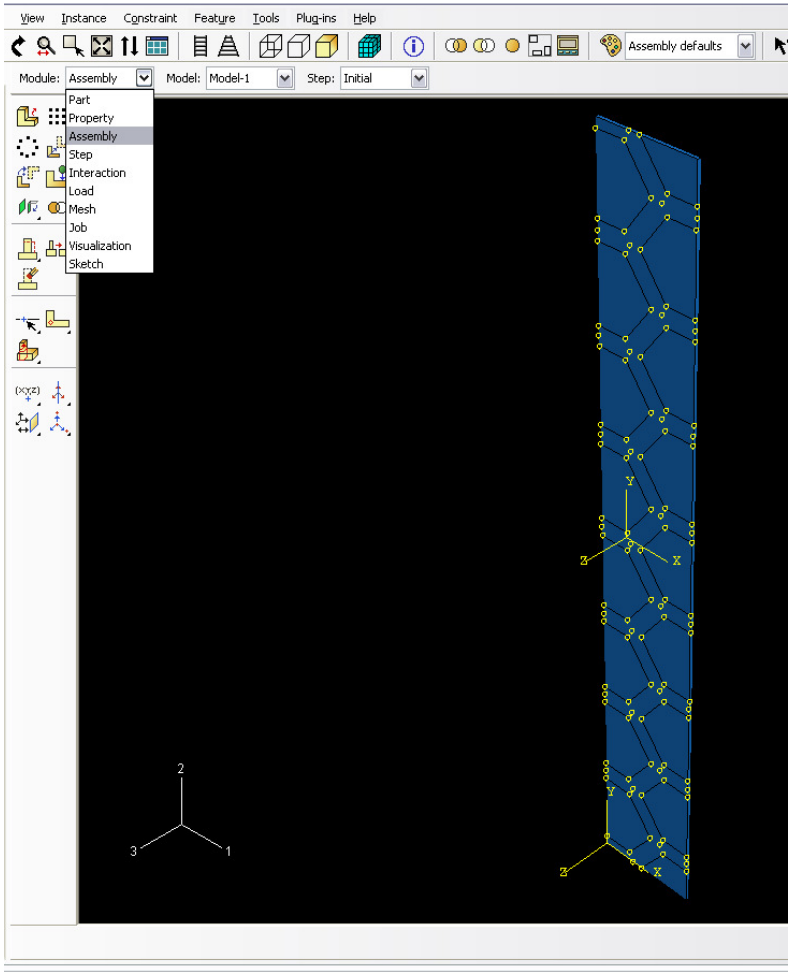

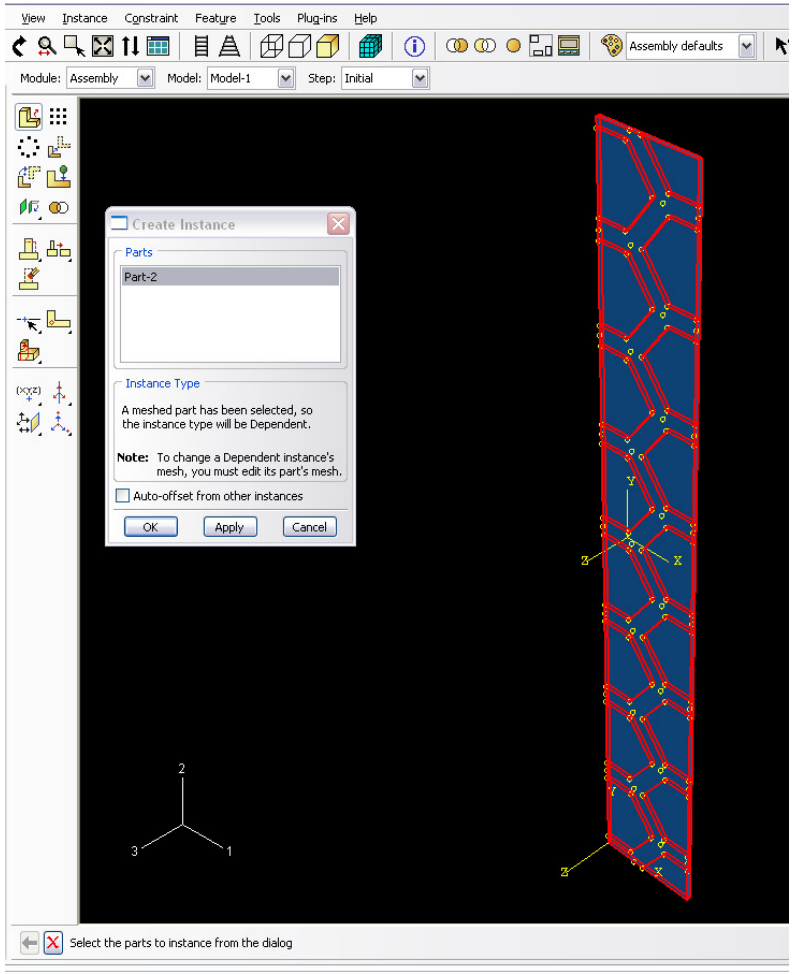

(21) Create step: Enter the module of “Step”. Click the icon of “Step Manager” on the left side toolbar to show the dialog box of “Step Manager”. Then click the “Create” button to show the frame of “Create Step”. In the frame of “Create Step”, define the Name of step, the position of step within the step list in the “Insert new step after” box and “Procedure Type” of “Static, General”. Then, click “Continue” button.

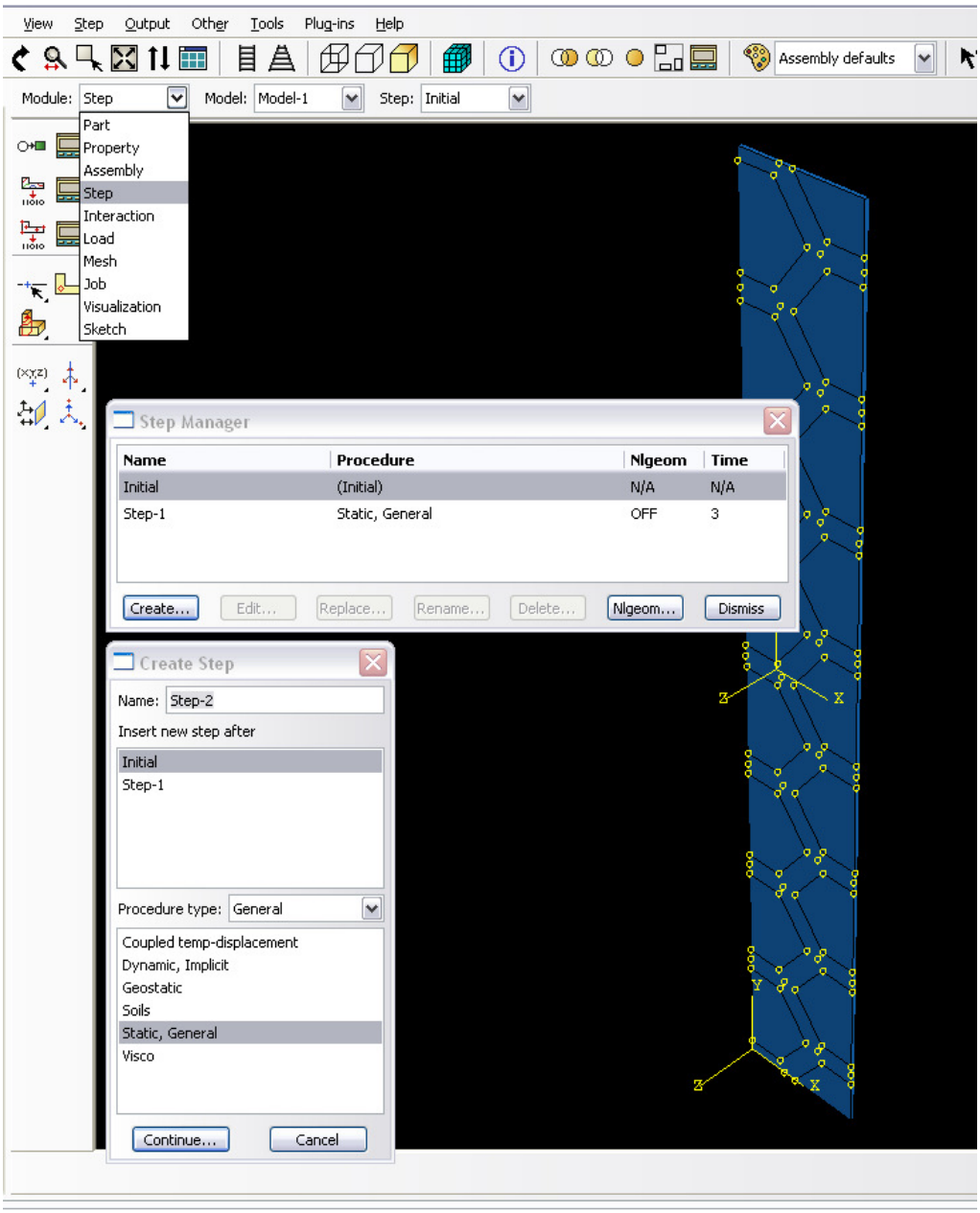

(22) Step setting: Enter the dialog box of “Edit Step”, in the sheet of “Basic”, write a brief description for the step in the “Description” box and input a value in the box of “Time period”. Switch to the sheet of “Incrementation”, select the “automatic“for the “Type”, input a value for the “Maximum number of increments” and values for the “Initial Increment Size”, “Minimum Increment Size” and “Maximum Increment Size”. Keep the default value and selection for other conditions. For the “Field Output” and “History Output”, use the default setting.

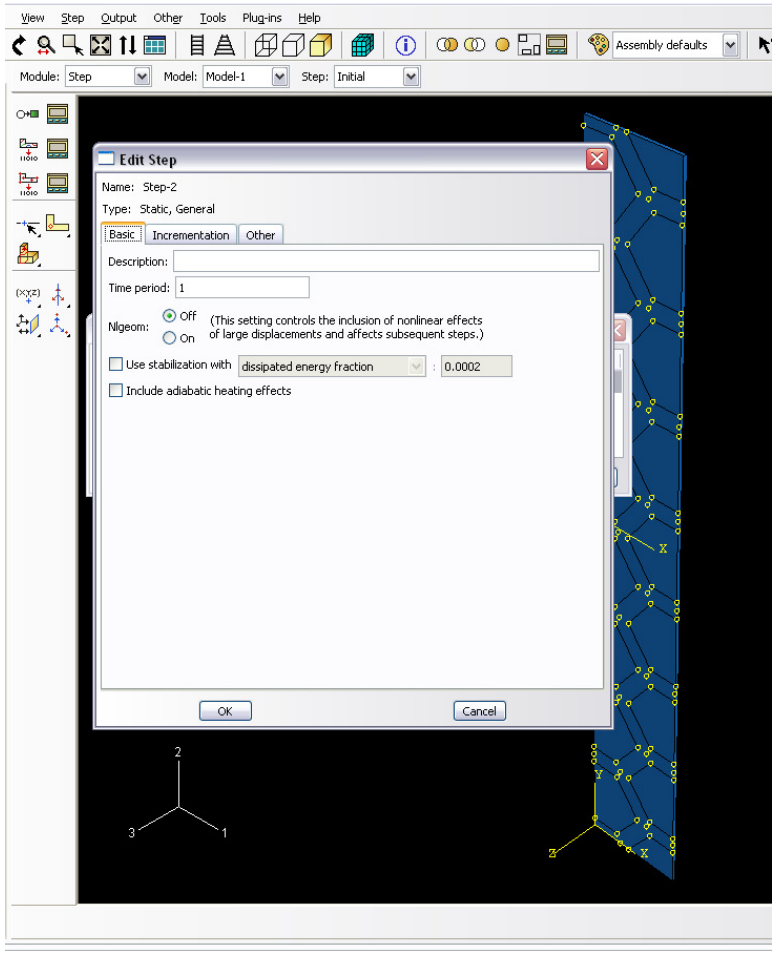

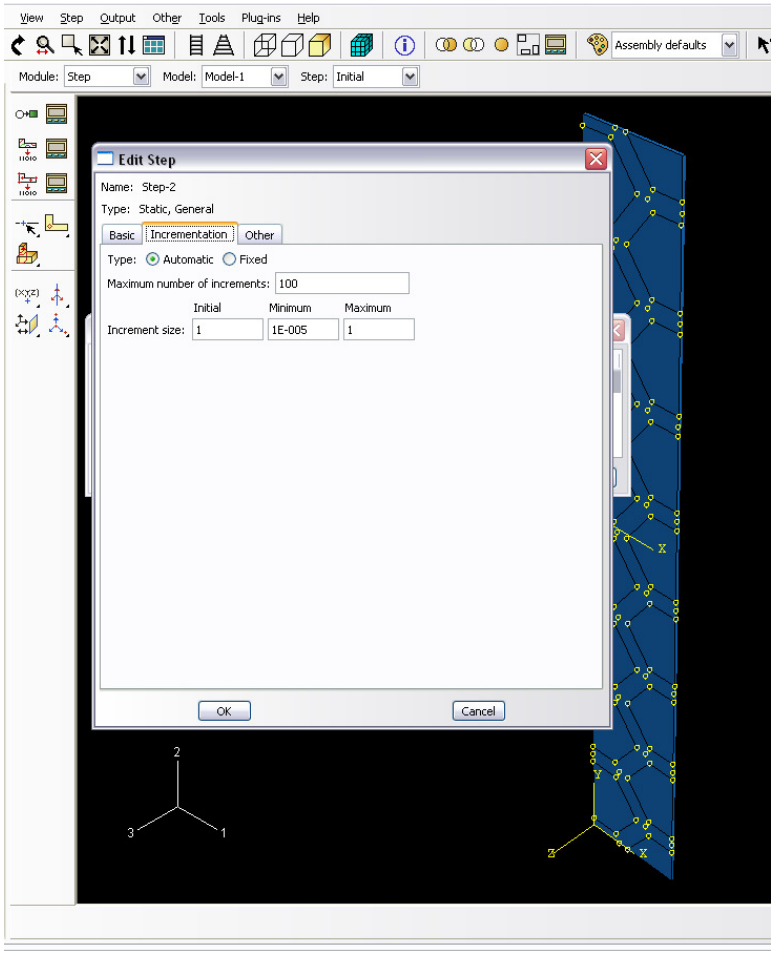

(23) Create sets: After entering the module of “Interaction”, the first step is to define the sets, which is for defining the constraint. Click the menu of “Tool” and put the arrow on the option of “Set” from the down list. A sublist will show on the right size, and then click “Manager”. The dialog box of “Set Manager” will pop up, and then click “Create” to show the box of “Create Set”. In this box, define a name for the set, and click “Continue”. Next, select the geometry (including point, line, or plane) for this set. Hold the key of “Shift” on the keyboard for multi-selection.

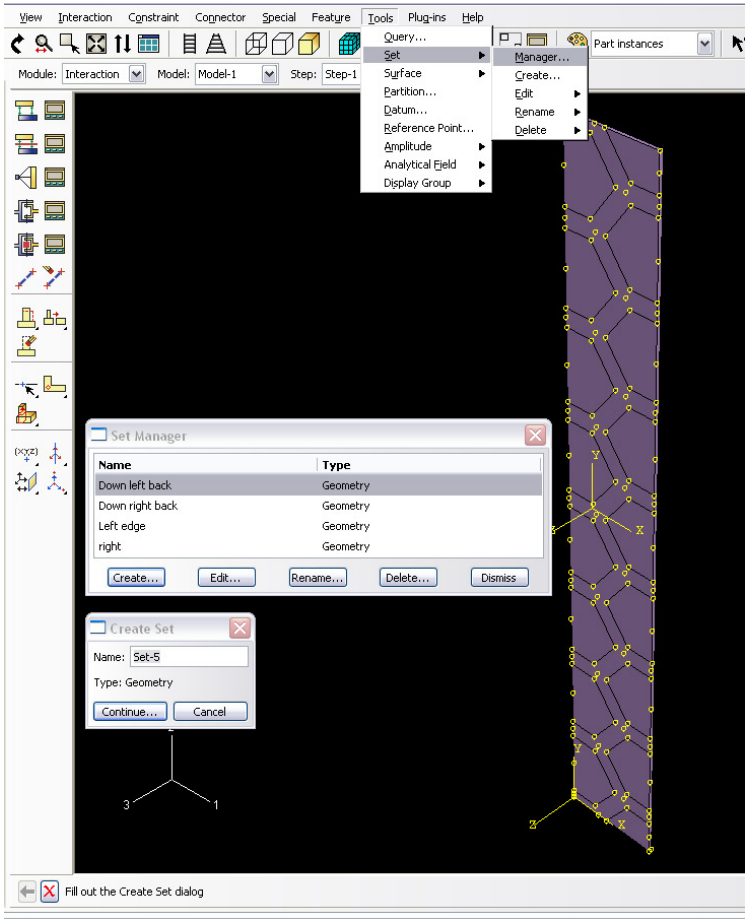

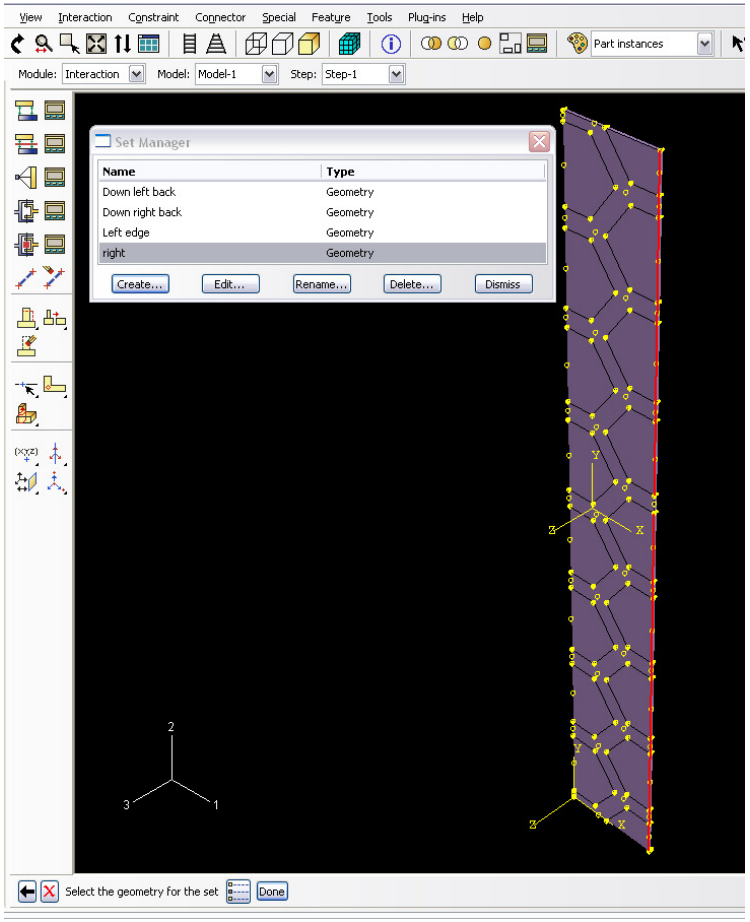

(24) Set constraint: In the same module, click the menu of “Constraint” and the option of “Manager” from the down list to show the dialog box of “Constraint Manager”. Click the “Create” button to pop up the box of “Create Constraint”. In this box, define the name for the constraint and select the “Equation” for constraint type. After clicking “Continue”, a new box appears. There are for parameters for definition, including the “Coefficient”, “Set Name”, “DOF” -- degree of freedom and “CSYS ID” – coordinate system. Input values for them.

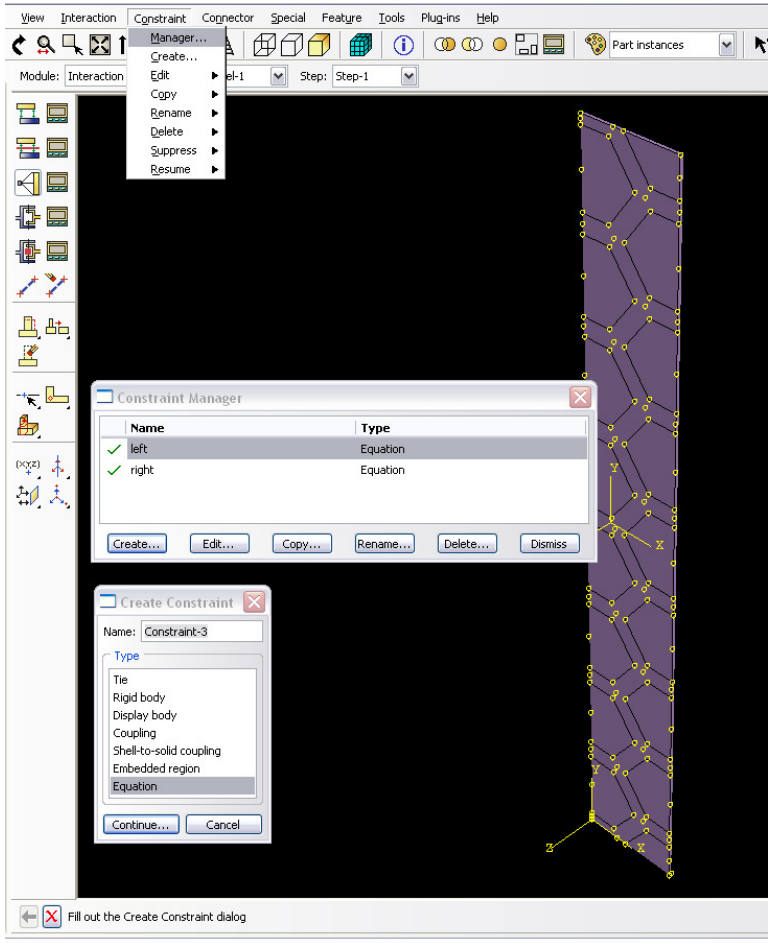

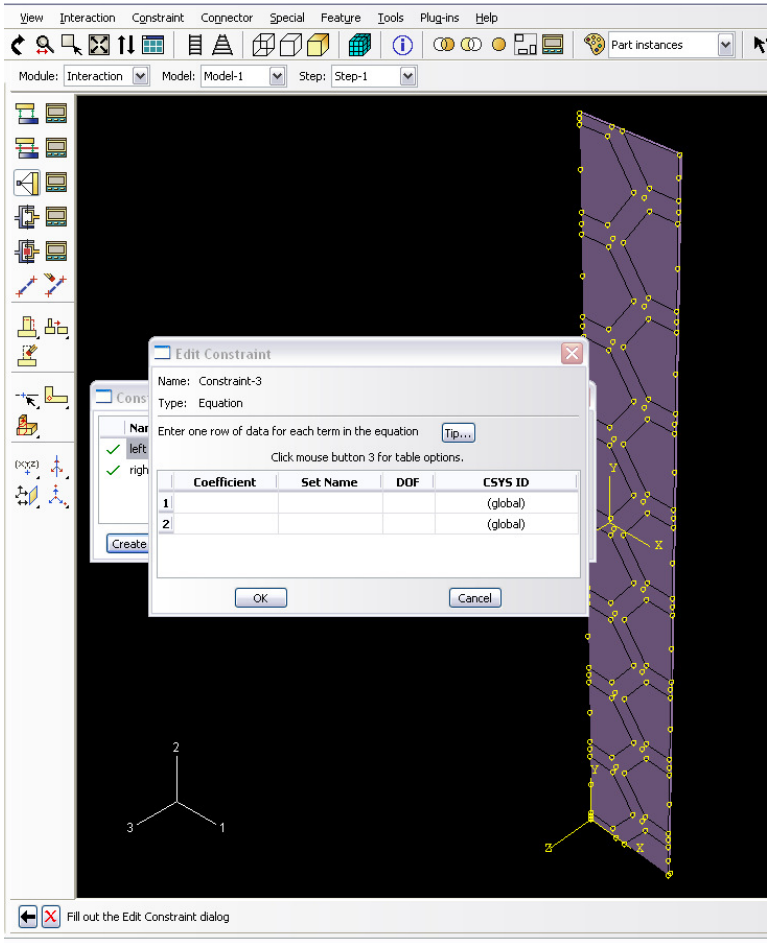

(25) Boundary condition: Enter the module of “Load”, and then click the icon of “Boundary Condition Manager” to show its dialog box. Click the “Create” button in this box to show the “Create boundary Condition” box. Then, define the name of the boundary condition, select the previously defined step, select the “Mechanical” for the “Category” and select “Displacement/Rotation” or “Velocity/Angular velocity” for the ”Types for Selected Step”. Finally, click “Continue”. The next step is selecting the point, line or plane to impose the created boundary conditions. A new dialog box will pop up, within which select “Global coordinate system” for “CSYS”, check the box in front of the mechanical components of interest and input the value. For other condition, keep the default option or value.

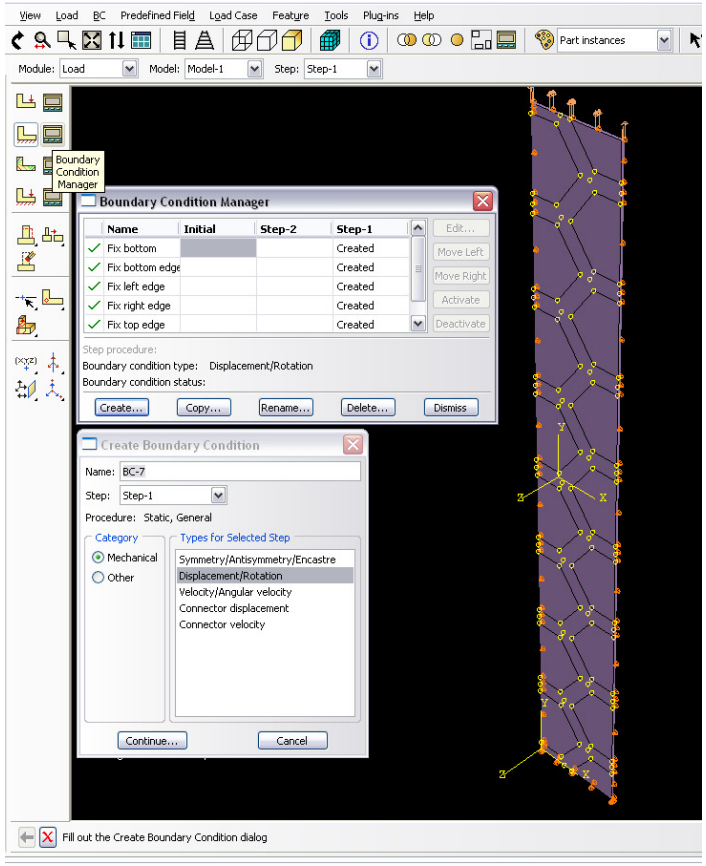

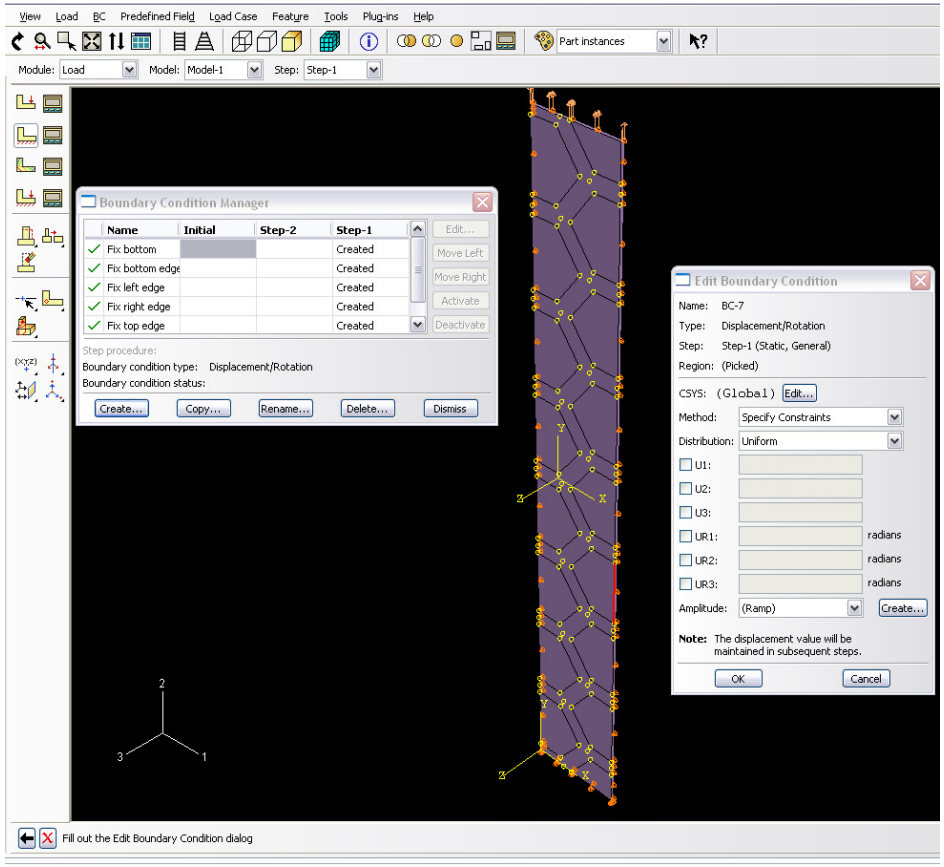

(26) Seeding: In the module of “Mesh”, create the seed for mesh first. Click the menu of “Seed” and the option of “Part” from the down list. In this pop-up box – “Global Seeds”, set the value for “Approximate global size” and keep other conditions as default.

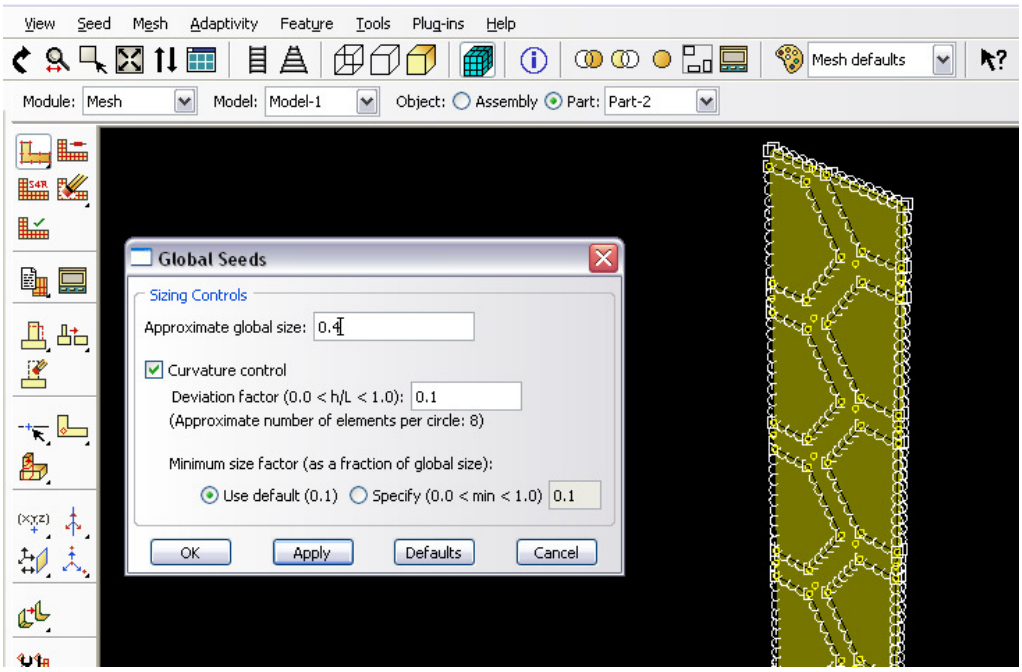

(27) Meshing control: Click the menu of “Mesh” and the option of “Control” from the down list. In the pop-up box, select the “Element Shape” and “Technique” for the selected region.

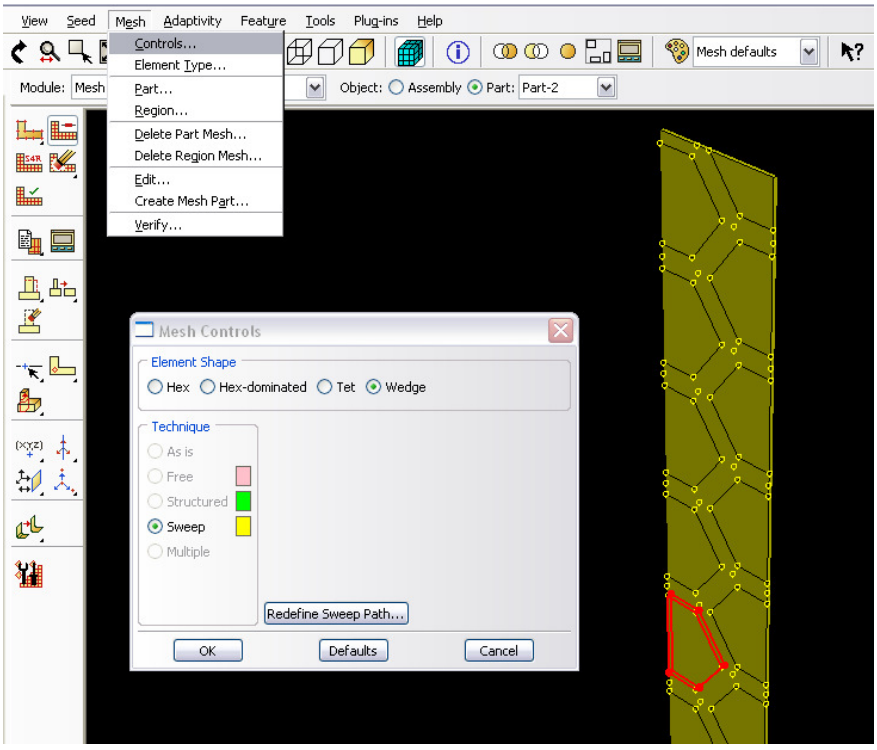

(28) Element type: Click the menu of “Mesh” and the option of “Element Type” from the down list. In the pop-up box, select the “3D Stress” in the “family” box, “Linear” in the ”Geometric Order” box, and keep other condition default for the selected region. Finally, click the menu of “Mesh” and the option of “Part” from the down list to accomplish the meshing step.

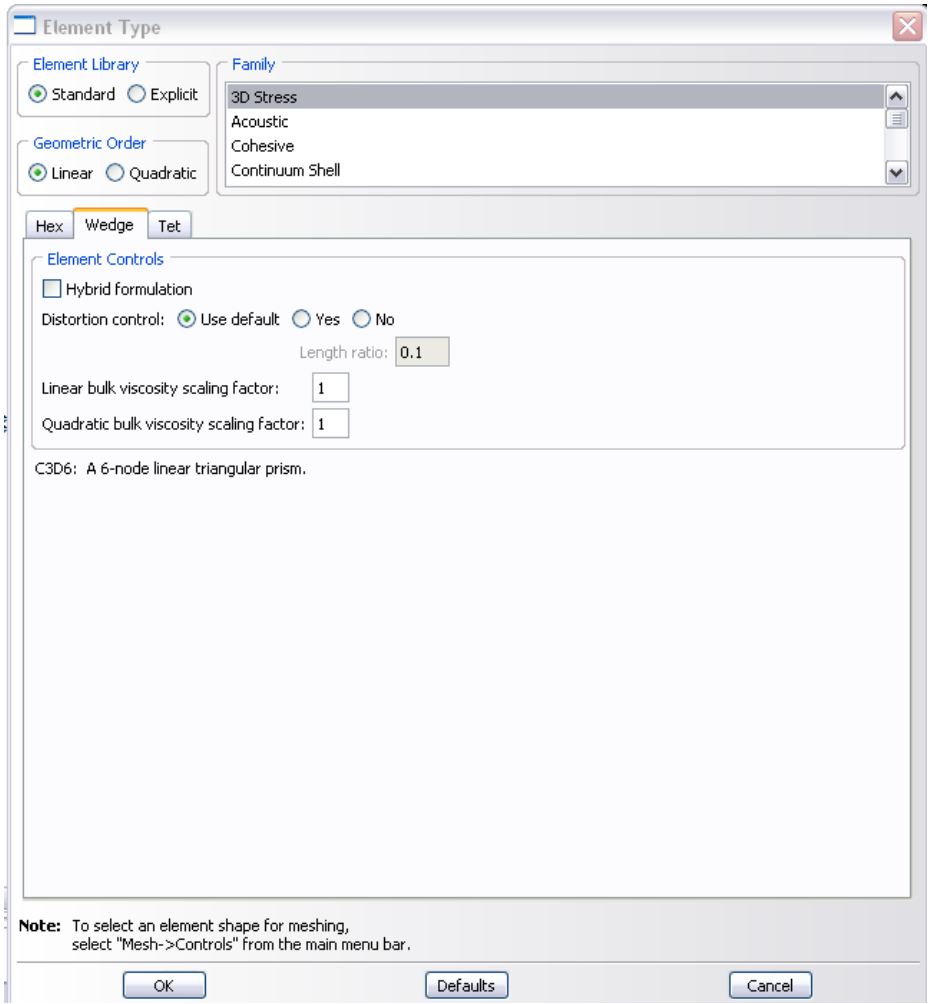

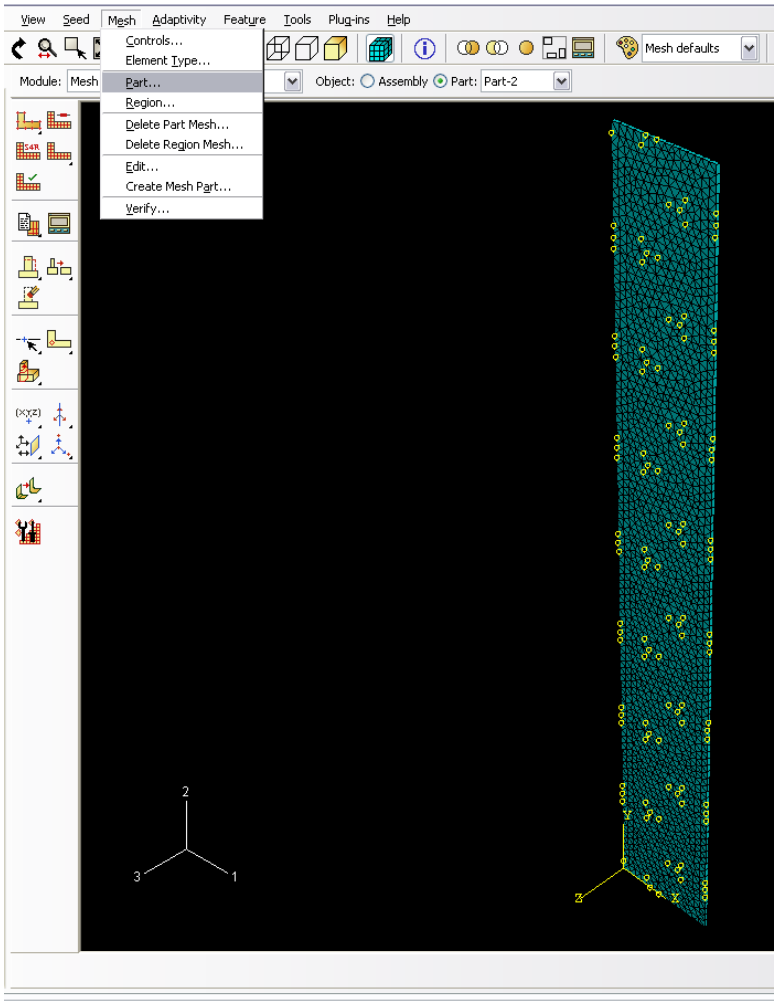

(29) Create job: Switch to the module of “Job”, and click the icon of “Job Manager”. Click the “Create” button to create a job, and define the name for the job, select the model for ‘Source” in the box of “Create Job”. Then, “Continue” to the box of “Edit Job”. In this box, input a brief “Description” for the created job and keep any other conditions as default, and then click “OK” to load this job to the box of “Job Manager”. Finally, highlight the job and click “Submit” to run the simulation. When the submitted job was completed, click “Results” to proceed to the module of “Visualization” and see the results.

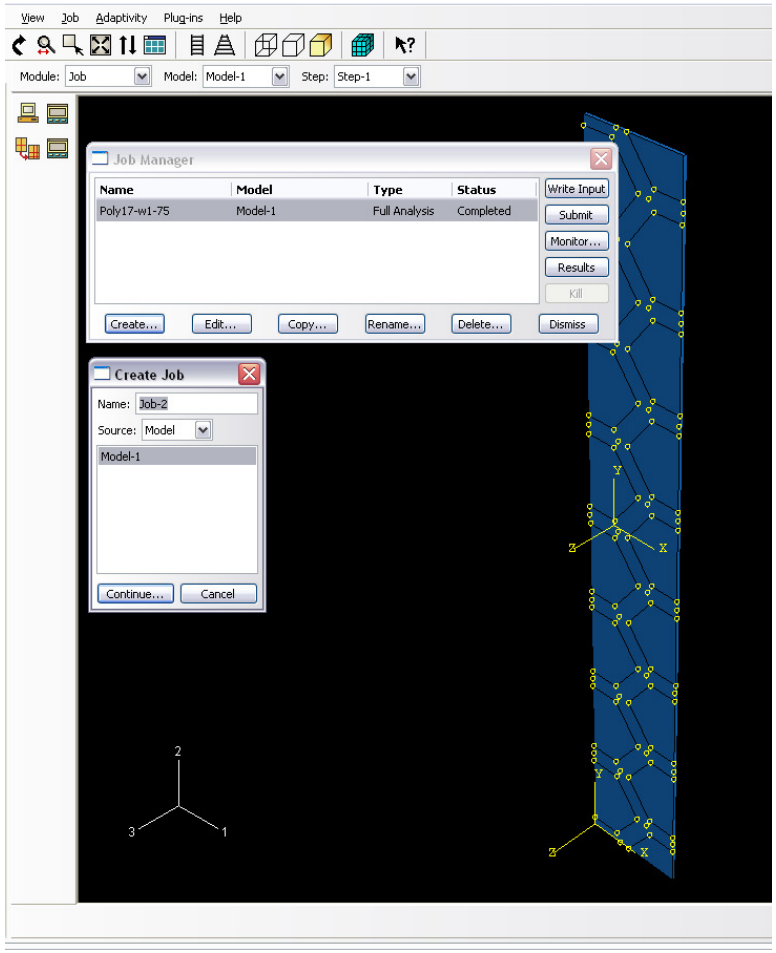

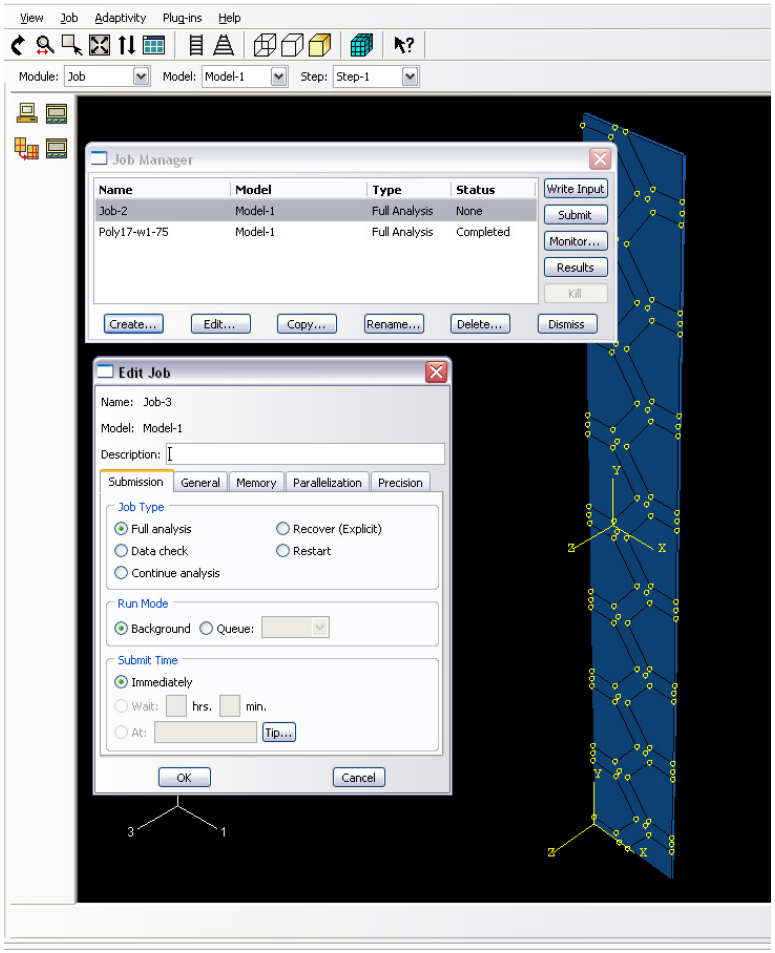

(30) Result: In the module of “Visualization”, click the menu of “Plot” and put the arrow on the option of “Contour” from the down list. Then select “On Deformed Shape” from the pop-up list on the right size. A contour map will appear on the part to display the simulated result. For various results, click the menu of “Result” and the option of “Field Output” from the down list. A dialog box will be displayed. Then, on the upper part of this box, select the step to see, and on the lower part, double click to select the “Output Variable” and “Invariant”.

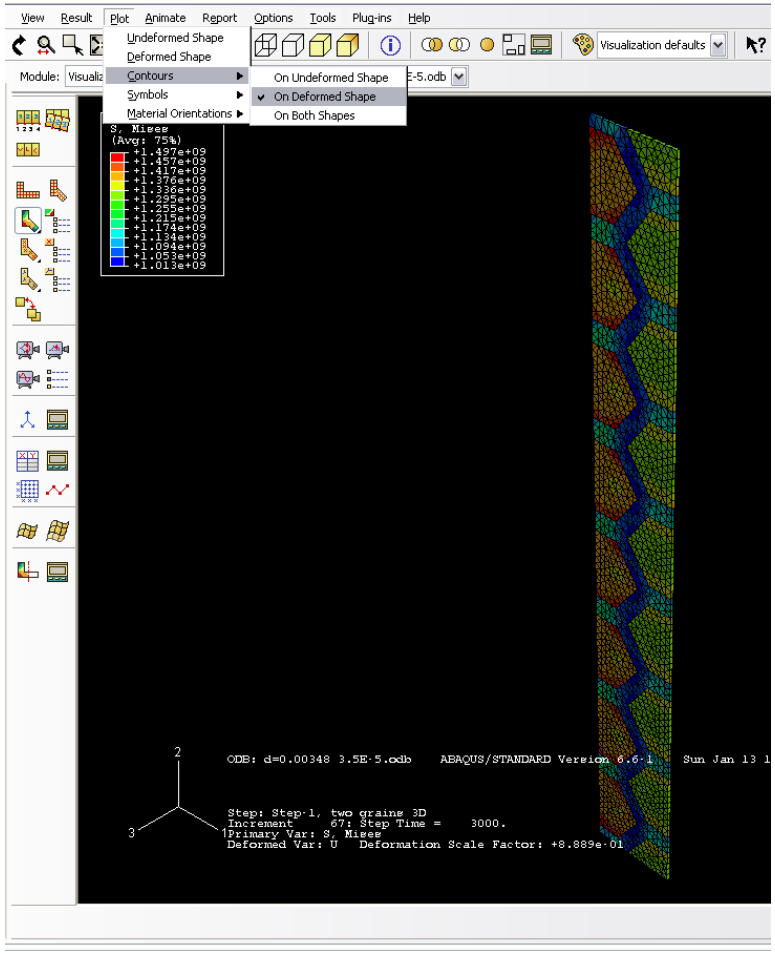

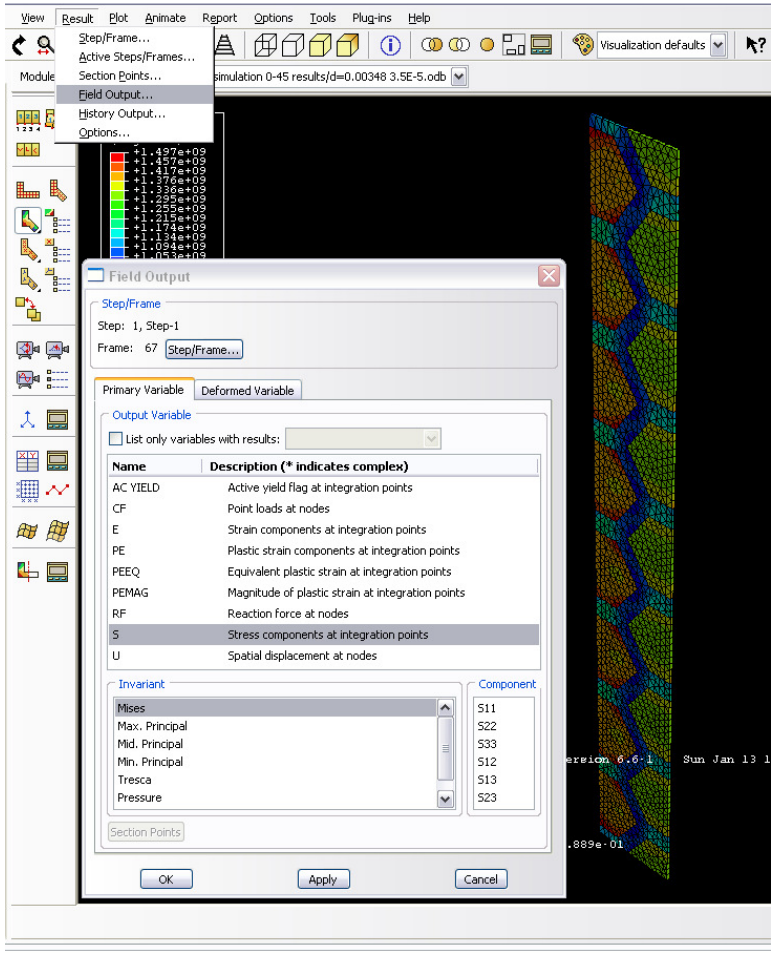

(31) Report data point: Click the menu of “Report” and the option of “Field Output” from the down list. A dialog box will display. In the sheet of “Output Variables”, check the box in front of variables of interest, and then switch to the sheet of “Setup”, in this sheet, define the name for the output file in the “File” frame, set the data format in the “Output Format” frame, and set the data type in the “Data” frame. Then, click “Step/Frame” button to activate the frame of “Step/Frame”. In this frame, double click the step of interest, and click the “Apply” button in the dialog box of “Report Field Output” to write the data to the named file.

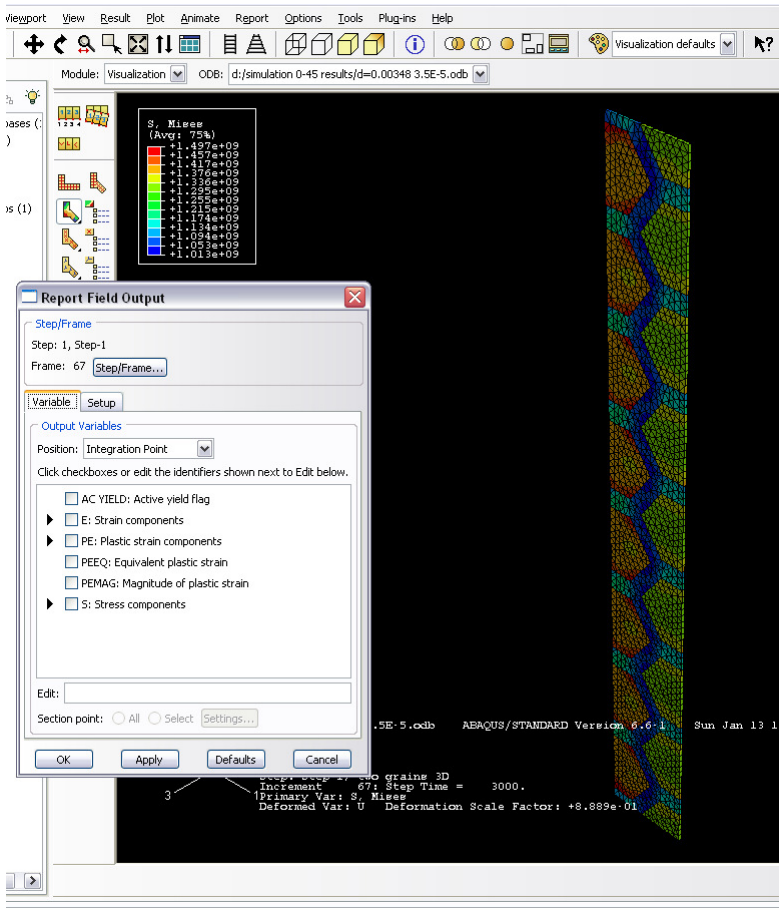

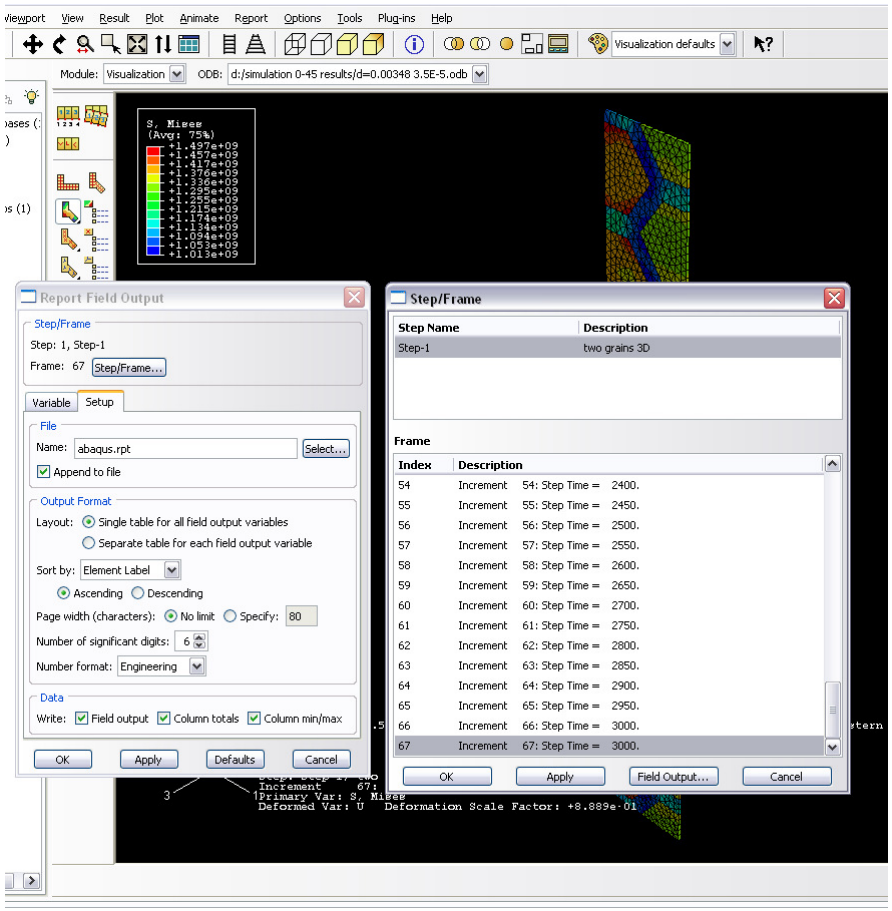

A1.2 Definition and Data Input

Part A. Single crystal

Geometry: ABAQUS®/CAE module was used to create the geometry of single crystal. As shown in Figure A1.1 (a), 3D solid and deformable part was created with 40 *units* (height) × 5.625 (width) *units* in-plane rectangle and 0.2 *units* for thickness. It is known that the result of *FEM* simulation is independent of geometric size. Therefore, this geometric model can be used to represent different physical sample sizes in calculation.

Material properties: Isotropic elasticity was assumed with the Young's Modulus of 200 *GPa* and Poisson's ratio of 0.3. The data points based on the various constitutive equations describing stress-strain behaviors of materials were generated and input to define the plastic property of materials. The anisotropic property of material was calculated by following the *Hill*'s theory. For the *Hill*'s theory, the function can be expressed in terms of rectangular *Cartesian* stress components as follows [31]:

$$f(\sigma) = \sqrt{F(\sigma_{yy} - \sigma_{zz})^2 + G(\sigma_{zz} - \sigma_{xx})^2 + H(\sigma_{xx} - \sigma_{yy})^2 + 2L\sigma_{yz}^2 + 2M\sigma_{zx}^2 + 2N\sigma_{xy}^2} \qquad \text{(A1-1)}$$

where F, G, H, L, M and N are constants obtained by test of material in different orientations. They are defined as

$$F = \frac{(\sigma^0)^2}{2}\left(\frac{1}{\overline{\sigma}_{yy}^2} + \frac{1}{\overline{\sigma}_{zz}^2} - \frac{1}{\overline{\sigma}_{xx}^2}\right) = \frac{1}{2}\left(\frac{1}{R_{yy}^2} + \frac{1}{R_{zz}^2} - \frac{1}{R_{xx}^2}\right) \qquad \text{(A1-2)}$$

$$G = \frac{(\sigma^0)^2}{2}\left(\frac{1}{\overline{\sigma}_{zz}^2} + \frac{1}{\overline{\sigma}_{xx}^2} - \frac{1}{\overline{\sigma}_{yy}^2}\right) = \frac{1}{2}\left(\frac{1}{R_{zz}^2} + \frac{1}{R_{xx}^2} - \frac{1}{R_{yy}^2}\right) \qquad \text{(A1-3)}$$

$$H = \frac{(\sigma^0)^2}{2}\left(\frac{1}{\overline{\sigma}_{xx}^2} + \frac{1}{\overline{\sigma}_{yy}^2} - \frac{1}{\overline{\sigma}_{zz}^2}\right) = \frac{1}{2}\left(\frac{1}{R_{xx}^2} + \frac{1}{R_{yy}^2} - \frac{1}{R_{zz}^2}\right) \qquad \text{(A1-4)}$$

$$L = \frac{3}{2}\left(\frac{\tau^0}{\overline{\sigma}_{yz}}\right)^2 = \frac{3}{2R_{yz}^2} \qquad \text{(A1-5)}$$

$$M = \frac{3}{2}(\frac{\tau^0}{\overline{\sigma}_{xz}})^2 = \frac{3}{2R_{xz}^2} \tag{A1-6}$$

$$N = \frac{3}{2}(\frac{\tau^0}{\overline{\sigma}_{xy}})^2 = \frac{3}{2R_{xy}^2} \tag{A1-7}$$

where each $\overline{\sigma}_{ij}$ is the measured yield stress value, σ^0 is the user-defined reference yield stress specified for metal plasticity definition, and $\tau^0 = \sigma^0 / \sqrt{3}$. R_{xx}, R_{yy}, R_{zz}, R_{xy}, R_{xz}, and R_{yz} are anisotropic yield stress ratios. For ABAQUS application, the anisotropic yield stress ratios are used as input. However, in practice, it is common to define the anisotropic property of material in terms of ratios of true width strain to true thickness strain of deformed sample. Therefore the mathematical relations as follows are needed to convert the strain ratios to stress ratios (refer to ABAQUS USER'S MANUAL). In present simulations, transverse anisotropy was assumed.

$$R_{xx} = R_{yy} = 1 \tag{A1-8}$$

$$R_{zz} = \sqrt{\frac{r_x + 1}{2}} \tag{A1-9}$$

$$R_{xy} = \sqrt{\frac{3(r_x + 1)r_y}{(2r_{xy} + 1)(r_x + r_y)}} \tag{A1-10}$$

Then, the user-defined material properties were used to create the section, which was assigned to the geometrical part.

Coordinates relations and boundary conditions: Figure A1.2 exhibits the coordinate relation between the loading direction and crystal axes. The sample axes were denoted as 1, 2 and 3, while the crystal axes was denoted as x, y and z. In present analysis, transverse anisotropy was assumed to the analyzed part. That is, the material has isotropic mechanical properties in x-y plane, while anisotropic mechanical properties in z direction. The loading direction is parallel to the 2-axis, which is the longitudinal direction of the part geometry. To estimate the stress-strain response of single crystal with different orientation with respect to the loading direction, the crystal axes of sample are rotated around the 1-axis of sample, which is parallel to the x-axis of crystal. In ABAQUS, to

define the materials orientation, a local coordinate system needs to be defined which is identical to the crystal axes defined above. The definition of material orientation was achieved by rotating the part about of a certain axis of this local coordinate system.

For boundary condition, free-standing boundary conditions were imposed on the analyzed part. The bottom cross section was fixed in the 2-direction (loading direction), while a displacement along the 2-direction with constant speed was put on the top cross section to produce the uniaxial tensile strain, which is shown in Figure A1.1 (b).

Calculation step: In order to reduce the calculating time, the general and static step procedure of analysis was selected with the initial time increment of 0.05 s and the maximum time increment of 0.07375 s. The actual time increment was automatically determined by the program.

Meshing: Because of the simple geometry of the analyzed part, the automated meshing was utilized to generate the mesh for the single crystal model. For mesh controls, the element shape of Hex and technique of Sweep was selected. Then, 3D-stress element type was assigned to the mesh. The total number of elements is 1400 with 1 element through the thickness (Figure A1.1 (c)). Mesh size of single crystal has little effect on simulation results, which has been confirmed by many calculations with various mesh sizes.

Part B. Polycrystal

Geometry: For polycrystals, the internal grains and grains on sample surface compose the bulk materials (illustrated in Figure A1.3). In this study, only the internal grains are considered. A repeat unit in internal region of sample is selected as simulation cell unit. For this cell unit, the same 3D geometry as that of single crystal was created with 40 *units* (length) ×5.625 *units* (width) in-plane rectangle and 0.2 *units* for thickness (refers to Figure 2B.1). The bulk geometry was partitioned into 17 hexagon regions and strip layers between hexagons, which represents grain interior and mantle zone within the polycrystals respectively (as denoted in Figure 2B.1). For the principle of geometric similitude in *FEM* calculation, the results of calculation are independent of geometric sample size. Therefore, the geometric dimension in *FEM* can be used to represent different physical dimensions. The various physical sample sizes represented by simulation cell are listed In Table A1.1, where *SCU* is defined as simulation cell unit for specific *FEM* simulation. Figure 2B.1 also shows the definition of grain boundary misorientation. As illustrated in Figure 2B.1, two neighboring crystals are assigned with different orientations. Crystal 1 has its *x*-*y* plane and *y* direction be parallel to the loading direction, while crystal 2 is rotated around 1-axis (in-plane horizontal direction) by 75 degrees, and has its *x* direction be parallel to the 1-axis. This relation of orientation creates the boundary misorientation, which is defined as 0-75^{o} twist boundary in present study.

For a constant bulk volume, the volume fraction of grain boundary increases with decreasing grain diameter. To create the simulation cells representing different physical grain diameters, the width of mantle zone in the simulation cell is varied to change the area fraction of mantle region as the boundary width in simulation cells for different cases referring physically to 1 *nm*. Table A1.2 lists the area fraction of mantle zone for cases with different physical grain diameter, where the area fraction of mantle zone, f_{gb} is defined as A_{gb}/A_{tot} (A_{tot} is total area in geometric simulation cell, and A_{gb} is mantle zone area in geometric simulation cell). The grain structures for selecting cases with various physical grain diameters are shown in Figure A1.4. For the definition of physical grain diameter, as illustrated in Figure A1.5, the hexagon grain shape is simplified by a circle. The grain diameter in simulation cell is derived by calculating the diameter of this circle. The diameter, d in unit of *SCU* is related to the grain area, A (area of hexagonal grain shape in unit of *SCU*) by following the equation of $d = \sqrt{\frac{4A}{\pi}}$. Then, the boundary width (δ) in simulation cell for different physical dimensions refers to the physical mantle zone width, δ' of 1 *nm*. Therefore, the corresponding physical grain diameter, d' is obtained by the following relation.

$$d' = \frac{d}{\delta} \times \delta' \quad (nm) \quad , \quad (\delta' = 1\ nm) \tag{A1-11}$$

Table A1.3 lists the relation between dimension in *SCU* and physical dimension for different cases.

Materials properties: For polycrystal model, the materials properties include the properties of grain interior and mantle zone. The material properties of grain interior refer to that of single crystal, which have been described in Part A. For mantle zone, isotropic elasticity is assumed with the Young's Modulus of 140 *GPa* and Poisson's ratio of 0.3. The definition of plastic property in ABAQUS follows the same method as that for single crystal, by which the data points based on the constitutive equation were generated and input. However, the mantle zone is assumed to have isotropic plasticity.

Coordinates relations and boundary conditions: As illustrated in Figure 2B.1, the tensile direction is in the in-plane vertical direction, which is parallel to the 2-axis in crystal. The coordinate system for a crystal within the polycrystal is identical to that of single crystal model described in Part A. For the boundary conditions, it is schematically shown in Figure A1.6. Constraint boundary conditions were imposed on the polycrystal sample. The bottom cross section was fixed in the loading direction, while a displacement along the loading direction with constant speed was put on the top cross section to produce the uniaxial tensile strain. The lateral edges of the front surface were restrained for displacement along plane-normal direction, while the lateral edges of the rear surface were free of restrain.

Calculation step: The same method as that for single crystal, which is to define the calculation step, was also applied to the polycrystal model.

Meshing: The automated meshing was also utilized to generate the meshes for polycrystal models, because of the simple geometry of the analyzed part. For mesh controls, the element shape of Hex and technique of Sweep was selected for single grain, and the element shape of Wedge for mantle zone since the mantle region has complicate geometry. Then, 3D-stress element type was assigned to the mesh (shown in Figure A1.7). The total number of elements varies with different cases, while 1 element through the thickness is for all the models. As shown in Figure A1.7, more elements were created within the geometrically wider mantle region. The effect of mesh size on simulation results of polycrystal models is quite small and can be ignored, which has been confirmed by many calculations with various mesh sizes.

Table A1.1 Physical sample size represented by simulation cell

Case No.	Physical sample size,	Simulation cell, *SCU**
1	$5.625 \times 40 \quad nm^2$	5.625×40
2	$18.75 \times 133.33\ nm^2$	5.625×40
3	$56.25 \times 400\ nm^2$	5.625×40
4	$562.5 \times 4000\ nm^2$	5.625×40
5	$5.625 \times 40\ \mu m^2$	5.625×40
6	$33.09 \times 235.29\ \mu m^2$	5.625×40
7	$56.25 \times 400\ \mu m^2$	5.625×40

*** *SCU* is defined as simulation cell unit for specific FEM simulation.**

Table A1.2 Area fraction of grain boundary region ("Mantle Zone") for cases with different grain diameter

Case No.	Area fraction of grain mantle region, f_{gb} (%)*
1	32.4
2	10.4
3	3.52
4	0.36
5	0.036
6	0.0060
7	0.0036

*** Area fraction of mantle region, $f_{gb} = A_{gb}/A_{tot}$, where A_{tot} is total area in geometric simulation cell, and A_{gb} is mantle region area in geometric simulation cell. Area fraction of grain, $f_g = 1 - f_{gb}$.**

Table A1.3 Relation between *SCU and physical dimension**

Case No.	Geometrical dimension, *SCU*		Physical dimension, μm	
	Mantle zone width, δ	Grain diameter, *d*	Mantle zone width, δ'	Grain diameter, *d'*
1	1	4.92	0.001	0.00492
2	0.3	5.66	0.001	0.0189
3	0.1	5.88	0.001	0.0588
4	0.01	5.97	0.001	0.597
5	0.001	5.98	0.001	5.98
6	0.00017	5.98	0.001	35.2
7	0.0001	5.98	0.001	59.8

*** *SCU* is defined as simulation cell unit for specific FEM simulation.**

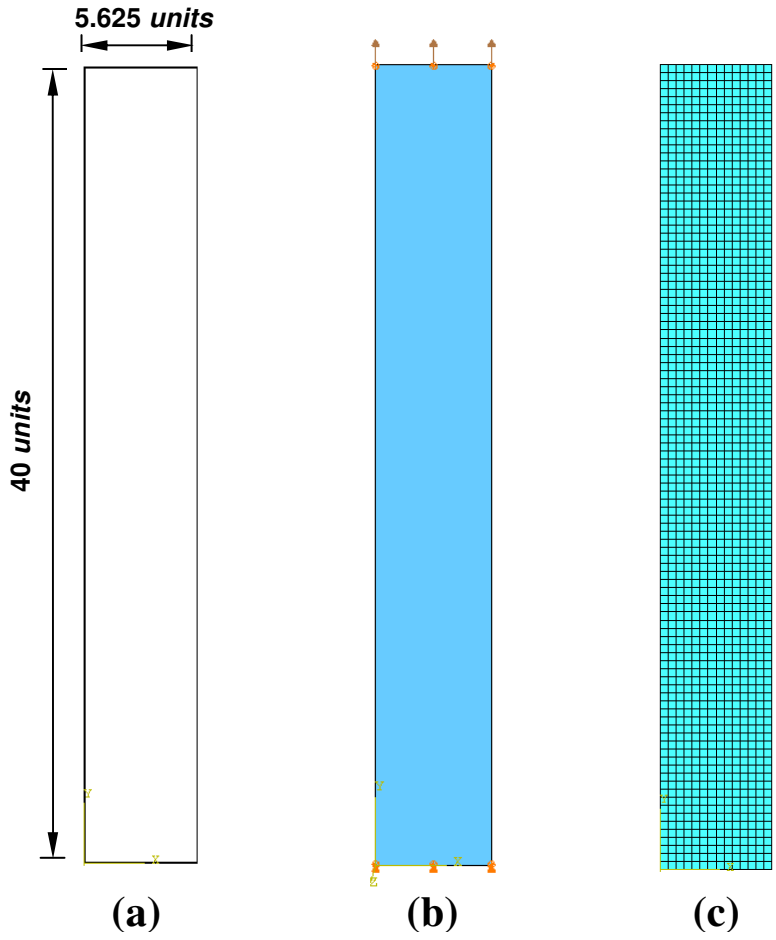

Figure A1.1 Simulation cell used for modeling stress-strain response of single crystal, (a) test sample geometry, (b) boundary condition and (c) FEM representation mesh

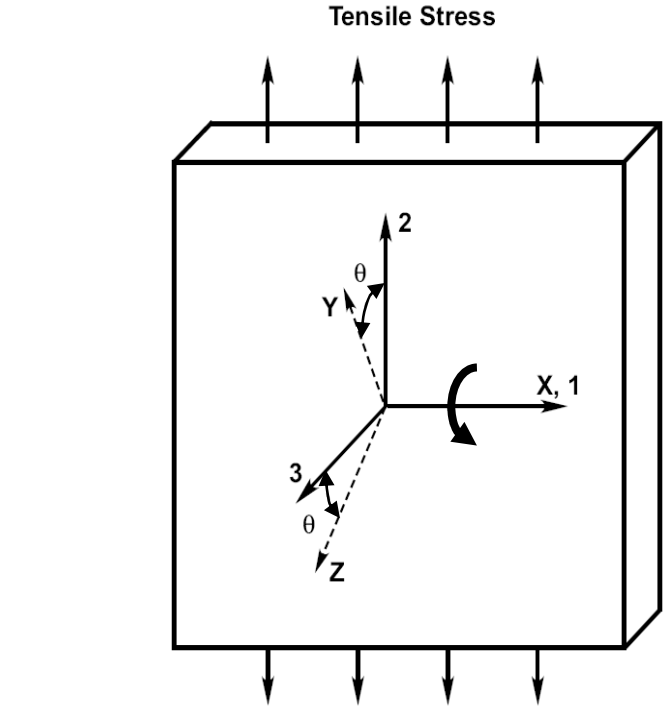

Figure A1.2 Orientation of single crystal with respect to the loading direction (2). The axis of crystal anisotropy is Z direction, (transverse anisotropy; X-Y plane is isotropic). Crystal orientation, θ is defined as the angle between sample plane normal and axis of anisotropy, Z, where tension direction is in the plane of sheet.

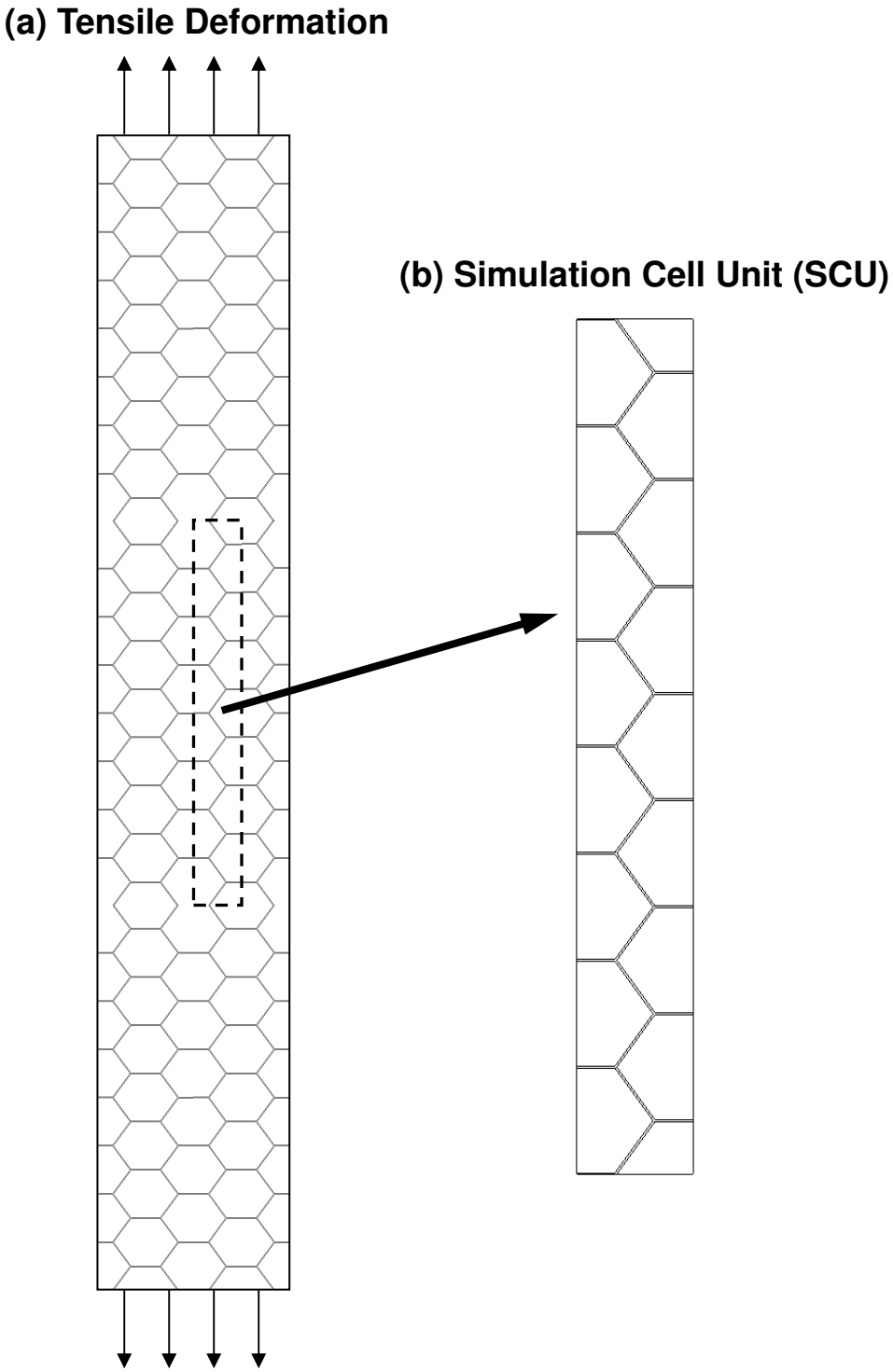

Figure A1.3. Selection of simulation cell unit as described in text.

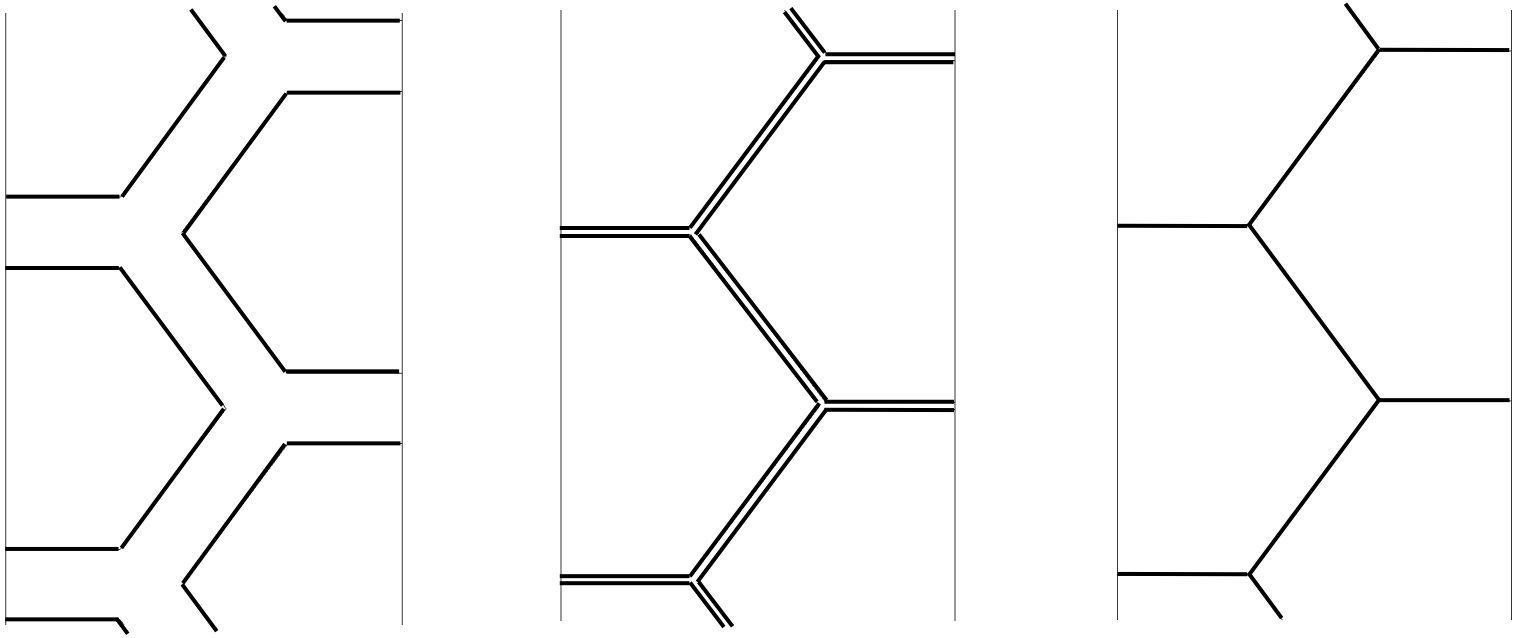

(a) Physical Grain Size: 4.92 *nm* **(b) Physical Grain Size: 58.8 *nm*** **(c) Physical Grain Size: 5.98 μm**

Figure A1.4 Grain structure for various physical grain diameters, (a) 4.92 *nm*, (b) 58.8 *nm* and (c) 5.98 μm

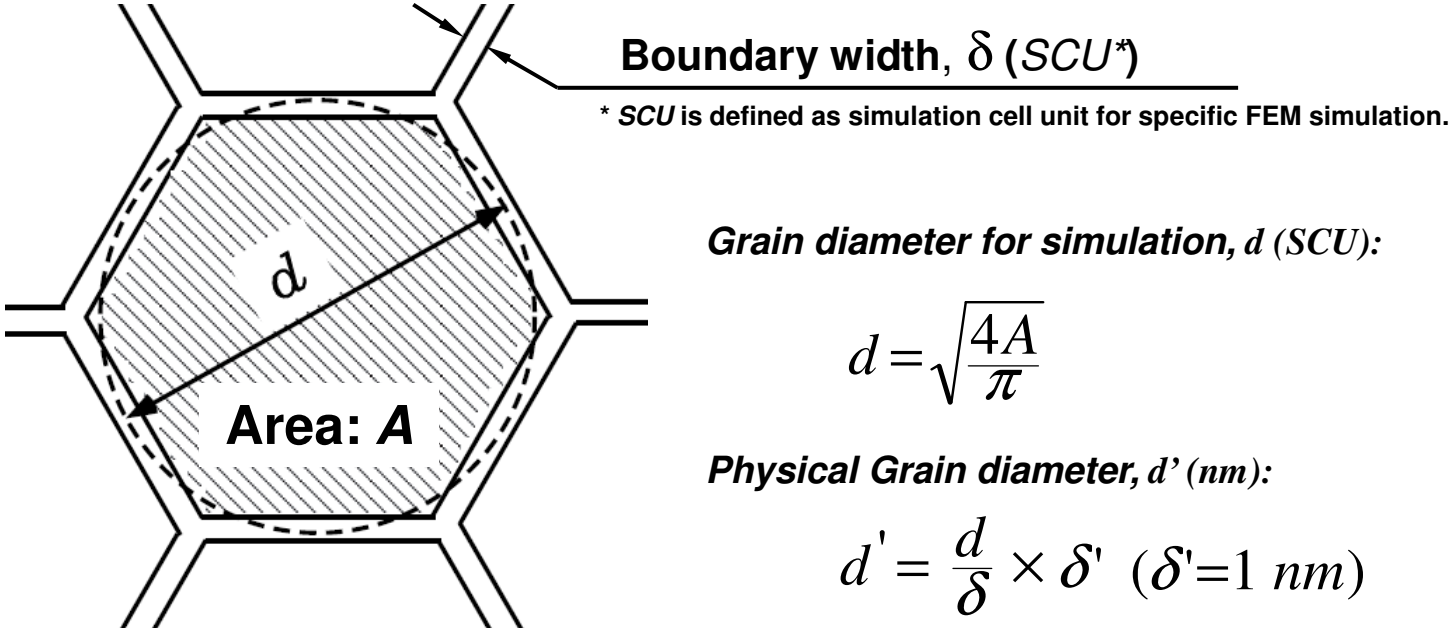

Figure A1.5 Equivalent grain diameter based on area for hexagonal grains used in simulation cell geometry, and ratios of physical size of grain to simulation cell size.

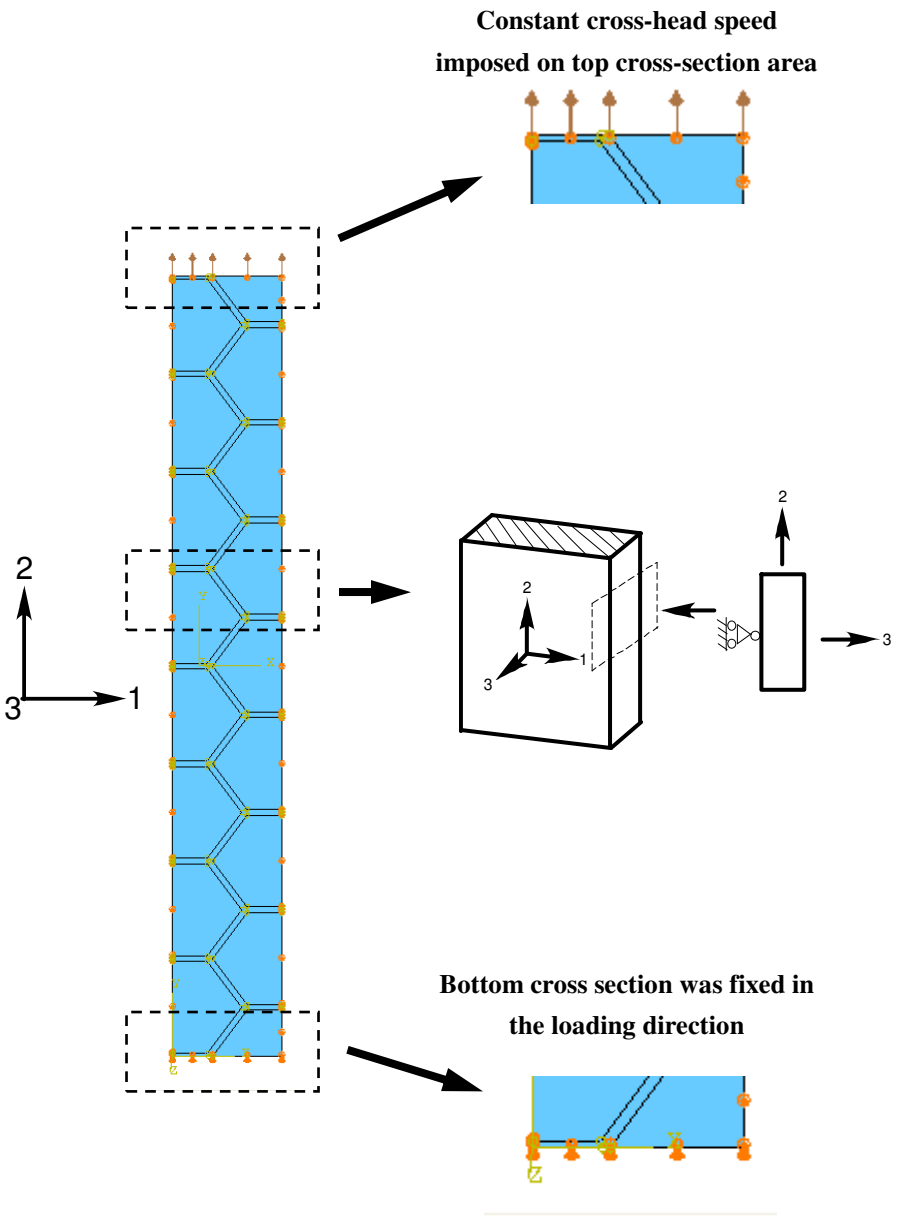

Figure A1.6 Schematic illustration of boundary conditions for polycrystal model at various locations in test specimen.

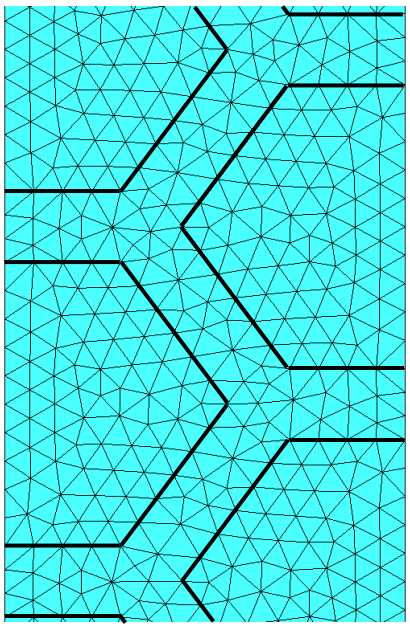

(a) Physical Grain Size: 4.92 *nm*

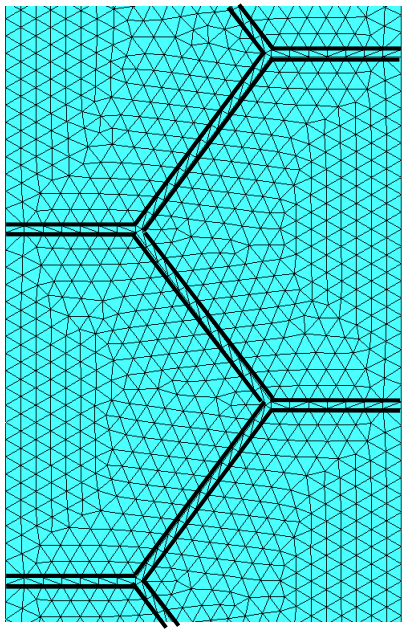

(b) Physical Grain Size: 58.8 *nm*

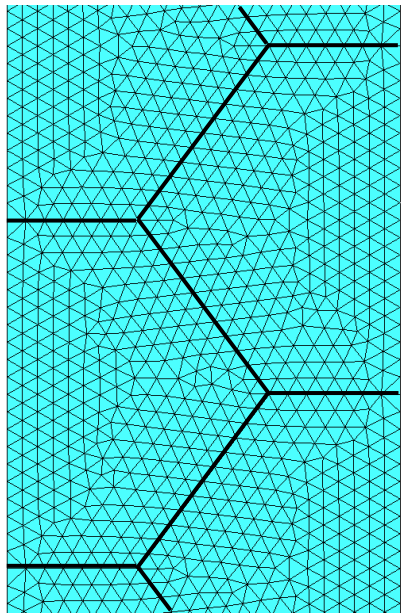

(c) Physical Grain Size: 5.98 *μm*

Figure A1.7 Meshing for specific cases of geometry used for representing various physical grain sizes, (a) 4.92 *nm*, (b) 58.8 *nm* and (c) 5.98 *μm*

Chapter 2 - Appendix 2:

Literature Review on Grain Size Strengthening and Weakening Effect

Original experiments on steels by Hall [1] and Petch [2] show the pronounced lower yield point stress and cleavage strength dependence on the reciprocal square root of average grain diameter of polycrystals. Based on those experimental results, the empirical relationship between the strength properties of metal polycrystals with the grain diameter was established, which is well-known as Hall-Petch relation. The Hall-Petch relation (as equation A2-1) depicts that low-temperature strength (σ) of polycrystalline materials normally increases when the grain size (d) is decreased.

$$\sigma = \sigma_0(\varepsilon) + k(\varepsilon)d^{-1/2} \tag{A2-1}$$

In equation (1), $\sigma_0(\varepsilon)$ is the friction stress below which dislocations will not move in a single crystal, and $k(\varepsilon)$ is the stress intensity for transmission of dislocation strains at the grain boundaries. These two material parameters are independent of the grain size (d), but dependent on strain history.

The Hall-Petch relation was extended to the many metal systems by other researchers [3-9]. The strengthening effect of grain refinement was typically observed up to the size range of a few microns (shown in Figure A2.1). It was even reported to be still valid for nickel and iron materials with nanometer-scale grain size of about 12 *nm* [3, 10]. This relation was firstly explained with dislocation pile-up theory by Eshelby, Frank and Nabarro [11]. Based on this theory, the yield strength increases as grain size decreases because pile-ups in the fine-grained materials contain fewer dislocations, the stress at the tip of the pile-up decrease and, thus, a larger applied stress is required to generate dislocations in the adjacent grain. The experiment about accurate measurements of the slip band step heights via interferometric observation provided the information about the early stages of plastic deformation in polycrystals [12, 13], which reasonably presented the direct evidence for validity of the dislocation pile-up model [14].

In spite of the fact that the Hall-Petch relation is widely known and accepted, where the yields stress is inversely proportional to the square root of grain diameter (σ_y *vs.* $d^{-1/2}$), by reviewing the published data for many metals, Baldwin [15] showed that in many cases the scatter in the data was such that yield stress versus inverse grain diameter (σ_y *vs.* d^{-1}), and inverse cube root of grain diameter (σ_y *vs.* $d^{-1/3}$) yielded as good a fit to the experimental results as the yield stress versus inverse square root of grain diameter. This

indicates that Hall-Petch relation may not be the only one for strengthening effect of grain refinement.

Moreover, if the Hall-Petch relation was extrapolated down to nanometer-scale, the applied stress approaching the theoretical strength should be expected. However, in Figure A2.2, lots of studies were reported where the Hall-Petch slope gradually decreases [16-19] or even becomes negative [20-22], which was called inverse Hall-Petch relation. According to the dislocation pile-up model, Pande et al. suggested that the reduced number of dislocations within the nanometer-scale grain and the elastic anisotropy can affect the Hall-Petch grain size exponent; also, the independence of grain boundary barrier stress on the grain size may not be true for small grain size [23]. However, the dislocation pile-up model is unable to explain the observed softening phenomenon in nanometer-scale materials. Other researchers thought that the volume fraction of the triple junction region becomes significant as the grain size is decreased to the nanometer-scale range; and the softening was ascribed to the increasing triple junction region [24, 25].

By reviewing the methods used to prepare the nanocrystalline materials, the validity of the inverse Hall-Petch effect was questioned in two aspects [22, 26]. One is the accurate determination of grain size and grain size distribution at the nanometer scale. In the another aspect, most of experiments reporting inverse Hall-Petch effect varied the grain size by annealing the smallest grain size samples to obtain grain growth and therefore a range of grain sizes. It was suggested that [27] that thermally treating nanophase samples in the as-produced condition may result in such changes in structure as densification [16, 17, 20, 22], stress relief, phase transformations [21], or grain boundary structure [17, 19], all of which may lead to the observed inverse Hall-Petch behavior.

Nevertheless, in some cases (Figure A2.3) in which the samples were free from obvious or possible artifacts, inverse Hall-Petch effects were also reported [18, 28, and 29]. The transition from hardening to softening within the same material was also exhibited. Moreover, in-situ straining HRTEM studies of nanocrystalline Au and Ag film by Ke and et al. [30] observed dislocation-based plasticity for 100 *nm* grain size samples, but no for 10 *nm* grain size films. Therefore, it is suggested that the inverse Hall-Petch effect is real, and the classical dislocation deformation mechanisms are not applicable to the finest nanocrystalline grain size metals.

Conclusively, some important statements can be summarized as follows,

(1) Generally, the strength of polycrystalline metals increases with decreasing grain size. The linear relationship between strength and square root of grain diameter are valid within the relatively coarse grain regime.
(2) However, with decreasing grain size, grain size strengthening effect starts to deviate

from the relation of $d^{-1/2}$. The strengthening effect of $d^{-1/3}$ or d^{-1} may occur with further reduction in grain size.

(3) Furthermore, when the grain size is refined down to nanocrystalline regime, the weakening effect of decreasing grain size is possible to exist, of which the underlying mechanism is still controversial and unclear.

(4) The explanation for weakening effect ascribed to the increasing triple junction region needs to be further examined. The argument of artifact effect on the observed weakening phenomenon may challenge the validity of inverse Hall-Petch relation.

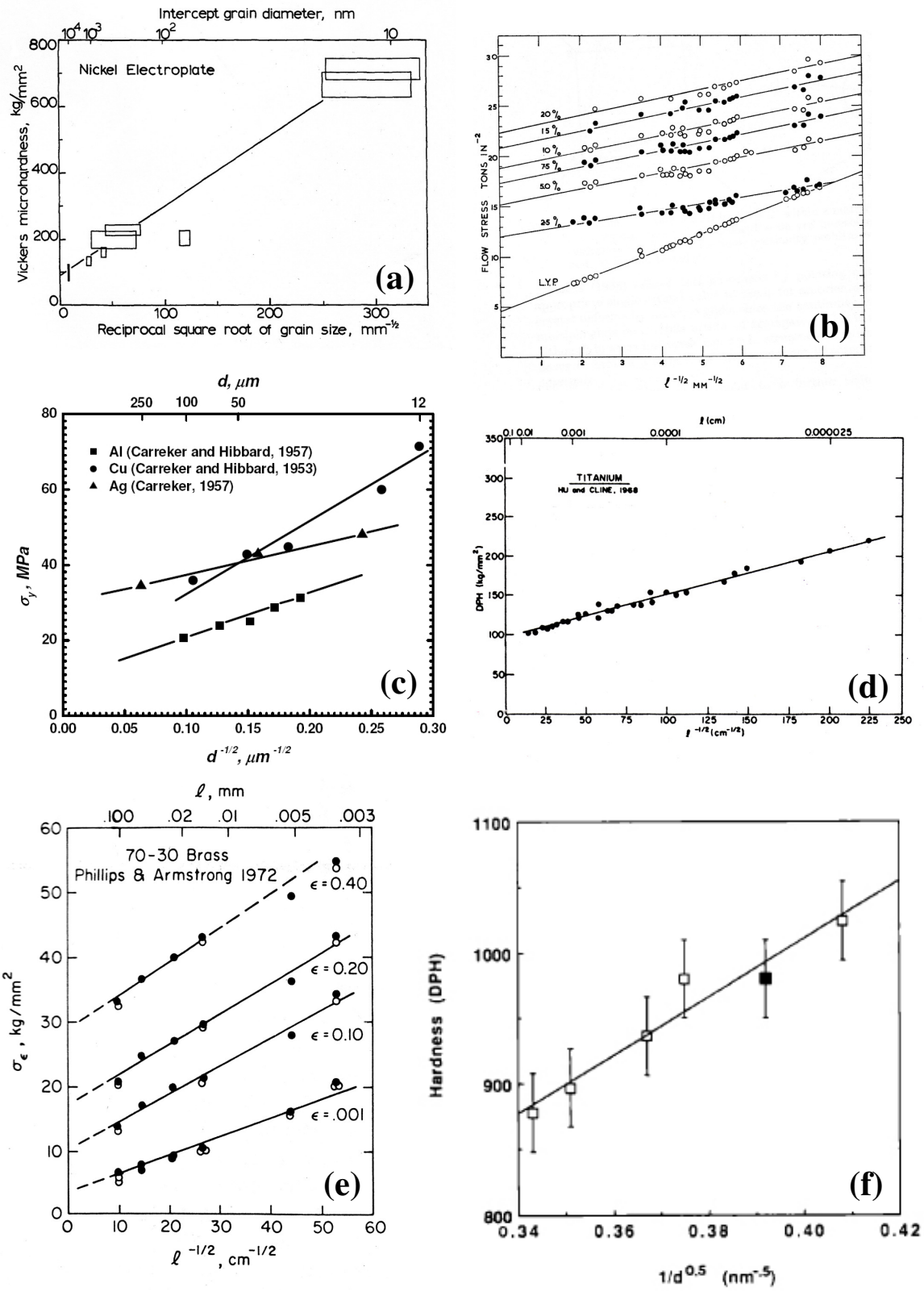

Figure A2.1 The Hall-Petch relation for different polycrystalline metals, (a) electrodeposited nickel, (b) mild steel, (c) aluminum, copper and silver, (d) α-titanium, (e) 70:30 brass and (f) iron

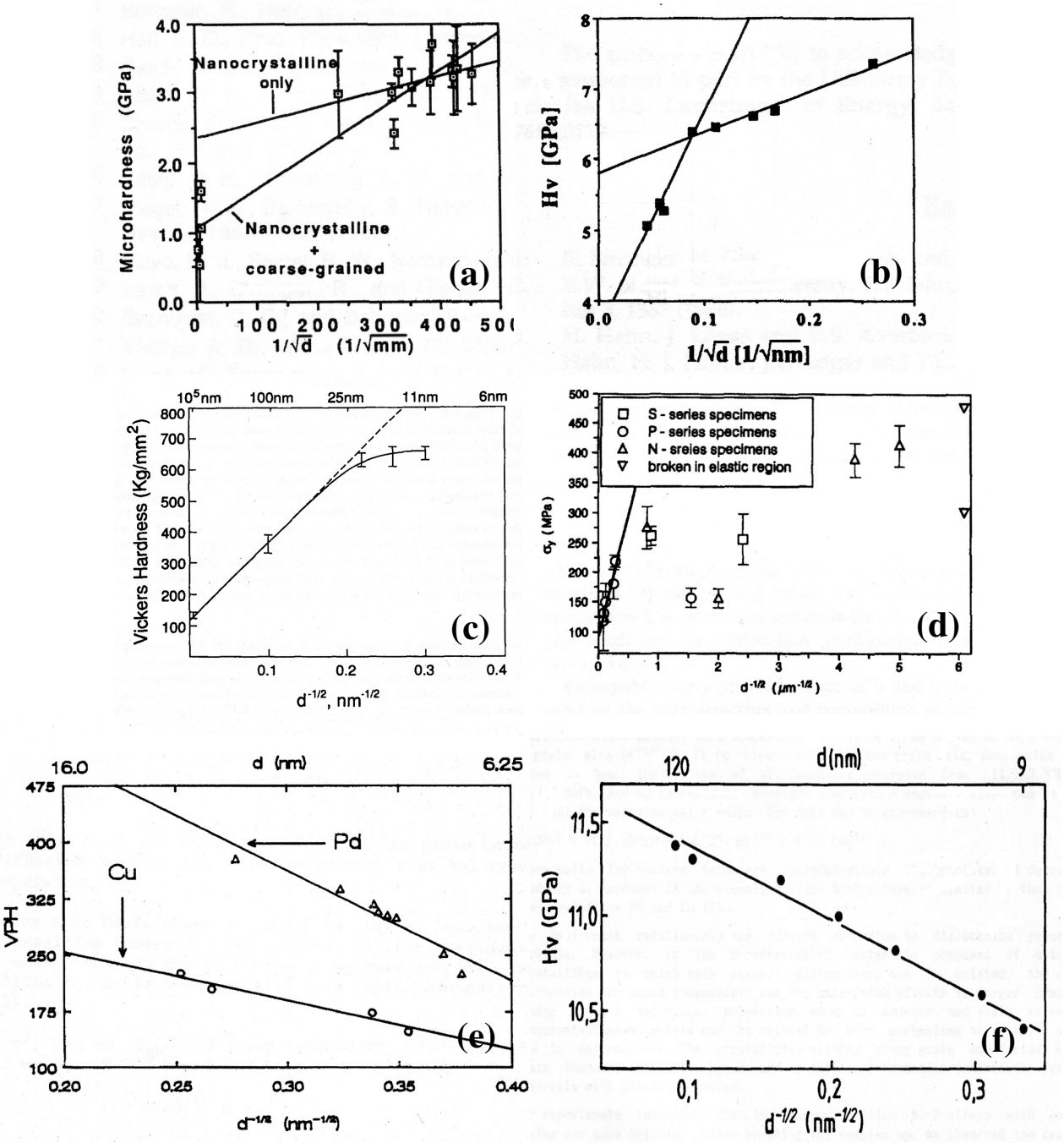

Figure A2.2 The relationships between strength properties and grain diameter of polycrystalline metals showing deviation from Hall-Petch relation ((a) palladium, (b) TiO_2, (c) nickel, (d) copper), or even inverse Hall-Petch relation ((e) copper and palladium, and (f) Ni-P alloy).

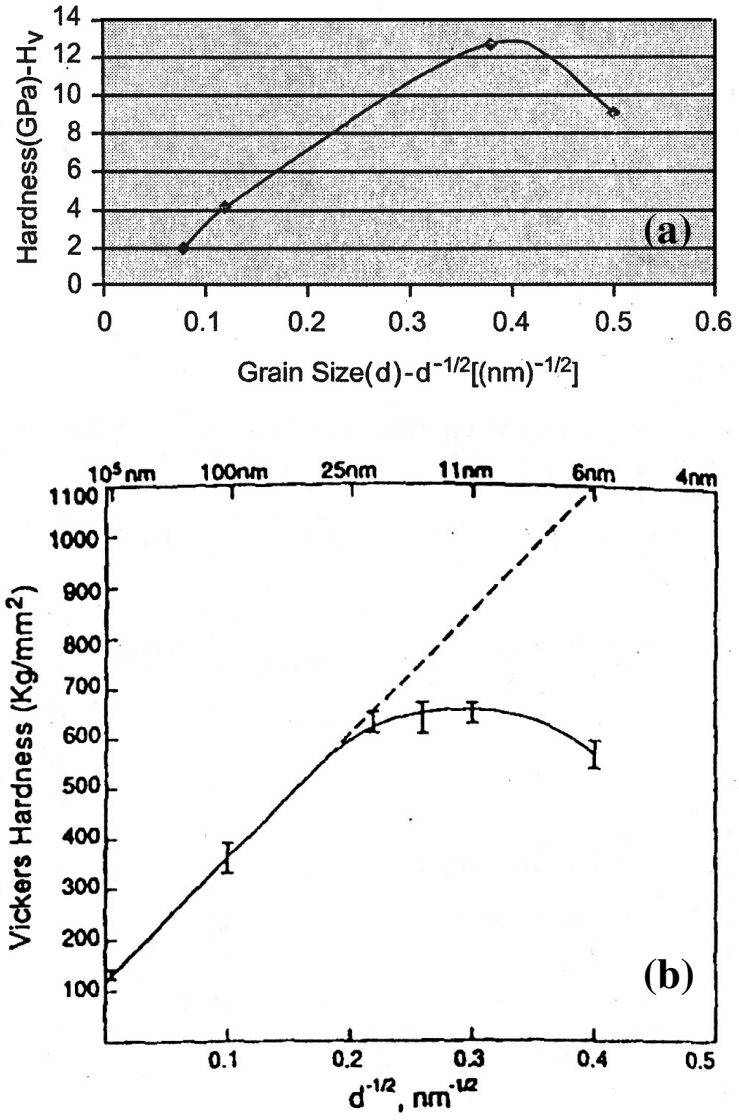

Figure A2.3 The relationships between strength properties and grain diameter of polycrystalline metals showing strengthening and weakening effect vs. decreasing grain size in the same materials, (a) copper and (b) nickel

Chapter 2 - Appendix 3:

Justification for Choice of Grain Boundary Mantle Zone Thickness in Simulation

In contrast to the grain interior where lattice is generally periodic in nature, grain boundary region is characterized with atomic disorder due to the high density of defects in these regions, such as dislocations, steps, ledges, vacancies and interstitials. The joining of two neighboring grains through grain boundary is considered to be in the form that several atom layers on either side of the boundary is to be involved in the deformation process as a cohesive layer sometimes referred to as a "Mantle Zone" [A3-1, A3-2].

When two grains with periodical lattice join with each other, many types of boundary are possible. Some boundaries may have coincidence lattice sites along the boundary where some atoms from both crystals match, or random boundary. As shown in Figure A3.1, boundary is thought to consist of dislocation network [A3-3]. The arrangement of dislocation network decides grain boundary geometry. High boundary misorientation accommodated by high dislocation density can increase boundary spacing. Figure A3.2 (a) and (b) [A3-4] show the influence of grain boundary structure on packing density of grain boundary, which is calculated by generalized coincidence site network (GCSN) Model and indicates that atom density of boundary is generally lower. Shown in Figure A3.2 (c), increasing boundary space can result in small shear strength in boundary; type of joining atom plane also influences the strength of boundary [A3-5].

From microscopic view, high resolution transmission electronic microscope (HRTEM) image of nanograin Al 1420 alloy reveals that the joining of the end points of atom planes along a grain boundary does not create a flat boundary (shown in Figure A3.3) [A3-6]. Even from macroscopic observation on cast Ni-base superalloy, large size grain boundary also shows undulations (Figure A3.4) [A3-7]. These observations reveal that grain boundary is not planar. When applied stress is resolved into normal and shear stress components, these components are therefore constantly changing their direction along a boundary. Thus, atoms in the vicinity of boundary will depart from their original periodic position under stress; and corresponding atomic displacements are also changing in magnitude with changing stress components. It means that atomic spacing in this region has no periodic distance, which is identical to disorder as in anamorphous state. This region can cover several atom layers on either side of boundary as illustrated in Figure A3.3. We have previously demonstrated that protrusions on the boundary can cause strain concentrations along the boundary under stress [A3-8]. In Figure A3.5, it can be seen that high strain concentration develops near the triple steps on the grain boundary, which increase the non-equilibrium area in the vicinity of boundary. Thus uniform state of stress within grain matrix

cannot be reached until this grain matrix is further away from the mantle zone within which atomic displacements are non-uniform.

The lines joining grain triple junctions define an envelope of a cohesive grain boundary zone, where atomic displacements are likely to be non-uniform and therefore non-equilibrium in nature. This zone (called mantle zone [A3-2]) is expected to have a viscous response which is possibly non-Newtonian in nature due to dislocation glide-climb effects near the boundary [A3-1]. This zone can have different thickness depending on the specific alloy and boundary misorientation. When a polycrystal is loaded, it is this effective thickness of mantle zone that has the greatest importance, rather than a boundary seen under TEM under static conditions. Thus the thickness of mantle zone can vary from 3-4 atom spacings around the boundary to 6-7 atom spacings on either side of the boundary, or more depending on the true nature of grain boundary in the alloy. Considering lattice spacing in metals is around 2.5 angstroms, one nanometer thickness of grain boundary cohesive zone is thus to be a reasonable assumption in preliminary simulation model used in this work.

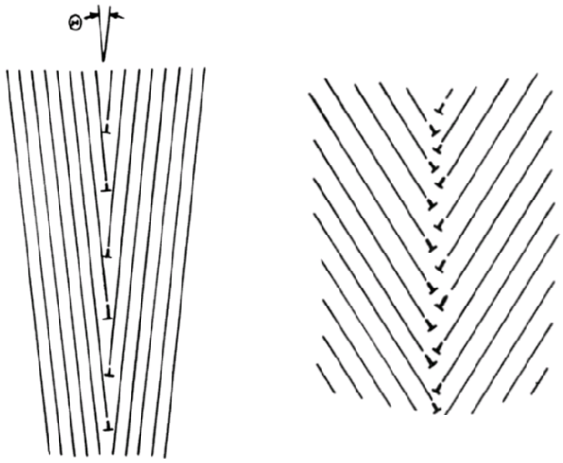

Figure A3.1 Dislocation arrays in boundaries of different misorientation.

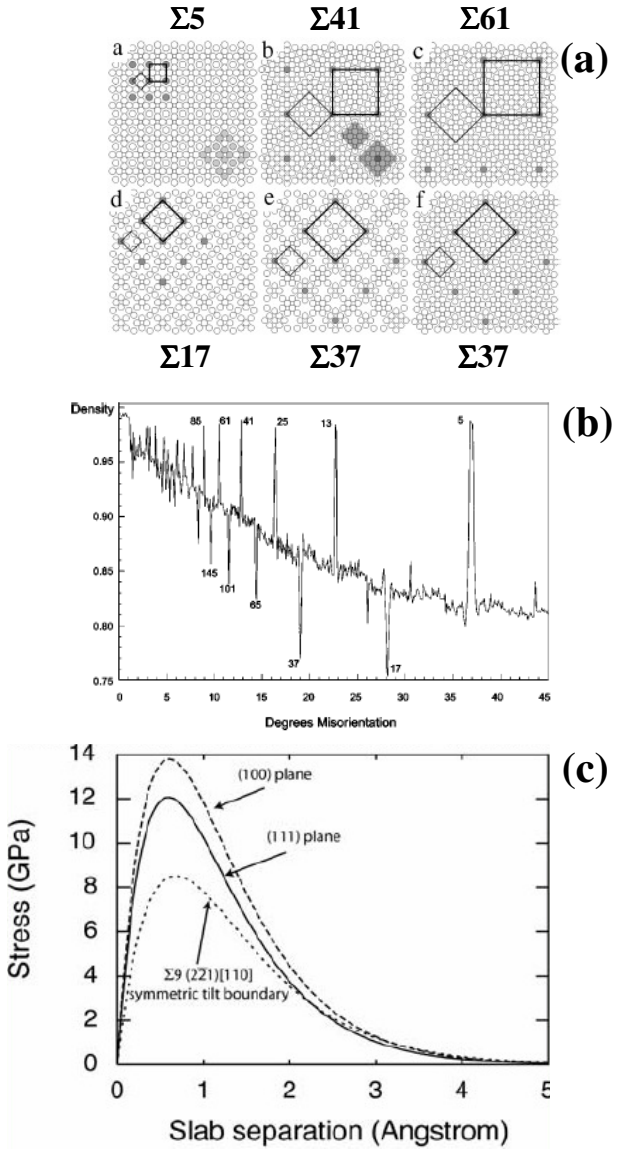

Figure A3.2.Influence of grain boundary structure on packing density and traction of grain boundary. (a) Various atomic models of grain boundary structure and (b) corresponding packing density. Atomic structures of Σ5, Σ41 and Σ61 [100] twist boundaries in fcc as generated by the GCSN model [A3-4], and (c) First-princiles calculated traction curves for decohesion between (100) planes, (111) planes and a Σ9, symmetric tilt boundary in fcc aluminum [A3-5].

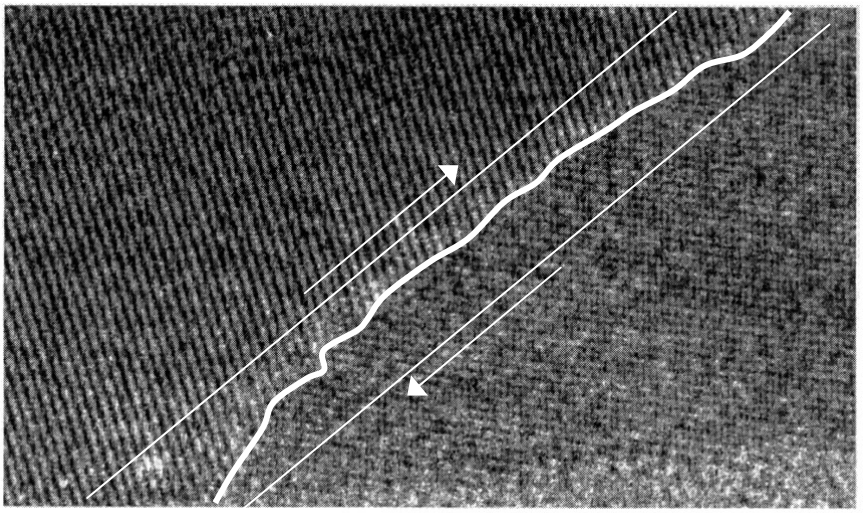

Figure A3.3 Mantle region shown on High Resolution TEM image of a grain boundary in nanograin Al 1420 [A3-6].

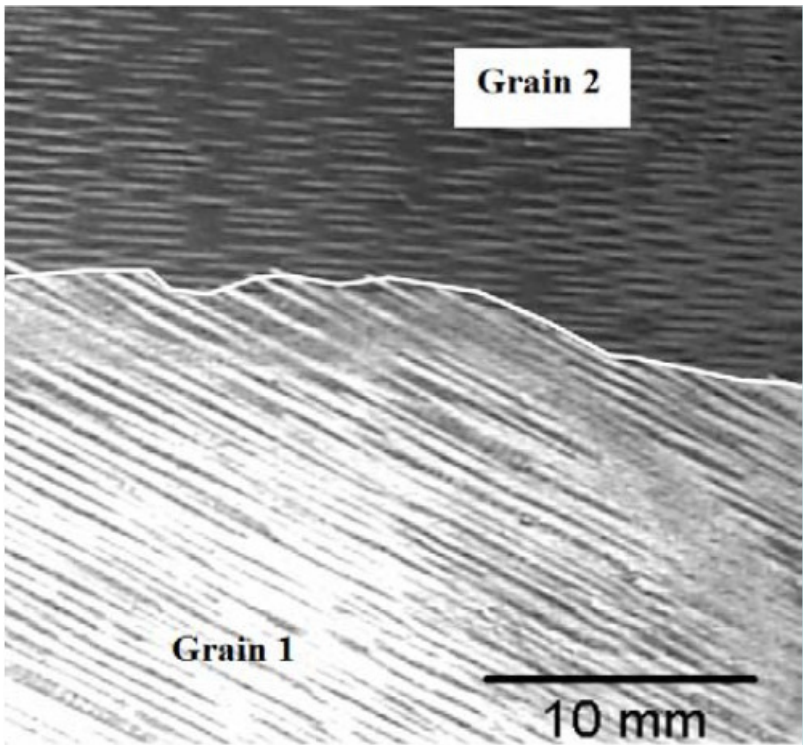

Figure A3.4 Grain boundary in a Cast Ni-base Superalloy showing large size grain boundary undulations [A3-7].

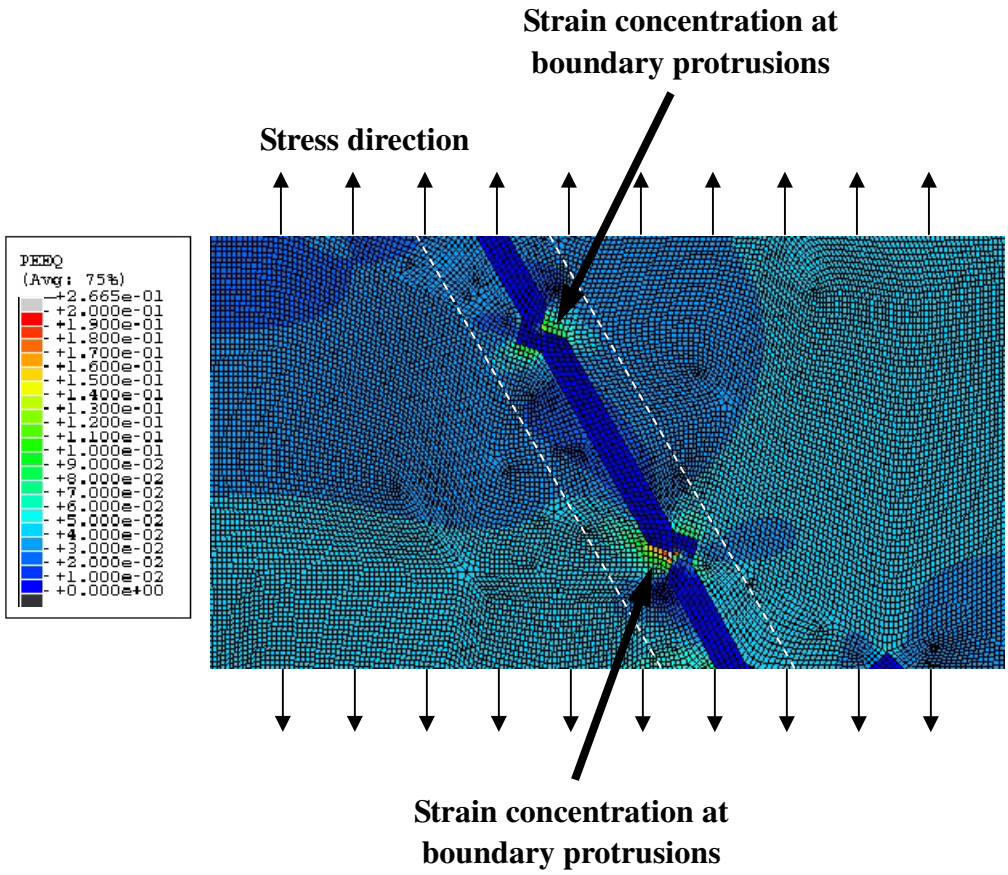

Figure A3.5 Strain map showing strain concentration on the grain boundary perturbations [A3-8].

Reference

[A3-1] Ghosh AK. Mater Sci Forum 1994; 170-172:39.

[A3-2] Ghosh AK. Constitutive Equations, Metalworking: Bulk Forming, ASM Handbook 2005, Vol. 14A, 582.

[A3-3] Hirth JP, Lothe J. Theory of Dislocations, John Wiley & Sons 1982, 697

[A3-4] Romeu D, Beltrán-del-Rio L, Aragón JL, Gómez A. Phys Rev B 1999; 59:5134

[A3-5] Anton Van der Ven, unpublished research, University of Michigan, 2007

[A3-6] Valiev RZ, Islamgaliev RK, Yunusova NF. Mater Sci Forum 2001; 357-359:449

[A3-7] Li X, Ghosh AK. unpublished research, University of Michigan, 2006

[A3-8] Li X, Ghosh AK. unpublished research, University of Michigan, 2006

CHAPTER 3

EFFECT OF SEVERE PLASTIC DEFORMATION ON THIXOMOLDED® AZ91D MG ALLOY

Abstract

Severe plastic deformation is imparted to the thixomolded AZ91D alloy plate by pure compression at 120 ^{o}C and Alternate Biaxial Reverse Corrugation (ABRC) at 300 ^{o}C followed by flattening at 280 ^{o}C [1]. Twinning dominates the deformation process within the "primary" solid particles of thixomolded materials at lower elevated temperature pure compression, but not in the fine grain eutectic structure. Extensive twinning occurs with increasing strain and assists the subdivision of initial coarse "primary" α grain, but the angle between the twinning plane and compression axis increases with increasing strain, as more slip occurs to accommodate plastic flow. The ABRC process produces an ultra-fine grained AZ91D alloy with more efficiency of grain refinement and more homogeneous grain structure. Mechanical properties are also improved by ABRC deformation process.

3.1 Introduction

Light weight magnesium alloys are materials of increasing interest in the auto and aircraft industry [2, 3]. Currently most magnesium alloy parts are produced by casting. Despite alloy additions for increasing strength, casting defects are of concern in terms of mechanical performance, and as a result of these defects, cast Mg alloys have lower ductility and formability compared to wrought alloys. The limited number of slip systems resulting from the HCP structure of Mg causes particularly poor formability and ductility near room temperature. Furthermore, twinning deformation mechanism and strong texture leads to inherent directional properties of Mg that make low-temperature forming of Mg alloys difficult. Although Mg alloys can be readily deformed at elevated temperature (generally above 250^{o}C), oxidation problem may become severe.

Previous investigations demonstrate that grain refinement could improve room-temperature strength and ductility of Mg alloys, and make them deformable at low level of elevated temperature (200-300 ^{o}C) [4, 5]. The severe plastic deformation method (SPD) is an effective method for grain refinement of bulk metal materials [6], as many such processes notably ECAP [7], HPT [8] and ARB [9] have demonstrated previously. Ultra-fine grained structure with grain size less than 1 μm has been achieved by these methods. An alternative SPD method, called Alternate Biaxial Reverse Corrugation (ABRC), has been developed at the University of Michigan [1, 10] to overcome some of the shortcomings for plate or sheet processing, which are not easy with ECAP and HPT methods. This method can be scaled up and incorporated into a continuous, rapid and automated mode. Previous study of Yang on AZ31B Mg alloy [1] demonstrated great

efficiency of this method for grain refinement (grain size of 1.4 μm). The author suggested that twinning deformation assisted in grain subdivision and dynamic recovery at early stage; subgrains develop near grain boundaries and twin boundaries, then new grains may be created by increasing boundary misorientation of subgrains. The results from this study shows that initial coarse bimodal grain structure in the hot-rolled plate was replaced by a nearly fine and uniform grain structure; room-temperature strength and ductility, as well as warm-temperature formability were highly improved. Thus, it is of interest to extend the application of SPD methods to other magnesium alloys, beyond what was studied in [1], especially to alloys such as AZ91D and AM60, which are strengthened by alloying to a higher degree.

AZ91D Mg alloy is a commonly used magnesium alloy for commercial application, and generally available in a cast or molded shape. So far, it is manufactured mostly by die casting and thixomolding. In this work, thixomolded AZ91D was selected as a starting material, because it is readily producible in plate form without large capital cost. Moreover, the thixomolding process can produce a structure with low porosity, isotropic and fine grain (4~5 μm). These features make thixomolded Mg Alloys favorable starting materials to attain sub-micron grain size and low anisotropic Mg alloys sheet. The details of the thixomolding process and equipment have been reported in earlier publications [11]. Compared with other casting methods [12, 13], the thixomolding process provides a different microstructure from those counterparts, including a fine eutectic phase and "primary" solid particles of nearly pure Mg (see Figure 3.1).

The purpose of this work is to examine the applicability of the ABRC process on AZ91D Mg alloy, study the deformability of AZ91D Mg alloys and observe the forming behavior of this material after microstructure evolution during severe plastic deformation. To extend the knowledge of deformation process of thixomolded AZ91D alloy to lower temperature, another method other than ABRC to avoid cracking was conducted by pure compression at 120^{o}C. Twinning characteristics, deformation texture, and annealing behavior were observed.

3.2 Experimental Methods

3.2.1 Material

Thixomolded AZ91D Mg alloy was provided by Thixomat Inc. in the form of 3.25 mm thick plates. The nominal composition was 9.0wt.% Al, 0.75wt.% Zn, 0.3wt% Mn, Fe and Ni below 0.001%. Figure 3.1 shows the microstructure of this material. The bright areas are the "primary" (term used in [14]) α-Mg phases (unmelted). The eutectic consists of dark particles of β-$Mg_{17}Al_{12}$ and fine α-Mg. (details in Figure 3.1 (c)). Most of "primary" (unmelted) α-Mg particles have a few regions that seem to have melted and solidified with eutectic regions. The particle-size analysis (Figure 3.2) shows finer particle sizes near the surface than in the middle with a tighter size distribution. This may be resulted from the flowing condition during injection and the gradient of cooling rate during solidification. Thank to the flexible operation in thixomolding process, the fraction of primary solid is controllable by changing the processing temperature.

3.2.2 Processing

Two severe plastic deformation methods were employed in the present study, (i) pure compression and (ii) alternate biaxial reverse corrugation (ABRC), which are illustrated in Figure 3.3.

a) Pure compression

For this method, three 15mm × 15mm pieces of thixomolded AZ91D alloy were stacked and compressed together at 120 ^{o}C. As shown in Figure 3.3 (a), the punch, die and workpiece are surrounded by a constraining ring equipped with band heaters. A pressurizing medium was used to impart constraint on the workpiece to avoid cracking. The temperature for compression was monitored by locating thermocouples on the positions indicated in Figure 3.3a). A thermocouple at position 2 was used for preexamination only. When the experiment was running, the testing temperature reading was obtained from position 1 and 3. In the present study, the temperature for compression was set to 120 ^{o}C, and the heating system controlled sample temperature to better than ±2 ^{o}C. The duration of heating was 60 minutes from room temperature. The strain rate during compression is approximately $2.0\times10^{-4}s^{-1}$. AZ91D samples with true strain of 0.24, 1.64, 1.96 and 2.37 were prepared.

The static annealing was performed on the deformed samples at 150 ^{o}C and 250 ^{o}C for 30 minutes by embedding in sand bath to study the annealing effects on the microstructure and properties.

b) Alternate biaxial reverse corrugation (ABRC)

The details of the deformation procedure for the ABRC process were previously described in [1]. Hereby, only illustration is presented in Figure 3.3 (b). In the present study, deformation temperature for thixomolded AZ91D was set at 300 ^{o}C. Final flattening of the ABRC processed sheet was made at 280 ^{o}C until a sheet thickness of 1.0 mm was obtained. The cumulative strain was about 4.0. The strain rate during deformation was approximately $5.0\times10^{-4}s^{-1}$.

3.2.3 Microstructure

The microstructural evolution was analyzed by optical microscope (OM). Specimens were sectioned in a plane containing compression axis. Specimens were mounted in self-curing resin, and mechanically polished and finally etched by acetic-picral solution (4.2g picric acid, 70ml ethanol, 10ml acetic acid and 10ml distilled water). Grain or particle size was measured from the micrographs by the area-based method [1]. Figure 3.4 shows the large "primary" particles with twins and a method for measuring the angle between the twinning plane and the compression axis. The twinning plane orientation is represented by this angle. The value of angle is between -90^{o} and +90^{o}. The twin density, number density of twinned particles and particle size distribution of twinned particles were also analyzed for each sample. The value of twin density was obtained by dividing the number of twins over the area of α phase having twins. The value of number density of particles with twins was in terms of the number of particles showing twinning per unit area. For the particle size distribution of twinned particles, the same method as above was used for measurement.

3.2.4 Mechanical tests

a) Microhardness

Vickers hardness was measured with an indentation load of 300g to determine the hardness of processed samples with different processing conditions. The loading time was 30 seconds. The hardness value was obtained by averaging over 10 measurements.

b) Room-temperature uniaxial tensile test

Room-temperature tensile tests were performed on samples with a gauge section of 15 mm long × 3 mm wide (about 1.0 mm thickness). The as-received thixomolded specimen was cut from the middle section along thickness. Tests were conducted in a computer-controlled 5505 Instron machine with constant cross head speed of 0.5 mm/min (initial strain rate of $5.6 \times 10^{-4} s^{-1}$). An extensometer with 12.7 mm gauge length was attached on the gauge section to measure the tensile strain.

c) Elevated-temperature uniaxial and biaxial tension test

For uniaxial tension test, specimens with a dimension of 6.35mm long and 3.175mm wide in gauge section were prepared. Specimens were tested at temperature of $300^{o}C$ and $2\times10^{-4}\ s^{-1}$, $350^{o}C$ and $2\times10^{-3}\ s^{-1}$ in air. To minimize the effect of material flowing from the specimen grip region on constant strain rate during testing, an improved crosshead control schedule [15] was used on a computer-controlled 4505 Instron machine. A graphic interface board (GPIB) was used for digital communication between Instron machine and computer. A clamshell furnace with three independent heating zones was

utilized to maintain specimen temperature within ±2°C of the test temperature. The specimens required about 30 minutes to equilibrate temperature before initiating of straining.

Biaxial forming tests were also conducted by gas pressure forming. A small circular sheet sample was used with the thickness of 0.36 mm and diameter of 24.2 mm. The sample was clamped around its edge and formed using Ar gas pressure of 1379 kPa with a starting temperature of 245°C until it cracked. Before forming, sample is preheated in sand bath for 10 mins to 245°C.

3.2.5 Texture measurement

Crystallographic texture measurement was made on the sheet plane using a Rigaku D/MAX-B rotating anode X-ray diffractometer. The source of X-ray was provided with Cu-Kα radiation at 40 kv and 100 mA. The method of Schulz reflection was employed to the specimen tilting from 15 to 90 degrees. The pole figure was obtained for full (0002) pole by recalculating the raw data with "***POPLA***" software obtained from the Los Alamos National Laboratory.

3.3 Results

3.3.1 Pure compression

After compression at 120 ^{o}C, a significant change in morphology of α-Mg occurred. Figure 3.4 (a) and (b) shows the microstructures of deformed thixomolded AZ91D. It can be seen that the shape of α-Mg gradually changed from originally equiaxed grains into a flat-shape with strain, and the network β phase became faint. With increasing strain, the coarse "primary" α particle was subdivided by twinning and some grains were broken off by shearing.

Twinning was observed within the coarse α grains. Many lens-shaped mechanical twins were formed inside the coarse α phase, mainly in parallel groups. Some twins intersected each other or grain boundaries, which subdivided the coarse grain into smaller areas that benefited subdivision of initial coarse grains. It was also found that the width of the twins increased with strain.

The distribution of twinning plane orientation relative to the compression axis on either side of the axis was analyzed (illustrated in Figure 3.4 (c)). The data were fitted to two separate Gaussian distributions and showed nearly symmetric distribution about the compression axis ($\theta = 0$). The peaks of the distributions occurred at an angle in the range of 36.4°~69.6° for the occurrence of twinning (Figure 3.5). It was found that the peak value of twinning orientation moves away from the compression axis with strain, but the frequency of the most probable twinning angle changes little with increasing strain. Figure 3.6 (a) shows the tendency of the twinning angle to change with strain. It shows

that the average values of the angle between the twinning orientation and compression axis increase with strain, and reach the maximum value when true strain is equal to 1.96. However, the value decreases slightly when the strain is beyond 1.96. This may be caused partly by experimental scatter and partly because of the shearing off of grains with large strain. Observation of sheared-off particles for the twin angle shows that the result can fluctuate with strain. Figure 3.6 (a) also shows twin density *vs*. strain. The twin density (i.e., the number of twins per μm^2) is counted within the "primary" solid region and almost linearly increased with strain. In Figure 3.6(b), it can be seen that the number of "primary" solid particle showing twinning increases linearly with strain, and reaches maximum value also around a strain of 1.96-2.0. Beyond this strain level, the number density of twinned particles changes little with increasing strain. Figure 3.7 plots the size distribution of particles showing twinning. Except the data resulting from low strain, the data with the other three strain levels was fitted to a Gaussian distribution function. At low strain, the twinned particle size has a random distribution (Figure 3.7 (a)). The twinned particle approximately 30 μm in size shows the highest frequency among the whole size range, which is consistent with the particle size distribution of as-received thixomolded sample. With increasing strain (Figure 3.7 (b)-(d)), the peak value in terms of mean particle size tends to decrease, while the frequency of peak value tends to increase. This result indicates that twinning only occurred within coarse particles at low strain, and the smaller particles become subjected to twinning with increasing strain. The postulation that subdivision of coarse particle is assisted by shearing during deformation is also supported by this result due to the disappearing of large particles.

Static annealing was conducted for deformed samples with true strain of 2.37 at 150^{o}C and 250^{o}C for 30 minutes to study the annealing effect on microstructure and properties of the deformed thixomolded AZ91D Mg alloy. Then, the Vickers hardness of the primary solid α phase and the eutectic phase were each measured. The microhardness of as-thixomolded and as-deformed samples were also measured for comparison. All values of hardness are listed in Table 3.2 and plotted in Figure 3.8. It can be seen that the as-thixomolded sample has the lowest hardness of 627.2 MPa and 772.2 MPa for the primary solid α phase and eutectic phase. After being deformed, the values were respectively increased to 828.1 MPa and 932.0 MPa. It was found furthermore that the hardness was increased further to 958 MPa in the eutectic region after annealing at 150^{o}C. However, the hardness was decreased when the deformed sample was annealed at 250^{o}C. Figure 3.9 shows the micrographs of thixomolded AZ91D alloy after pure compression at 120 ^{o}C with true strain of 2.37 plus annealing at 150^{o}C and 250^{o}C for 30 minutes each. It is obvious that twins still existed in some primary α grains after annealing at 150^{o}C for 30 minutes, and the sample shows slight recovery. By increasing the annealing temperature to 250^{o}C, recrystallized structures formed within the original coarse α grains, which were subdivided into equiaxed finer gains. Moreover, the volume of β phase was clearly reduced.

3.3.2 ABRC processing

The thixomolded AZ91D alloy was treated by imparting 8 steps of sinewave pressing at 300 ^{o}C, and subsequently flattened at 280 ^{o}C to a thickness of about 1.0 mm. Figure 3.10

shows the microstructure of thixomolded AZ91D after ABRC processing and grain size distribution. As can be seen in the Figure 3.10 (a), some "primary" solid particles still exist with elongated shape, within which no twin is visible. Magnification of the eutectic region showed (Figure 3.10 (b)) that the original $\alpha + \beta$ eutectic thixomolded structure was transformed into a continuously distributed equiaxed fine gain structure. Many fine particle-like grains seen in the image are believed to be β phase, suggesting that breakup of the β phase is more complete after sinwave processing. The average grain size of ultrafine grains can reach 0.8 μm. The grain structure exhibits relative homogenous size distribution. The overall planar area fraction of "primary" solid was reduced to 8.2% (Figure 3.10 (c)).

In the Figure 3.11 (a), the relationship between Vickers hardness and the inverse square root of grain size is plotted. After ABRC processing, thixomolded AZ91D samples without "primary" solid phase show clearly higher hardness than the AZ31B alloys [16, 17] with the same grain size level, which can be attributed to the presence of ultra-fine β particles in the Al-rich AZ91D alloy. Figure 3.11 (b) and Table 3.1 present the room-temperature uniaxial tensile test results. The room-temperature mechanical properties of thixomolded AZ91D were significantly improved by ABRC processing. The 0.2% yield stress was increased from 180 MPa to 285 MPa, and the ultimate tensile strength from 215 MPa to 332 MPa. The ductility at room temperature was also improved. The fracture strain was increased from 0.038 to 0.091. The dimple morphology of fracture surface (Figure 3.12) of the tensile tested sample indicates the improved ductility of ABRC-processed structure. Additionally, compared with the data from other research [14],

ABRC-processed AZ91D alloy also shows significant increase in tensile strength of about 90 MPa (Figure 3.11.(c)). However, because of the existence of coarse "primary" α Mg, the mechanical properties of ABRC-processed thixomolded AZ91D are limited.

The elevated-temperature stress-strain curves of ABRC-processed AZ91D alloy are shown in Figure 3.13. To evaluate the effect of deformation history on the stress-strain response, three sets of stress-strain curves representing different processing condition are plotted together, including the as-received materials (thixomolded), 1-pass ABRC-processed materials and 2-pass ABRC-processed materials. It should be mentioned that one pass ABRC processing consists of four sequent sinwave pressing; and 90 degrees rotation was implemented between two adjacent pressings. As can be seen, 1-pass processing has a little effect on the stress-strain behavior of thixomolded AZ91D compared with as-received counterpart. 1-pass ABRC processed AZ91D samples have lower yielding stress and more pronounced strain hardening than as-received materials. However, the elongation to failure changes little (listed in Table 3.3). With more deformation processing for 2-pass processing, the elongation to failure were remarkably improved from 112% to 172% for test at 300^{o}C and 2×10^{-4} s^{-1}; and strain hardening tends to increase. It is believed that increasing deformation processing reduces the fraction of large primary α particles, and increases the uniformity of grain structure.

The biaxial tension test results (Figure 3.14) show that, the as-thixomolded AZ91D sample fractured prematurely. By contrast, the ABRC-processed counterpart shows superplasticity, and a smooth surface after forming. The dome height of the gas-pressure

formed sample increased from 1.7 mm to 4.4 mm. Observation on fracture surfaces of deformed samples (Figure 3.15) reveals that ABRC-processed material has more homogeneous structure than thixomolded material. As can be seen on Figure 3.15 (a), many large α primary particles distribute along the fracture surface. It can be suggested that the fracture was nucleated from the interface between the large α primary particle and fine-grained region, because of strain incompatibility between these two phases. ABRC processing reduces the fraction of large α primary particles, consequently reduces the tendency of strain incompatibility within the grain structure, and improves the formability of thixomolded AZ91D alloy.

3.3.3 Texture evolution

To investigate orientation change due to different processing conditions, full pole figures for the basal (0002) crystallographic plane of thixomolded AZ91D after deformation were analyzed. For the as-thixomolded materials (shown in Figure 3.16 (a)), a relatively random texture existed in the plate. Under pure compression, the texture evolved into a basal texture with increasing strain, and the intensity of the (0002) pole was strengthened with strain as shown in the center of the pole figure. When the true strain was increased up to 2.37 (Figure 3.16 (b)), the basal pole was split into two poles around the center symmetrically. The maximum intensity of the basal pole in the deformed sample is 4.86 times of that of random. Compared with pure compression, the ABRC-processed sample has a similar orientation preference (Figure 3.16 (c)). The initial random texture evolved into a basal texture, which shows two split poles around the center. However, the pole

intensity is 3.48 times of that of a random sample, and is lower than that for the pure compression sample, despite higher strain in the sample.

3.4 Discussions

3.4.1 Pure compression

Earlier investigations of the single or polycrystalline magnesium have suggested that basal slip, $\{10\bar{1}2\}$ twinning and $\{10\bar{1}1\}$ banding, consisting of $\{10\bar{1}1\}$ twinning followed by $\{10\bar{1}2\}$ retwinning and basal slip within the doubly twinned band, are deformation mechanisms from room temperature to 307 ^{o}C [18]. At the beginning stage of deformation, twinning takes place within those grains unfavorably oriented for basal slip. Kocks and Westlake have noted that stress concentration at grain boundary resulting from incompatible plastic strain can be relieved by twinning [19]. Moreover, large strain for arbitrary shape change can be accommodated through the double-twinning mechanism. However, the reported maximum compression strain on single crystal magnesium before fracture at 116 ^{o}C is for a true strain of 0.4. To accommodate higher strain level up to a true strain of 2, other slip systems may be activated when basal slip is suppressed. The investigation of Obara et al. on magnesium showed the activities of (a+c) slip occurred from room temperature to 500 ^{o}C [20]. Yoo also emphasized the importance of this type of slip in deformation of polycrystals [21]. Moreover, it has been postulated that stress concentration produced by the intersection of various non-basal slip systems may be necessary for the activation of double-twin mode [18, 22], since those orientations most favorable for non-basal slip exhibited the lowest shear stress to activate

$\{10\bar{1}1\}$ twinning [23]. In the present case, this slip system, which accommodates the expansion or contraction along c-axis, should be included beyond basal slip to accommodate the large strain under severe plastic deformation. Also, Figure 3.6 (a) shows twin density in "primary" solid grains progressively increases with strain; and Figure 3.7 reveals that the peak value in terms of mean size of twinned particle tends to decrease, while the frequency of peak value tends to increase. These indicate that new twins are continually generated as stress increases to initiate twinning in the smaller particles. These results reveal that twinning is grain size dependent.

An important observation is that the twin angle distribution changes with strain, and average twin angle tended to increase with strain. This finding indicates the rotation of twins with further compression. This characteristic also has been observed by other investigators [18, 24]. It is believed that slip occurring between the twinned areas is responsible for this effect. As shown in Figure 3.17, extensive dislocation plasticity can take place within a volume bounded by twins. With further compression, the dynamic recovery and cross-slip of a-type dislocation near the twin boundary where high density of dislocation develops may cause the migration of twin boundaries, which results in the increasing width of twins and the rotation of twins. Furthermore, within the inter-twin region, where basal slip is suppressed, a non-basal slip system may be activated under high stress concentration to accommodate the contraction deformation. At the same time, slipping activity causes the tilting of twins away from the compression axis. As stress increases, the unloading of stress along the twin/matrix interface causes the shearing and break-off of the initial coarse grain.

Twinned particles initially of size about 30 μm show the highest frequency of twins among the whole size range, which is consistent with the particle size distribution of the as-thixomolded sample. With increasing strain, the peak value in terms of mean particle size tends to decrease. It seems that twinning occurs within coarse particles at low strain, and the smaller particles became subjected to twinning with increasing strain. Subdivision of coarse particles occurs by shearing during deformation and this was also observed in particle size distribution (Figure 3.7). This process causes the disappearance of initial coarse grains. Compared with shear stress for slip, the twinning stress has a larger dependence on grain size [16]. The reduction of grain size inhibits twinning [1], and increases slip to accommodate the plastic deformation because of the increasing shear stress for twinning and more grain boundary activity.

3.4.2 ABRC processing

It is believed that improved room-temperature and elevated-temperature mechanical properties are resulted from grain refinement and homogenous grain structure. In the fine grain alloy, dislocation activity primarily accommodates plastic deformation, and the finer structure (i.e., smaller obstacle spacing) and increasing fraction of grain (or phase) boundaries significantly increase yield strength [1]. Moreover, for the thixomolded AZ91D alloy, solute segregation exists. A compositional gradient of Al, from the Al-rich interface between α and β phases to the almost Al-free center of α Mg, develops. Zinc within the materials has a similar distribution to that of Al [14]. After high temperature ABRC processing, a considerable amount of diffusion occurs and reduces segregation.

This also helps to reduce the size of the coarse α phase particles, while it may also contain precipitates from enriched Al and Zn. These effects can strengthen the alloy further without loss of ductility, as shown in Figure 3.11 (b) and (c). Continuous distributions of α Mg with the β phase as strengthening second phase dominate the microstructure. Both the α and β phases are refined to submicron level, which inhibits the twinning tendency and encourages the grain boundary dominated deformation process. Moreover, the fraction of the large primary α particles was greatly reduced by deformation processing at elevated temperature, which reduces the strain incompatibility between coarse grain and fine-grained region within the grain structure. Grain boundary structures required for superplasticity consequently develop within the materials, which improve the elevated-temperature formability, tend to lower the forming temperature and increase the strain rate. Also, both the improved uniformity of grain structure and low texture by ABRC processing are favorable to improve formability (see Figure 3.14).

3.4.3 Texture evolution

For Mg alloy, it is believed that basal slip and mechanical twinning dominate the deformation process at low temperature deformation (below 200 ^{o}C) [18, 26]. The fact that the basal texture developed in the sheet plane and its intensity increased with strain has been attributed to the activity of basal slip (as shown in Figure 3.16) [27]. To accommodate the deformation compatibility with neighboring grains for severe strain, a non-basal slip system (a+c) may be activated by stress concentration near grain boundaries [26, 28]. It was found that the operation of the (a+c) slip system is responsible

for the tilting of the basal pole away from the normal direction (as shown in the Figure 3.16 (b)) [29]. Because of the thermal sensitivity of the (a+c) slip mode, this slip mode becomes easier with increasing temperature in the sample processed by ABRC method (300 ^{o}C), showing more pronounced tilting of the basal pole than that of pure compression at 120 ^{o}C. Moreover, as the grain size becomes finer by ABRC processing, the operation of grain boundary sliding or shearing becomes easier such that the large plastic deformation of the sample can be accommodated by slip near grain boundaries. Grain rotation and possible dynamic recrystallization can help reduce the intensity of basal texture [1].

3.5 Conclusions

The severe plastic deformation of thixomolded AZ91D Mg alloy was studied in this work by pure compression and ABRC process followed by flattening. It was found that,

1) Twinning process dominated the deformation process under pure compression at lower elevated temperature, and caused shearing off of the coarse "primary" solid α grains to cause their subdivision.
2) Extensive twinning occurs with increasing strain, but the angle between the twinning plane and compression axis increases with increasing strain, as more slip occurs to accommodate plastic flow in the inter-twin region. This caused rotation of twin planes --- an effect that is generally overlooked.
3) With increasing strain, basal texture was developed and it strengthened in a direction normal to sheet plane.

4) After ABRC-processing, ultra-fine grained structure was created from the thixomolded materials with average grain size of 0.8 μm (in the eutectic region), and the uniformity of grain structure is improved. Initial brittle cast structure was significantly refined to fine continuous distribution of α Mg with the β phase as strengthening second phase.

5) Grain refinement significantly improved the room-temperature mechanical properties and elevated-temperature formability (250 ~ 350^{o}C) of thixomolded AZ91D alloy.

6) Basal texture is developed in a direction normal to sheet plane, but its intensity is lower than that for compressed sample at 120 ^{o}C in spite of higher processing strain. Compared with low temperature pure compression, increasing the processing temperature from 120 ^{o}C to 300^{o}C improves the structural uniformity.

Table 3.1 Mechanical Property of Test Materials

Properties / *Materials*	*Yield Strength*	*Ultimate Tensile Strength*	*Elongation*	*Fracture Strain*
Thixomolded	180 MPa	215 MPa	2.4 %	0.038
ABRC-processed	285 MPa	332 MPa	5.5 %	0.091

Table 3.2 Microhardness of thixomolded AZ91D at different processing step

region / processed state	primary solid region MPa	eutectic region MPa
as-thixomolded	627.2±34.3	772.2±25.5
as-deformed	828.1±13.7	932.0±17.6
as-annealed (150 °C/30 mins)	843.8±14.7	958.4±14.7
as-annealed (250 °C/30 mins)	771.3±34.3	858.5±11.8

Table 3.3 Elongation to failure of thixomolded AZ91D with different processing conditions

Materials/Processing		Temperature, ˚C	Strain rate, s^{-1}	Elongation to failure, %
As-received	Thixomolded	300	2×10^{-4}	112
		350	2×10^{-3}	65
As-processed	1-pass processing	300	2×10^{-4}	116
		350	2×10^{-3}	55
	2-pass processing	300	2×10^{-4}	172
		350	2×10^{-3}	87

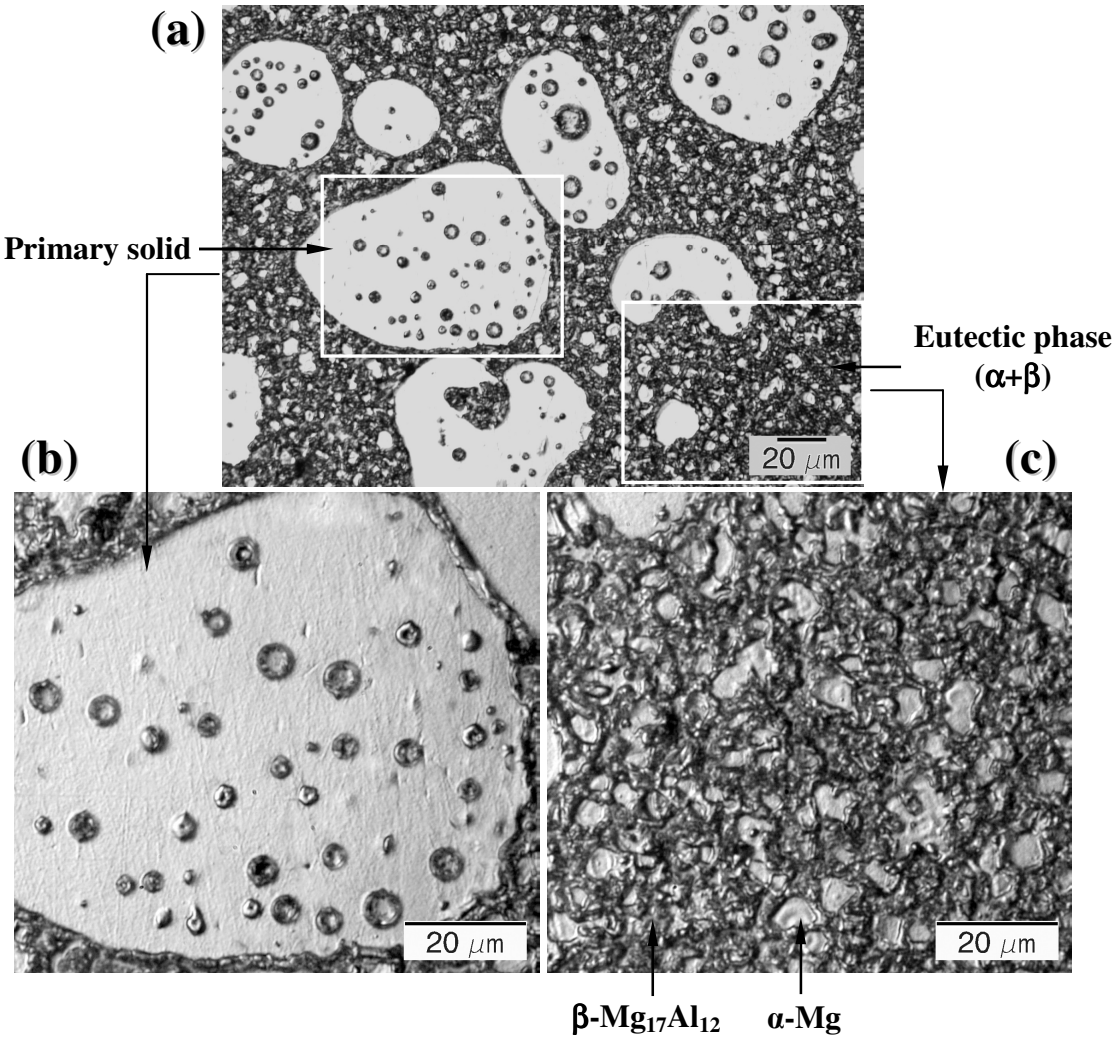

Figure 3.1 Thixomolded microstructure of AZ91D alloy (a) showing primary solid phase (b) and eutectic phase (c).

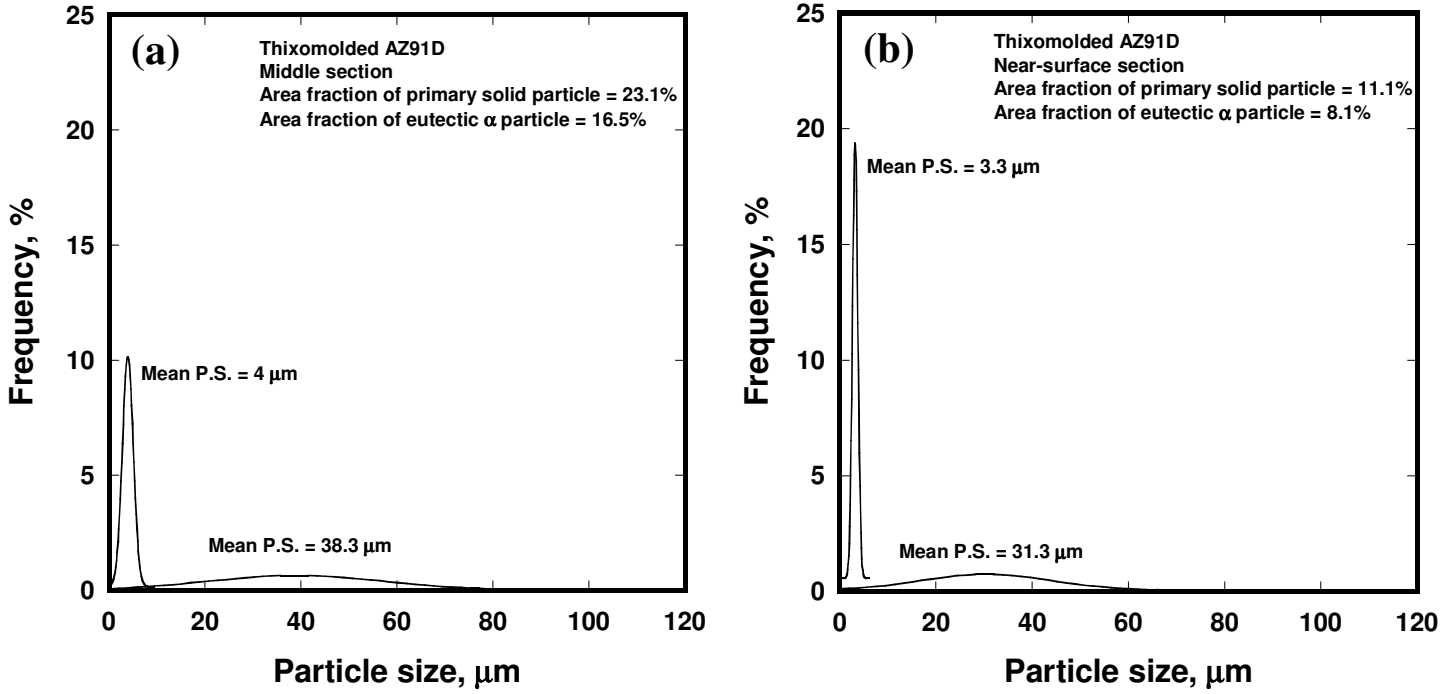

Figure 3.2 Particle size distribution of α particles of thixomolded AZ91D Mg alloy, (a) middle section, (b) near-surface section

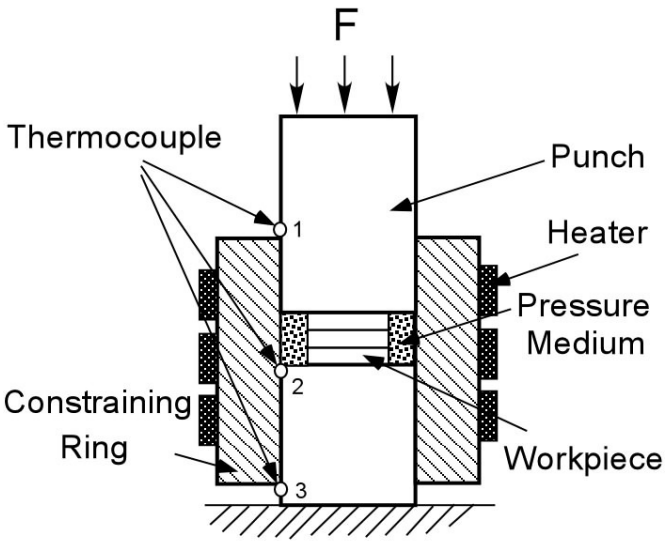

(a)

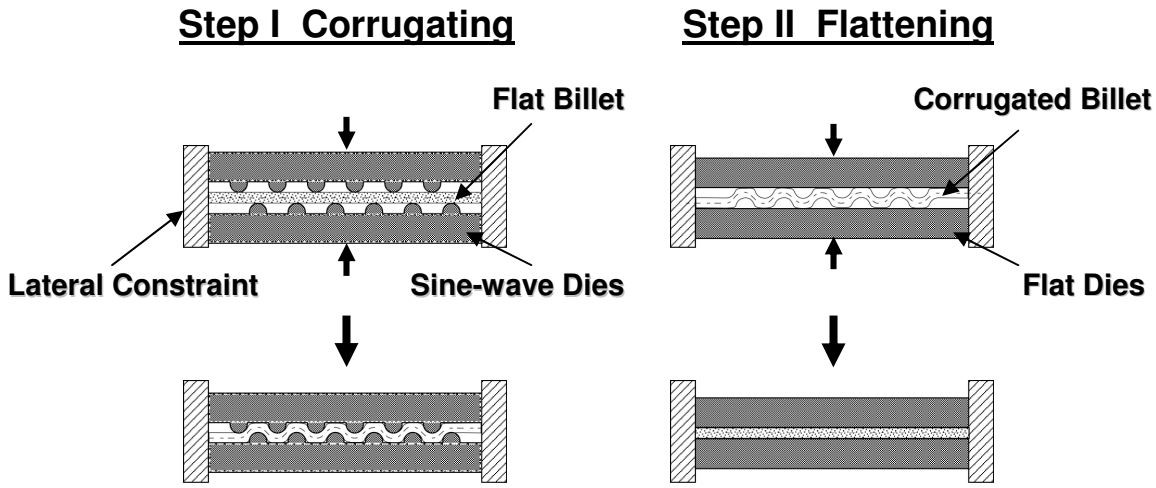

(b)

Figure 3.3 Illustrations of processing methods for thixomolded AZ91D alloy at elevated temperature: a) Pure compression, b) Alternate Biaxial Reverse Corrugation (ABRC).

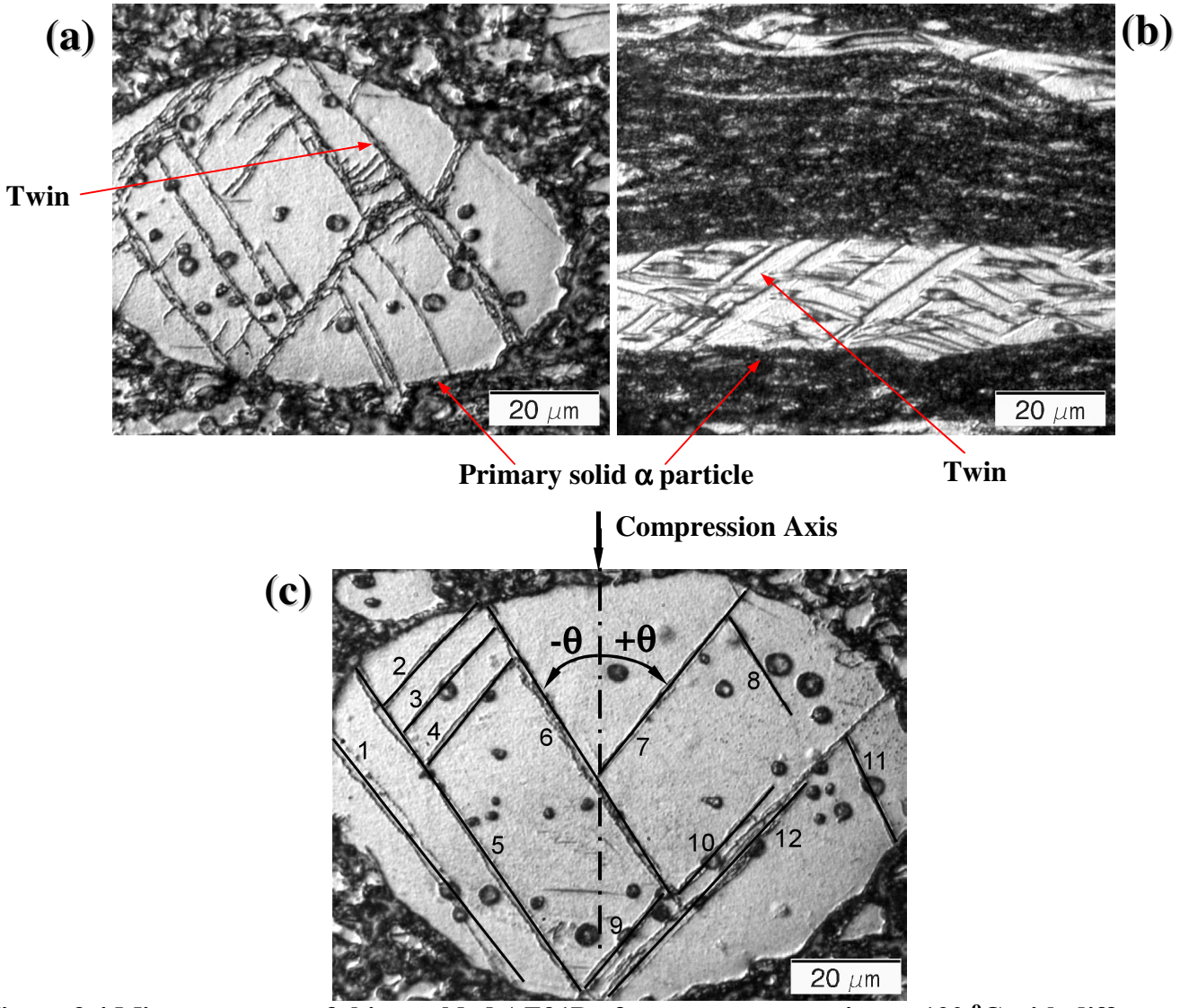

Figure 3.4 Microstructure of thixomolded AZ91D after pure compression at 120 ^{o}C with different strain level (Primary solid particle) (a) $\varepsilon = 0.24$, (b) $\varepsilon = 2.37$, and (c) shows the method for measuring the angle between twinning plane and compression axis.

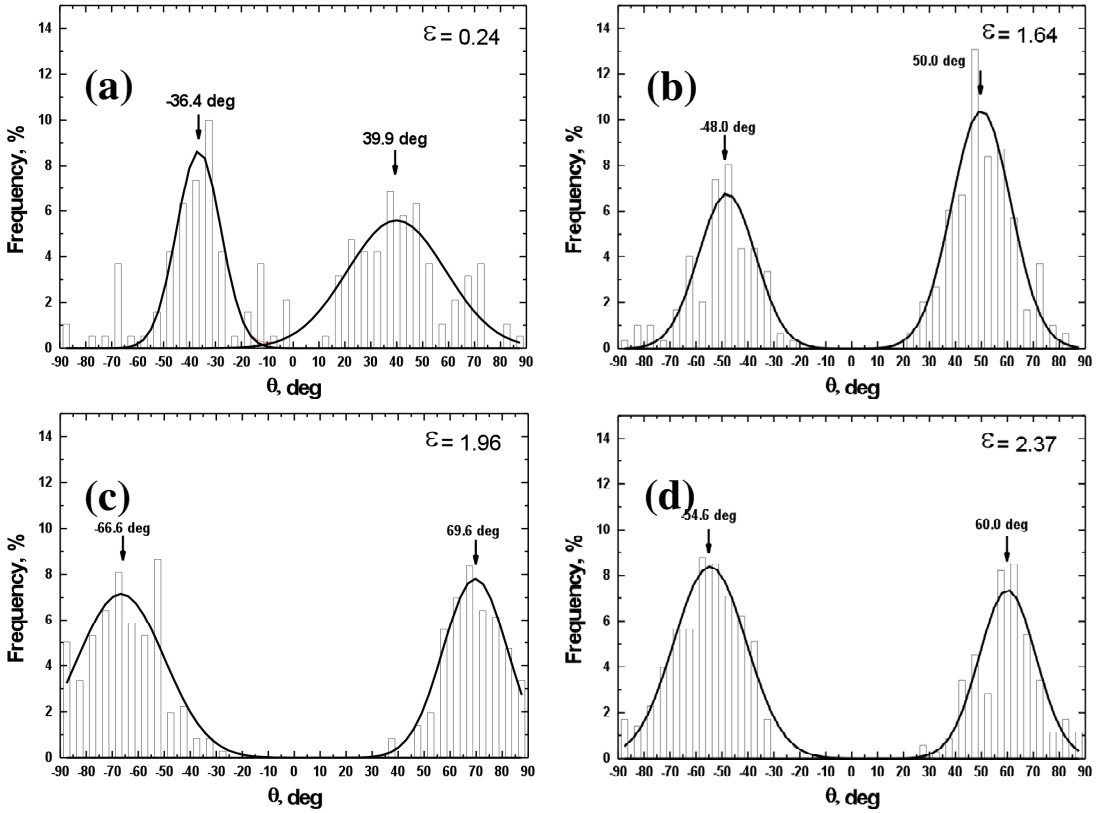

Figure 3.5 Distributions of angles between the twinning plane and compression axis in thixomolded AZ91D after pure compression at 120 ^{o}C with various strain level, (a) ε = 0.24, (b) ε = 1.64, (c) ε = 1.96, (d) ε = 2.37

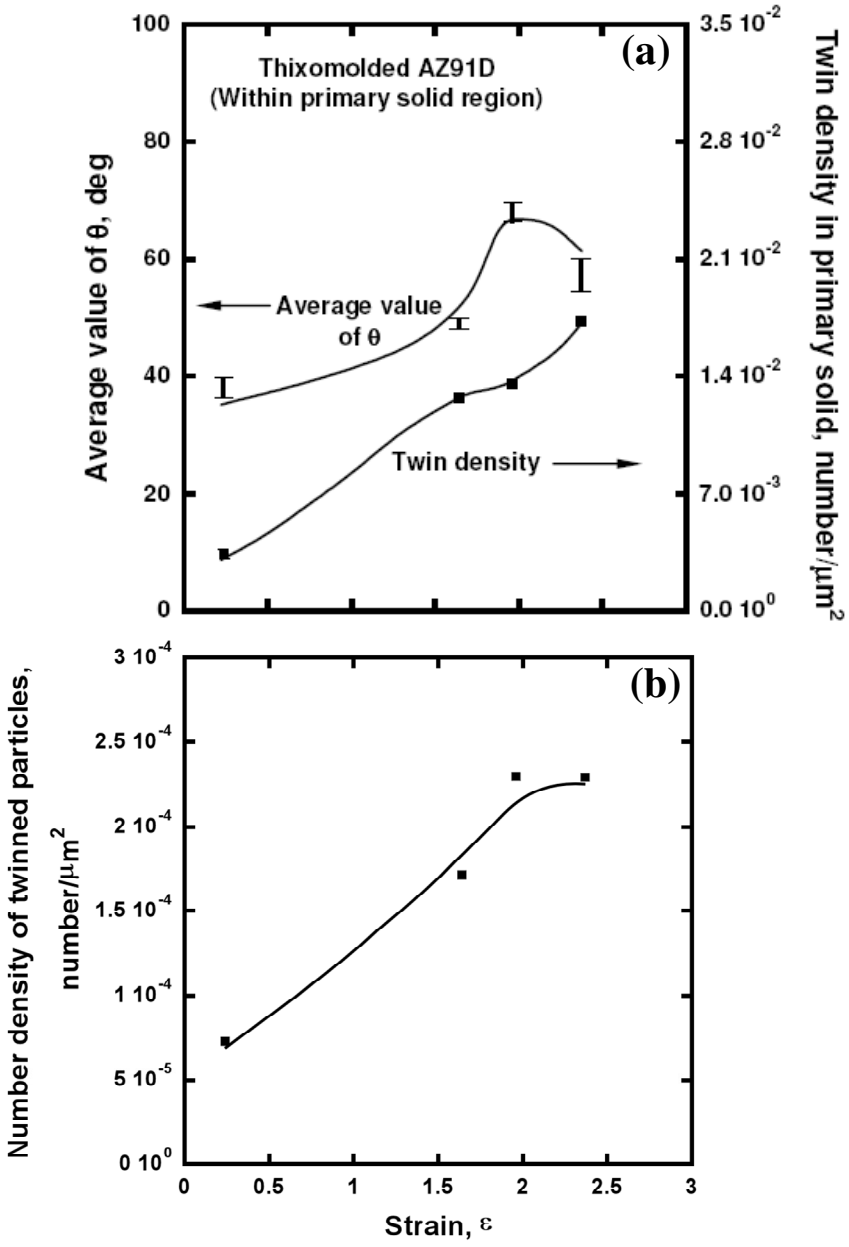

Figure 3.6 Twinning characteristics, (a) the average values of angle between the twinning plane and compression axis and twin density in primary solid α particles vs. strain of thixomolded AZ91D after pure compression at 120 °C, (b) the number density of particles with twin (number/μm^2) vs. strain of thixomolded AZ91D after pure compression at 120°C.

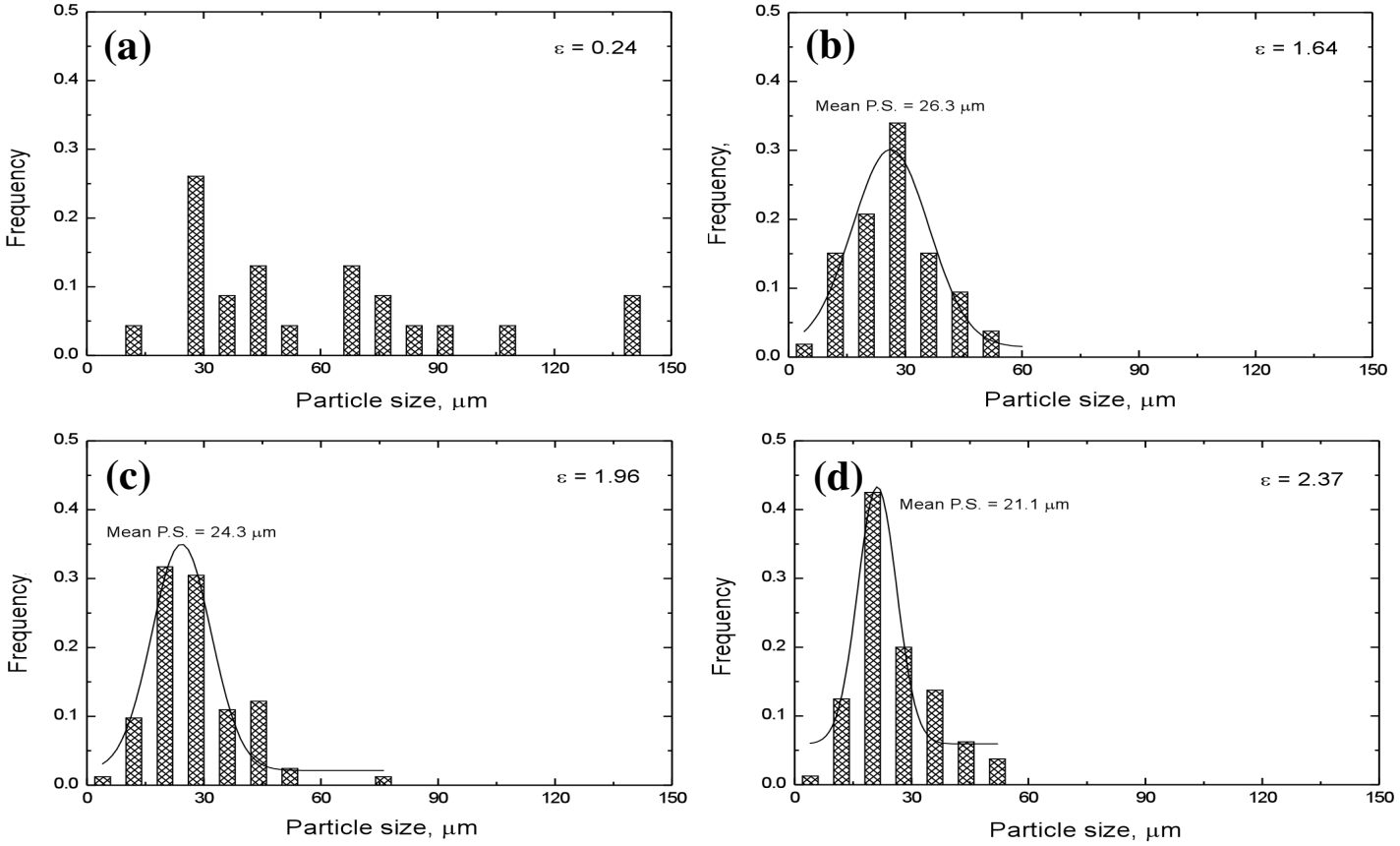

Figure 3.7 Size distributions of primary solid particles that are twinned in the thixomolded AZ91D after pure compression at 120^{o}C vary with strains.

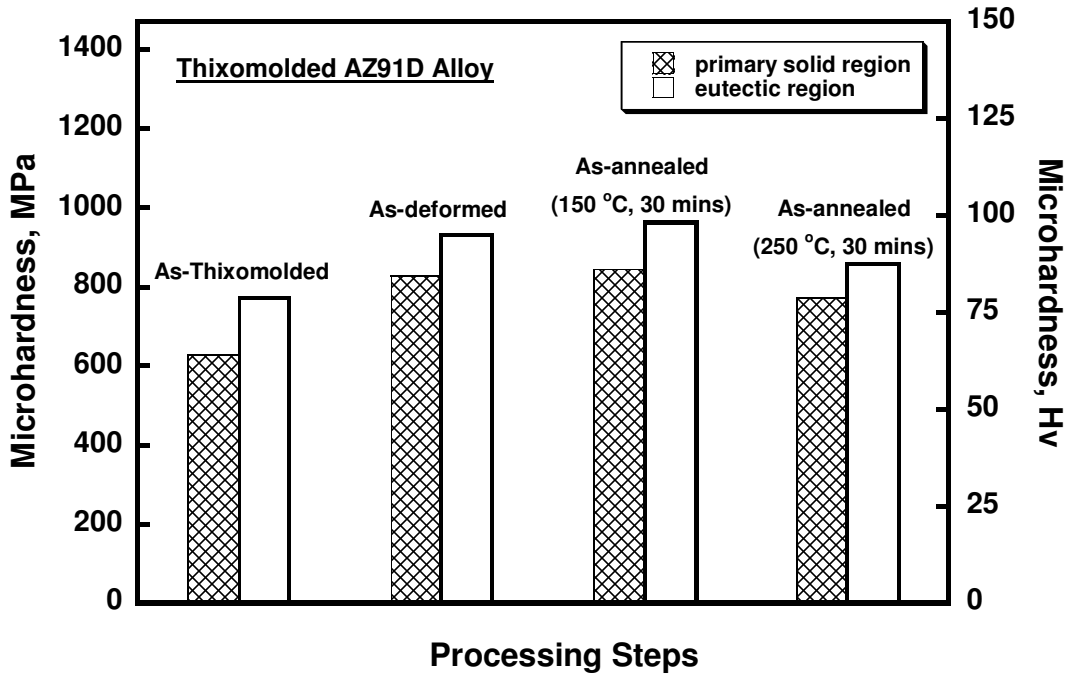

Figure 3.8 Variation of microhardness of the AZ91D alloy at different processing step.

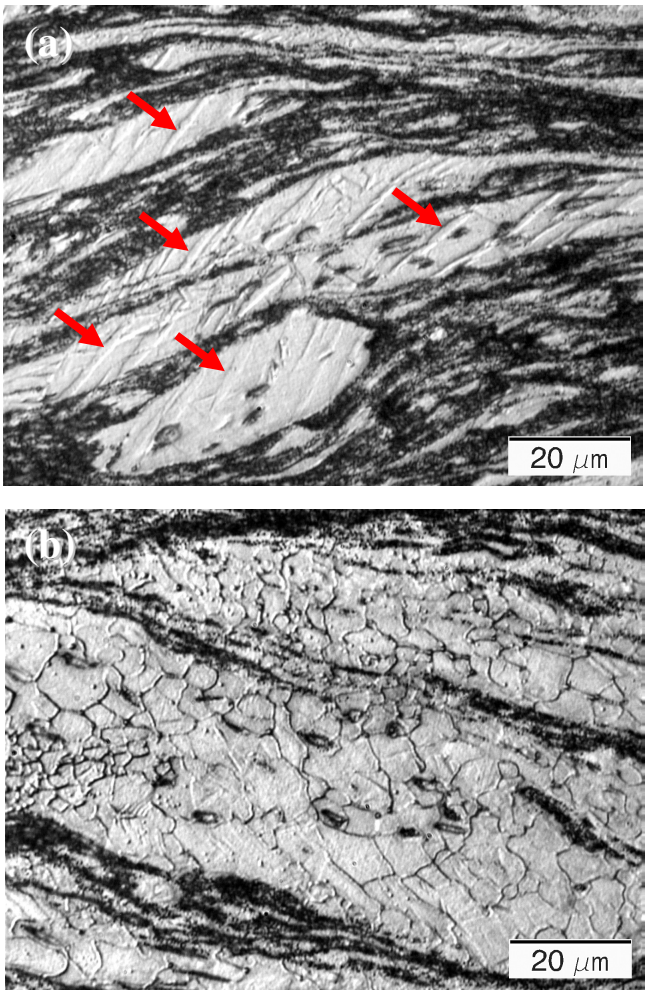

Figure 3.9 Microstructure of thixomolded AZ91D after pure compression at 120°C with strain of 2.37 and annealing at (a) 150°C and (b) 250°C

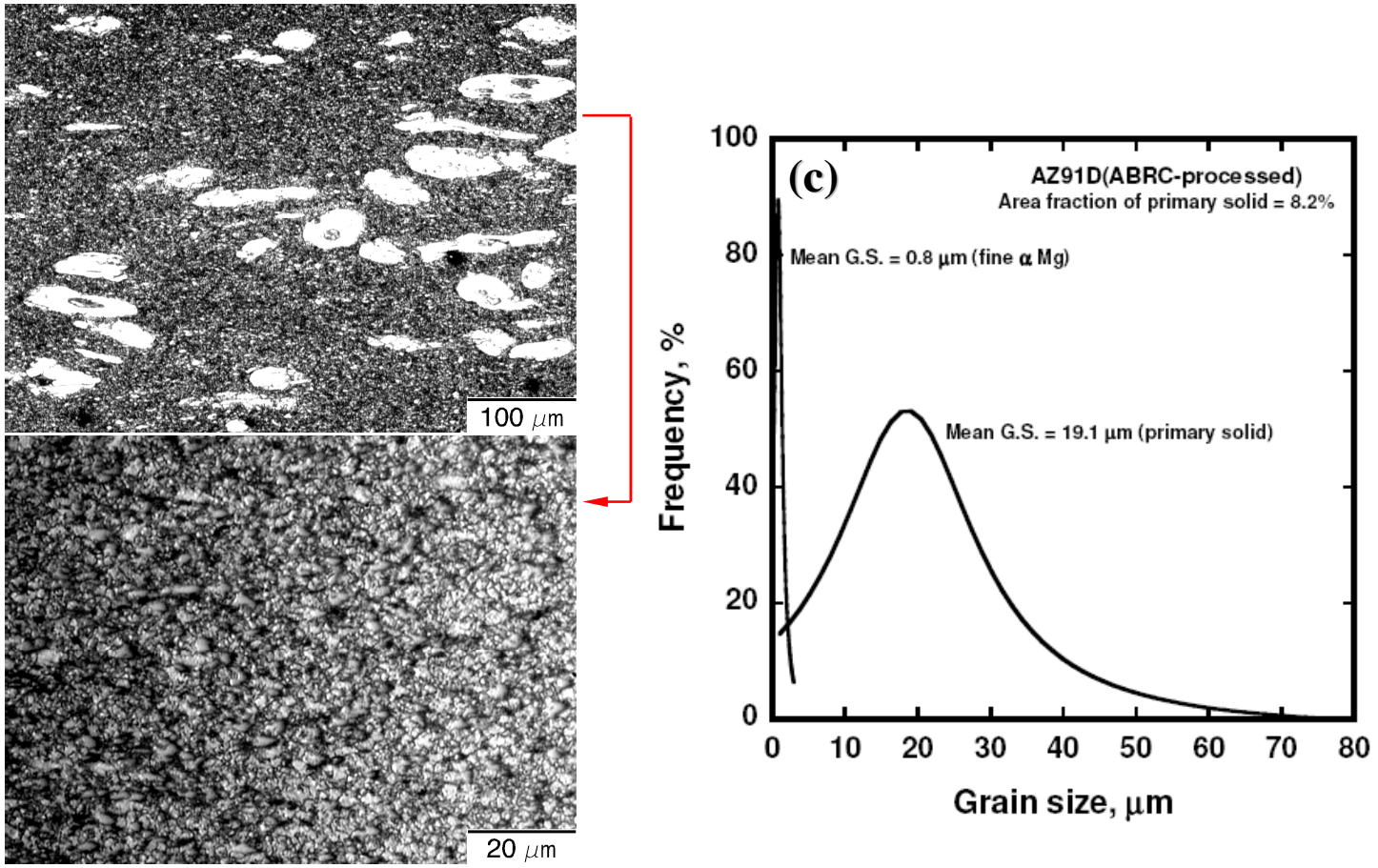

Figure 3.10 Microstructure of thixomolded AZ91D alloy after ABRC processing with true strain 4.13 and grain size distribution (a) low magnification showing original primary solid phase and eutectic phase, (b) fine grain region, (c) grain size distribution

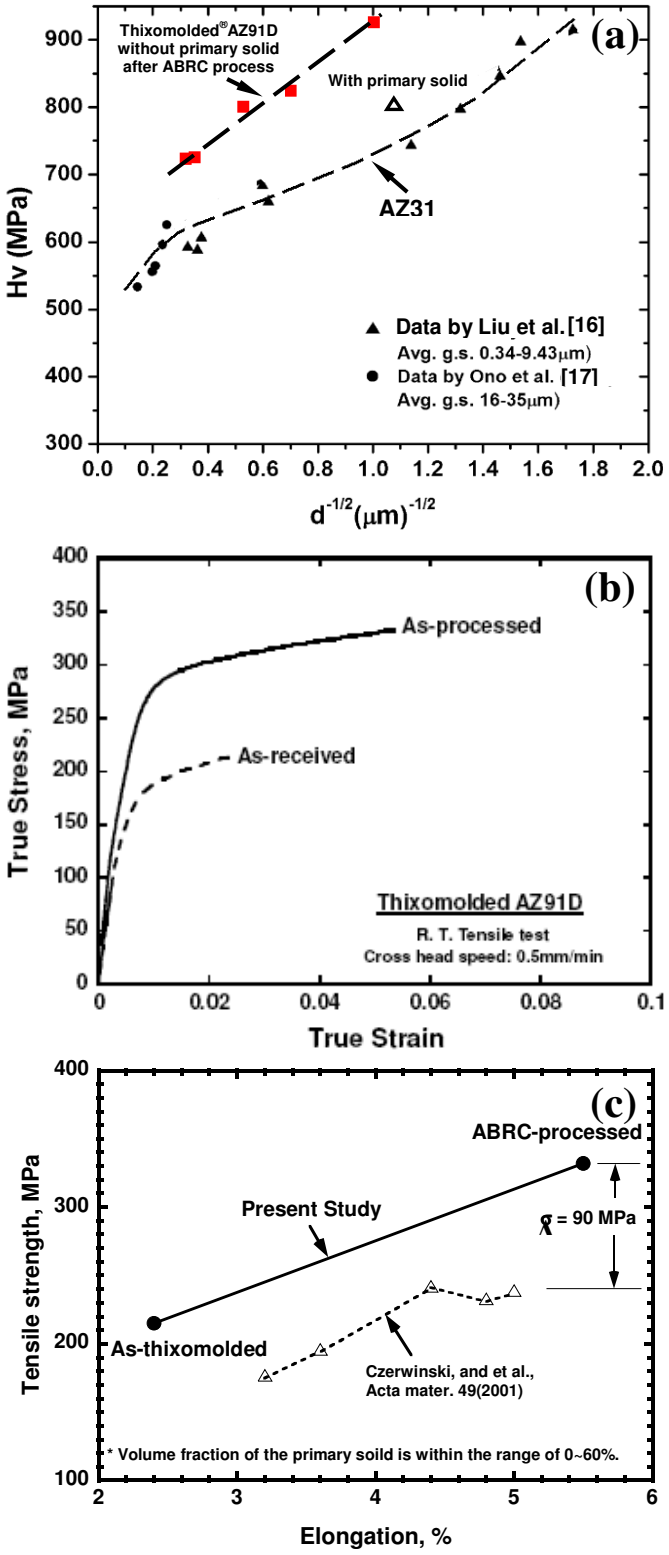

Figure 3.11 Room-temperature mechanical properties of thxiomolded and ABRC-processed AZ91D alloys, (a) the relationship of Vickers hardness vs. grain size, (b) room-temperature tensile stress versus strain curve, and (c) tensile strength vs elongation.

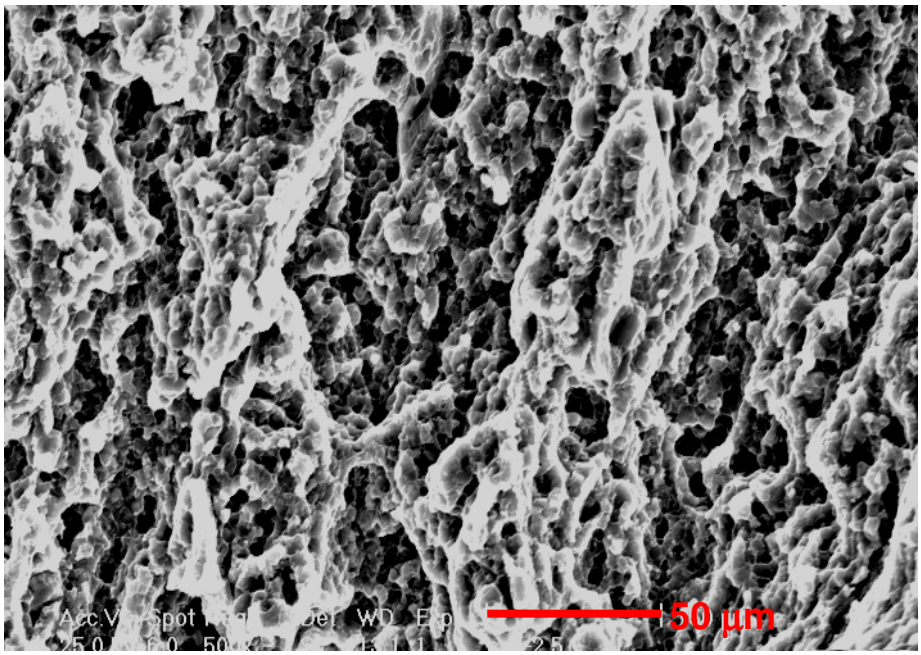

Figure 3.12 SEM image of fracture surface of ABRC-processed thixomolded AZ91D after room-temperature tensile test.

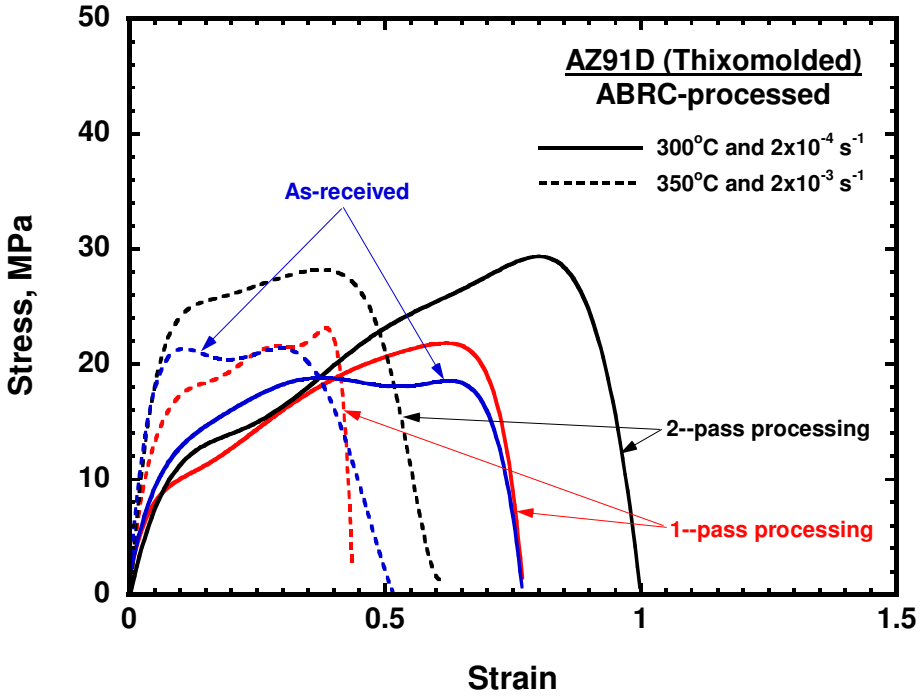

Figure 3.13 Stress-strain curves of thixomolded AZ91D with different processing condition

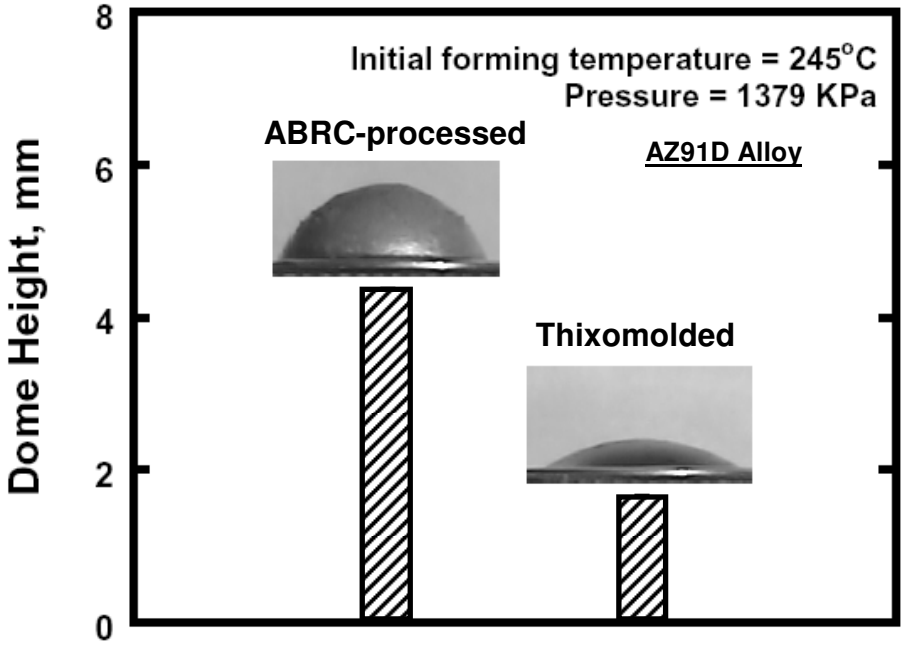

Figure 3.14 Dome height of ABRC-processed thixomolded AZ91D alloy and as-thixomolded material after gas pressure forming, showing that as-received alloy fractures prematurely under biaxial tension while as-processed material of fine grain structure shows improved biaxial formability.

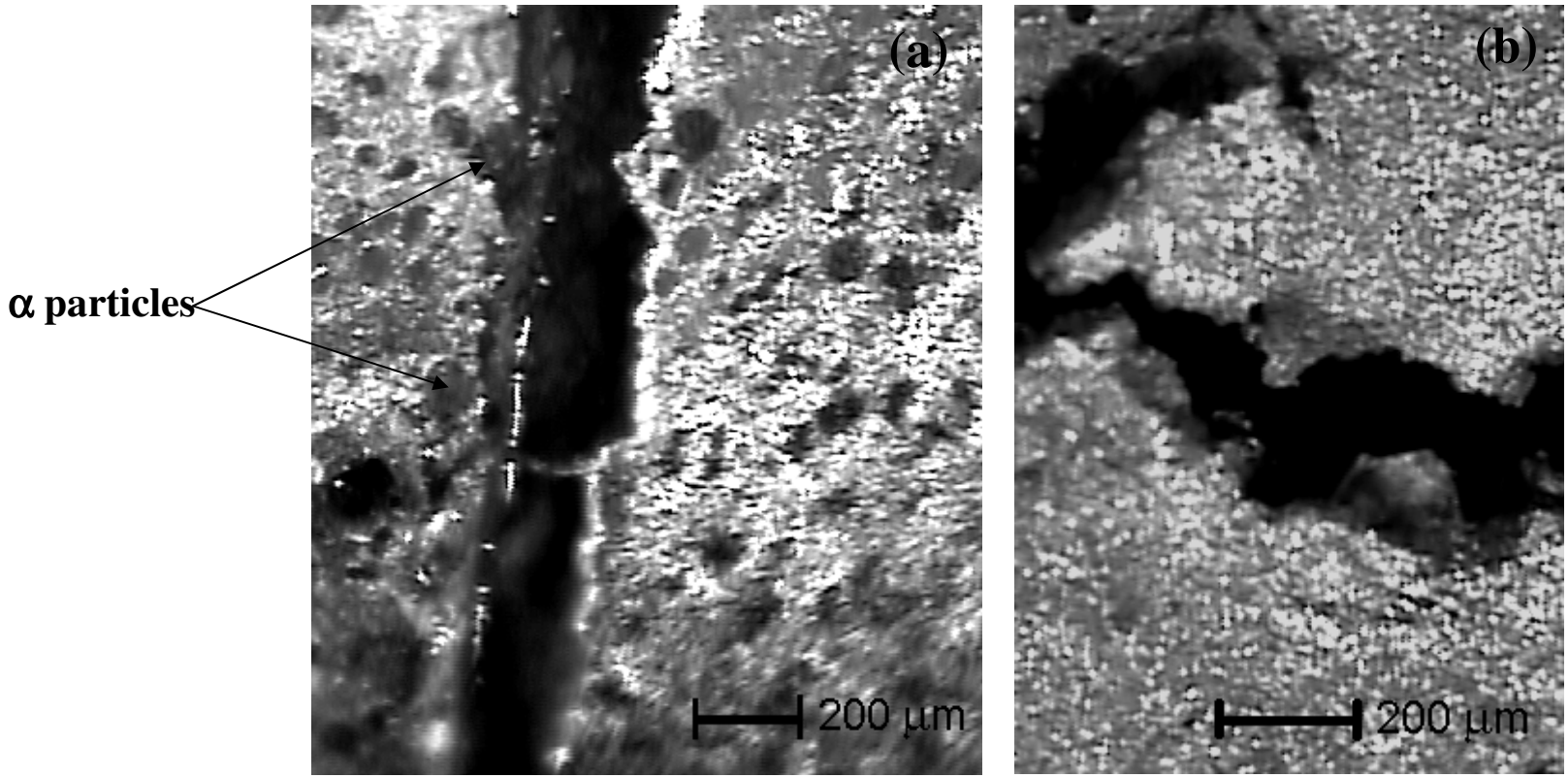

Figure 3.15 Observation of fracture surfaces of biaxially deformed samples shows that ABRC-processed material has more homogeneous structure (a) as-thixomolded, (b) ABRC-processed

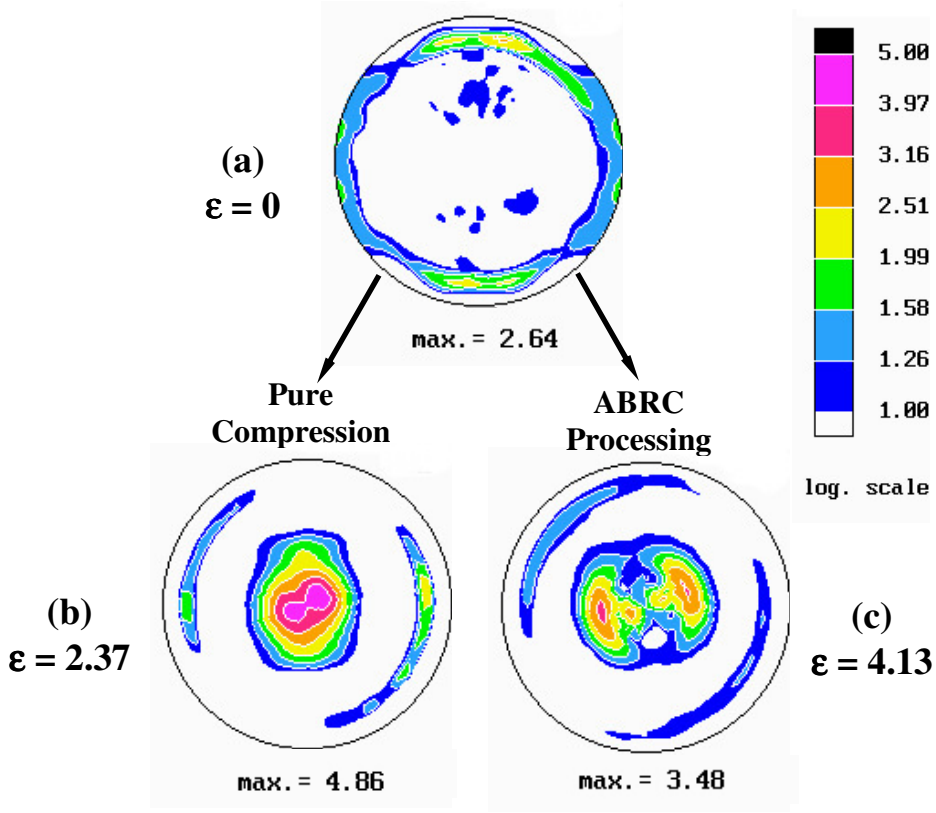

Figure 3.16 Pole figures for (0002) crystallographic plane of (a) as-thixomolded AZ91D, (b) after pure compression and (c) after ABRC processing

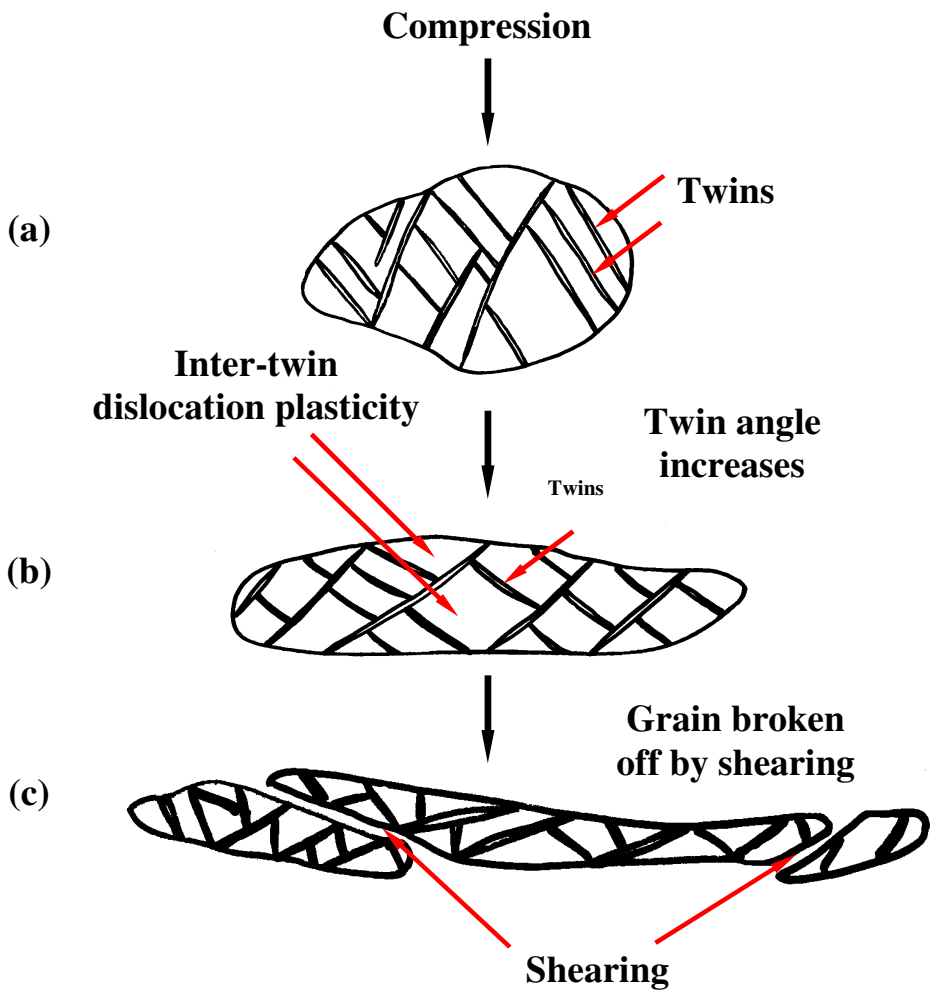

Figure 3.17 Sketch of subdivison of initial coarse primary solid grain.
(a) Twinning at low strain level, (b) Slip within inter-twin region at medium strain level and (c) Shearing off with high strain level

3.6 References

[1] Yang Q, Ghosh AK. Acta Mater 2006; 54:5147.

[2] Cole GS. Mater Sci Forum 2003; 419-422:43.

[3] Furuya H, Matunaga S, Kogizo N. Mater Sci Forum 2003; 419-422:261.

[4] Valiev RZ, Krasilnikov NA, Tsenev NK. Mater Sci Eng A 1991; 137:35.

[5] Kubota K, Mabuchi M, Higashi K. J Mater Sci 1999; 34:2255.

[6] Lowe TC, Valiev RZ. J Mater 2004; 56:64.

[7] Mabuchi M, Ameyama K, Iwasaki H, Higashi K. Acta Mater 1999; 47:2047.

[8] Galiyev A, Kaibysgev R. Mater Trans 2001; 42:1190.

[9] Pérez-Prado MT, del Valle JA, Ruano OA. Scripta Mater 2004; 51:1093.

[10] Yang Q, Ghosh AK. Acta Mater 2006; 54:5147.

[11] LeBeau S, Decker R, Walukas DM Technical paper of *Thixomat Inc.*

[12] Pravdic F, Kilian H, Brandecker M, Wogerer C, Traxler G. Mater Sci Forum 2005; 488-489:349.

[13] You B, Yim C, Kam B, Park W. Mater Sci Forum 2005; 488-489:337.

[14] Czerwinski F, Zielinska-Lipiec A, Pinet PJ, Overbeeke J. Acta Mater 2001; 49:1225.

[15] Friedman PA, Ghosh AK. Metall Mater Trans A 1996; 27A:3030.

[16] Meyers MA, Vöhringer O, Lubarda VA. Acta Mater 2001; 49:4025.

[17] Liu Y, Ghosh A. TMS 2005; 139.

[18] Wonsiewicz BC, Backofen WA. Trans Metall Soci AIME 1967; 239:1422.

[19] Kocks UF, Westlake DG. Trans Metall Soci AIME 1967; 239:1107.

[20] Obara T, Yoshinga H, Morozumi S. Acta Metall 1973; 21:845.

[21] Yoo MH. Metall Trans A 1981; 12A:409.

[22] Bell RL, Cahn RW. Proceedings of the Royal Society of London, Series A (Mathematical and Physical Sciences) 1957; 239:494.

[23] Kelley EW. Ph.D. Thesis, University of Michigan, 1967

[24] Couling SL, Pashak JF, Sturkey L. Trans ASM 1959; 51:94.

[25] Ono N, Nakamura K, Miura S. Mater Sci Forum 2003; 419-422:195.

[26] Galiyev A, Kaibyshev R, Gottstein G. Acta Mater 2001; 49:1199.

[27] Wang YN, Huang JC. Mater Chem Phys 2003; 81:11.

[28] Ion SE, Humphreys FJ, White SH. Acta Mater 1982; 30:1909.

[29] Agnew SR, Yoo MH, Tome CN. Acta Mater 2001; 49:4277.

CHAPTER 4

LOW-TEMPERATURE SUPERPLASTICITY OF SUBMICROCRYSTALLINE TI-6AL-4V PROCESSED BY NON-ISOTHERMAL SEVERE PLASTIC DEFORMATION

Abstract

New method of severe plastic deformation was introduced to successfully produce ultra-fine grained (UFG) Ti-6Al-4V alloy. Non-isothermal condition and aid by superimposed hydrostatic pressure was utilized during severe plastic deformation of materials. This method produced an equiaxed and homogeneous grain structure with average grain size of 0.4 μm for α phase. The Ti-6Al-4V after severe plastic deformation shows enhanced superplasticity at low homologous temperatures between 600 ~ 700^{o}C (0.36 ~ 0.42 T_m). The microstructure evolution during processing, strain-rate sensitivity for superplastic deformation and possible rate controlling mechanism accommodated the deformation were discussed in present study.

4.1 Introduction

Ti-6Al-4V alloy is characterized as a two-phase ($\alpha + \beta$) alloy in which particular Al-V balance provides attractive mechanical properties. It is widely applied in the aerospace industry, due to high specific strength, good corrosion resistance and high formability associated with superplasticity [1]. The superplasticity of this material with grain size of a few microns has been demonstrated at high temperature (above 900^{o}C) [2]. The excellent superplasticity of this alloy enables to achieve weight and cost saving.

It is well-known that refinement of grain structure can lead to a reduction in the optimum superplastic temperature at constant strain rate, or an increase in the optimum superplastic strain rate at constant temperature [3]. These factors are important for a technological application. In recent decades, extensive investigations of grain refinement for metallic materials to submicrocrystalline or even nanocrystalline level have been conducted with the development of severe plastic deformation (SPD) technique [4]. Some SPD methods have been successfully utilized to generate UFG Titanium alloys [5-8]. The mechanical properties of those fine-grained Ti-6Al-4V have been evaluated at wide temperature range of 600 ~ 875^{o}C and enhanced superplasticity was found [9-11].

Although some of the SPD methods can be operated successfully for Ti-6Al-4V alloy at room temperature [5, 8], most of commonly used SPD methods are utilized at elevated

temperature and labored with multistep processing and heat treatment, such as multistage 'abc' forging (~ 550^{o}C) [6], multistep isothermal forging (600 ~ 700^{o}C) [11] and ECAP (600^{o}C) [12]. On the viewpoints of decreasing the processing tool costs, material saving due to reduced contamination and energy saving for industrial manufacturing, it is necessary to find improved method that can reduce the working temperatures both for fabrication of fine grained bulk materials and succeeding parts forming.

Stimulated by the result [13] that Ti-6Al-4V was successfully extruded at room temperature without cracking, and the improved workability was attributed to the increase of hydrostatic pressure in the forming zone, it has high possibility to deform the Ti-6Al-4V alloy aided by superimposed hydrostatic pressure at lower temperature than those for other methods. Moreover, the temperature-sensitive shearing [14] and possible twinning [15] effects will favorite the grain refinement process during low-temperature severe plastic deformation.

In present study, a new method of severe plastic deformation for producing the UFG Ti-6Al-4V alloy was introduced. Superimposed hydrostatic pressure and non-isothermal condition was applied during processing. The deformation processing was started at relative low temperature of 350^{o}C, and gradually increasing temperature to 475^{o}C. It is believed that the increasing deformation temperature can be of benefit for relaxation of high internal stress resulted from the concurrent SPD, and it is possible to eliminate the

post heat treatment. Subsequently, the as-processed microstructure was examined, and the superplasticity of UFG Ti-6Al-4V alloy was evaluated with constant strain rate at temperature of 600 ~ 700^{o}C and strain rate of 5×10^{-4} ~ $10^{-2}s^{-1}$. The kinetics of static and dynamic grain growth accompanying superplastic deformation, and potential rate controlling mechanisms were discussed.

4.2 Materials and Procedures

4.2.1 Materials

The material of interest in present study is the commercial grade Ti-6Al-4V alloy, provided in the form of hot-extruded bar with diameter of 76.2 mm. Its typical composition (in weight percentage) is ~ 6 Al, ~ 4 V, 0.05 N, 0.10 C, 0.3 Fe, 0.2 O and balanced Ti. The starting microstructure is showing in Figure 4.1. It consists of equiaxial alpha phase (dark) with average grain size of 8 μm, and polygonal or laminal beta phase (bright) with particle size around 1 μm, distributing on the alpha-alpha phase boundary. Cylindrical specimen of dimension 9.5 (D)×24 (H) mm was prepared by wire EDM. The machined surface was removed by slight grinding. The axis of cylinder is parallel to the extrusion direction of the raw billet. To generate superimposed hydrostatic pressure on the specimen, a mild steel (1008 grade) block was machined with 25.4 mm in height and 25.4×25.4 mm in cross-section. A through hole with diameter of 10 mm was drilled in the center of cross-section.

4.2.2 Setup of equipment and processing

Figure 4.2 shows the setup of equipment and workpiece. To avoid oxidation of specimen, and bonding between the Ti alloy specimen and steel block, the surface of cylindrical Ti alloy specimen was coated with Boron Nitride lubricant, and then inserted into mild steel block, as shown in Figure 4.2 (b). The illustration of assembled punch and bottom flat die with workpiece for pressing is shown in Figure 4.2 (a) also. The punch, bottom flat die and workpiece were surrounded by four semi-circular splits with the flat side facing the workpiece, which can provide high back pressure on workpiece during pressing. This setup was within a constraining ring equipped with band heaters. Forney FX700 hydraulic press was used for loading. The testing temperature was monitored by putting the thermocouples on the positions 1, 2 and 3 labeled on illustration. Thermocouple at position 2 was used only for pre-examination. During the experiment run, the testing temperature was obtained from position 1 and 3. The heating system provided a controlled sample temperature to be better than $\pm 2\ ^{o}C$.

4.2.3 Experimental procedures

a) <u>Processing of *UFG* materials</u>:

A preform of Ti-6Al-4V alloy specimen was produced by beta annealing at $1020\ ^{o}C$ for

30 minutes. During annealing, the Ti-6Al-4V alloy specimen was enclosed within a quartz tube filling with argon gas in order to avoid the oxidation causing the problem of alpha casing. The annealing was followed with quenching the specimen in icy water. Then, Ti-6Al-4V specimen was assembled into the steel block and dies as described above. Warm-temperature pressing of specimen was performed on Forney FX700 hydraulic press. The whole setup was preheated for 60 minutes to 350^{o}C at beginning. During preheating, 3% of final load (180,000 lbs) was applied to improve the heat transfer between dies and specimen. Step heating and loading schedule was applied during processing (shown in Figure 4.3). Each step has 25^{o}C in temperature and 10% in load of increase. The finishing temperature was set at 475 ^{o}C. The average strain rate for pressing is ~ $1\times10^{-4}s^{-1}$. The cross section of steel block was grinded to initial dimension by removing the side stuff after each press. The non-isothermal pressing was repeated several times to reach the final thickness of specimen to 1.2 mm. Finally, the cumulative true strain of 3 was imposed on specimen. In present study, 3 pieces of Ti-6Al-4V alloy materials were prepared by this method for mechanical testing. The produced grain size is in the range of 0.18 ~ 0.62 μm. To isolate thermal effect from the thermomechanical processing, separate heat treatments were conducted to investigate the thermal effect on transformation and grain refinement of beta-annealed Ti-6Al-4V specimen.

b) <u>Microstructure</u>:

Microstructure examination was performed by using optical microscope (OM, Olympus,

PME-3), Scanning electron microscope (SEM, Philip FEG-XL30) and Transmission electron microscope (TEM, JEOL-3011 HRTEM). The metallographic specimens for OM and SEM were sectioned in the plane parallel to the extrusion direction for raw material and beta-heat treated specimen, and traverse plane for UFG specimen. The metallographic samples were mechanically polished by standard method and etched by Kroll's reagent (1.5 Vol.% HF, 4 Vol.% HNO3, and 94 Vol.% distilled water). Thin foil specimen for TEM was prepared by mechanical thinning to 50 μm, followed by twin-jet electropolishing for final thinning with the solution of 5% perchloric acid and methanol, and the voltage of 40V, the operation temperature below -30^{o}C. TEM was operated at a nominal accelerating voltage of 300 kV. To study the static and dynamic microstructure evolution of UFG Ti-6Al-4V materials during superplastic testing, specimen was sectioned in the plane including the normal direction of sample sheet and tension direction. Several areas with various strains along the gauge length and grip region of superplastically tested specimens were selected to examine microstructure. Grain or particle size was measured from the micrograph by the area-based method [16].

c) <u>Mechanical testing</u>:

Tensile specimens were cut by wire EDM from the UFG Ti-6Al-4V alloy sheet with a dimension of 6.35mm long and 3.175mm wide in gauge section. Due to the elevated temperature processing, tensile specimens were slightly grinded to remove the surface layer for the purpose of eliminating the effect of alpha casing on ductility of specimen

[17]. Specimens were tested at temperature of 600°C and selected constant strain rates of 5×10^{-4} s^{-1}, 10^{-3} and $10^{-2}s^{-1}$. Strain rate of 5×10^{-4} s^{-1} was used for tensile testing at temperature 650°C and 700°C also. For comparison, tensile specimens of commercially produced Ti-6Al-4V alloy sheet were prepared and tested at temperatures of 600°C and 700°C, and strain rate of 5×10^{-4} s^{-1}. To evaluate strain rate sensitivity, decremental step-strain rate test [18] were performed at 600°C and strain rates range of 5×10^{-6} ~ 10^{-2} s^{-1} for both UFG and commercial Ti-6Al-4V alloys. The strain rate sensitivity of UFG Ti-6Al-4V alloy at 650°C was analyzed by the method of strain rate jump test with strain rate of 2×10^{-4} s^{-1} and 5×10^{-4} s^{-1} to evaluate the effect of strain on strain rate sensitivity [19]. For the purpose of avoiding oxidation, gauge sections of all tensile specimens were coated with boron nitride, which can reduce the contact of specimen with air. Moreover, argon gas flow was filled into the heating chamber to reduce the concentration of oxygen. To minimize the effect of material flowing from the specimen grip region on constant strain rate during testing, an improved crosshead control schedule [20] was used on a computer-controlled 4505 Instron machine. A graphic interface board (GPIB) was used for digital communication between Instron and computer. A clamshell furnace with three independent heating zones was utilized to maintain specimen temperature within ±2°C of the test temperature. The specimens required about 30 minutes to equilibrate temperature before initiating of straining.

4.3 Results

4.3.1 Microstructural evolution

Figure 4.4 shows the microstructure of Ti-6Al-4V alloy after β annealing plus water quench. This treatment produced coarse grain structure with average size of 254 μm (Figure 4.4 (a)). Many groups of parallel martensite α' platelets develop within the coarse grains, which exhibit acicular shape. In Figure 4.4 (b), it can be seen from the SEM image that groups of parallel martensitic α' platelets intersect with each other, and break the coarse grain into small segments, which is a favorable structure for further grain refinement Results from other researchers [21, 22] show that α' martensite has hexagonal structure, and a substructure containing predominately dislocations, stacking faults and occasionally twins. To examine the thermal effect on the microstructure evolution alone, separate thermal treatments were conducted. The results of separate thermal treatments (Figure 4.5 (a)) show that little change of microstructure occurs for β annealed Ti-6Al-4V during heating from room temperature to 350 ^{o}C. Furthermore, without exposing to mechanical processing, this microstructure was quite stable within the temperature range of thermomechanical processing (350 ~ 475^{o}C) (Figure 4.5 (b)).

By combining thermal and mechanical effects, the non-isothermal processing on this treated Ti-6Al-4V sample with increasing temperature from 350 to 475^{o}C produced distinct equiaxed α and β phases. It is known that α phase has hcp structure, β phase has

bcc structure. SEM image in Figure 4.6 (a) of UFG Ti-6Al-4V sample shows recognizable grain structure consisting of α and β phases. α phase presents in different gray gradient resulted from different grain orientation, while β phase shows white color and disperses on the alpha-alpha boundaries. Due to the low-temperature deformation, somewhat residual stress may exist within the specimen, which deteriorates the image quality.

Figure 4.6 (b) is the TEM image of UFG Ti-6Al-4V sample. It shows that considerable structure refinement take place after non-isothermal processing; and well-defined equiaxed grain structure can be seen. The average grain size for bulk sample was determined to be 0.42 μm. The microstructure is characterized with a mixture of well-defined high angle grain boundaries and diffusive low angle subgrain/grain boundaries. Some grains exhibit high density of dislocations. The diffraction pattern (inset) shows numerous spots arranged discontinuously along the circles, which indicates the presence of mixed high angle and low angle boundaries. However, the appearance of equiaxed diffraction spots indicates the low internal stresses and elastic distortions of crystal lattice presenting in the processed structure. This result suggests that simultaneously rising temperature with deformation during processing may promote the recovery of highly strained structure because of low internal stress and equiaxed grain structure.

4.3.2 Superplastic properties

To evaluate the low-temperature superplasticity of UFG Ti-6Al-4V sample and compare with commercial materials, elevated-temperature tensile testing was performed for both of materials at the temperature range between 600 and 700°C, with strain rate of 5×10^{-4} s^{-1} ~ $10^{-2}s^{-1}$. It should be mentioned that three pieces of UFG Ti-6Al-4V sample were prepared in this study, which have various average α grain sizes from 0.18 μm to 0.62 μm; and the commercial Ti-6Al-4V sample has average α grain size of 1.26 μm.

Figure 4.7 shows the flow curves of UFG and commercial Ti-6Al-4V samples at selected temperatures and strain rates. It should be mentioned that the calculation of stress and strain is based on instantaneous cross-section area and an assumption that specimens undergo uniform deformation. In Figure 4.7 (a), the UFG alloy shows strong strain rate effect at 600°C. The flow stress rapidly increases with increasing strain rate at this temperature. Moreover, it exhibits large difference in the flow behaviors of material at those three selected strain rates. At strain rate of 10^{-2} s^{-1}, flow stress increases rapidly with small strain at the beginning, then drops sharply after reaching peak stress without the stage of steady flowing. When increasing the strain rate to 10^{-3} s^{-1}, the elastic strain shows obvious offset; and the increase of stress become smooth and the peak stress is much lower than that of higher strain-rate. Furthermore, the drop of stress become smoothly after passing the peak stress; and quite larger elongation was produced.

Compared with the testing at 10^{-2} s^{-1} and 10^{-3} s^{-1}, the specimen shows totally different flow behavior at strain rate of 5×10^{-4} s^{-1}. The flow curve reveals evident strain hardening and much larger elongation. When the UFG alloy was tested under constant cross-head speed (CHS) with initial strain rate of 5×10^{-4} s^{-1}, the flow curve shows more pronounced strain hardening behavior due to the decreasing true strain rate. However, the observed higher stress level may be due to the larger grain size for this sample. For the testing at 650 and 700^{o}C, similar strain hardening behaviors were found. The flow stress decreases with increasing temperature. At the same time, strain hardening behaviors become stronger with increasing temperature, which produces larger elongation. For the commercial Ti-6Al-4V samples (Figure 4.7(b)), comparing with the samples prepared in present study, commercial sample shows higher elastic modulus and faster approaching to peak stress under the same testing conditions of 600^{o}C and 5×10^{-4} s^{-1}. Over the peak stress, stress decreases quickly and produced smaller strain to failure. Increasing testing temperature to 700^{o}C, commercial sample present clear steady flowing within whole strain range; and little strain hardening effect was observed.

To connect the stress-strain response with the configurations of tested specimen, Figure 4.8 exhibits the figures of specimens before and after testing under different testing conditions. In this figure, the labeled elongation beside specimens is calculated on large gauge length (length between specimen shoulders). It can be seen that most of UFG specimens show diffuse necking with different level, except the testing of highest strain

rate (10^{-2} s^{-1}). The UFG specimen has the largest uniform strain at 700°C and 5×10^{-4} s^{-1}. The commercial specimen reveals visible localized necking at 600°C, which was reduced by increasing testing temperature to 700°C. Commercial specimen also shows large degree of diffuse necking and elongation at 700°C.

In present study, an improved crosshead control schedule [20] was used to impose precise strain rate condition on gauge region of specimen during superplastic testing. To verify the strain rate condition, measurement of extension on different region of specimen was performed (Figure 4.9), which is important for precisely evaluating the true formability of materials. Measurement was taken on grip region, grip hole and specimen with total length scale, as well as gauge region. Two gauge lengths were used as reference. One is the gauge length (0.15 in) without radius, while another reference is the length (0.25 in) between the specimen shoulders which includes radius. The calculated extension based on these two gauge lengths and specified strain rate were also shown in Figure 4.9. It can be seen that quite small extension occurs on grip region and grip hole, which indicates a little amount of material in this region flowing into gauge section. The strain rate on position 1 and position 2 was determined by calculating the reduction of cross-section area at those positions and total testing time. It can be seen that, for all of tests with various strain rate, the measured extensions within straight gauge region and whole length scale of specimen well match the calculated extension based on gauge length of 0.15 in. This suggests that smaller reference gauge length should be chosen to determine

the true elongation to failure.

Suggested by the above verification of elongation measurement, the total elongations to failure for different conditions are listed in Table 4.1. The measurements based on two reference gauge lengths (0.15 in and 0.25 in) are used at the same time for comparison. At 600^{o}C, the elongation to failure of UFG alloy shows great dependence on strain rate. The elongation to failure increases with decreasing strain rate. The testing at 5×10^{-4} s^{-1} has elongation of 695%, which is more than 5 times as that of testing at 1×10^{-2} s^{-1}. Even, an elongation to failure of 377% was obtained at strain rate of 1×10^{-3} s^{-1}. Furthermore, elongation shows increase with increasing temperature. The largest elongation to failure (1175%) was obtained at 700^{o}C and 5×10^{-4} s^{-1}. Comparing with commercial samples, larger elongation to failure was obtained at same testing condition. This indicates highly improved formability for UFG Ti-6Al-4V alloy.

The results of superplastic testing show that the UFG Ti-6Al-4V alloy has great dependence of flow stress and elongation to failure on temperature. It is believed that thermal activating diffusion process plays an important role in deformation process. Figure 4.10 shows the determination of activation energy for deformation in temperature range of 600 ~ 700^{o}C at constant strain rate. The activation energy for deformation is determined by equation (4-1) [3].

$$\frac{Q}{2.303R} = \frac{\partial Log[\sigma^n / (G^{n-1} \cdot T)]}{\partial (1/T)} \quad (4\text{-}1)$$

where Q, activation energy (kJ/mol); R, gas constant (8.314 J/(K•mol)); σ, flow stress (*MPa*); G, shear modulus (*MPa*); n, stress exponent (the reciprocal of m); and T, absolute deformation temperature (K). In present calculation, flow stress was collected at strain of 0.1; the value of m is 0.55 for the temperatures within 600 ~ 700°C and the strain rate of $5 \times 10^{-4} s^{-1}$. The shear modulus (G) can be derived by equation (4-2) [23].

$$G(GPa) = 42.55 - 1.181 \times 10^{-2} T - 9.625 \times 10^{-6} T^2 (T/^oC) \quad (4\text{-}2)$$

The activation energy was obtained from the slope of $\log[\sigma^n / (G^{n-1} \cdot T)]$ *vs.* $1/T$, which is 172 kJ/mol. This value is close to that of lattice diffusion of α-Ti (150 kJ/mol) [24] and β-Ti (153 kJ/mol) [25], but much smaller than that of power-law creep of α-Ti (242 kJ/mol) at same temperature[26].

Table 4.2 lists the diffusion types and the corresponding diffusion coefficients for Ti-6Al-4V alloy at 600 and 700°C. The equations as follows were used to determine the diffusion coefficients at designated temperatures.

Vanadium in β-Ti [27]: $D_V^{\beta} (\mu m^2 / s) = 77{,}000 \exp(-17{,}460 / T(K))$ (4-3)

Titanium in β-Ti [28]: $D_{Ti}^{\beta}(\mu m^2/s) = 20{,}000\exp(-15{,}000/T(K))$ (4-4)

Aluminum in β-Ti [27]: $D_{Al}^{\beta}(\mu m^2/s) = 199{,}200\exp(-18{,}040/T(K))$ (4-5)

It seems that diffusion coefficients of β-Ti derived from the above equations for present study are close to the values of dislocation core diffusion, which is larger than that of boundary diffusion of β-Ti. However, the much larger boundary diffusion coefficients for α-Ti indicate that boundary diffusion of α-Ti has much stronger influence on the diffusion process. Due to the quite large volume fraction of α phase in the UFG sample, the boundary diffusion of α-Ti therefore is expected to be the primary rate-controlled mechanism for superplastic deformation, and to be assisted by the core diffusion of β-Ti.

Decremental step-strain rate tensile testing was performed to evaluate the strain-rate sensitivity of UFG and commercial Ti-6Al-4V samples at 600^{o}C. The flow stress and *m* value as a function of strain are shown in Figure 4.11 (a) and (b). The flow stress for both of the materials is found to increase with increasing strain rate. Within the investigated range of strain rate, commercial sample has higher flow stress than UFG alloy. However, as strain rate increases, flow stress of UFG material increases more promptly. Even, the flow stresses are close to each other for both of materials at strain rate of $10^{-2}s^{-1}$. Moreover, the UFG material shows two separate development of flow stress with strain rate at low strain rate level. Each one is corresponding different strain level. It can be seen that higher flow stress was developed at larger strain level, which may indicate the

dependence of flow stress for UFG material on strain, which may be due to the concurrent grain growth.

Furthermore, in Figure 4.11 (b)), the *m* value ($\frac{d\log\sigma}{d\log\dot{\varepsilon}}$) of UFG material varies slightly between 0.5 ~ 0.6 at small strain, which suggests grain boundary sliding mechanism [29]. When exposing to large strain, the *m* value decreases to be less than 0.4. In contrast, the *m* value of commercial material shows decrease with increasing strain rate, and is between 0.2 ~ 0.45, which is much lower than that of UFG material. However, improved formability at high strain rates was not observed while almost constant *m* value at 600^{o}C was obtained within wide strain rate range. This indicates that other effect such as strain hardening may play an important role in improving the formability of materials.

To analyze the effect of strain on *m* value of UFG material, strain-rate jump test between strain rates of 2×10^{-4} s^{-1} and 5×10^{-4} s^{-1} at 650^{o}C was conducted. The tensile testing was performed at constant strain rate of 5×10^{-4} s^{-1}. The *m* value is periodically determined by departures of strain rate to 2×10^{-4} s^{-1}, and maintenance for around 2% of plastic strain and bringing back to the original strain rate. The plot of *m* value *vs.* true strain is illustrated in Figure 4.12. It is obvious that the *m* value generally decreases with increasing strain. This result is consistent with the finding in previous studies [2, 30, and 31].

By measuring grain size for different region with different strain level, the evolution of grain size for UFG Ti-6Al-4V deformed at 650°C and 5×10^{-4} s^{-1} is illustrated in Figure 4.13. Because of relatively large fraction of α phase within two-phase structure, the grain size refers to α phase. It can be seen that rapid grain growth with deformation occurs at the beginning until the true strain reaches 1.8. This finding is consistent with the decreasing *m* value with increasing strain in Figure 4.12. It was reported that the concurrent grain growth and associated hardening lead to a drop in strain-rate sensitivity [2]. When experiencing further deformation, grain size starts to decrease with increasing strain, and tend to be stable. It may indicate the occurring of dynamic recovery and recrystllization during deformation.

In Figure 4.7, UFG and commercial Ti-6Al-4V samples show quite different flow behaviors with strain at 700°C and 5×10^{-4} s^{-1}. To connect this mechanical response with microstructure evolution, the kinetics of grain growth during superplastic deformation was analyzed. Figure 4.14 illustrates the plots of grain size *vs.* time for both of the materials. The initial grain size for UFG and commercial Ti-6Al-4V are 0.43 and 1.26 μm respectively. For static grain growth, both of materials show linear relationship between grain size and time due to the limit data points; while for dynamic grain growth, they show faster growth rate. Especially for UFG materials, the growth rate shows increase with time. Furthermore, UFG material shows much faster growth rate than commercial material for static and dynamic grain growth. The data points of static grain growth were

collected from grip region where no strain was imposed, while the dynamic data was collected from the gauge region with different strain level. It should be mentioned that the study of grain growth focuses on the α phase only. Therefore, the empirical equation for normal grain growth in a single phase material is generally accepted as [32]

$$d^q - d_o^q = K_0 t \tag{4-6}$$

This equation can be approximated as follows for $K_o t >> d_o^q$.

$$d = Kt^n \tag{4-7}$$

where $n = 1/q$; d and d_0 are the initial and final grain sizes respectively; $K = K_o^n$ and n are constants and functions of solute concentration, interfacial energy, and atomic diffusion [33, 34]. The n value is derived from $d\log(d)/d\log(t)$, and is 0.24 and 0.013 for UFG and commercial materials respectively. Although the so low n value for commercial material has never been reported, the n value for UFG material is between the n = 0.2 where the rate controlling mechanism is assumed to be determined by dislocation cores diffusion [33], and n = 0.25 for grain boundary diffusion [33, 34]. It may indicate the mixed rate controlling mechanism accommodating the superplastic deformation, which is consistent to the determination of diffusion coefficients in Table 4.2. Compared with static condition, it is obvious that dynamic grain growth has much

larger time exponent *n* with stress assistance. Therefore, other mechanisms may be suggested to contribute to deformation process, such as lattice diffusion [35] and diffusion across a particle matrix interface [36].

4.4 Discussions

In present study, the obtained results demonstrated successful production of submicroncrystalline Ti-6Al-4V alloy by non-isothermal and increasing temperature forging aided by superimposed hydrostatic pressure in the temperature range of 350 ~ 475^{o}C. The material processed by this severe plastic deformation method has gained the grain size in the range of 0.18 ~ 0.62 μm and enhanced superplasticity at low homologous temperature (600 ~ 700^{o}C). 1175% tensile elongation was obtained at 700^{o}C and $5\times10^{-4}s^{-1}$. The possible mechanisms for successful grain refinement and enhanced superplasticity are discussed here.

4.4.1 Microstructure evolution

Firstly, it is necessary to analyze the refinement process of UFG Ti-6Al-4V sample. After β heat treatment plus water quench, initial coarse and equiaxed grain structure of raw material was completely transformed to martensitic α' platelets Small segment forms by intersection between groups of martensite platelets (Figure 4.4 (b)). TEM studies [21, 22]

show that α' has hexagonal structure, and characterizes predominately with dislocations, stacking faults and occasionally twins. The investigation of isolated thermal effect on this transformed structure reveals little change in structure within the processing temperature range (Figure 4.5). However, with thermomechanical processing, the long orthogonally orientated martensitic α' plates was transformed to equiaxed α phase within the β matrix. The modification of alpha morphology in Ti-6Al-4V alloy by hot pressing has been studied extensively within the temperature range of 815 ~ 1050^{o}C [14, 37-39]. Two possible mechanisms for this transformation were suggested by Weiss et al. [14]. One is that during hot deformation, both low and high angle boundaries across the alpha plates are formed. The β phase can penetrate into the plate-like α phase along these sub-boundaries. If the α phase lamella width is small, the separation of α plate will occur readily. Another possible mechanism of α plate break-up is that the localized shear and rotation of the α lamella can occur during hot deformation. The β phase may also penetrate readily into the α phase along the shear bands and partially or fully separate the α plates into shorter segments. In present study, due to the quite low starting processing temperature, shear deformation can be the primary deformation process at beginning. Moreover, the low internal stress existing in the processed sample, which is revealed by diffraction pattern inset in Figure 4.6 (b), indicates the occurring of recovery or even recrystallization during processing when the processing temperature keeps increasing; and large amount of high angle boundaries was generated. Therefore, both of the mechanisms are applicable to interpret the grain refinement process. That is, at low

temperature, initial long α platelets were subdivided into small segment with low aspect ratio by shearing. α platelets may be separated into shorter segments by some β phase penetrating into the α phase along the shear bands. When increasing the temperature during processing, the recovery or even recrystallization accompanying the straining promotes the formation of high angle boundary. Some β phase can penetrate into the platelet-like α phase along these sub-boundaries. Eventually, the feature of high dislocation density around the shear bands or high angle boundary provides dislocation core diffusion path for the globularization of segmented α plates and precipitation of β phase. The strain-induced phase transformation has been reported by Ding. et al. [39].

4.4.2 Enhanced superplasticity

The results of tensile tests show highly enhanced superplasticity at most of the temperature and strain rate conditions for UFG Ti-6Al-4V sample. Compared with the commercial material used in present study and the results from other researchers [5, 40], at the same testing temperature and even higher strain rate, the UFG Ti-6Al-4V alloy show much lower yielding stress at the beginning of deformation. This can be attributed to the increasing boundary shearing accommodated by thermal-activated boundary diffusion for UFG Sample. However, for commercial materials, the larger grain size of material should account for the higher stress at the beginning of strain for high temperature. Furthermore, the results of step-strain rate test show that the *m* values are

0.5 and 0.37 for UFG material and commercial material respectively at strain rate of $5\times10^{-4}s^{-1}$, which indicates higher superplasticity for UFG material. However, the small difference in strain rate sensitivity can not individually interpret the much larger formability for UFG material. In Figure 4.7, commercial material shows long steady flowing at 700°C and $5\times10^{-4}s^{-1}$, while the UFG shows an increasing flow stress with increasing strain at the same condition. By comparing the static and dynamic grain growth for both materials in Figure 4.14, UFG material shows faster kinetics of grain growth. The fast grain growth results in increasing work hardening rate and retards the necking in materials, though grain growth will reduce the *m* value also. Therefore, larger total elongation for UFG sample should be contributed by large strain rate sensitivity and strain hardening rate together.

4.4.3 Strain-rate sensitivity

In present study, the UFG Ti-6Al-4V sample shows large strain-rate sensitivity (*m*) in the range of 0.37 ~ 0.6 for 600°C and strain rate of 5×10^{-6} ~ $1\times10^{-2}s^{-1}$. Strain-rate jump test also reveals high strain-rate sensitivity of 0.34 ~ 0.6 at 650°C and 5×10^{-4} s^{-1}. However, the plot of *m* value *verse* strain rate for UFG material at 600°C (Figure 4.11 (b)) shows the influence of strain on strain rate sensitivity. At the large strain level, the *m* value shows small. This can be related to the strain-induced grain growth, since increasing grain size will reduce the strain-rate sensitivity. The results in Figure 4.12 and Figure 4.13,

which show the effect of strain on strain rate sensitivity and grain size, are the direct evidences. Those results are also consistent with previous findings about strain-induced grain growth [41].

4.4.4 Activation energy for deformation

The activation energy for deformation determined in Figure 4.10 shows the value of 172 kJ/mol. Arieli et al have reported [40] that the activation energy for grain boundary diffusion is ~ 189 kJ/mol at 800 ~ 950^{o}C. A smaller activation energy (173 kJ/mol at 600 ~ 700^{o}C) [9] reported by Ko et al. also suggested that the deformation was governed by grain boundary sliding (GBS) accommodated by grain boundary diffusion. Thus, it was suggested that the deformation of samples prepared in present study was governed by grain boundary sliding (GBS) accommodated by grain boundary diffusion and possible core diffusion. However, the activation energy derived in present study is higher than those of lattice diffusion (150 kJ/mol for α-Ti [24], 153 kJ/mol for β-Ti [25]), boundary diffusion (97 kJ/mol for α-Ti [26], 153 kJ/mol for β-Ti [26]) and core diffusion (97 kJ/mol for α-Ti [26], 153 kJ/mol for β-Ti [26]), but lower than that of power-law creep (242 kJ/mol for α-Ti [26]). Briottet et al has discussed the observation that the activation energy for two phase flow is much higher than the flow activation energy of the individual phases for Ti-6Al-4V [42]. It was suggested the apparent activation energy for the flow of a two phase material is not generally related to a specific mechanism since an

additional mesoscopic term is involved. This term depends on the relative values of flow stresses of the low and high temperature phases, as well as on the temperature dependence of the volume fraction of the low temperature phase. It is highly possible that the activation energy for two phase structure is greater than that of either constituent. Moreover, the determination of diffusion coefficients (Table 4.2) for V, Ti and Al in β-Ti at 600 and 700^{o}C suggests that the grain boundary diffusion assisted by core diffusion may be the primary mechanism for rate-controlled deformation. Also, the facts that no cavities were observed after high elongations and fast grain growth indirectly suggest the high diffusivity during deformation, which prevents the nucleation of cavity and facilitates the migration of grain boundary.

4.5 Conclusions

New method of severe plastic deformation was used to produce UFG Ti-6Al-4V alloy. Step heating and loading schedule was utilized to impose non-isothermal temperature condition during deformation processing. The generation of UFG structure at quite low temperature was possible by assistance of superimposed hydrostatic pressure. The superplasticity of Ti-6Al-4V after severe plastic deformation was evaluated within the temperature range of 600 ~ 700°C and the strain rate range of 5×10^{-4} ~ $10^{-2}s^{-1}$. Some conclusions can be summarized as follows.

(1) The method of non-isothermal severe plastic deformation aided by superimposed hydrostatic pressure successfully produced UFG Ti-6Al-4V alloy without cracking, and generated equiaxed and homogeneous grain structure; the deformation processing within the temperature range of 350 ~ 475°C produced a structure with grain size of 0.18 ~ 0.62 μm for α phase.

(2) The UFG Ti-6Al-4V alloy after SPD exhibits enhanced superplasticity at low homologous temperature between 600 ~ 700°C (0.36 ~ 0.42 T_m); the strain-rate sensitivity of UFG Ti-6Al-4V was within 0.5 ~ 0.6, which suggests the grain boundary sliding accommodated deformation; the largest elongation to failure of 1175% was achieved at 700°C and $5\times10^{-4}s^{-1}$.

(3) The flow curves of UFG Ti-6Al-4V show low yield stress at elevated temperature at

the beginning of straining, then pronounced strain hardening occurred with increasing temperature, which is related to the concurrent grain growth during deformation.

(4) The apparent activation energy for deformation at the temperature region of 600 ~ 700^{o}C and strain rate of $5\times10^{-4}s^{-1}$ was determined to be 172 kJ/mol, which is substantially lower than activation energy for dislocation creep (242 kJ/mol). The diffusion mechanism was suggested to be a combination of grain boundary diffusion assisted by core diffusion, which indicates rate controlling mechanism to be grain boundary sliding and accommodation of grain boundary or core diffusion as in mantle-core model [43].

(5) Kinetics of static grain growth shows the time exponent (n) to be 0.24, which is between the value of dislocation cores diffusion (n = 0.2), and grain boundary diffusion (n = 0.25). However, the slope of grain size *verse* time reveals that the time exponent for dynamic grain growth is much larger than the one of static condition, and increases with time. This suggests grain boundary sliding accommodated by boundary and possible core diffusion is the primary mechanism controlling dynamic grain growth at beginning, and other diffusion mechanisms may take place with grain growth.

Table 4.1 Elongation to failure for UFG Ti-6Al-4V alloys with various temperature and strain rate

Name	Grain Size, μm	Temperature, ^{o}C	Strain Rate, s^{-1}	Elongation to Failure, % G.L. = 6.35 mm (0.25 in)	Elongation to Failure, % G.L. = 3.81 mm (0.15 in)
UM-1	0.18	600	5×10^{-4}	412	**695**
UM-3	0.62	600	Constant CHS 5×10^{-4}	343	**579**
UM-3	0.62	600	1×10^{-3}	224	**377**
UM-3	0.62	600	1×10^{-2}	74	**126**
UM-1	0.18	650	5×10^{-4}	463	**781**
UM-2	0.43	700	5×10^{-4}	696	**1175**
Commercial	1.26	600	5×10^{-4}	181	**305**
Commercial	1.26	700	5×10^{-4}	543	**917**

Table 4.2 Determination of diffusion coefficient for UFG Ti-6Al-4V alloy

Parameter / Diffusion Types	*Q*, *kJ/mole*		*D*$_0$	
	α-Ti	β-Ti	α-Ti	β-Ti
Lattice diffusion D_v , m^2/s	150 [24]	153[25]	8.6×10^{-10} [24]	1.9×10^{-7}[25]
Boundary diffusion δD_b, m^3/s [26]	97	153	3.6×10^{-16}	5.4×10^{-17}
Core diffusion $a_c D_c$, m^4/s [26]	97	153	7.8×10^{-29}	1.6×10^{-26}
Power-law creep D_{cr} , m^2/s [26]	242	---	1.3×10^{-2}	---
Vanadium in β-Ti [27] $D_V^{\beta}(\mu m^2/s) = 77{,}000\exp(-17{,}460/T(K))$	145		---	
Titanium in β-Ti [28] $D_{Ti}^{\beta}(\mu m^2/s) = 20{,}000\exp(-15{,}000/T(K))$	125		---	
Aluminum in β-Ti [27] $D_{Al}^{\beta}(\mu m^2/s) = 199{,}200\exp(-18{,}040/T(K))$	150		---	

Diffusion Coefficient / Diffusion Types	$D_{600\,^oC}$, m^2/s		$D_{700\,^oC}$, m^2/s	
	α-Ti	β-Ti	α-Ti	β-Ti
Lattice diffusion D_v	9.1×10^{-19}	1.3×10^{-16}	7.6×10^{-18}	1.2×10^{-15}
Boundary diffusion D_b [26]	5.4×10^{-13}	3.7×10^{-17}	2.2×10^{-12}	3.3×10^{-16}
Core diffusion D_c [26]	1.4×10^{-15}	1.4×10^{-16}	5.5×10^{-15}	1.2×10^{-15}
Power-law creep D_{cr} [26]	4.3×10^{-17}	---	1.3×10^{-15}	---
Vanadium in β-Ti [27] $D_V^{\beta}(\mu m^2/s) = 77{,}000\exp(-17{,}460/T(K))$	1.59×10^{-16}		1.24×10^{-15}	
Titanium in β-Ti [28] $D_{Ti}^{\beta}(\mu m^2/s) = 20{,}000\exp(-15{,}000/T(K))$	6.90×10^{-16}		4.03×10^{-15}	
Aluminum in β-Ti [27] $D_{Al}^{\beta}(\mu m^2/s) = 199{,}200\exp(-18{,}040/T(K))$	2.11×10^{-16}		1.77×10^{-15}	

Note: ① $D_{T,K} = D_0\exp(-\frac{Q}{RT})$, ② $\delta = 3.5b$ (b --- Burgers Vector), ③ $a_c=b^2$

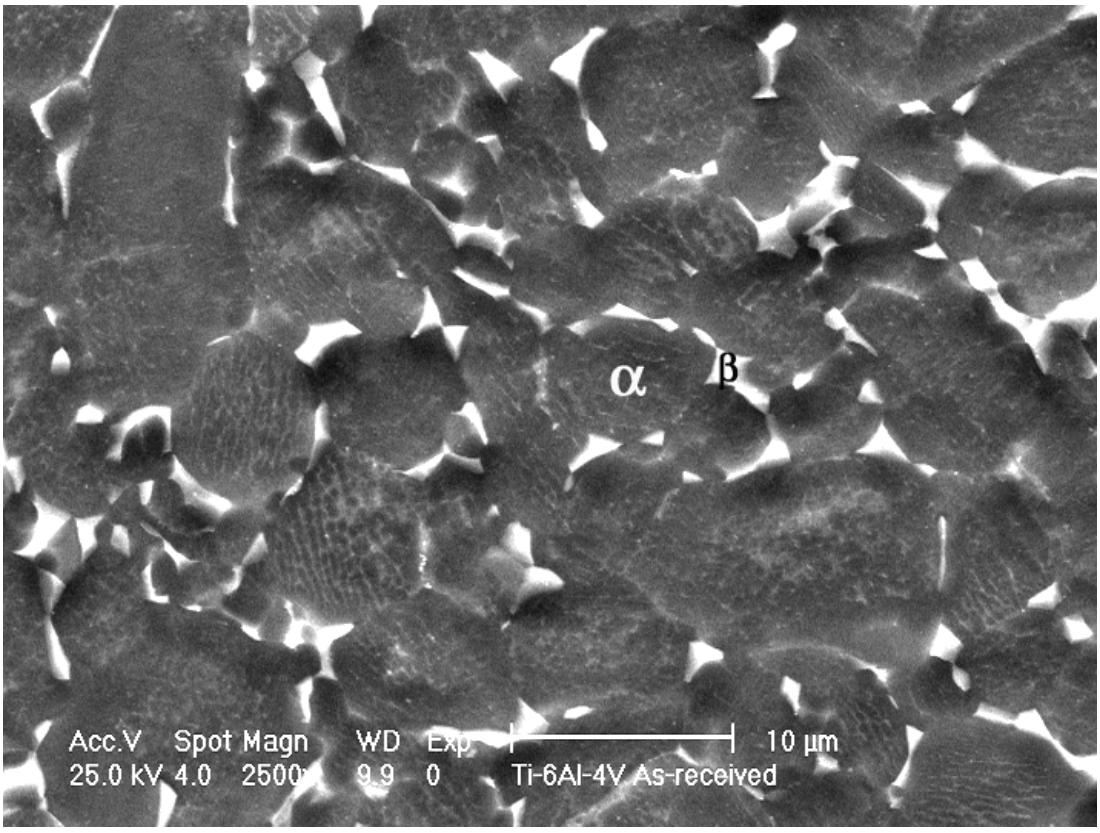

Figure 4.1 Microstructure of as-received Ti-6Al-4V alloy showing equiaxial alpha (gray in color) + beta matrix (white in color); average grain size of alpha phase is 8 µm.

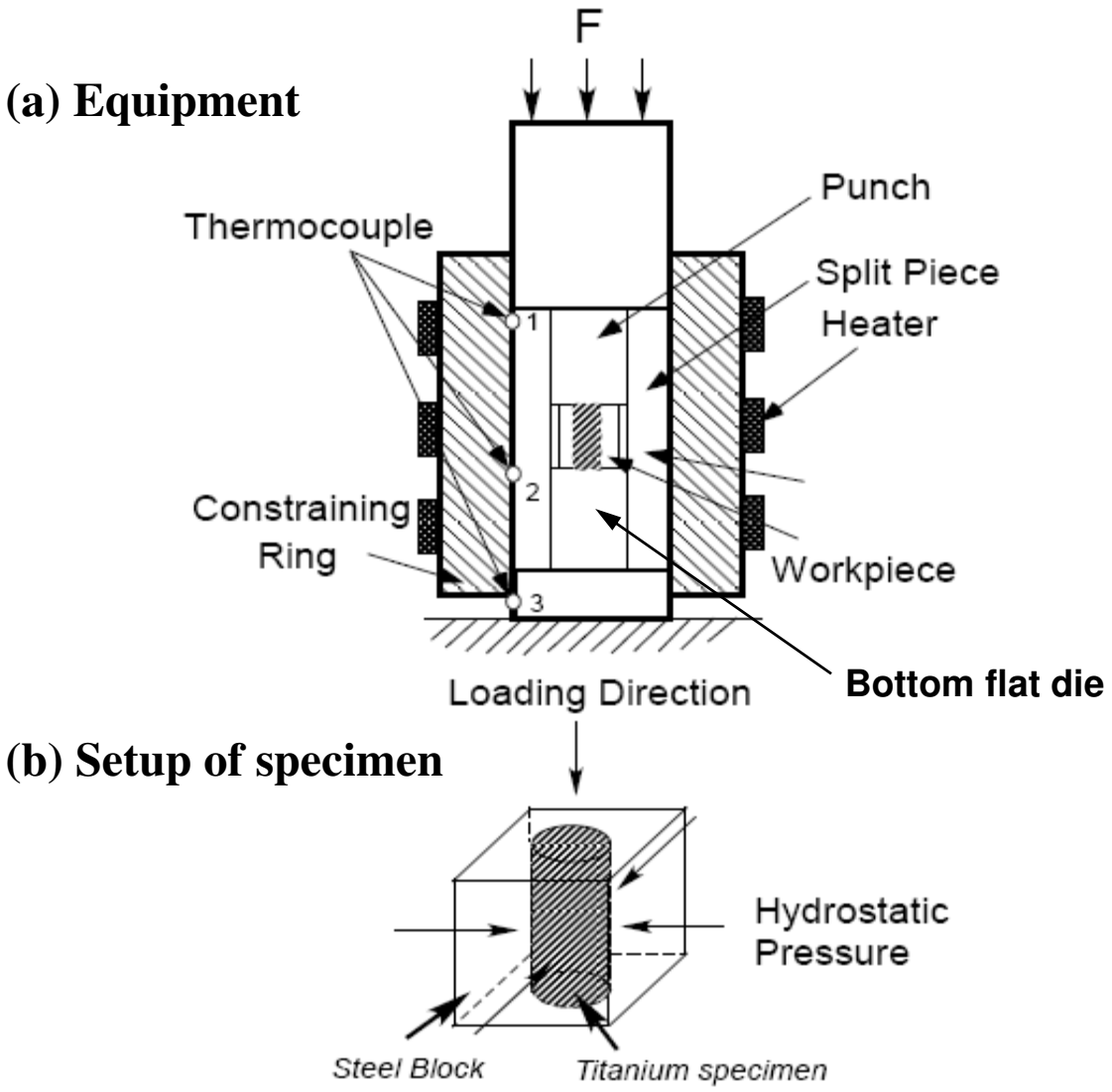

Figure 4.2 Illustration of setup for severe compression under superimposed hydrostatic pressure. (a) setup of equipment and (b) setup of specimen and pressure medium (steel block with hole in center).

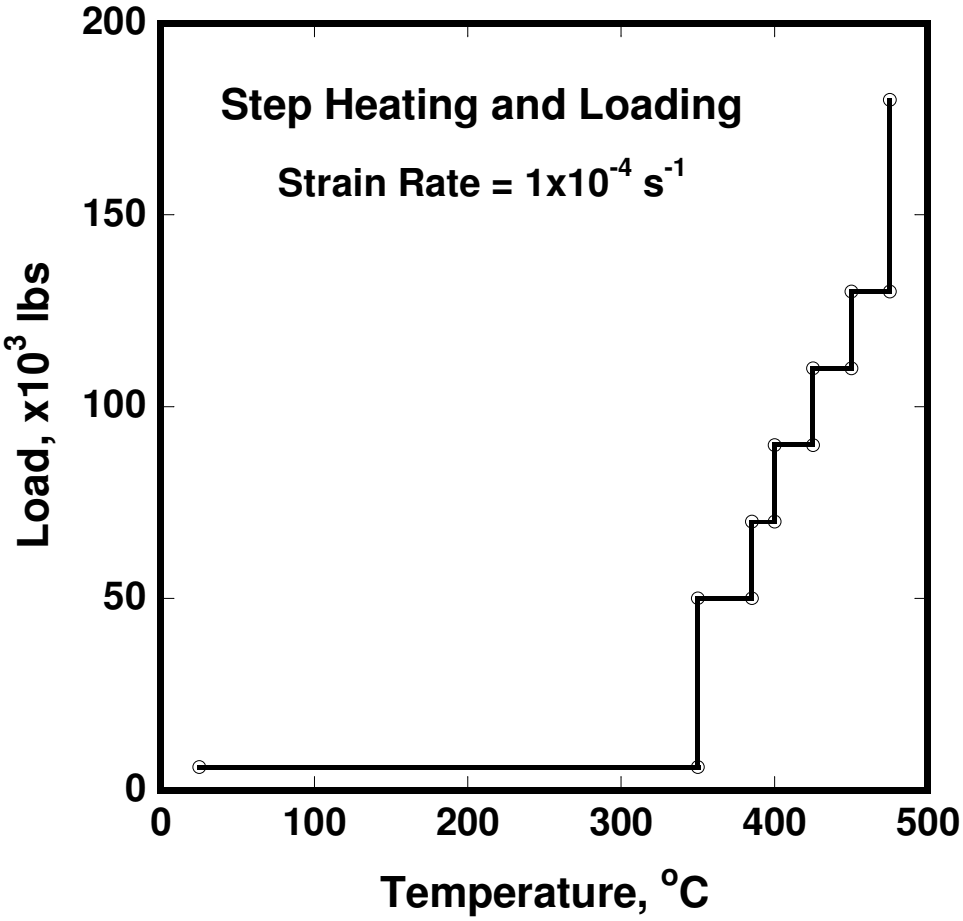

Figure 4.3 Schedule of step heating and loading shows simultaneously rising temperature during deformation

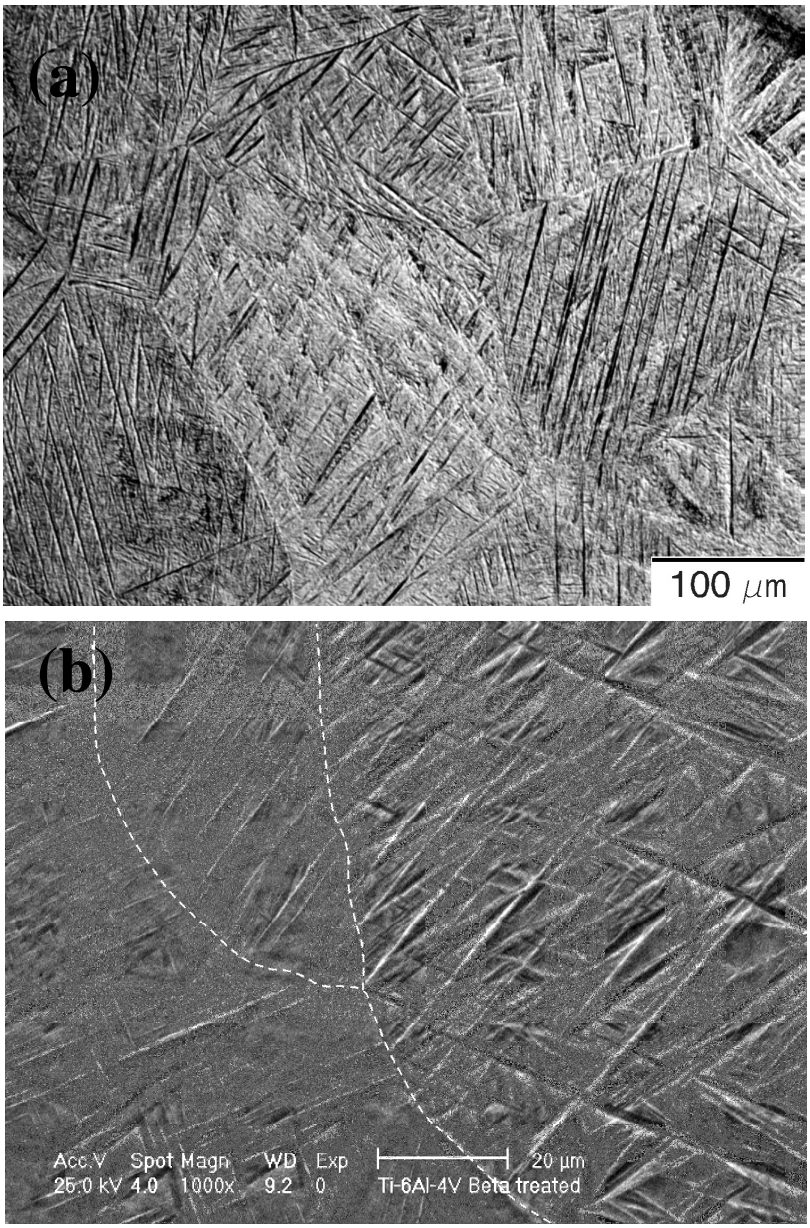

Figure 4.4 Microstructures of Ti-6Al-4V alloy after beta heat treated at 1020 ^{o}C and 30 minutes show acicular martensite alpha phase, (a) Optical Image and (b) Secondary Electronic Image. Many group of parallel martensite intersect with each other to subdivide the coarse into small segments.

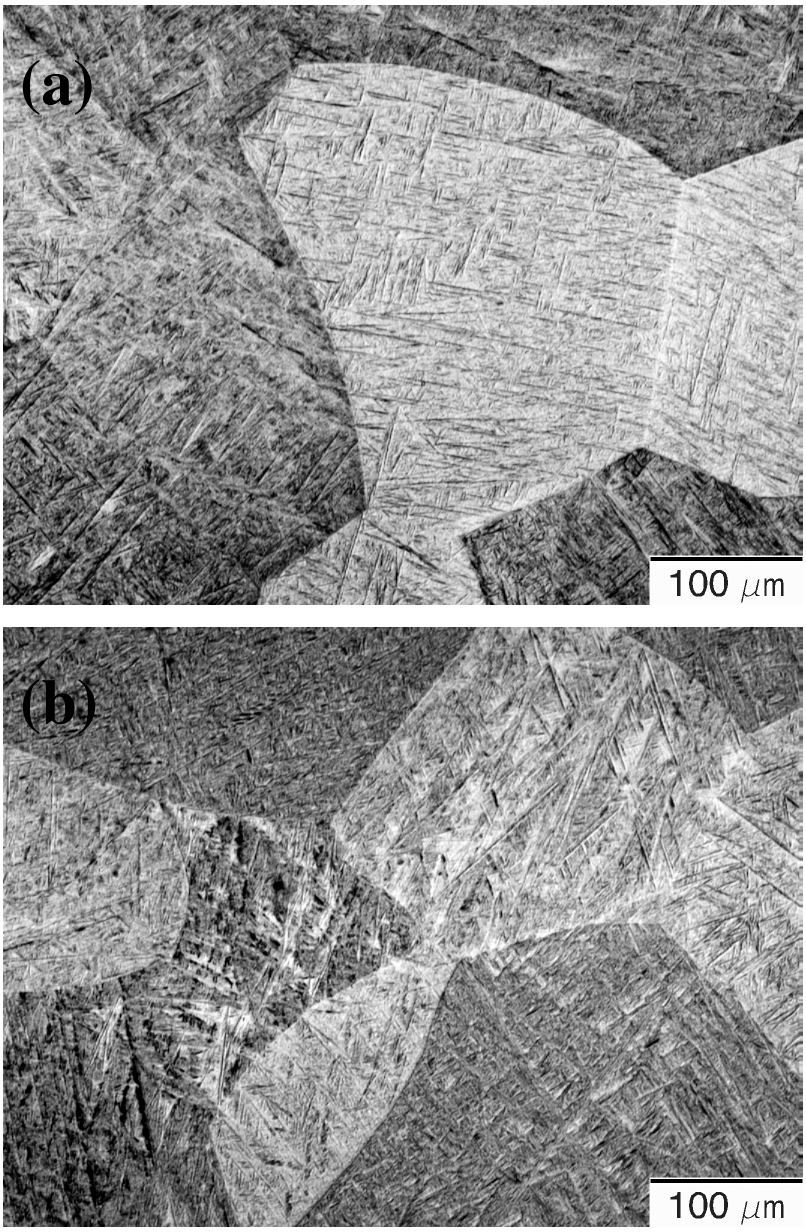

Figure 4.5 Microstructures of Ti-6Al-4V alloy after beta heat treated 1020^{o}C for 30 minutes and static annealing (a) Annealed from room temperature to 350 ^{o}C for 60 minutes, (b) Annealed from room temperature to 350 ^{o}C for 60 minutes plus secondary annealing from 350 ^{o}C to 475 ^{o}C for 60 minutes, microstructure shows stable martensite structure under static thermal condition.

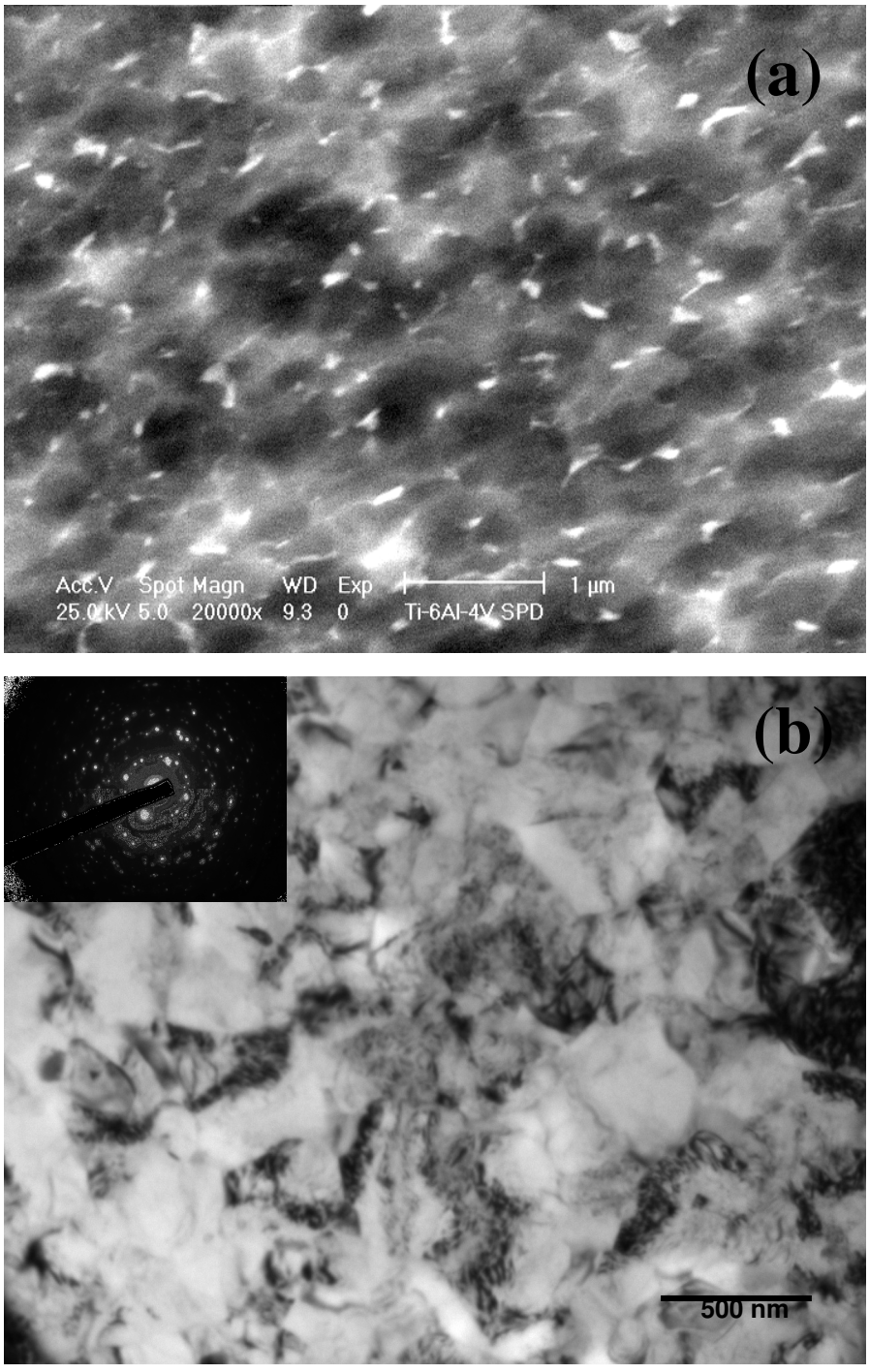

Figure 4.6 SEM (a) and TEM (b) micrograph of Ti-6Al-4V alloy after anisothermal severe plastic deformation shows submicrocrystalline and equiaxed grain structure.

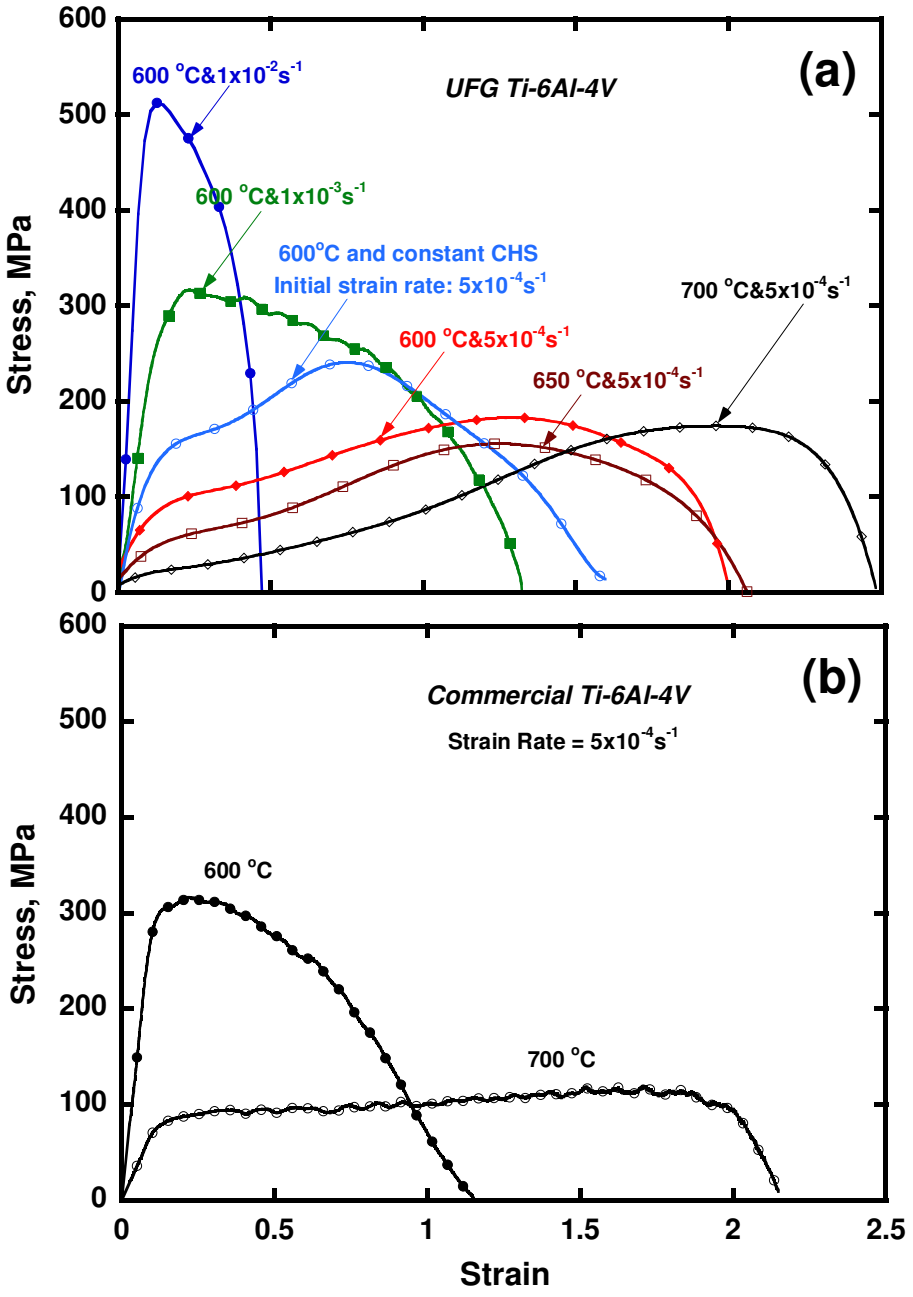

Figure 4.7 Stress-strain curves for both UFG and commercial Ti-6Al-4V alloys tested at various temperature and strain rate.

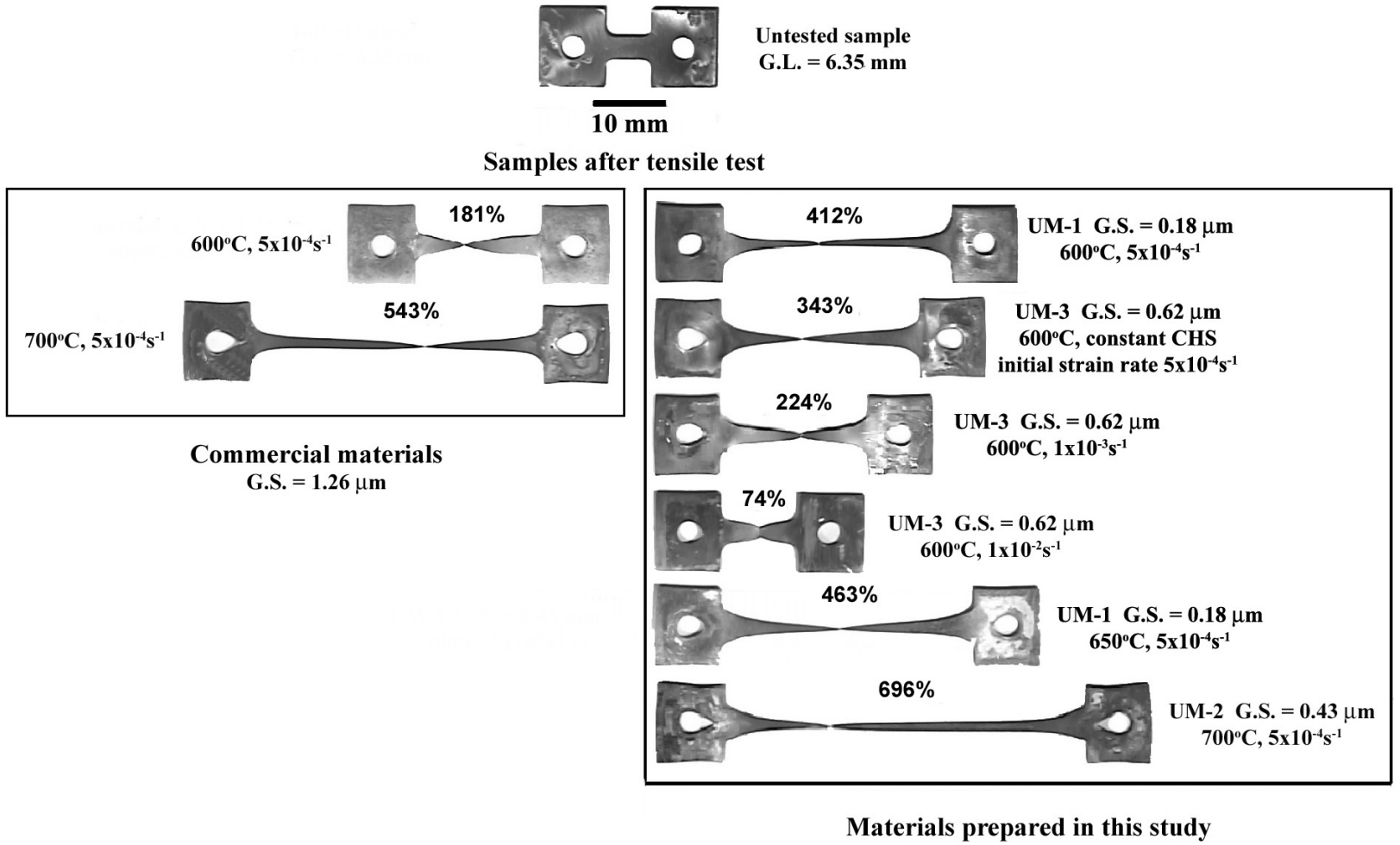

Figure 4.8 Pictures of samples before and after tensile testing. Enhanced superplasticity was shown on materials prepared in this study.

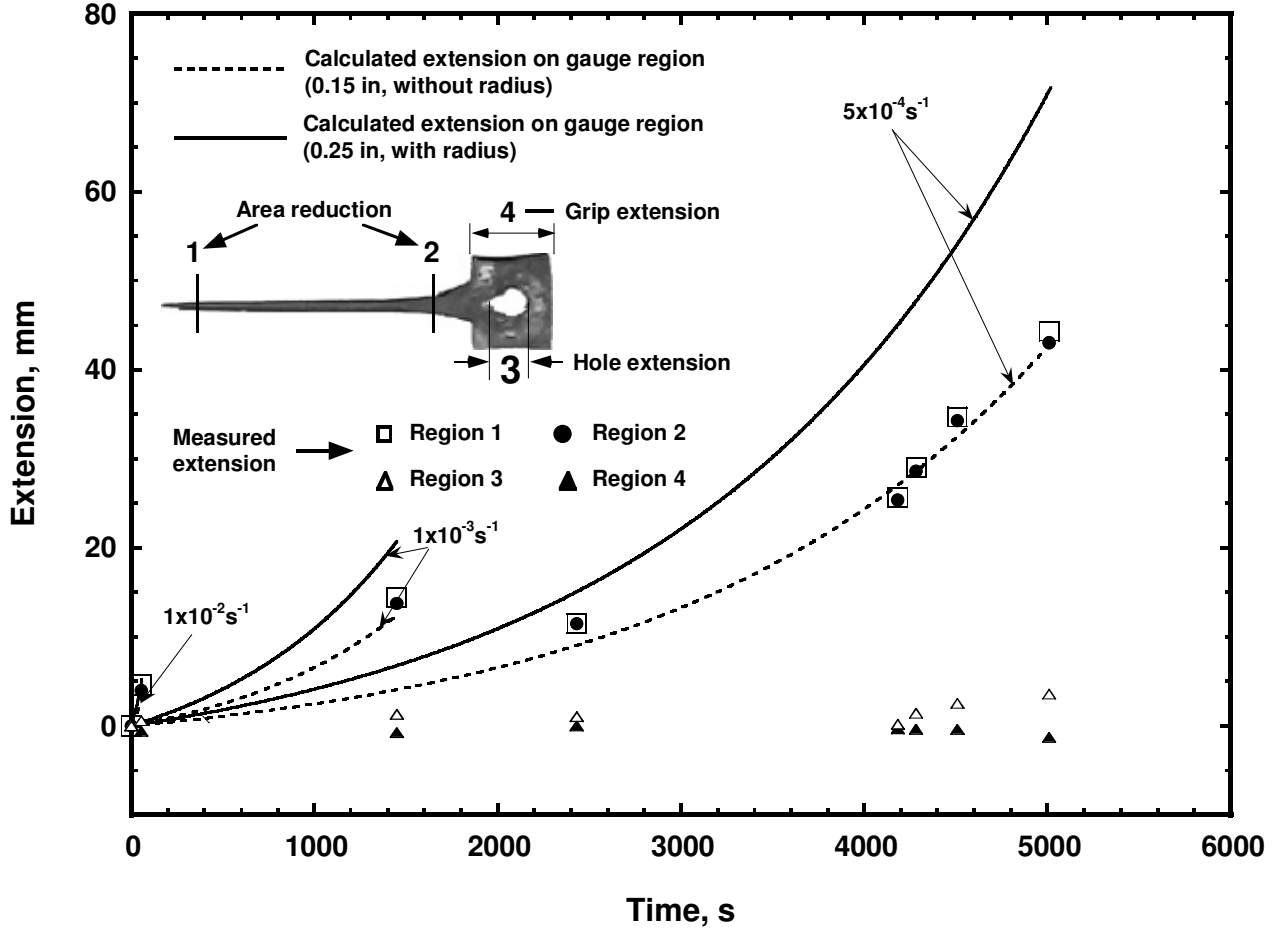

Figure 4.9 Extension measurements on different regions of tensile tested specimen. This is to verify the strain rate condition in on sample during tensile test.

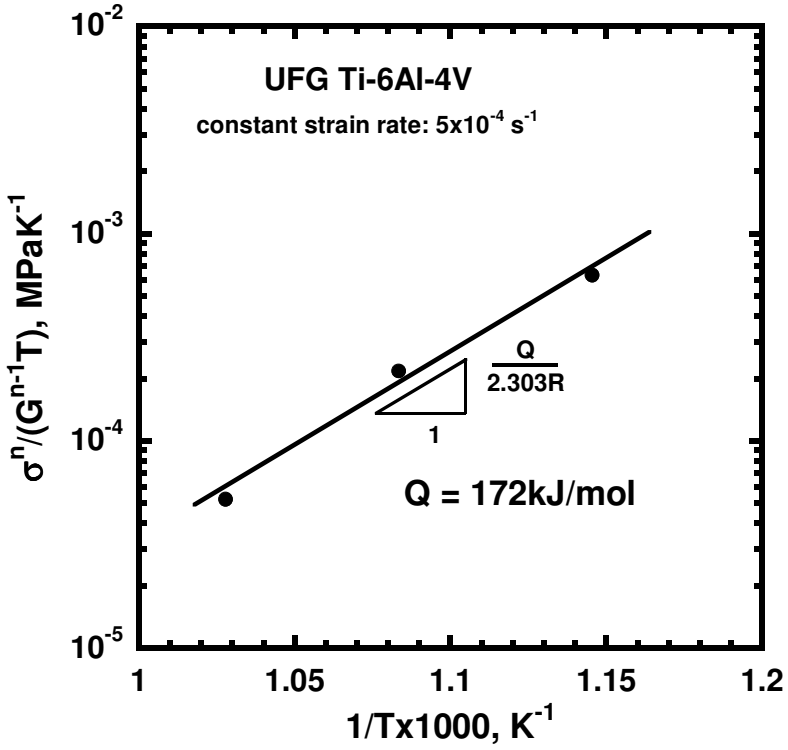

Activation Energy (kJ/mol):

$$\frac{Q}{2.303R} = \frac{\partial Log[\sigma^n/(G^{n-1}T)]}{\partial(1/T)} \quad [8]$$

Flow stress:

$\sigma = \sigma_{0.1}$

Stress exponent:

$n = 1/m,\ m = 0.55$

Shear modulus (MPa):

$$G(GPa) = 42.55 - 1.181\times10^{-2}T - 9.625\times10^{-6}T^2 \quad (T/^{\circ}C) \quad [9]$$

Figure 4.10 Calculation of activation energy for superplastic tensile testing of UFG Ti-6Al-4V within temperature range of interest. It shows activation energy for deformation is close to grain boundary sliding accommodated by boundary diffusion.

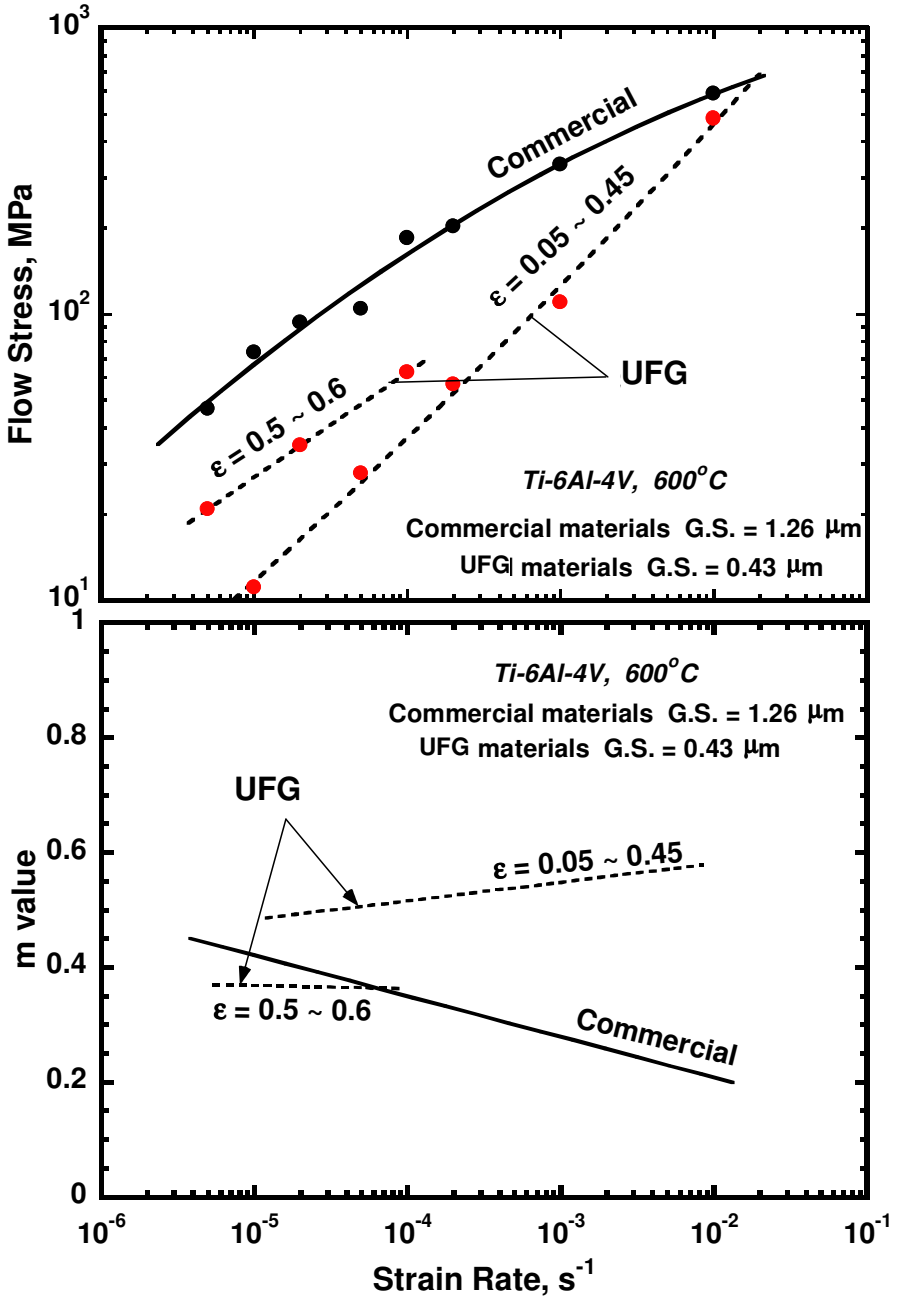

Figure 4.11 Evaluation of strain-rate sensitivity of ultra-fine grain Ti-6Al-4V alloy by decremental step-strain rate test at 600 °C. Materials prepared in this study show larger strain rate sensitivity within wide range of strain rate.

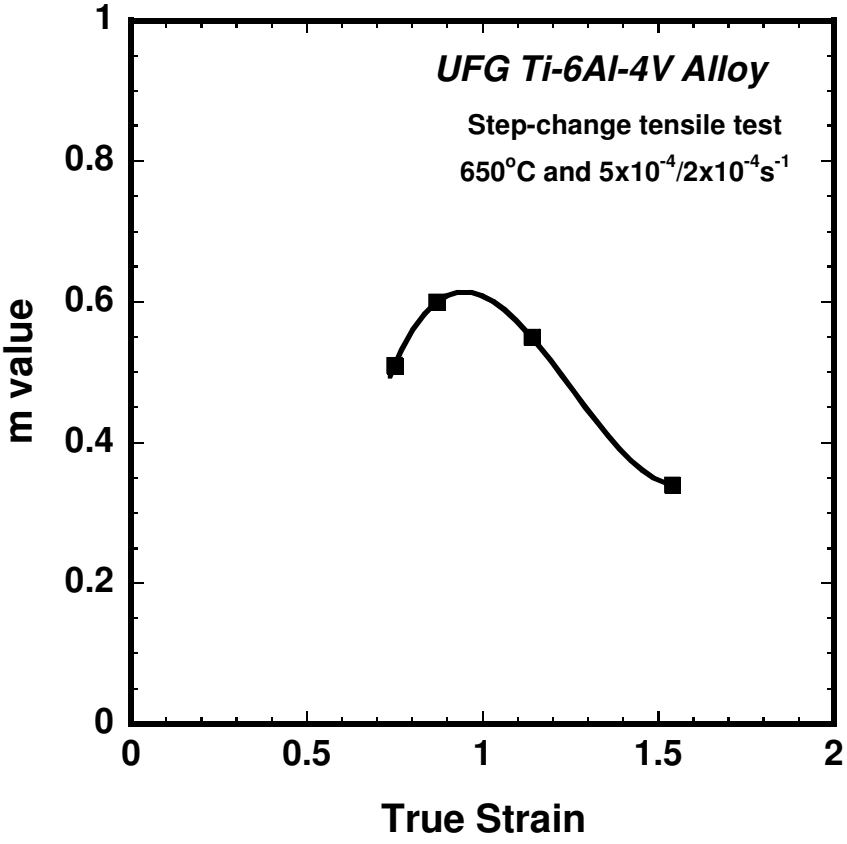

Figure 4.12 Evaluation of strain rate sensitivity of ultra-fine grain Ti-6Al-4V alloy by jump test at 650 ^{o}C. It shows decrease of strain rate sensitivity with increasing strain.

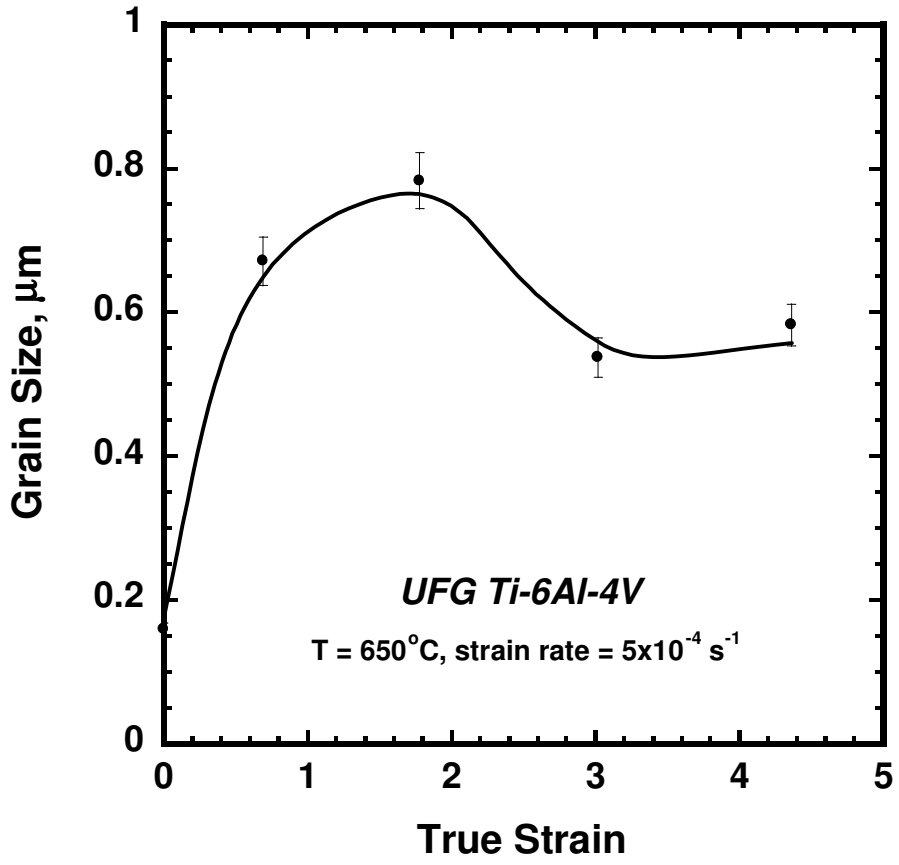

Figure 4.13 Evolution of grain size with true strain for ultra-fine grain Ti-6Al-4V alloy at 650 ^{o}C and 5×10^{-4} s^{-1} shows strain-induced grain growth at beginning of deformation, and grain refinement with increasing strain at large strain level.

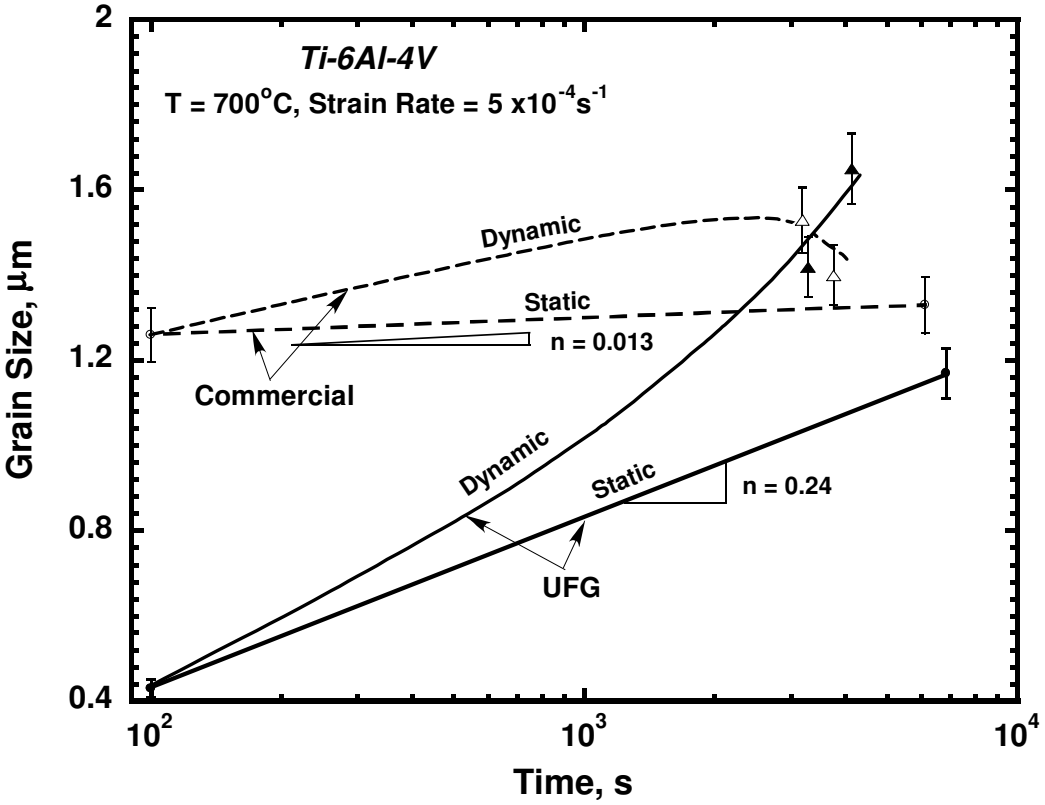

Figure 4.14 Grain growth behaviors of ultra-fine grain Ti-6Al-4V alloy during superplastic tensile testing at 700 °C shows rapid dynamic grain growth of materials prepared in this study.

4.6 References

[1] Boyer R, Welsch G, Collings EW. Materials Properties Handbook: Titanium alloys, ASM International, Materials Park 1994; 483.

[2] Ghosh AK, Hamilton CH. Metall Trans A 1979; 10A:699.

[3] Edington JW, Melton KN, Cutler CP. Prog Mater Sci 1976; 21:82.

[4] Valiev RZ, Islamgaliev RK, Alexandrov IV. Prog Mater Sci 2000; 45:103.

[5] Sergueeva AV, Stolyarov VV, Valiev RZ, Mukherjee AK. Scripta Mater 2000; 43: 819.

[6] Zherebtsov SV, Salishchev GA, Galeyev RM, Valiakhmetov OR, Mironov SYu, Semiatin SL. Scripta Mater 2004; 51:1147.

[7] Shin DH, Kim I, Kim J, Kim YS, Semiatin SL Acta Mater 2003; 51:983.

[8] Daisuke Terada, Seiya Inoue, Nobuhiro Tsuji. J Mater Sci 2007; 42:1673.

[9] Ko YG, Kim JH, Lee CS, Han SY, Shin DH, Semiatin SL. Ultrafine Grained Materials 3 Symposium 2004; 659.

[10] Sergueeva AV, Stolyarov VV, Valiev RZ, Mukhjerjee AK. Mater Sci Eng A 2002; 323:318.

[11] Patankar SN, Escobedo JP, Field DP, Salishchev G, Galeyev RM, Valiakhmetov OR, Froes FH. J Alloys Comp 2002; 345:221.

[12] Kim SM, Kim J, Shin DH, Ko YG, Lee CS, Semiatin SL. Scripta Mater 2004; 50:927.

[13] Wagener HW, Haats J, Wolf J. J Mater Proc Tech 1992; 32:451.

[14] Weiss I, Froes FH, Eylon D, Welsch GE. Metall Trans A 1986; 17A:1935.

[15] Karaman I, Yapici GG, Chumlyakov YI, Kireeva IV. Mater Sci Eng A 2005; 410-411:243.

[16] Yang Q, Ghosh AK. Acta Mater 2006; 54:5147.

[17] Patankar SN, Kwang YT, Jen TM. J Mater Proc Tech 2001; 112:24.

[18] Bae DH, Ghosh AK. Acta Mater 2000; 48:1207.

[19] Hamilton CH, Ghosh AK. Metall Trans A 1980; 1A:1494.

[20] Friedman PA, Ghosh AK. Metall Mater Trans A 1996; 27A:3030.

[21] Williams JC, Blackburn MJ. Trans ASM 1967; 60:373.

[22] Ahmed T, Rack HJ. Mater Sci Eng A 1998; 243:206.

[23] Queheillalt DT, Choi BW, Schwartz DS, G.Wadley HN. Metall Trans 2000; 21A:261.

[24] Dyment F, Libanati CM. J Mater Sci 1968; 3:349.

[25] Walsoe de Reca, NE, Libanati CM. Acta Metall 1968; 16:1297.

[26] Frost HJ, Ashby MF. Deformation-mechanism maps: the plasticity and creep of metals and ceramics, Oxford, New York: Pergamon Press 1982

[27] Semiatin SL, Brown TM, Goff TA, Fagin PN, Barker DR, Turner RE, Murry JM, Miller JD, Zhang F. Metall Mater Trans A 2004; 35A:3015.

[28] Zwicker U, Titanium and Titanium Alloys, Springer-Verlag, Berlin, 1974

[29] Sherby OD, Wadsworth J. Prog Mater Sci 1989; 33:169.

[30] Arieli A, Mukherjee A. Mater Sci Eng 1980; 43:47.

[31] Jain M, Chaturvedi MC, Richards NL, Goel NC. Mater Sci Eng A 1991; 138:205.

[32] Porter DA, Easterling KE. Phase transformation in metals and alloys, Van Nostrand Reinhold, Wokingham, U. K. 1988; 101

[33] Ardell AJ. Acta Metall 1972; 20:601.

[34] Speight MV. Acta Metall 1968; 16:133.

[35] Grewal G, Ankem S. Metall Trans A 1990; 21A:1645.

[36] Hu H, Rath BB. Metall Trans 1970; 1:3181.

[37] Chen CC, Coyne JE. Metall Trans A 1976; 7A:1931.

[38] Semiatin SL, Seetharaman V, Weiss I. Mater Sci Eng A 1999; 263:257.

[39] Ding R, Guo ZX, Wilson A. Mater Sci Eng A 2002; 327:233.

[40] Arieli A, Rosen A. Metall Trans A 1977; 8A:1591.

[41] Ghosh AK, Hamilton CH. Metall Trans A 1982; 13A:733.

[42] Briottet L, Jonas JJ, Montheilet F. Acta Mater 1996; 44:1665.

[43] Ghosh AK. Constitutive Equations, Metalworking: Bulk Forming ASM Handbook 2005, Vol. 14A, 582.

CHAPTER 5

ROLE OF DEFORMATION TEMPERATURE ON TRANSFORMATION INDUCED PLASTICITY IN ADVANCED TRIP STEEL SHEET

Abstract

Deformation assisted transformation of retained austenite into martensite phase is responsible for enhanced strain hardening in TRIP steel. Saturation of the transformation process directly influences the hardening mechanism and the uniform strain in a tensile test. The mechanical properties of low-alloyed TRIP steel (0.15wt%C-2.22wt%Mn-0.08wt%Si-1.35wt%Al) were investigated at the temperature range of 25 ~ 400^{o}C. Thermal activation effects on the transformation process have been studied by monitoring the hardening rate and fracture during tensile test. The results help to study the strengthening mechanism at elevated temperature, and provide the way to understand temperature dependence of ductility in these materials. Attainment of greater strengthening at elevated temperature was found to be related to the following mechanisms: (i) a more gradual but sustained transformation of retained austenite, (ii) carbide precipitation within ferrite grains, and (iii) stretching of the bainitic ferrite, the exact mechanism depending on the specific temperature. The enhanced ductility at elevated temperature was attributed to the increasing strain hardening and strain-rate hardening sensitivities.

5.1 Introduction

Conventional high strength steels have an inferior ductility, which decreases almost linearly with increasing strength. Study by Zackay et al on high-alloyed austenite steels shows potential combination of high strength and ductility [1]. The concept of transformation-induced plasticity (TRIP) originated from the martensite transformation of retained austenite during straining, which results in increasing work-hardening rate, then, enhanced strength， large uniform elongation and high energy absorption [1]. These characteristics make TRIP steel an attractive material for automotive industry to reduce vehicle weight by reducing part thickness, and enhance crash resistance. Recently, study on high-alloyed TRIP/TWIP steels (15-30 wt.% Mn, 2-12 wt.% Al, and 0-4 wt.% Si) shows super ductility (up to 95%) and high flow stress (up to 1100 MPa) at room temperature [2-4]. Their mechanical properties show typical trend that both yield strength and ultimate tensile strength decreases with increasing deformation temperature from room temperature to 400^{o}C, and the peak elongation is near room temperature. Although the high addition of alloy elements produces attractive mechanical properties, from the consideration of cost, reducing the alloys content is much more practical and necessary. Therefore, the corresponding mechanical properties of low-alloyed TRIP steel are essentially to be examined and compared with high-alloyed counterpart. In the present study, the interest is to study the mechanism of strengthening and improved ductility of low-Mn TRIP steel at elevated temperature, and how strength and formability of commercial low-Mn TRIP steel compare with high – Mn (more expensive) TRIP steel as a function of forming temperature.

5.2 Materials and Experiments

5.2.1 Materials

The chemical composition of as-received TRIP steel is listed in Table 5.1. It is a commercial galvanized low-alloy TRIP steel (0.15wt%C-2.22wt%Mn-0.08wt%Si-1.35wt%Al) with a thickness of 1.0 mm. For comparison, cold-rolled TRIP steel was also prepared by imparting an equivalent plane strain of 0.28 to the as-received TRIP steel.

5.2.2 Microstructure analysis

To reveal the multiphase microstructure of TRIP steel, the LePera method of color tint-etching was used in metallographic analysis under light optical microscope. The details of etching solution and procedure are described in [5]. Scanning Electronic Microscope (SEM) was also used to assist in identifying different phases and observing fracture surfaces. The existence of retained austenite was confirmed by 2theta/theta scan results of X-ray diffraction. The source of X-ray was provided with Cu-K_α radiation at 40kV and 100mA. Quantitative measurement for the image-based area fraction of different phase was conducted via image analysis software.

5.2.3 Mechanical tests

The uniaxial tensile samples were cut with the tensile axis parallel to the rolling direction of TRIP steel sheet. Experiments were performed at temperature of 25^{o}C, 250^{o}C and 400^{o}C in the air. For room temperature test, the specimens have dimension of 15 mm

long and 3 mm wide in gauge section. Tests were conducted in computer-controlled 5505 Instron frame with constant cross head speed of 0.5 mm/min (equivalent initial strain rate of 5.6×10^{-4}/s). An extensometer with 12.7 mm gauge length was attached on the gauge section to measure the tensile strain.

For elevated temperature tests, the specimens have the dimension of 6.35 mm long and 3.18 mm wide in gauge section. The straining was conducted with constant cross-head speed (CHS) mode in air by 4505 Instron machine. A graphic interface board (GPIB) was used for digital communication between Instron machine and computer. CHS speed was selected at 0.01 and 0.5 mm/min, which had corresponding initial strain rate of and 1×10^{-3}. Extra test at 500°C and 1.5 mm/min (corresponding $\dot{\varepsilon}$ of 3.5×10^{-3}/s) was conducted. A clamshell furnace with three independent heating zones was utilized to maintain specimen temperature within ±2°C of the test temperature. The specimen required about 20 minutes to equilibrate temperature before initiation of straining.

To evaluate the strain rate sensitivity for the investigated TRIP steel, both CHS jump test and stress-relaxation test methods were used to determine the m-value at selected temperature, which were schematically shown in Figure 5.1. For the method of CHS jump test, m-value was calculated as

$$m = \frac{\log(P_2 / P_1)}{\log(V_2 / V_1)} \tag{5-1}$$

For stress-relaxation test, the m-value was obtained from slope of stress-strain rate plot.

To estimate the strength of deformed samples, Vickers hardness was measured on uniaxial tensile tested samples. Two or more regions with various strain levels were selected in the gauge section for measurement. The indentation load is 300g, loading time 15 seconds. The hardness value was obtained by averaging over 10 measurements.

5.3 Results

5.3.1 Microstructure

Figure 5.2 shows the microstructure for the as-received TRIP steel. As can be seen, the nearly equiaxed ferrite phases (appearing in dark yellow) distribute within non-ferrite phase matrix. Compared with the optical image, the contrast is clearer in SEM image. Ferrite phase appears in deep gray, while non-ferrite phases in white. In Figure 5.2 (a), among non-ferrite phases, bainitic ferrite appears dark brown color, while retained austenite reveals in light yellow. Carbide and martensite may also exist. Due to the limitation of etching method for optical image, austenite and martensite are not separately identifiable. X-ray diffraction method was used to identify phases within the multiphases structure. The result of 2-theta/theta scan in Figure 5.3 confirmed the existence of retained austenite and some carbide. From the diffraction intensity peaks, γ (111) and γ (220) planes were related to retained austenite, and α (110), α (200) and α (211) for ferrite.

5.3.2 Stress-strain behaviors

Figure 5.4 shows the engineering stress-strain curves and true stress-strain curves for as-received TRIP steel. The logarithm of true stress-strain curves was also shown in the same figures (Figure 5.4(c) and Figure 5.5(c)). Compared with the result of room temperature, the true stress-strain curves of as-received samples at elevated temperature (Figure 5.4 (b)) reveal that strain hardening effect becomes gradual as the testing temperature rises. By Considére construction method,

$$(d\sigma / d\varepsilon) = \sigma \tag{5-2}$$

uniform strain can be determined for different temperature testing. The results show that uniform strain increases when the testing temperature rises to 250^{o}C. The strain hardening exponent (n-value) can be obtained from the slope of logarithm of true stress-strain curves (Figure 5.4(c)). For the room temperature tensile testing, the n-value gradually decreases with the increasing strain. In contrast, n-value increased with increasing strain at rising temperature.

As seen from Figure 5.5, compared with as-received TRIP steel, considerable strengthening can be observed on the cold-rolled materials due to pre-strain effect. This strain hardening still took effect at elevated temperature up to 250^{o}C. Meanwhile, uniform strain determined by Considére construction increases when the temperature rise from room temperature to 250^{o}C for the cold-rolled TRIP steel. However, increasing temperature from 250^{o}C to 400^{o}C has little effect on uniform strain (Figure 5.5 (b)). In

contrast to the as-received materials, n-value for all testing temperature (Figure 5.5(c)) decreases with increasing strain. Moreover, the decreasing of n-value is faster at room temperature. This may be resulted from the transformation saturation of retained austenite, which deteriorates the TRIP effect. Result from extra testing at 500^{o}C (Figure 5.5 (a)) shows smaller rate of necking, though the strain rate is much higher for this testing, which indicates the important role of temperature on deformation.

5.3.3 Mechanical Properties

Table 5.2 summarizes the mechanical properties for both the as-received TRIP steel and cold-rolled TRIP steel. For as-received TRIP steel, temperature has slight effect on yield stress and ultimate tensile strength. As testing temperature rises from room temperature to 400^{o}C, yield stress increases slightly from 394 MPa to 422 MPa, while ultimate tensile strength decreases from 793 MPa to 740 MPa. However, the values of elongation show large dependence on testing temperature. When testing temperature increases to 250^{o}C, the uniform elongation rises to be more than two times that at room temperature, as well as the post-uniform and total elongation. At 400^{o}C, the total elongation is almost the same as the result obtained at 250^{o}C, whereas the uniform strain is smaller than that at 250^{o}C (shown in Figure 5.6).

Comparing with as-received materials, prestraining causes large increase in the yield stress for cold-rolled TRIP steel from 394 MPa to 950 MPa at room temperature, as well as ultimate tensile strength from 793 MPa to 986 MPa. Within the overall investigated temperature range, the cold-rolled materials have higher strength than as-received

materials. Moreover, the ratio of yield stress to ultimate tensile strength is larger which indicates lower work hardening effect with strain. In contrast to as-received samples, the yield stress of the cold-rolled TRIP steel decreases considerably with increasing temperature. At the same time, temperature has complex effect on ultimate tensile strength. That is, the ultimate tensile strength of the cold-rolled TRIP steel increases as the testing temperature rises from room temperature to 250^{o}C, but decreases as the testing temperature rises from 250^{o}C to 400^{o}C. This may indicate different strengthening mechanisms at these two testing temperature. Furthermore, compared with as-received materials, pre-strained samples have much lower elongation. The uniform elongation is almost one-tenth to that of the as-received materials at room-temperature. For cold-rolled TRIP steel, both the uniform elongation and total elongation increase linearly with increasing temperature. Temperature has more obvious effects on post-uniform elongation.

By comparing the fracture strain and fracture strength between these two materials, it can be seen that the fracture strength is quite close, while as-received steel shows higher fracture strain within overall testing temperatures. The strain for both materials linearly increases with increasing temperature. The true strain in the thickness and width direction were also measured as shown in Figure 5.7 (a) and (b) for as-received and cold-rolled specimens respectively. Both two materials show more reduction in thickness than in width. As shown in Figure 5.7 (c), as-received materials attained higher strain both in thickness and width. Moreover, increasing temperature from 250^{o}C to 400^{o}C increases thickness strain significantly.

5.3.4 Effects of strain hardening and strain rate hardening

To examine the strain hardening rate and strain rate sensitivity for investigated TRIP steel, the n-value and m-value were plotted with temperature in Figure 5.8. The n-value is determined by slope of logarithm of true stress-true strain curves. Terminal n values were chose for comparison, because it is related to uniform strain and formability. The left side curves in Figure 5.8 show the change of terminal n-value with temperature. Both as-received and cold-rolled TRIP steels show larger terminal strain hardening rate at elevated temperature; and largest terminal strain hardening rates were obtained at 250^{o}C. However, terminal n-values of the cold-rolled steel have one magnitude lower than that of the as-received one. Moreover, the largest terminal n-value of 0.31 was obtained at 250^{o}C for as-received sample. Similarly, larger m-values were shown at elevated temperature for both of the as-received and cold-rolled TRIP steels. However, as temperature rises from 250^{o}C to 400^{o}C, the m-value of as-received TRIP steel drops. The fact that n-value and m-value simultaneously increase with increasing temperature is uncommon to other metallic alloys.

5.3.5 Post-deformed properties

The combining effect of tensile strain and temperature on the strength of TRIP steel was examined by Vickers hardness test. The regions for hardness test were selected from grip and gauge regions of tensile tested samples, in which different strain levels were obtained during testing. On grip region, it is assumed that the strain is zero. The largest strain is at

the region where is close to facture surface. Figure 5.9 shows the change of hardness with tensile strain at different temperatures. From Figure 5.9 (a), it can be seen that heat treatment at different temperature has little effect on strength of non-strain as-received materials. However, thermal effect assists in strengthening during deformation, and causes about 20% increase of hardness or strength of the material, indicating that the volume fraction of martensite in the warm-formed material is higher. Moreover, as-received steel has higher strain-hardening rate at 250^{o}C than that at the other two selected temperatures. For cold-rolled materials, tensile strain and temperature have similar effect on strength to as-received materials. Moreover, prestrain and post-heat treatment causes high strengthening of TRIP steel.

In Figure 5.10, the mechanical properties of low-Mn TRIP steel (0.15wt%C-2.22wt%Mn-0.08wt%Si-1.35wt%Al) in present study were compared with those of high-Mn TRIP steel (20.1wt%Mn-2.8wt%Si-2.9wt%Al, and 400ppm of C) [2] within the temperature range of 25 ~ 400^{o}C. As can be seen, in the overall investigated temperature range, the low-Mn TRIP steel has higher strength than the high-Mn TRIP steel. The higher strength can be attributed to the higher carbon content in low-Mn TRIP steel. However, the uniform and total strain for these two materials are close to each other between 250 ~ 400^{o}C.

5.4 Discussions

The volume fraction of each phase in microstructure largely determines the final properties of TRIP steel. Especially, the amount and thermal stability of retained

austenite play key roles for TRIP effect. The constituents of microstructure were essentially decided by chemical composition and processing path. Compared with conventional C-Mn-Si TRIP steel, the advantages of partial or complete substitution of Si by Al has been studied [6, 7]. Substitution of Si by Al can increases the volume fraction of retained austenite, as well as bainite, which causes higher strength and ductility than for C-Mn-Si steel. In present study, more Al content (1.35wt %) was alloyed than Si (0.08wt %).

For as-received steel, the largest uniform elongation was obtained at 250^{o}C. Figure 5.11 (a) shows the microstructure after static heat treatment at 250^{o}C, which was taken from the grip area of tested specimen. It can be seen that retained austenite has little change comparing with the as-received material. It indicates that the retained austenite in investigated TRIP steel is quite stable at 250^{o}C. After deformation (Figure 5.11 (b)), both ferrite matrix and boundary phases were elongated. The image-based analysis shows that the volume fraction of non-ferrite phase increased after elevated temperature stretching (Figure 5.12). Moreover, XRD scanning has no detection from the retained austenite phase. It is believed that martensite transformation has undergone with straining. However, for room-temperature test, the ferrite grains were elongated (Figure 5.13), while the non-ferrite phase has little change in shape and amount. Void formation occurs in the interfaces between the ferrite and non-ferrite phase. Also, the austenite still can be detected after severe straining. It indicates that the transformation of retained austenite was incomplete. With regard to composite-like nature of microstructure for TRIP steel, strain incompatibility causes high stress concentrations developing in phase interfaces

during straining. Strain-induced transformed martensite or bainite dispersed along the phase boundaries of soft ferrite grains generates high dislocation density in the adjoining ferrite phases. The incremental work-hardening rate and thus the strength-ductility balance at the onset of necking are mainly influenced by the rate of creation of supplementary dislocations in ferrite. It has been concluded that the transformation rate of retained austenite and thus its mechanical stability are the key factors influencing the work-hardening behavior of TRIP-aided steels [8]. For straining at room temperature, too high value of rate of the martensite transformation at the beginning of deformation results in preliminary fracture. The break between the ferrite phases and martensite releases the stress concentration on interface, and cease further straining on retained austenite. Thus, the further strain mainly concentrates on cavity growth, which deteriorates the TRIP effect. Consequently, strain hardening rate decreases with increasing straining for room temperature tension.

However, being assisted with thermal effect, the kinetics of phase transformation is slowed down [9]. When the testing temperature rises, martensite and bainite were softened at elevated temperature. Compatible strain can be developed on phase interfaces to keep continuity in microstructure. Martensitic transformation can sustain to cause gradual work hardening on materials, which reflects on the continuous increasing of strain hardening rate on true stress-true strain curve for 250^{o}C of as-received TRIP steel. Furthermore, because of the stretching on hard bainite and martensite, higher stress is needed to cause strain on them. Therefore, the yield stress for as-received TRIP steel at 250^{o}C is slightly higher than that at room temperature. When increasing the temperature

to 400°C, the true stress-true strain of the as-received material is similar to that of 250°C, while the initial strain hardening rate is smaller, and yield stress is slightly higher than that at the lower testing temperature. Figure 5.14 (a) shows the microstructure after static heat treatment at 400°C, which was taken from the grip region of tested specimen. Compared with other testing temperatures, the volume fraction of the non-ferrite phase was reduced greatly. Large amount of fine particles precipitated within ferrite grains. It was suggested that the retained austenite is stable up to 350°C, and the austenite begins to decompose into ferrite and cementite at the temperature higher than 370°C due to solute carbon redistribution for 0.2 wt.%C-1.51 wt.%Mn-1.96 wt.%Si steel [10]. For 0.183 wt.%C-1.56 wt.%Mn-1.73 wt.%Al-0.02 wt.%Si steel, it was reported that the retained austenite decomposed at 450°C [7]. Koistinen and Marburger's athermal equation also predicts that the retained austenite can decompose into ferrite and carbides if the retained austenite is held for prolonged times at higher temperature [11]. In present study, specimen was held for 20 mins to equilibrate temperature at 400°C. The holding time is much longer than the typical time (4-8 mins) for isothermal bainite transformation [12]. Thus, for the test at 400°C, similar thermal effect is expected to take place. Therefore, the interaction between dislocation motion and carbide precipitate, the redistribution of solute carbon within the ferrite phases, as well as the rest of retained austenite take effect on the strengthening of TRIP steel.

For pre-strained TRIP steel, certain amount of retained austenite transformed to martensite during cold rolling, which increase the volume fraction of martensite. Hard martensite phase and strain-hardening effect strengthen the TRIP steel at the beginning of

deformation. However, the work-hardening rate and elongation were heavily deteriorated. The strain mode of rolling is similar to plane strain. It has been reported that the mode of plane strain tension can faster the transformation rate of retained austenite [13, 14]. Low volume fraction of retained austenite is not enough to exert TRIP effect.

5.5 Conclusions

1) TRIP steel at room temperature exhibits high yield strength of 394.4 MPa and ultimate tensile strength of 793.2 MPa with uniform strain of 16%. Increasing deformation temperature above room temperature slows down initial strain hardening rate for TRIP steel, but terminal *n value* increases, and total elongation increases.
2) For deformation-assisted phase transformation, transformation induced hardening slows down possibly due to thermally activated flow stress, but transformation appears to go to a greater degree of completion, which causes a 20% increase in hardness or strength of the materials, indicating that the volume fraction of martensite in the warm-formed materials is higher.
3) Both n and m values increase simultaneously with increasing temperature in these alloys thereby enhancing overall formability of TRIP steel. Uniform strain goes up from 16.2% to 37.1%.
4) Deformation at elevated temperature causes stretching of the multiphase interfaces, and when local strains are high, void formation can occur.
5) Attainment of greater strengthening at elevated temperature was found to be related to the following mechanisms: (i) a more gradual but sustained transformation of

retained austenite, (ii) carbide precipitation within ferrite grains, and (iii) stretching of the bainitic ferrite, the exact mechanism depending on the specific temperature

Table 5.1 Chemical composition of commercial TRIP steel used in this study, %

C	Mn	Si	Al	Cr	Mo
0.15	2.22	0.08	1.35	0.1	0.1

Table 5.2 Mechanical Properties of TRIP Steel for Tests at Various Temperatures

	As-received			*Cold-rolled*		
	Room-temp	***250 °C***	***400 °C***	***Room-temp***	***250 °C***	***400 °C***
σ_y, *MPa*	394.4	400.0	422.2	950.0	927.8	850.0
σ_{UTS},*MPa*	793.2	760.4	739.6	985.9	1055.8	945.0
e_U, *%*	16.2	37.1	28.6	1.8	5.2	5.6
$e_{post\text{-}U}$, *%*	11.4	20.4	29.3	6.0	16.0	24.1
e_{total}, *%*	27.6	57.5	57.9	7.8	21.2	29.7
Frac. Strain	0.74	0.90	1.19	0.52	0.64	0.94
Frac. Strength, MPa	1376.9	1511.4	1650.9	1344.4	1625.3	1386.9
Terminal n	0.18	0.31	0.27	0.017	0.072	0.064
m	0.0069	0.0155	0.0115	0.0071	0.0167	0.0169

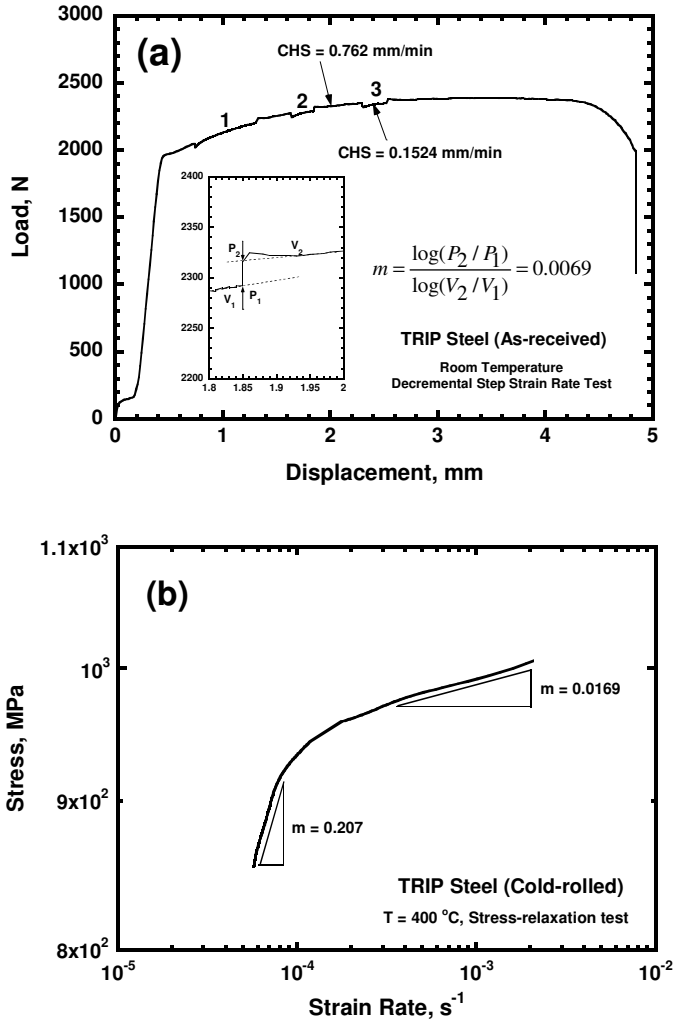

Figure 5.1 Schematics of test methods to determine *m*-value (a) CHS jump test, and (b) stress-relaxation test

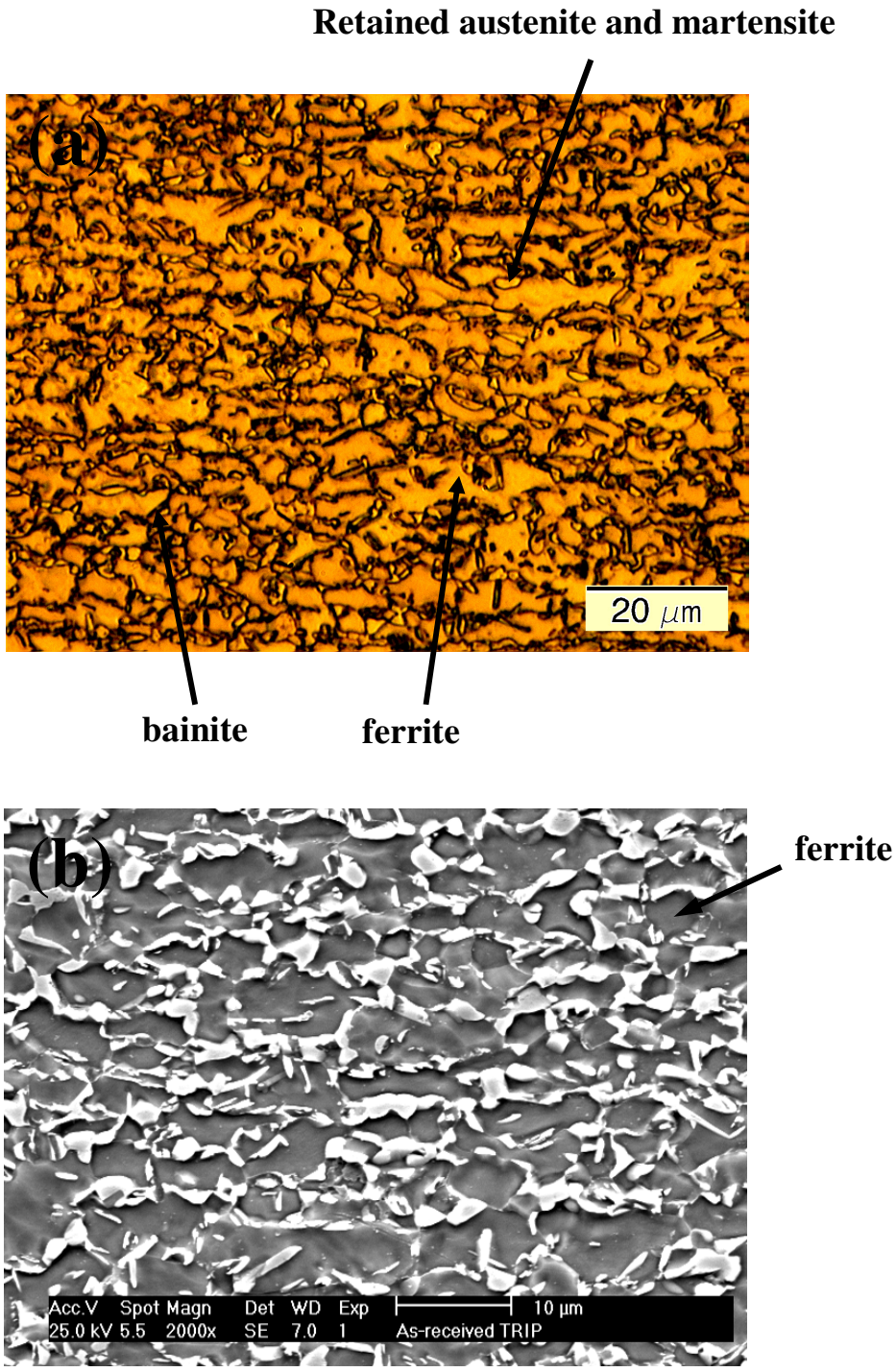

Figure 5.2 Microstructure of as-received TRIP steel showing multiphase structure (a) Light optical image, (b) SEM image

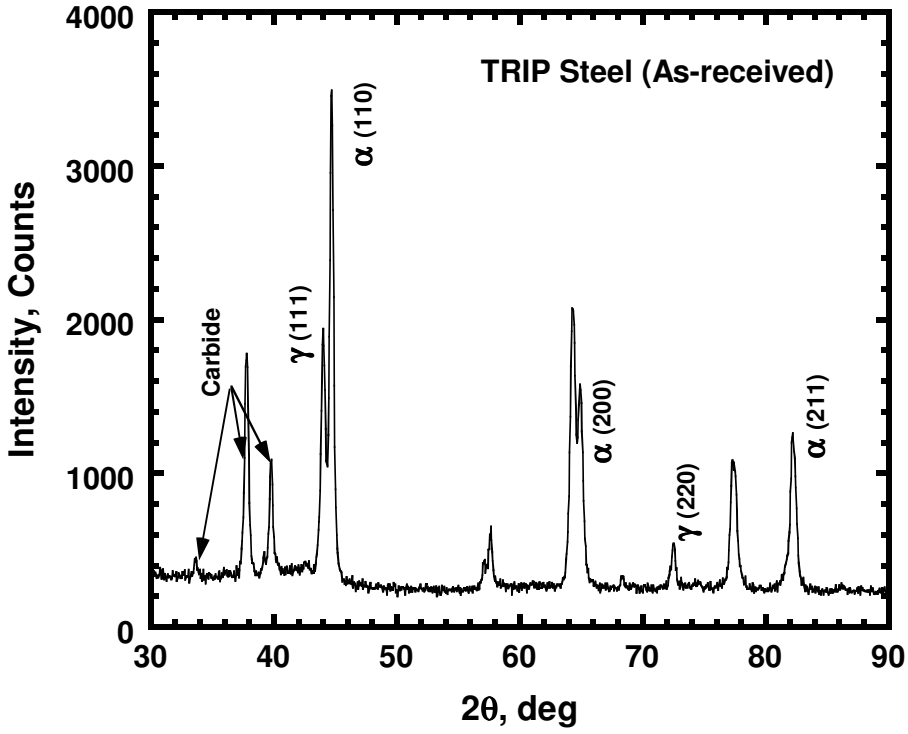

Figure 5.3 X-ray diffraction pattern of as-received TRIP steel confirms the exist of retained austenite.

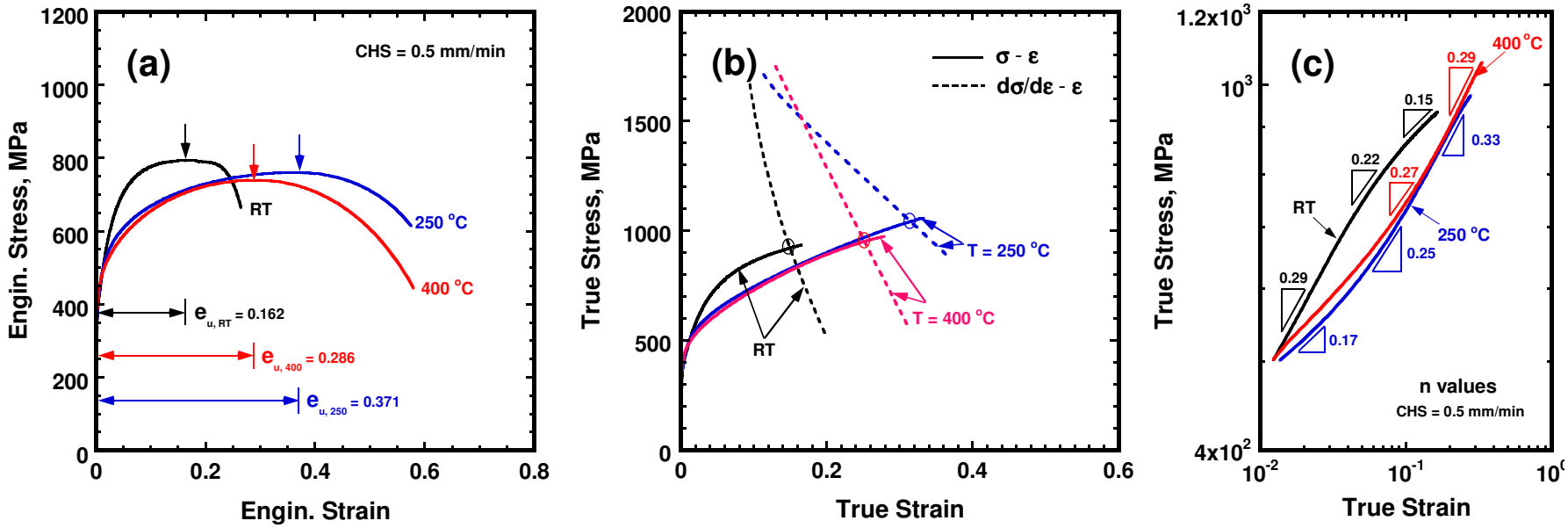

Figure 5.4 Stree-strain curves of as-received TRIP steel,
(a) engineering stress-engineering strain, (b) true stress-true strain, (c) log stress-log strain

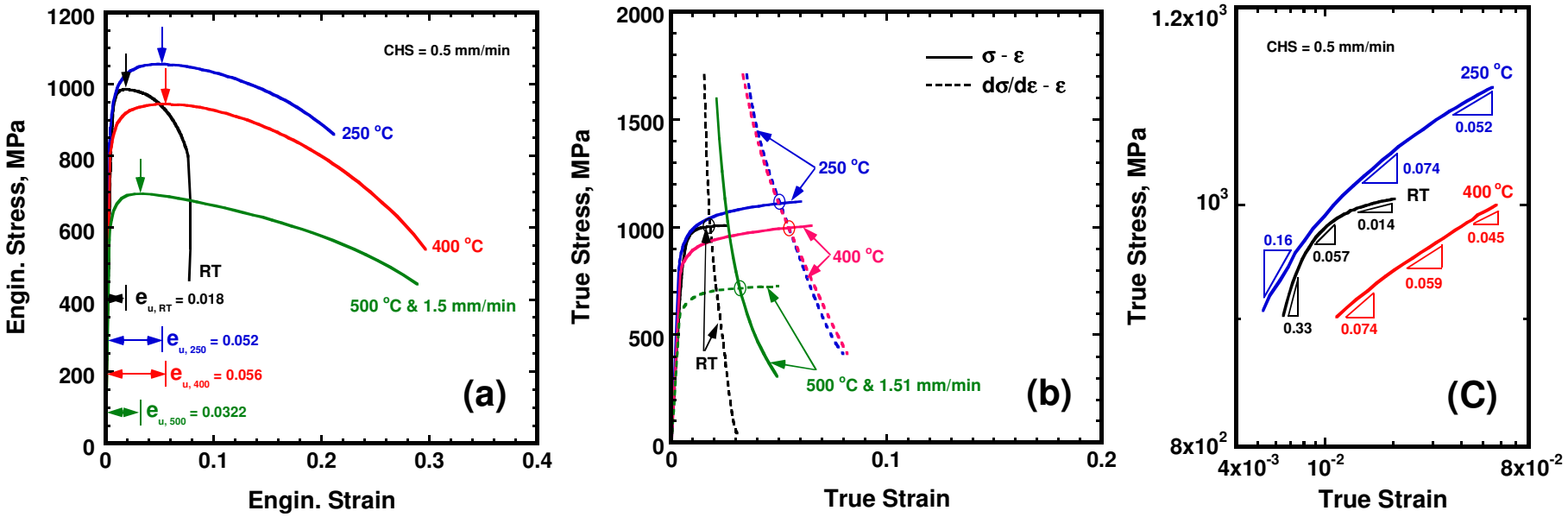

Figure 5.5 Stree-strain curves of cold-rolled TRIP steel (ε = 0.28),
(a) engineering stress-engineering strain, (b) true stress-true strain, (c) log stress-log strain

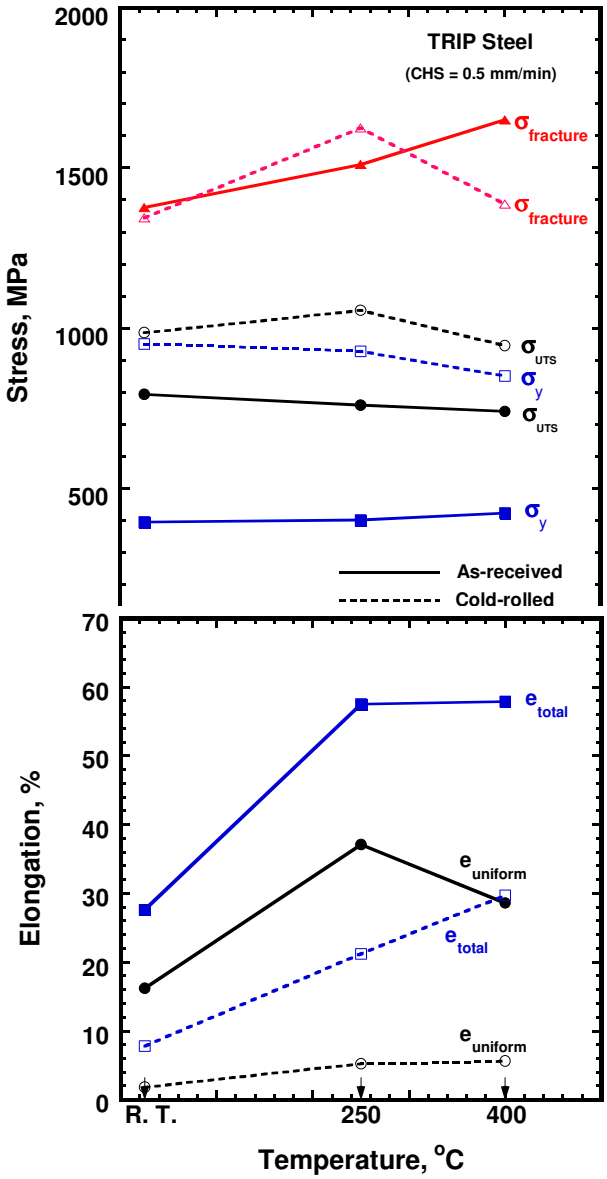

Figure 5.6 Mechanical properties of investigated TRIP steels

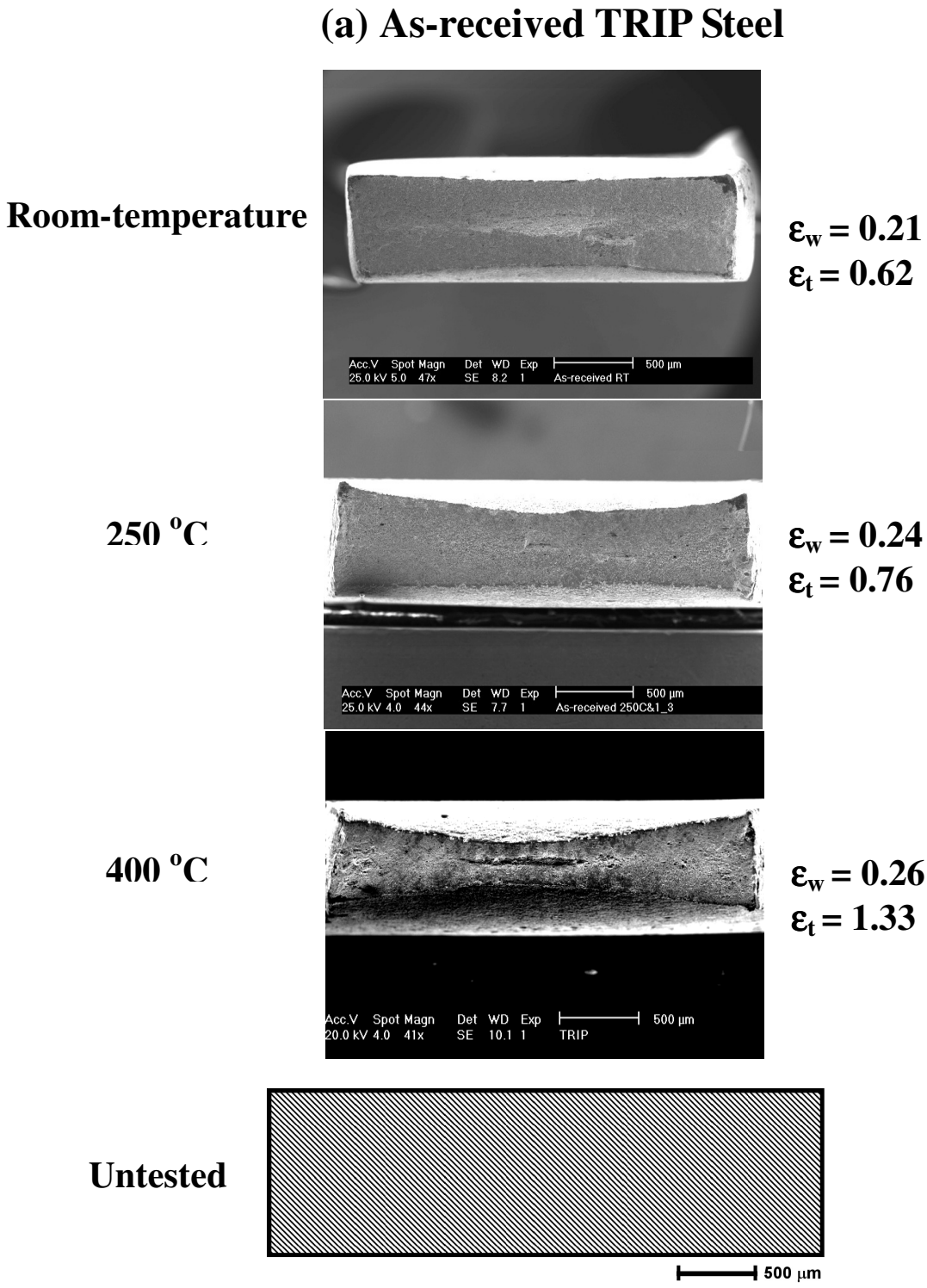

Figure 5.7 (a) Fracture surfaces of tensile tested specimen at various temperatures for as-received TRIP steel, where ε_w is strain in width direction and ε_t is strain in thickness direction. It shows increasing thickness reduction with rising temperature.

(b) Cold-rolled TRIP Steel

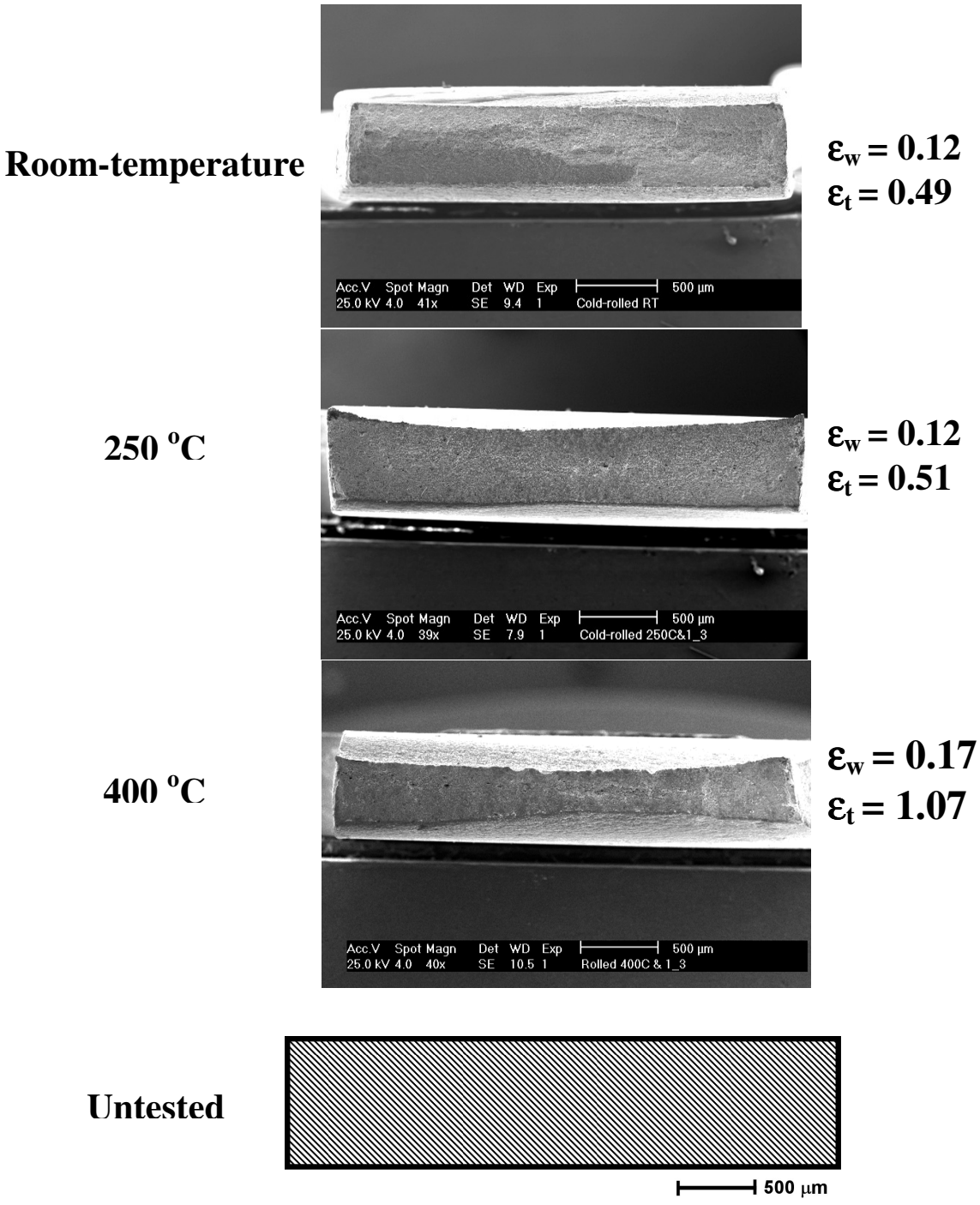

Figure 5.7 (b) Fracture surfaces of tensile tested specimen at various temperatures for cold-rolled TRIP steel, where ε_w is strain in width direction and ε_t is strain in thickness direction. It shows increasing thickness reduction with rising temperature.

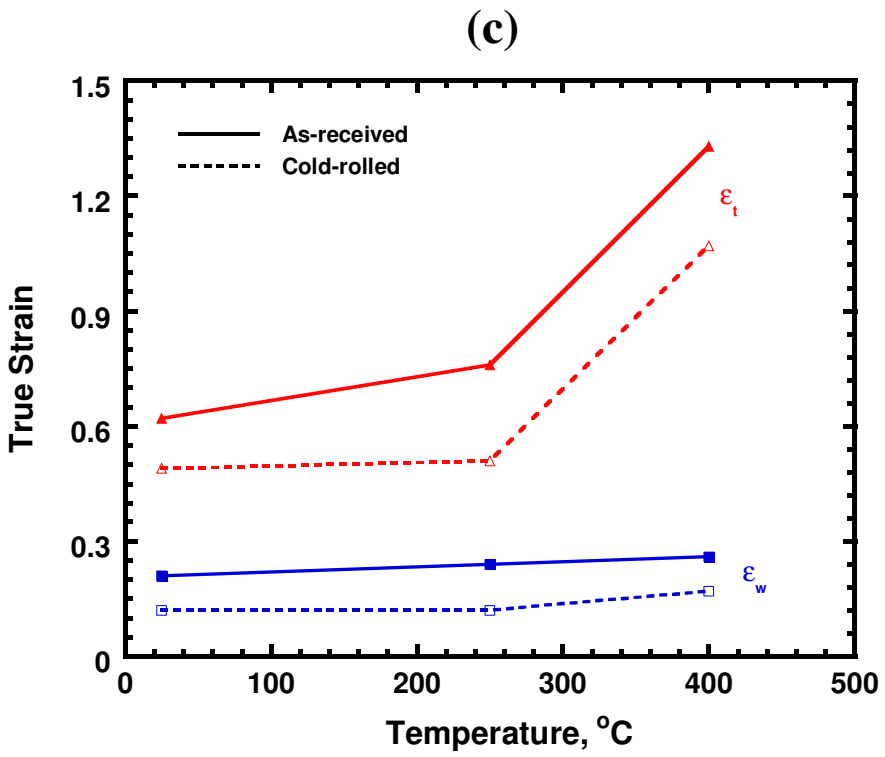

Figure 5.7 (c) Changes of fracture strain with temperature show that increasing temperature increases the strain in thickness. Compared with cold-rolled specimen, as-received TRIP materials show larger fracture strain.

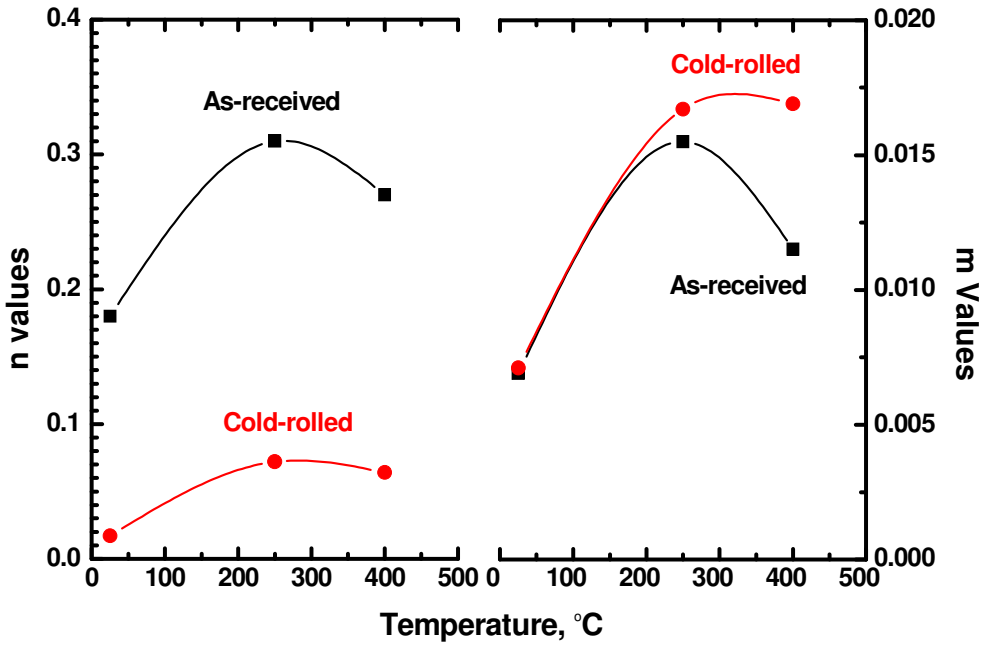

Figure 5.8 Changes of *n-value* and *m-value* of investigated TRIP steel with temperature show large strain hardening and strain rate sensitivity at elevated temperature.

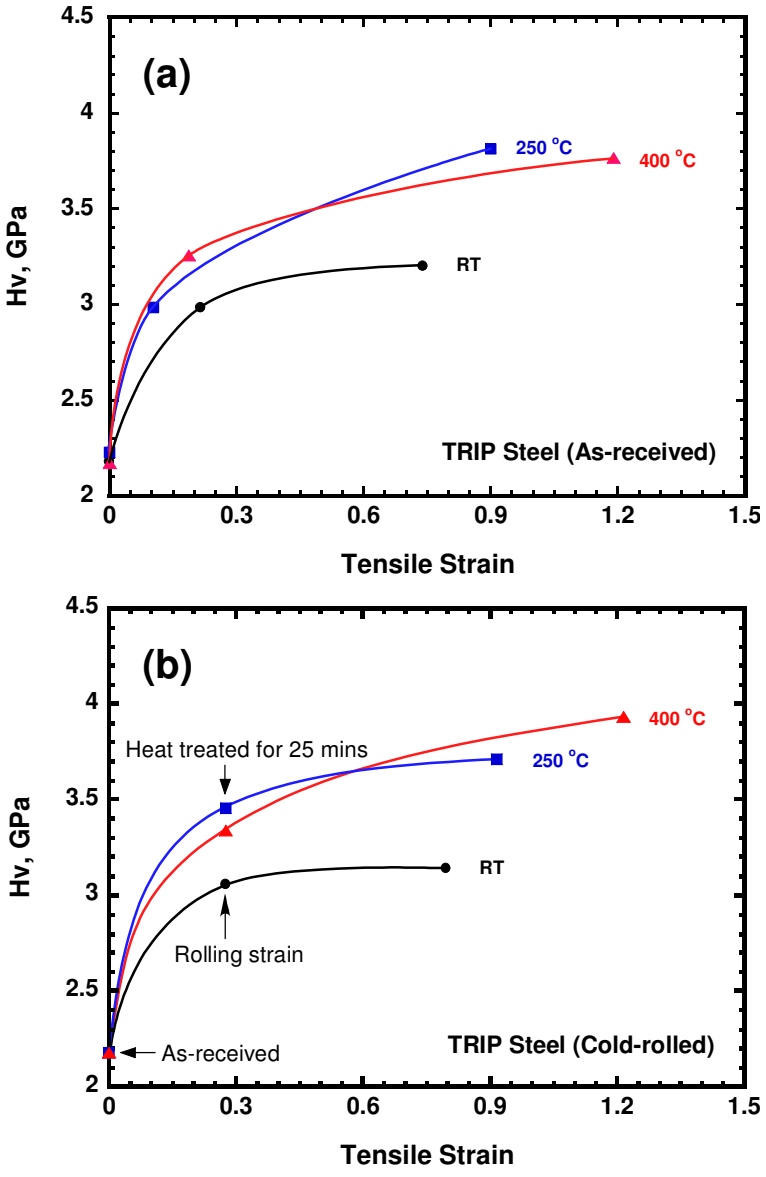

Figure 5.9 Microhardness of investigated TRIP steel for various temperatures shows strengthening effect after deformation at elevated temperature.
(a) As-received, (b) Cold-rolled

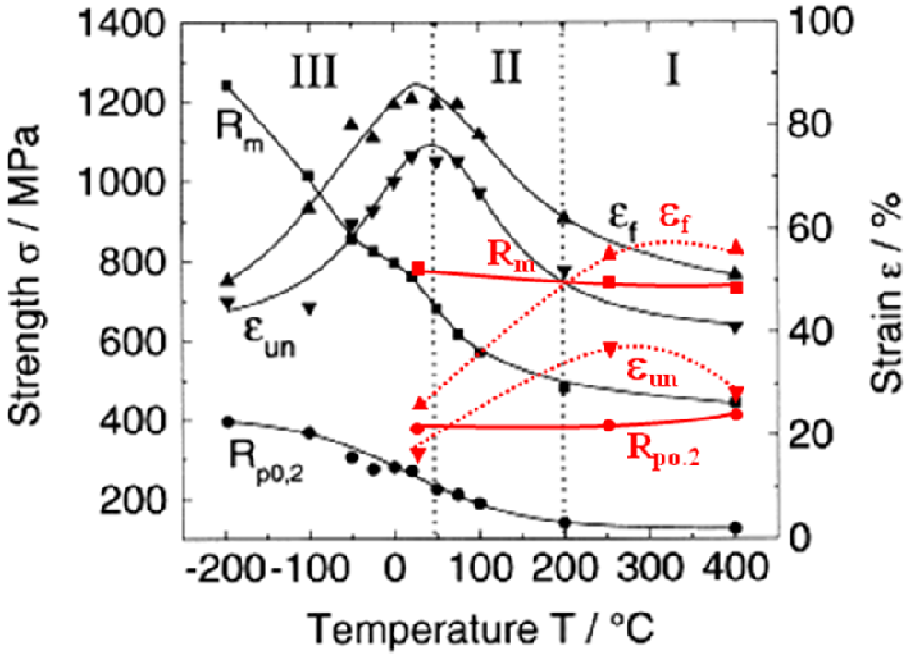

Figure 5.10 Effects of temperature on the strength and strain of high-Mn and low-Mn TRIP steel (in presnt study). The data of black curves is from reference [2], the data of red curves is for the present study.

Note: $R_{p0.2}$ --- Yield stress, R_m --- Tensile strength, e_{un} --- Uniform elongation, and e_f --- Total elongation.

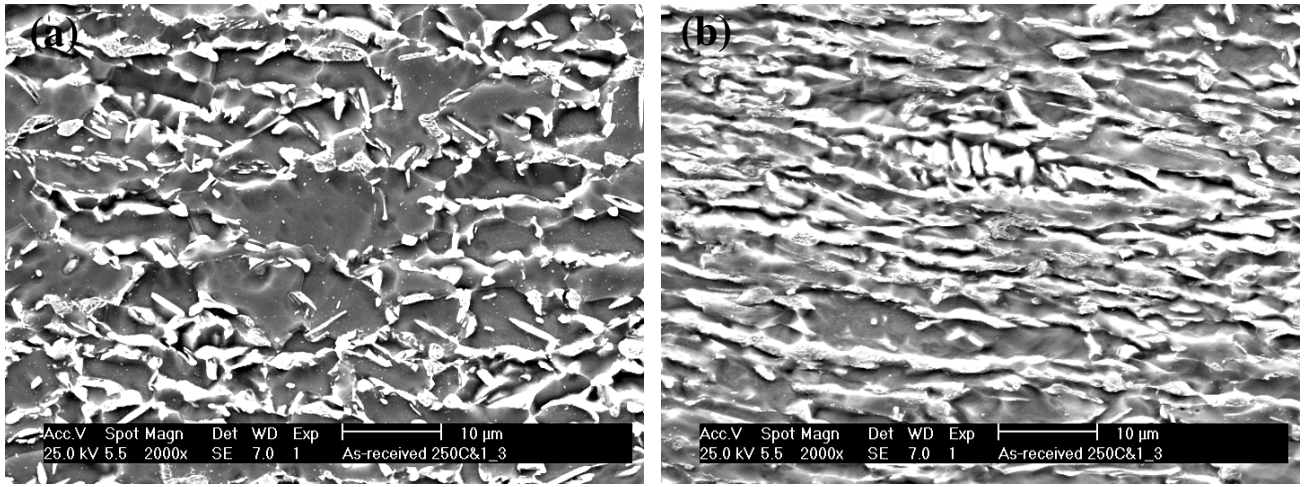

Figure 5.11 Microstructures of specimen tested at 250^{o}C for as-received TRIP steel show stretching of ferrite and non-ferrite phase during deformation. (a) grip region, (b) gauge region

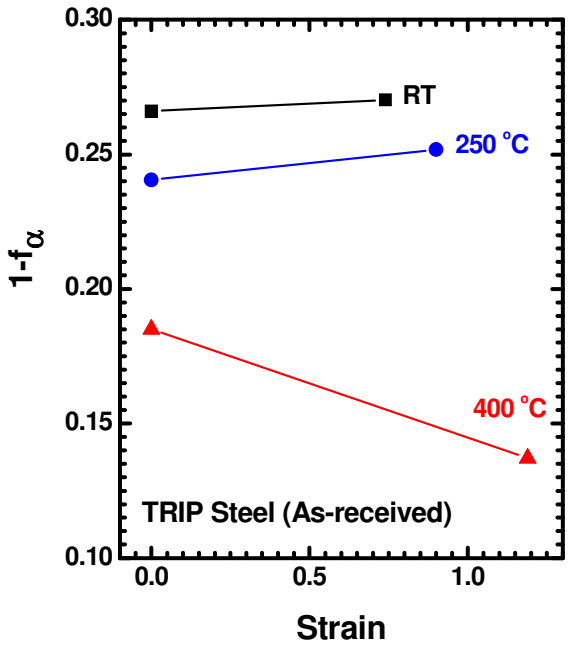

Figure 5.12 Temperature and strain effects on the change of volume fraction of non-ferrite phase.

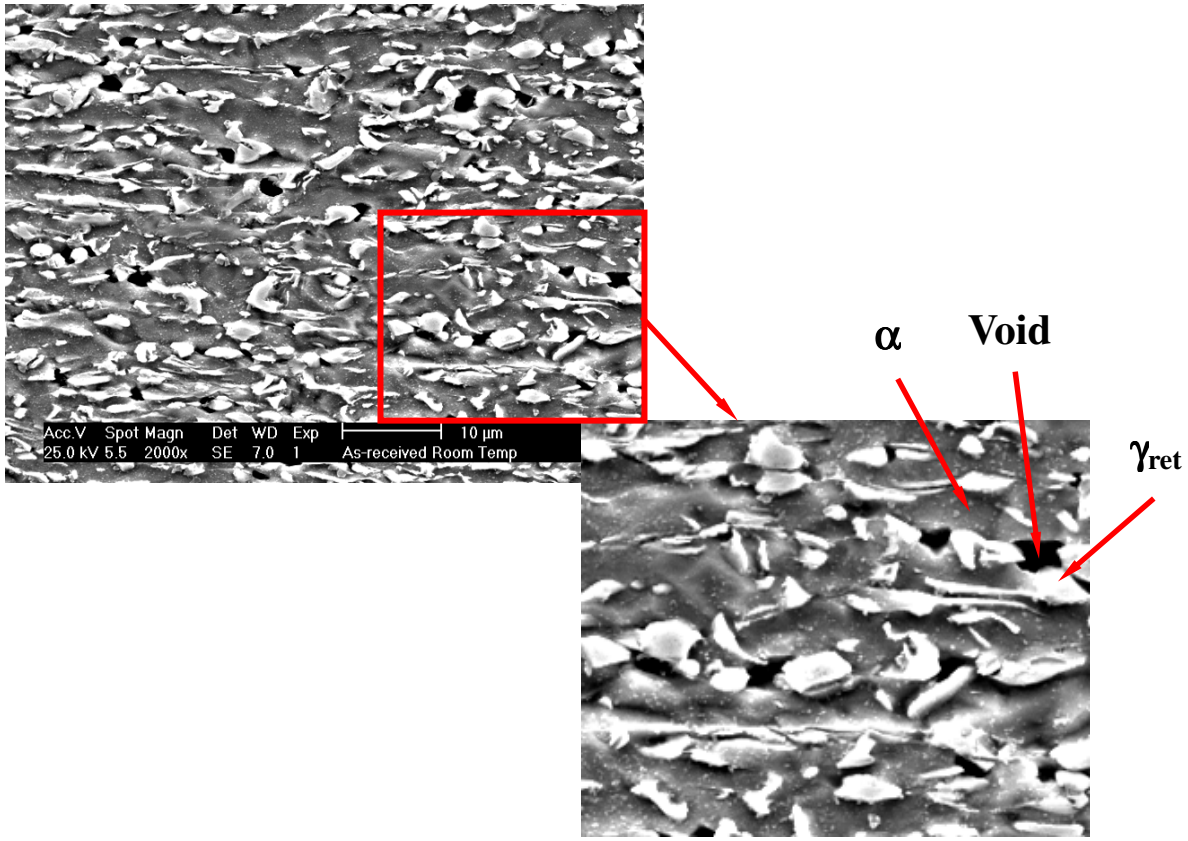

Figure 5.13 Deformed microstructure of as-received TRIP steel tested at room temperature shows void formation.

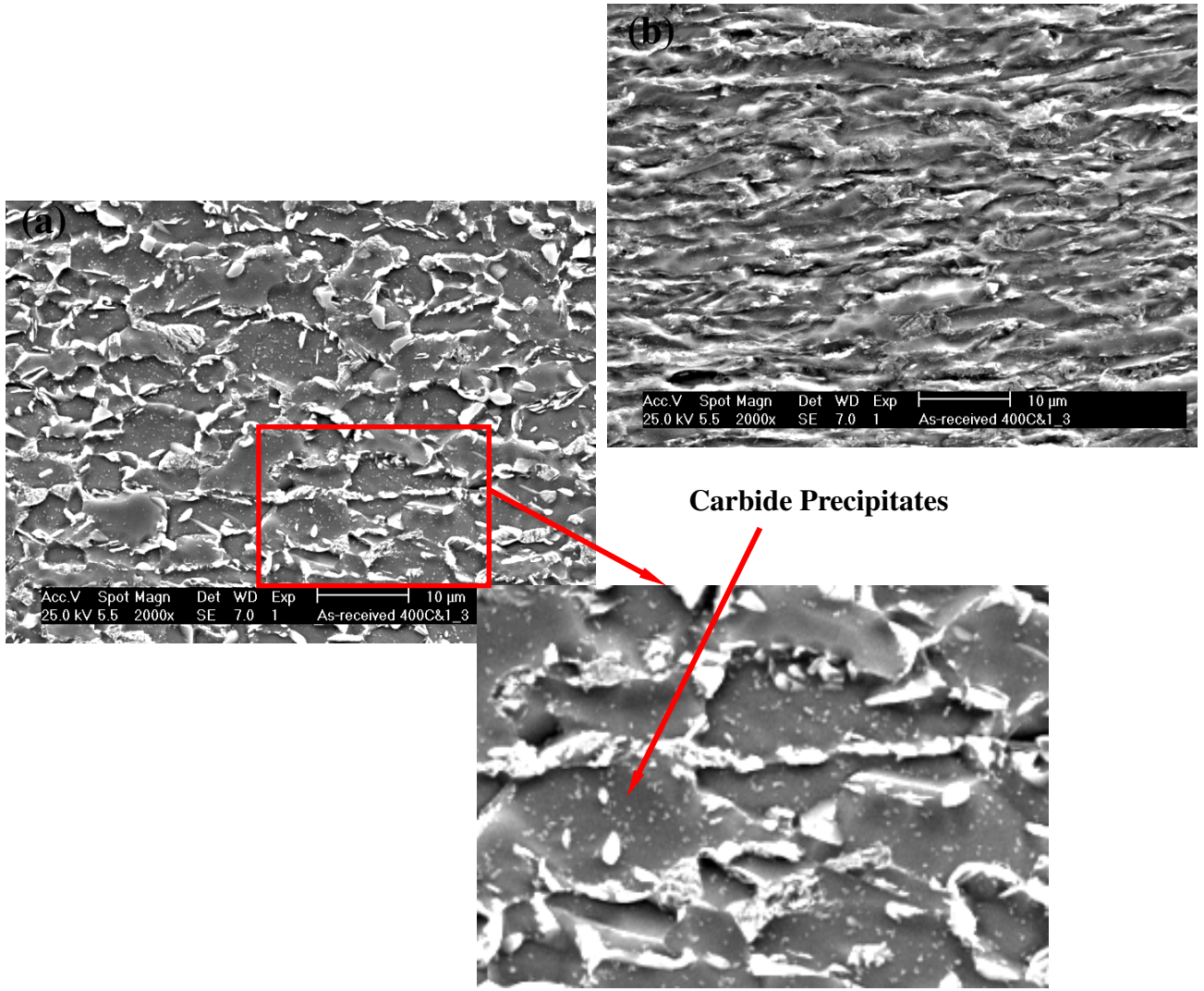

Figure 5.14 Deformed microstructure of as-received TRIP steel tested at 400°C shows carbide precipitation at this temperature,(a) grip region, (b) gauge region

5.6 References

[1] Zackay VF, Parker ER, Fahr D, Busch R. Trans ASM 1967; 60:252.

[2] Grassel O, Kruger L, Frommeyer G, Meyer LW. Inter J Plast 2000; 16:1391.

[3] Frommeyer G, Brux U, Neumann P. Iron Steel Inst Inter 2003; 43:438.

[4] Frommeyer G, Brux U. Steel Res Inter 2006; 77:627.

[5] De AK, Speer JG, Matlock DK. Adv Mater Proc 2003; 161:27.

[6] De Meyer M, Vanderschueren D, De Cooman BC. Iron Steel Inst Inter 1999; 39:813.

[7] Mahieu J, Maki J, De Cooman BC, Claessens S. Metall Mater Trans A 2002; 33A:2573.

[8] Jacques P, Furnémont Q, Mertens A, Delannay F. Phil Mag A 2001; 81:1789.

[9] Berrahmoune MR, Berveiller S, Inal K, Moulin A, Patoor E. Mater Sci Eng A 2004; 378:304.

[10] Jun HJ, Park SH, Choi SD, Park CG. Mater Sci Eng A 2004; 379:204.

[11] Wilson EA, Medina SF. Mater Sci Tech 2000; 16:630.

[12] Cooman BC. Curr Opin Sol Stat Mater Sci 2004; 8:285.

[13] Larour P, Verleysen P, Bleck W. J Phys IV 2006; 134:1085.

[14] Yu HY, Gao YK, Meng DJ. Mater Sci Eng A 2006; 441:331.

CHAPTER 6

SUMMARY AND RECOMMENDATIONS FOR FUTURE WORK

6.1 Summary

Grain refinement provides a potential approach to improve formability and strength of polycrystalline metal materials. Analytical and experimental work was performed to evaluate these effects.

In the analytical work, stress-strain response of polycrystals was estimated by an anisotropic continuum model, which consists of grain interior and grain boundary. Grain interior behavior is controlled by crystal slip with strain hardening and anisotropy as well as size effect; and grain boundary behavior is controlled by viscous response. The predicted dependence of strength on grain size was in agreement to Hall-Petch relation with strength varying from (grain size)$^{-0.38}$ to (grain size)$^{-0.76}$ in many cases that was studied. The simulation also predicted weakening of materials at very fine grain size when grain boundary viscosity is low or it approaches Newtonian viscous behavior. Simulation results also show that flow stability of polycrystals is affected by strength of grain boundary, and relative fraction of total strain contributed from grain interior and grain boundary.

For processing of AZ91D alloy, it was found that twinning dominates the deformation processing and helps subdivide the coarse primary α particles in thixomolded alloy. Slip occurs in the inter-twin region with strain. Extensive twinning occurs with increasing strain, but the previously twinned segments rotate with slip, to accommodate plastic flow. By ABRC processing, ultra-fine grained structure was produced with average grain size of 0.8 μm, and the uniformity of grain structure is improved. Basal texture was developed in the sheet plane, but texture intensity is weaker by this process. The processed material shows increase in both strength and ductility at room temperature. Elevated Temperature formability is improved significantly over that of thixomolded alloy.

Submicrocrystalline Ti-6Al-4V alloy can be successfully produced by compression under constraint. With anisothermal condition, initial coarse grain structure (produced by β annealing and water quench) was refined into equiaxed grains with grain size of 0.4 μm. This ultra-fine grained structure was created by breaking up of fine marteniste platelets within the initial coarse grain at low temperature, and recovery or recrysllization at increasing temperature. Enhanced superplasticity at low temperature (600 ~ 700^{o}C), and high strain-rate sensitivity (0.5 ~ 0.6) were observed on the processed Ti-6Al-4V. Low yielding stress at the beginning of deformation, and pronounced strain hardening was developed with increasing temperature, which is related to the concurrent grain growth during deformation. The determined apparent activation energy (172 kJ/mol) and diffusion coefficient at temperature range of 600 ~ 700^{o}C and strain rate of $5\times10^{-4}s^{-1}$

suggested rate controlling mechanism to be grain boundary sliding accommodated by grain boundary or core diffusion.

Thermal-assisted plastic flow improves the formability of low-Mn TRIP steel. Strain hardening rate and strain rate sensitivity were found to increase simultaneously with increasing temperature in these alloys, thereby enhancing overall formability. Failure of TRIP steel at room temperature is caused by stress concentration on multiphase interfaces where local strain incompatibility leads to void formation. Stress concentration is reduced at elevated temperature (250-400^{o}C) due to thermal assist, thereby allowing a more complete transformation of retained austenite to occur before void formation begins. Transformation is therefore induced by the amount of local interfacial strain. Attainment of greater strengthening at elevated temperature was found to be related to the following mechanisms: (i) a more gradual but sustained transformation of retained austenite, (ii) carbide precipitation within ferrite grains, and (iii) stretching of the bainitic ferrite, the exact mechanism depending on the specific temperature.

6.2 Recommendations for future work

(1) For analytical work, FEM simulation can (a) be extended to evaluate many other effects on the strength and formability of polycrystals, such as boundary type (tilt boundary, twist boundary and mixed boundary), boundary misorientation (low angle

and high angle boundary), and boundary geometry (non-uniform or non-equilibrium boundary) by designing complex boundary geometry, by which stress and strain concentration could be predicted; and (b) be extended to predict mechanical behavior of polycrystals at elevated temperature by incorporating elevated-temperature stress-strain behaviors of grain boundary and grain interior; and (c) be extended to simulate the mechanical properties of multiphase polycrystalline material by defining individual constituent with different mechanical properties.

(2) For magnesium alloy, strengthening and increased formability were found by grain refinement and high alloying. Due to the dissolution of β phase ($Mg_{17}Al_{12}$) into matrix of α phase above 200°C, the stability of this phase at elevated temperature should be evaluated to determine optimum superplastic conditions. Other heat treatable magnesium alloys such as ZK60 and ZE41 should be explored to determine and understand the role of precipitates on the grain refinement and strengthening of materials. Stable precipitates can pin grain boundary during elevated-temperature deformation to suppress dynamic grain growth; and during severe plastic deformation, high stress concentration may develop around coarse precipitates to promote grain refinement of materials.

(3) For the method used for processing ultra-fine grained Ti-6Al-4V alloy, large scale operation could be extended by conducting wrap-rolling, for which softer materials

such as low-carbon steel can be used as pressure media to execute constraint deformation; or by conducting rolling by shaped rolls. Also, post-deformed properties need to be evaluated.

(4) For TRIP steel, work should be done to analyze the evolution of martensitic transformation of retained austenite during deformation to optimize the TRIP effect for forming applications, such as biaxial forming.